

In-depth characterization and cell culture- based production of influenza A virus defective interfering particles

Dissertation

zur Erlangung des akademischen Grades

Doktoringenieur

(Dr.-Ing.)

von M.Sc. Lars Pelz

geb. am 22.10.1993 in Ludwigsburg

genehmigt durch die Fakultät für Verfahrens- und Systemtechnik
der Otto-von-Guericke-Universität Magdeburg

Gutachter/innen: Prof. Dr.-Ing. Udo Reichl
Laura Cervera Gracia, PhD
Dr.-Ing. Boris Hundt

Promotionskolloquium am: 05.08.2024

Abstract

Infections with the highly contagious influenza A virus (IAV) cause a significant disease and economic burden. Annual influenza vaccination is the best prevention of the influenza disease. However, vaccination and antiviral therapy are limited by emerging viral resistance. A promising antiviral modality are defective interfering particles (DIPs) of IAV that are considered to be safe, effective and broadly-acting. Conventional DIPs (cDIPs) harbor a large internal deletion in one of the eight viral RNA (vRNA) segments of IAV and are replication-deficient. Upon co-infection with infectious standard virus (STV), the missing protein is provided and DIPs can propagate. In a co-infection scenario, DIPs suppress the spread of STVs. A cell culture-based process for production of purely clonal cDIPs in the absence of STVs is available by complementing the genetic defect *in trans* by genetically modified Madin-Darby canine kidney (MDCK) suspension cells. This development eliminated safety and regulatory concerns of previous DIP preparations that required the use of STV and subsequent UV inactivation. Recently, the IAV DIP “OP7” was discovered, which has multiple point mutations within segment (Seg) 7 of its vRNA and exhibited superior antiviral activity compared to cDIPs. Yet, cell culture-based OP7 production is still dependent on co-infection with STVs.

In the first publication, an IAV DIP evolution study was performed to select highly interfering natural DIP isolates and to investigate *de novo* generation and propagation competition between DIPs. A small-scale two-stage cultivation system allowed for long-term STV and DIP propagation. Data obtained from next-generation sequencing demonstrated that the most competitive defective interfering (DI) vRNAs occur on the polymerase-encoding segments (Seg 1–3). Moreover, DI vRNAs comprised a short, but optimal length for replication. During long-term propagation, distinct DI vRNAs accumulated to high fractions towards the end of cultivation, while others decreased. DIPs harboring these highly abundant DI vRNAs showed a superior interfering efficacy relative to known IAV cDIPs and could be very promising candidates for antiviral therapy.

The second manuscript describes the investigation of the replication dynamics on intracellular and cell population level for a broad range of infection regimes of DIPs and STVs using suspension cells. A high load of DIPs at low STVs input could prevent virus-induced cell death and shut down STV propagation. The data was used by a collaborating partner for establishment and validation of a mathematical multiscale model of IAV STV and DIP infection, which enabled the prediction of an optimal DIP dosing ratio.

In the third publication, the broad-spectrum antiviral activity of IAV DIPs was assessed *in vitro*. Co-infection experiments in human lung cells (A549) revealed that IAV DIPs suppress the replication of respiratory syncytial, yellow fever, and Zika virus. The antiviral effect depended on innate immunity, more specifically, the Janus kinase/signal transducers and activators of transcription (JAK/STAT) signaling pathway. Results suggested that IAV DIPs are broadly-acting antiviral agents that might also be used to combat interferon (IFN)-sensitive virus infections, especially of respiratory viruses.

Further, a cell culture-based production system for OP7 chimera DIPs free of STVs was investigated. A mixture of OP7 chimera DIPs and cDIPs was generated by reverse genetics by a collaborating partner and used as DIP seed. Multiplicity of infection (MOI) had a strong effect on virus titers, fraction of OP7 chimera DIPs, and interfering efficacy (efficacy of DIPs to inhibit STV propagation *in vitro* or *in vivo*) for production in genetically engineered suspension cells in shake flasks. Production at an optimal MOI of 10^{-3} and 10^{-4} resulted in maximum interfering efficacies, yet, only relatively low virus titers were achieved and only a part of the DIP harvest was OP7 chimera DIPs (78.7% and 38.3%, respectively). In addition, OP7 chimera DIP material was tested in mice carried out by collaborating partners. OP7 chimera DIP material exhibited a high tolerability and antiviral efficacy *in vivo*.

Next, a scalable cell culture-based production process for OP7 chimera DIPs free of STVs was developed. A temperature decrease from 37°C to 32°C for virus production resulted in the presence of almost pure OP7 chimera DIPs preparations (99.7%) and an 11-fold higher total virus yields relative to the initial process. In addition, subsequent process intensification by perfusion cultivation applying an alternating tangential flow

filtration (ATF) system with perfusion rate control allowed for up to a 79-fold increase in total virus yields relative to the initial batch-process in shake flasks. However, only a subset of virus particles (26%) was able to pass through the hollow fiber membrane (0.2 μm pore size, polyethersulfone).

Continuous virus harvesting would enable direct virus harvest cooling, thus, increasing virus stability and virus yields. Hence, a proof-of-concept study was carried out to test a tangential flow depth filtration (TFDF) system (pore size 2–5 μm) as a novel cell retention system for intensification of virus production. Recombinant vesicular stomatitis virus (rVSV)-based constructs were used as a virus test model. The TFDF system did not only allow for high cell retention efficiencies and cultivations at high viable cell concentrations, but also for continuous virus harvesting and clarification in a single-step.

Taken together, results obtained clearly demonstrated that the development of a safe, highly effective and broadly-acting IAV DIP treatment against respiratory virus infections should be feasible. A production process under good manufacturing practice (GMP), based on the process platform established in this thesis, is currently under development to initiate (pre-) clinical trials.

Kurzfassung

Infektionen mit dem hochansteckenden Influenza-A-Virus (IAV) verursachen erhebliche gesundheitliche und wirtschaftliche Belastungen. Die beste Vorbeugung gegen die Grippe stellt die jährliche Grippeimpfung dar. Allerdings sind der Impfung und antiviralen Therapien durch aufkommende Resistenzen im (*genetischen Code des*) Virus Grenzen gesetzt. Ein vielversprechendes antivirales Therapeutikum sind vom IAV abstammende defekte interferierende Partikel (DIPs), die als sicher, wirksam und breit wirkend gelten. Konventionelle DIPs (cDIPs) weisen eine große interne Deletion in einem der acht viralen RNA-Segmente (vRNA) von IAV auf und sind nicht replikationsfähig. Bei einer Koinfektion mit dem infektiösen Standardvirus (STV) wird das fehlende Protein bereitgestellt und DIPs können sich vermehren. In einem Koinfektionsszenario unterdrücken DIPs die Ausbreitung von STVs. Ein zellkulturbasiertes Verfahren zur Herstellung rein klonierter cDIPs in Abwesenheit von STVs wurde dadurch ermöglicht, dass der genetische Defekt *in trans* durch genetisch veränderte *Madin-Darby canine kidney* (MDCK)-Suspensionszellen ergänzt wird. Durch diese Entwicklung konnten die Sicherheits- und Zulassungsbedenken früherer DIP-Präparate, die den Einsatz von STV und eine anschließende UV-Inaktivierung erforderten, ausgeräumt werden. Vor kurzem wurde das IAV-DIP "OP7" entdeckt, das mehrere Punktmutationen im Segment (Seg) 7 seiner vRNA aufweist und im Vergleich zu cDIPs eine höhere antivirale Aktivität zeigte. Die Produktion von OP7 in Zellkulturen ist jedoch nach wie vor von der Koinfektion mit STV abhängig.

In der ersten Veröffentlichung wurde eine IAV-DIP-Evolutionsstudie durchgeführt, um stark interferierende natürliche DIP-Isolate zu selektieren und die *de novo* Generation und den Vermehrungswettbewerb zwischen DIPs zu untersuchen. Ein zweistufiges Kultivierungssystem im kleinen Maßstab ermöglichte die langfristige Vermehrung von STVs und DIPs. Daten aus *Next generation sequencing* zeigten, dass die wettbewerbsfähigsten defekten interferierenden (DI) vRNAs auf den Polymerase-kodierenden Segmenten (Seg 1-3) auftreten. Darüber hinaus wiesen DI vRNAs eine kurze, aber optimale Länge für die Replikation auf. Während der Langzeitvermehrung reicherten sich bestimmte DI vRNAs bis zum Ende der Kultivierung zu hohen Anteilen

an, während andere abnahmen. DIPs, die diese äußerst häufigen DI vRNAs enthielten, zeigten im Vergleich zu bereits bekannten IAV-cDIPs eine erhöhte interferierende Wirksamkeit und könnten vielversprechende Kandidaten für eine antivirale Therapie sein.

Das zweite Manuskript beschreibt die Untersuchung der Replikationsdynamik auf intrazellulärer Ebene und auf Ebene der Zellpopulationen für ein breites Spektrum von Infektionsregimen von DIPs und STVs unter Verwendung von Suspensionszellen. Eine hohe DIP-Konzentration bei geringer STV-Konzentration konnte den virusinduzierten Zelltod verhindern und die Vermehrung von STVs unterbinden. Die Daten wurden von einem Kooperationspartner zur Entwicklung und Validierung eines mathematischen Multiskalenmodells der IAV-STV- und DIP-Infektion verwendet, welches die Vorhersage eines optimalen DIP-Dosierungsverhältnisses ermöglichte.

In der dritten Veröffentlichung wurde die antivirale Breitbandaktivität von IAV-DIPs *in vitro* untersucht. Koinfektionsexperimente in menschlichen Lungenzellen (A549) zeigten, dass IAV-DIPs die Replikation vom Respiratorischen Synzytial-Virus, Gelbfieberevirus und Zika-Virus unterdrücken. Die antivirale Wirkung hing von der angeborenen Immunität ab, genauer gesagt vom *Janus kinase/signal transducers and activators of transcription* (JAK/STAT)-Signalweg. Die Ergebnisse deuten darauf hin, dass IAV-DIPs breit wirkende antivirale Wirkstoffe sind, die auch zur Bekämpfung von anderen Interferon (IFN)-empfindlichen Virusinfektionen, insbesondere von Atemwegsviren, eingesetzt werden könnten.

Darüber hinaus wurde ein zellkulturbasiertes Produktionssystem für OP7-Chimären-DIPs ohne STVs untersucht. Eine Mischung aus OP7-Chimären-DIPs und cDIPs wurde von einem Kooperationspartner durch reverse Genetik erzeugt und als DIP-Saatgut verwendet. Die Multiplizität der Infektion (MOI) hatte einen starken Einfluss auf die Virustiter, den Anteil der OP7-Chimären-DIPs und die interferierende Wirksamkeit (Wirksamkeit der DIPs zur Unterdrückung der STV-Replikation *in vitro* oder *in vivo*) bei der Produktion in genetisch veränderten Suspensionszellen in Schüttelkolben. Die Produktion bei einer optimalen MOI von 10^{-3} und 10^{-4} führte zu einer maximalen interferierenden Wirksamkeit, wobei jedoch nur relativ niedrige Virustiter erreicht wurden und nur ein Teil der DIP-Ernte OP7-Chimären-DIPs waren

(78,7 % bzw. 38,3 %). Darüber hinaus wurde Material von OP7-Chimären-DIPs in Mäusen von Kooperationspartnern getestet. Das Material von OP7-Chimeren-DIPs zeigte eine hohe Verträglichkeit und antivirale Wirksamkeit *in vivo*.

Anschließend wurde ein skalierbarer zellkulturbasierter Produktionsprozess für STV-freie OP7-Chimäre-DIPs entwickelt. Eine Temperatursenkung von 37°C auf 32°C für die Virusproduktion führte zu nahezu reinem Material an OP7-Chimeren-DIPs (99,7 %) und zu einer 11-fachen Steigerung der Gesamtvirusausbeute im Vergleich zum ursprünglichen Prozess. Die anschließende Intensivierung des Prozesses durch Perfusionskultivierung unter Verwendung eines alternierenden Tangentialflussfiltrationssystems (ATF) mit Regelung der Perfusionsrate ermöglichte eine bis zu 79-fache Steigerung der Gesamtausbeute an Viren im Vergleich zum ursprünglichen Batch-Prozess in Schüttelkolben. Allerdings konnte nur eine Teilmenge der Viruspartikel (26 %) die Hohlfasermembran (0,2 µm Porengröße, Polyethersulfon) passieren.

Eine kontinuierliche Virusernte würde eine direkte Kühlung der Virusernte ermöglichen und damit die Stabilität der Viren und die Virusausbeute erhöhen. Daher wurde eine Machbarkeitsstudie durchgeführt, um ein Tangentialfluss-Tiefenfiltrationssystem (TFDF) (Porengröße 2-5 µm) als neuartiges Zellrückhaltesystem zur Intensivierung der Virusproduktion zu testen. Als Virustestmodell wurden rekombinante Konstrukte auf Basis des vesikulären Stomatitis-Virus (rVSV) verwendet. Das TFDF-System ermöglichte nicht nur hohe Zellrückhalteeffizienzen und Kultivierungen bei hohen Lebendzellkonzentrationen, sondern auch eine kontinuierliche Virusernte und Aufreinigung in einem einzigen Schritt.

Insgesamt zeigten die Ergebnisse deutlich, dass die Entwicklung einer sicheren, hochwirksamen und breit wirkenden IAV-DIP-Behandlung gegen Virusinfektionen der Atemwege machbar sein sollte. Ein Produktionsprozess unter guter Herstellungspraxis (GMP), der auf der in dieser Arbeit etablierten Prozessplattform basiert, wird derzeit entwickelt, um (prä-)klinische Studien zu initiieren.

Declaration

During the preparation of this work the author used DeepL and ChatGPT to improve readability and language. After using this tool, the author reviewed and edited the content as needed and takes full responsibility for the content of the publication.

Penzberg, 15.03.2024

Lars Pelz

Table of Contents

1. Introduction	1
2. Theoretical background	5
2.1. Viruses	5
2.1.1. Influenza A virus	5
2.1.2. Respiratory syncytial virus	10
2.1.3. Flaviviruses - Yellow fever virus and Zika virus	12
2.2. Recombinant vesicular stomatitis virus-based vectors	14
2.3. Defective interfering particles for IAV	15
2.3.1. Structure and formation of DI vRNAs	16
2.3.2. Interference mechanisms	18
2.3.3. DIPs for antiviral treatment	19
2.4. Innate immune response	23
2.4.1. Recognition of IAV	24
2.4.2. Interferon response	25
2.4.3. JAK/STAT signaling pathway	27
2.4.4. Interferon-stimulated genes	28
2.5. Viral vaccines	30
2.5.1. Influenza vaccines	30
2.6. Production of influenza vaccines	32
2.6.1. Egg-based production	32
2.6.2. Cell culture-based production	33
2.7. Production of defective interfering particles	35
2.7.1. Influenza A virus	35
2.7.2. Other viruses	38

Table of Contents

2.8.	Process intensification by perfusion culture	40
2.8.1.	Cultivation at high viable cell concentrations	40
3.	Manuscripts	44
3.1.	First Manuscript	45
3.2.	Second Manuscript	46
3.3.	Third Manuscript	47
3.4.	Fourth Manuscript	48
3.5.	Fifth Manuscript	49
3.6.	Sixth Manuscript	50
4.	Conclusion and Outlook	51

List of Abbreviations

AAV	Adeno-associated virus
ATCC	American-Type Culture Collection
ATF	Alternating tangential flow filtration
C	Capsid protein
cDIP	Conventional DIP
cGAS	Cyclic GMP-AMP synthase
CRM1	Chromosomal region maintenance 1
cRNA	Complementary RNA
cRNP	Complementary ribonucleoprotein
DARPA	Defense Advanced Research Projects Agency
DENV	Dengue virus
DI	Defective interfering
DI vRNA	Defective interfering vRNA
DIP	Defective interfering particle
DO	Dissolved oxygen
dsRNA	Double-stranded RNA
E	Envelope protein
ECACC	European Collection of Authenticated Cell Cultures
ER	Endoplasmic reticulum
EU	European Union
F	Fusion protein
FDA	Food and Drug Administration
FL	Full-length
G	Attachment glycoprotein
HA	Hemagglutinin
HEK-293T	Human embryonic kidney cells, containing the SV40 large T antigen
HEK-293T-PB2(adh)	Adherent HEK-293T cells stably expressing PB2
HEK293-SF	Human embryonic kidney 293 cells growing in suspension and serum-free medium
HFM	Hollow fiber membrane
HIV	Human immunodeficiency virus
HIV-1	Human immunodeficiency virus type 1
HZI	Helmholtz Centre for Infection Research
IAV	Influenza A virus

List of Abbreviations

IBV	Influenza B virus
IFITM	IFN-induced transmembrane
IFN	Interferon
IFN- λ R1	IFN- λ receptor 1
IFNR	IFN receptor
IL-10R2	Interleukin-10 receptor 2
IL-6	Interleukin-6
INTERCEPT	INTERfering and Co-Evolving Prevention and Therapy
IRF	Interferon regulatory factor
ISG	IFN-stimulated gene
ISGF3	IFN-stimulated gene factor
ISRE	IFN-stimulated response element
JAK/STAT	Janus kinase/signal transducers and activators of transcription
JAK1	Janus kinase 1
JAK2	Janus kinase 2
JEV	Japanese encephalitis virus
L	Large polymerase
LAIV	Live attenuated influenza vaccine
LGP2	Laboratory of genetics and physiology 2
LNP	Lipid nanoparticle
LV	Lentiviral vector
M (RSV)	Matrix protein of RSV
M'	Membrane protein of flavivirus
M1	Matrix protein 1 of IAV
M2	Matrix protein 2 of IAV
MDA5	Melanoma differentiation-associated protein 5
MDCK	Madin-Darby canine kidney
MDCK-PB2(adh)	Adherent MDCK cells stably expressing PB2
MDCK-PB2(sus)	Suspension MDCK cells growing in Xeno™ stably expressing PB2
MDCK(sus)	MDCK cells, derived from ECACC, and adapted to suspension growth in Xeno™
MDCK(sus).A	MDCK cells, derived from ATCC, and adapted to suspension growth in Xeno™
MLV	Murine leukemia virus
MODIP	Multiplicity of DIP
MOI	Multiplicity of infection
MPI	Max Planck Institute for Dynamics of Complex Technical Systems, Research group Bioprocess Engineering

List of Abbreviations

mRNA	Messenger RNA
Mx	Myxovirus resistance
MyD88	Myeloid differentiation primary response protein 88
N	Nucleoprotein of RSV
NA	Neuraminidase
NCR	Noncoding region
NDV	Newcastle disease virus
NEP	Nuclear export protein
NF- κ B	Nuclear factor kappa-light-chain-enhancer of activated B cell
NGS	Next-generation sequencing
NP	Nucleoprotein of IAV
NS1 (IAV)	Non-structural protein 1 of IAV
NS1 (RSV)	Non-structural protein 1 of RSV
NS1 (ZIKV)	Non-structural protein 1 of ZIKV
NS2	Non-structural protein 2
P	Phosphoprotein
PA	Polymerase acidic protein
PAMP	Pathogen-associated molecular pattern
PB1	Polymerase basic protein 1
PB2	Polymerase basic protein 2
pDC	Plasmacytoid dendritic cell
PR8	Influenza virus strain A/PR/8/34 (H1N1)
prM	Pre-membrane protein
PRR	Pattern recognition receptor
PVM	Pneumonia virus of mice
RdRp	RNA-dependent RNA polymerase
RIG-I	Retinoic acid-inducible gene-I
RLR	RIG-I-like receptor
RSAD2	Radical S-adenosylmethionine domain containing 2
RSV	Respiratory syncytial virus
RT-qPCR	Real-time reverse transcription-quantitative PCR
rVSV	Recombinant vesicular stomatitis virus
rVSV-GFP	Recombinant VSV-based vector expressing a green fluorescent protein
rVSV-NDV	Recombinant VSV harboring the surface protein of NDV
SARS-CoV-2	Severe acute respiratory syndrome coronavirus type 2
Seg	Segment
Seg 7-OP7	Seg 7 of OP7

List of Abbreviations

SH	Small hydrophobic protein
SIAT1	α -2,6-sialtransferase
ssRNA	Single-stranded RNA
STAT1	Signal transducer and activator of transcription 1
STAT2	Signal transducer and activator of transcription 2
STR	Stirred-tank bioreactor
STV	Standard virus
SXC	Steric exclusion chromatography
TFDF	Tangential flow depth filtration
TFF	Tangential flow filtration
TLR	Toll-like receptor
TOI	Time of infection
TRIF	Toll/interleukin-1 receptor domain-containing adapter inducing IFN- β
TYK2	Tyrosine kinase 2
Viperin	Virus inhibitory protein, ER-associated, IFN-inducible
VLP	Virus-like particle
vRNA	Viral RNA
vRNP	Viral ribonucleoprotein
VSV	Vesicular stomatitis virus
VSV G	Envelope glycoprotein of VSV
WHO	World Health Organization
WT	Wild-type
YFV	Yellow fever virus
YFV-17D	Live attenuated yellow fever vaccine virus
ZIKV	Zika virus

List of Symbols

CSVY	Cell-specific virus yield	virions/cell
STY	Space-time yield	virions/L/day
VCC	Viable cell concentration	cells/mL
VCC _{max}	Maximum viable cell concentration	cells/mL
VVP	Volumetric virus productivity	virions/L/day

1. Introduction

Human infections with influenza A virus (IAV) are characterized by respiratory disease, and annual epidemics account for 300,000–500,000 deaths each year (Krammer et al., 2018). In addition, IAV can cause sporadic pandemic outbreaks with excessive mortality, the deadliest being the Spanish flu in 1918, which infected about 500 million individuals and killed around 50 million worldwide (Martini et al., 2019). The best prevention of influenza disease is vaccination despite its moderate vaccine effectiveness (Javanian et al., 2021). However, rapid mutations of IAV result in new IAV variants, which escape from neutralizing antibodies induced by vaccines (Han and Marasco, 2011). Therefore, an annual reformulation of influenza vaccines is needed. In addition, resistance to currently available antivirals is increasing, thereby reducing drug efficacy (Lampejo, 2020, Sarker et al., 2022). Besides, there are strong efforts to develop a universal influenza vaccine, yet, clinical studies are ongoing and ultimate success remains to be seen (Wang et al., 2022). In addition to IAV, many other virus infections represent a tremendous health and economic burden, with only a limited number of approved vaccines and antiviral agents. Consequently, new antiviral approaches that are safe, effective, affordable, and have a broad-spectrum antiviral activity are urgently sought as rapid countermeasure.

Defective interfering particles (DIPs) of IAV are considered as a promising new antiviral agent targeting IAV and unrelated virus infections. DIPs hold an extremely low risk for an emergence of resistance (Dimmock and Easton, 2015). IAV DIPs occur in natural IAV infections. Conventional DIPs (cDIPs) harbor at least one internal deletion in its segmented genome, which confers the defect in viral replication. Recently, a new type of IAV DIP, named “OP7” with a hypermutated form of the viral RNA (vRNA) of segment (Seg) 7 was discovered (Kupke et al., 2019). OP7 displays a superior antiviral activity relative to cDIPs (Hein et al., 2021a, Hein et al., 2021c, Rand et al., 2021). The antiviral effect of DIPs is based on i) a replication advantage relative to infectious standard virus (STV) and ii) stimulation of the innate immune response. IAV DIPs inhibit the replication of many IAV strains (homologous virus

infection) (Dimmock et al., 2008, Kupke et al., 2019). Moreover, IAV DIPs suppress unrelated virus infections including severe acute respiratory syndrome coronavirus type 2 (SARS-CoV-2) by their ability to induce innate immunity (Easton et al., 2011, Rand et al., 2021, Scott et al., 2011). In animal trials, IAV DIPs were found to be safe and effective for treatment of IAV infections (Dimmock et al., 2008, Hein et al., 2021a). Therefore, IAV DIPs could be deployed as broad-spectrum antiviral agents against emerging interferon (IFN)-sensitive viruses and stockpiled for pandemic readiness. In a pandemic scenario, when vaccines are not developed yet and other antiviral drugs do not confer sufficient protection, IAV DIP treatment could provide a rapid countermeasure to protect in particular elderly and immunocompromised individuals.

Initially, cDIPs were produced in embryonated chicken eggs in co-infection with STVs to complement the defect (Dimmock et al., 1986, Duhaut and Dimmock, 2003). To improve i) process control, ii) scalability, iii) sterility, and iv) flexibility regarding manufacturing scale, our group developed cell culture-based production processes for cDIPs upon co-infection with STVs (Tapia et al., 2019, Wasik et al., 2018). To inactivate STVs present in DIP harvests, UV inactivation was required, which reduced interfering efficacy. Moreover, potential residual STVs present in the inactivated DIP harvests posed safety and regulatory concerns. Therefore, a genetically engineered cell-based production system was developed to produce purely clonal cDIPs free of STVs (Bdeir et al., 2019, Hein et al., 2021a). To increase productivity, a production process in perfusion mode was established in a laboratory-scale stirred-tank bioreactor (STR) (Hein et al., 2021b). However, the cause of the defective OP7 replication is yet unclear and the creation of a production system in the absence of STVs was not possible. Thus, a cell culture-based OP7 production process was developed that still relies on co-infection with STVs (Hein et al., 2021c).

This PhD thesis aimed to provide a basis towards GMP-production and initiation of clinical trials of highly efficacious IAV DIPs. In order to achieve the presented major goals, the initiation and management of collaborative research projects with various partners was an important aspect of this doctoral thesis. Moreover, the work covered in this dissertation led to six manuscripts (Fig. 1). The first aim of this thesis was the in-depth characterization of IAV DIPs concerning e.g. DIP evolution and competition,

deletion junction characteristics, DIP and STV interaction, and broad-spectrum antiviral activity. In the first manuscript, data obtained from next-generation sequencing (NGS) shed light on characteristics of the DIP population in a semi-continuous culture. Moreover, novel cDIP candidates with improved antiviral activity compared to known IAV cDIPs were screened during this long-term propagation. Those cDIP candidates were, then, produced in the absence of infectious STVs and evaluated for efficacious antiviral therapy (Pelz et al., 2021). In the second paper, the replication of IAV DIPs and STVs for a broad range of DIP and STV inputs was analyzed. This helped to assess the impact on virus-induced apoptosis and to calibrate a mathematical multiscale model of IAV and STV infection (Daniel Rüdiger, Max Planck Institute for Dynamics of Complex Technical Systems, Research group Bioprocess Engineering (MPI)) enabling the prediction of optimal dosing ratio for IAV DIPs (Rüdiger et al., 2021). The scope of the third manuscript was to investigate the broad-spectrum antiviral activity of IAV DIPs by inhibiting the replication of IFN-sensitive viruses (Pelz et al., 2023).

The second aim of this thesis was the establishment, optimization and intensification of a scalable cell culture-based production process of highly efficacious OP7 (chimera DIPs) free of STVs. In the fourth manuscript, a novel production system, developed by Tanya Dogra (MPI), was optimized regarding virus titers, OP7 chimera DIP fractions (as OP7 chimera DIPs and cDIPs are present), and interfering efficacy (Dogra et al., 2023). In the fifth paper, the development of a scalable, more productive and robust process for production in STR of highly efficacious and almost pure OP7 chimera DIP preparations is presented. Moreover, production was intended to be maximized by exploring the possibility of process intensification for production of OP7 chimera DIPs in perfusion mode (Pelz et al., 2024). In the sixth manuscript, a proof-of-principle study to apply the tangential flow depth filtration (TFDF) module for high-titer production of viruses with continuous virus harvesting and clarification was performed. Results obtained indicate that an integration of the upstream and downstream process might be feasible and more cost-effective and productive production platforms could be established (Göbel et al., 2024).

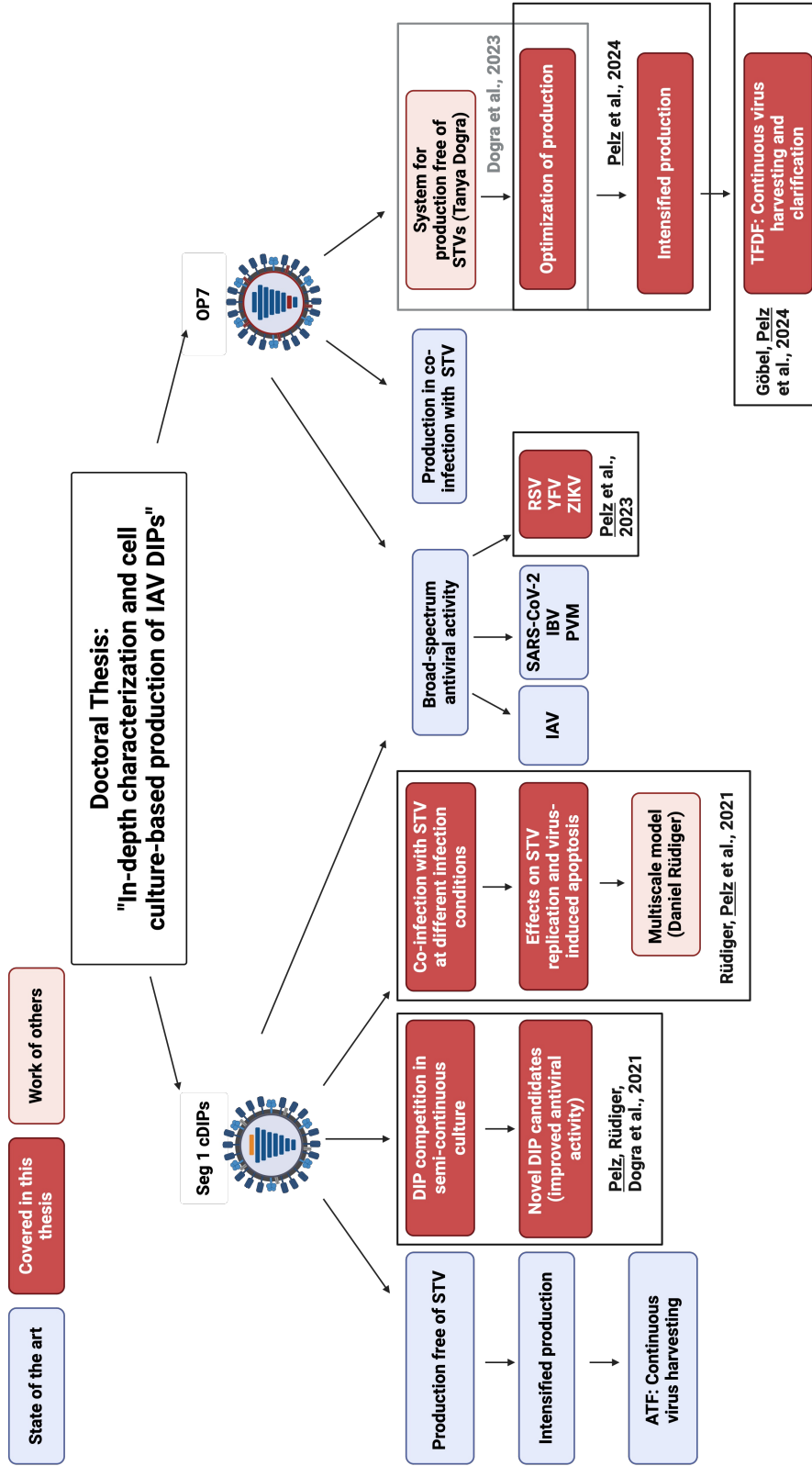


Figure 1: Overview of the state of the art and aim of this doctoral thesis. This cumulative dissertation with the title "In-depth characterization and cell culture-based production of influenza A virus defective interfering particles" comprises six manuscripts (first author: black frame, co-author: grey frame). Those manuscripts were developed in collaboration with various partners. Work by others carried out in our research group is partially highlighted. Two different types of IAV DIPs (cDIPs and OP7) are covered in this thesis. IAV: influenza A virus, DIP: defective interfering particle; Seg 1: Segment 1; cDIP: conventional DIP; STV: standard virus; ATF: alternating tangential flow filtration; SARS-CoV-2: severe acute respiratory syndrome coronavirus type 2; IBV: influenza B virus; PVM: pneumonia virus of mice; RSV: respiratory syncytial virus; YFV: yellow fever virus; ZIKV: Zika virus; TFDF: tangential flow depth filtration. The image was generated with BioRender.com.

2. Theoretical background

As main topic of this doctoral thesis, a detailed overview on DIPs is given, with a special focus on IAV DIPs, which is relevant for all manuscripts. In particular, their structure, formation, interference mechanisms, and use for antiviral treatment is highlighted. All viruses covered in this thesis, IAV (all manuscripts), flaviviruses (third manuscript), respiratory syncytial virus (RSV, third manuscript), and VSV (sixth manuscript) are shortly introduced. Subsequently, a background on the innate immune response is given. This supports the interpretation of the study regarding broad-spectrum antiviral activity of IAV DIPs against IFN-sensitive viruses in human cells (third manuscript) and the study regarding testing the efficacy of IAV DIPs against IAV in mice (fourth manuscript). To cover the overall goal of process development for DIP manufacturing (fifth and sixth manuscript), information on virus production for influenza vaccines and DIPs is given, and process intensification by perfusion cultivation is explained.

2.1. Viruses

2.1.1. Influenza A virus

IAV is a member of the *Orthomyxoviridae* family, which consists of enveloped, segmented, negative-stranded RNA viruses. Influenza viruses are classified in four types: A, B, C, and D. In humans, seasonal epidemics are caused by types A and B, and sporadic pandemics occur due to type A every 10-50 years. In total, 18 possible hemagglutinin (HA) and 11 neuraminidase (NA) subtypes for IAV have been described so far (Kosik and Yewdell, 2019). Three combinations of HA and NA have managed to persist in the human host and triggered pandemic outbreaks. These combinations are H1N1 (1918 and 2009), H2N2 (1957), and H3N2 (1968) (Morens et al., 2009). Influenza virus infections cause a highly contagious respiratory illness with symptoms

including headache, high fever, sore throat, runny nose, cough, myalgia, and malaise. Severe and sometimes lethal influenza virus infection are more likely to occur in patients with comorbidities and in pregnant women, in the elderly (>65 years), and in very young infants (<1 year) (Klenk et al., 2013, Krammer et al., 2018). In this PhD thesis, only IAV will be addressed, which is the main target for antiviral treatment of humans.

2.1.1.1. Viral structure

IAV particles are spherical or filamentous and have an diameter of about 100 nm (Bouvier and Palese, 2008). They consists of a viral envelope, an inner matrix layer, and a viral core (Nayak et al., 2013) (Fig. 2). The viral envelope is formed by a lipid bilayer derived from the host cell membrane and carries two glycoproteins known as HA and the NA. The glycoproteins are important for viral attachment (HA), viral entry (HA), and viral release (NA) and are the major antigens that trigger a host immune response (Krammer et al., 2018). The matrix protein 2 (M2) spans the viral envelope and is an ion channel protein that is crucial for viral replication. Underneath the membrane, the inner matrix consists of matrix protein 1 (M1) (Nayak et al., 2013). The viral genome resides within the viral core, comprising eight genomic vRNA segments. Each vRNA segment is associated with the vRNA-dependent RNA polymerase (RdRp) at the 5' and 3' termini, consisting of the polymerase basic protein 1 and 2 (PB1, PB2) and polymerase acidic protein (PA), and a nucleoprotein (NP) scaffold, forming a rod-shaped complex called the viral ribonucleoprotein (vRNP). The eight vRNPs are arranged in a "7+1" configuration during the viral genome packaging, with seven vRNPs surrounding one central vRNP (Noda and Kawaoka, 2010, Noda et al., 2012).

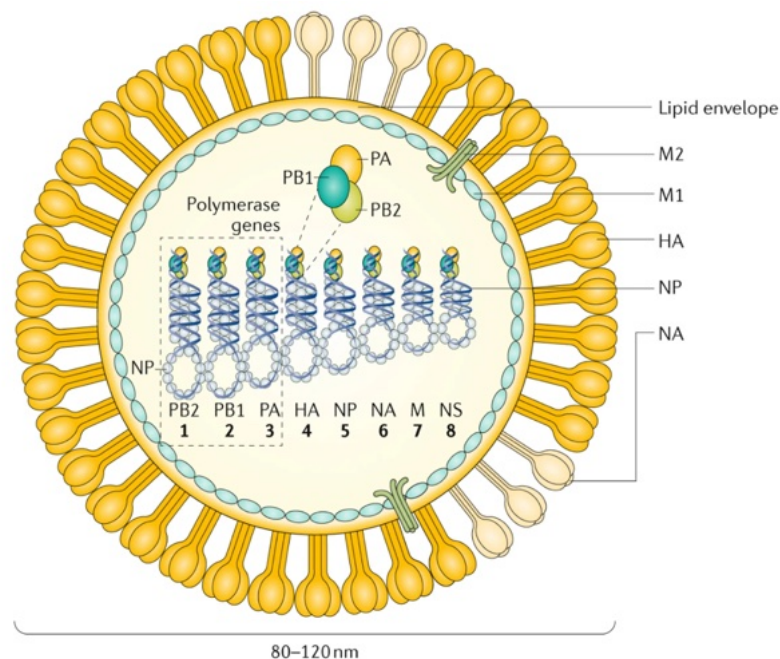


Figure 2: Structure of IAV. The viral envelope is formed by a lipid bilayer, which is derived from the host cell membrane, and harbors HA (encoded by Seg 4), NA (Seg 6) and M2 (Seg 7). The inner matrix, located below the membrane, consists of M1 (Seg 7). Within the viral core, each of the eight vRNA segments is associated with multiple NPs (Seg 5) as well as the viral RNA-dependent RNA polymerase (PB2 (Seg 1), PB1 (Seg 2), and PA (Seg 3)). Seg 8 encodes for the non-structural protein 1 (NS1 (IAV)) and not a component of the IAV particle structure. Figure taken from (Krammer et al., 2018).

2.1.1.2. Genome organization

The eight negative-sense, single-stranded vRNAs (Bouvier and Palese, 2008) code for at least 14 proteins (Pinto et al., 2021). The largest vRNAs are those of the polymerase subunit. More specifically, the vRNA Seg 1 encodes PB2, Seg 2 encodes PB1, and Seg 3 encodes PA. At both the 3' and 5' ends, the noncoding regions (NCRs) flank the coding regions (Krug and Fodor, 2013). The NCRs consist of a highly conserved promoter region that initiate vRNA replication and transcription (Bouvier and Palese, 2008). In the NCRs and terminal coding regions at both the 3' and 5' ends of each vRNA reside the packaging signal. This signal is divided into the incorporation signal within the NCR and the bundling signal at the terminal ends of the coding region. The incorporation signal is important to guide the packaging of the vRNA containing the signal. The bundling signal ensures the incorporation of the complete set of the eight vRNA segments into the progeny virus (Goto et al., 2013).

2.1.1.3. Viral replication cycle

In humans, IAV replication typically occurs in epithelial cells of the respiratory tract (Krammer et al., 2018). The first step in the virus life cycle involves attaching to the host cell (Fig. 3). To accomplish this, the HA glycoproteins of the virus interact with the sialic acids of glycoproteins located on the host cell's membrane (Skehel and Wiley, 2000). Following binding to the host cell, the virus enters the endosome via receptor-mediated endocytosis (Samji, 2009). The acidic environment within the endosome (pH ~5) leads to the HA-mediated membrane fusion of the viral and cell membrane (Hamilton et al., 2012). Upon fusion, release of the vRNPs into the cytoplasm occurs with subsequent transportation to the nucleus via the cellular transport machinery (Martin and Helenius, 1991, Whittaker et al., 1996).

Inside the nucleus, viral replication and transcription take place and are catalyzed by the viral RdRp. The viral replication is a two-step process, that does not require a primer. Initially, a replication intermediate, called the complementary RNA (cRNA), is synthesized. This cRNA assembles with RdRps and multiple NPs to form the complementary ribonucleoprotein (cRNP). Subsequently, the cRNA is used as a template for the synthesis of vRNA. Finally, the vRNA associates with RdRps and multiple NPs, resulting in the formation of vRNP (te Velthuis and Fodor, 2016).

For viral transcription, the viral RdRp transcribes the negative-sense vRNA into 5' capped and 3' polyadenylated viral messenger RNA (mRNA) (Fodor and Te Velthuis, 2020). As the viral transcription is primer-dependent, a process called cap-snatching is required to generate priming of the vRNA (Plotch et al., 1981). In this process, the viral polymerase associates with the cellular RNA polymerase II (Engelhardt et al., 2005) to cleave the 5' capped primers from nascent host transcripts (Plotch et al., 1981, Reich et al., 2014) to use this fragment as 5' cap and primer. The 5' cap also facilitates escape from innate immunity (Furuichi and Shatkin, 2000) and cap-snatching is associated with host shut-off by inhibiting cellular mRNA translation (Bercovich-Kinori et al., 2016). Polyadenylation to the 3' end of the IAV mRNA occurs by reiterative copying of a poly-U sequence near the 5' end of the vRNA template (Poon et al., 1999, Robertson et al., 1981).

The polyadenylated and capped viral mRNA is exported from the nucleus into the cytoplasm, where the cellular machinery translates the information of the mRNA into viral proteins. To support vRNA synthesis, the generated viral polymerase subunits (PB1, PB2, PA) and NPs are transported into the nucleus (Krammer et al., 2018). Translation of the viral surface proteins (HA, NA, and M2) occurs at endoplasmic reticulum (ER)-associated ribosomes.

After folding and glycosylation in the ER, the viral surface proteins are trafficked through the Golgi apparatus for post-translational modification. Subsequently, they are transported to the apical plasma membrane for viral assembly and budding (Bouvier and Palese, 2008, Nayak et al., 2009). Nuclear export of vRNPs to the cytoplasm occurs via the cellular chromosomal region maintenance 1 (CRM1)-dependent pathway (Huang et al., 2013) and is directed by interactions of CRM1, nuclear export protein (NEP, adaptor protein) and viral M1 (bound to vRNPs) (Cros and Palese, 2003, Paterson and Fodor, 2012). Subsequently, the vRNPs are transported from the cytoplasm to the plasma membrane by interacting with the endosomal membrane recycling system through Rab11a (Eisfeld et al., 2011). All viral components (all eight vRNPs, HA, NA, M1, M2) assemble at the apical plasma membrane (Nayak et al., 2013). To form an infectious virus particle, a full set of the eight different vRNPs needs to be packaged. In the past, the packaging was understood as a random process, however, there is strong evidence for a selective packaging process mediated by the packaging signal of the vRNA (Fujii et al., 2003, Hutchinson et al., 2010, Noda, 2021). The newly assembled IAV bud from the cell plasma membrane. Viral budding is a multistep process and involves multiple viral proteins (HA, NA, M2, M1) (Rossman and Lamb, 2011). To facilitate viral release, the enzymatic activity of the NA protein removes the sialic acid from the glycoproteins on the cell surface and the progeny virus to prevent viral attachment to the cell or viral aggregation (Krammer et al., 2018).

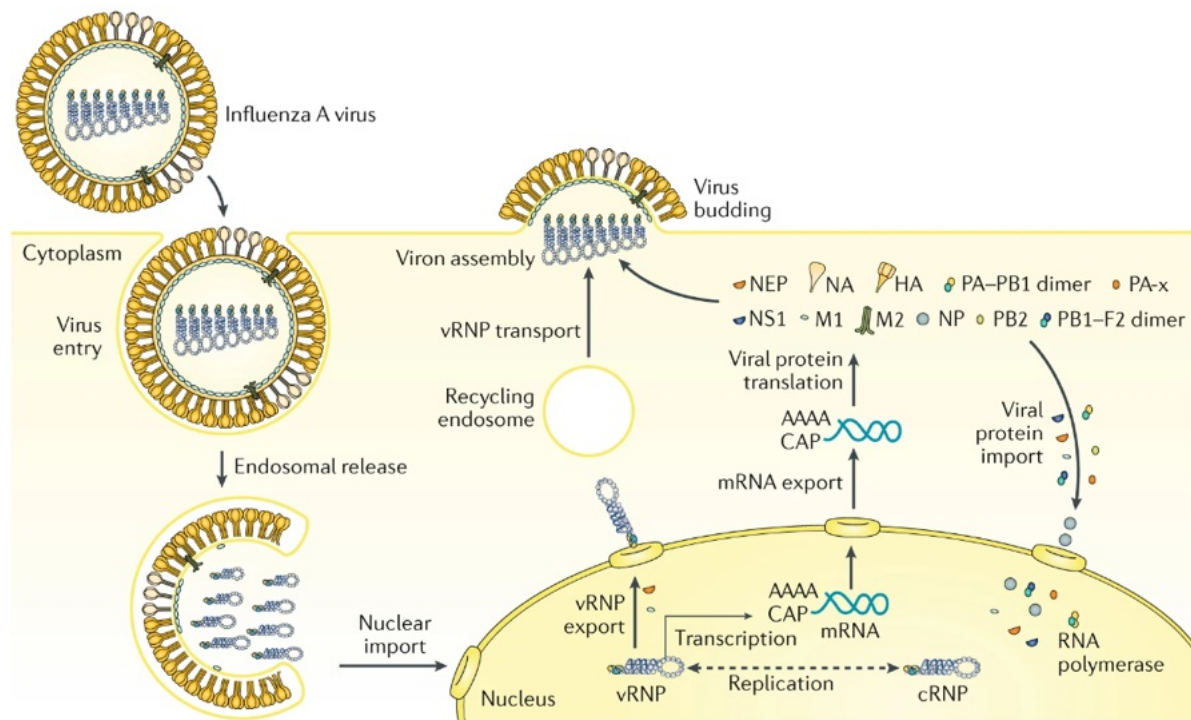


Figure 3: Replication cycle of IAV. IAV attaches to the cell and enters via receptor-mediated endocytosis. The vRNPs are released into the cytoplasm and imported into the nucleus for viral replication (vRNA synthesis through a cRNA intermediate) and viral transcription (mRNA synthesis). The mRNA is exported into the cytoplasm for viral protein translation of the viral polymerase subunits (PB2, PB1, PA), NP, HA, NA, M2, M1, NEP, and NS1 (IAV). At the plasma membrane, viral assembly and budding takes place. Figure taken from (Krammer et al., 2018).

2.1.2. Respiratory syncytial virus

RSV was discovered in 1957 and is a member of the pneumovirus genus in the family *Paramyxoviridae*. RSV is spherical, enveloped and has a negative-sense, single-stranded RNA as genome of 15.2 kb in size, encoding for 11 proteins (Fig. 4). The genome is coated with the nucleoprotein (N), phosphoprotein (P), and large polymerase (L) that form the nucleocapsid. The matrix protein of RSV (M (RSV)) is located between the nucleocapsid and the lipid bilayer. Three surface proteins protrude from the viral envelope, the fusion protein (F), the attachment glycoprotein (G), and the small hydrophobic protein (SH). F is the main target of neutralizing antibodies and highly conserved (McLellan et al., 2013). Two antigenically distinct human RSV subtypes (A and B) are known, and their predominance alternates during different epidemic seasons (Laham et al., 2017). RSV is a highly contagious virus that causes respiratory infections. In infants and young children, RSV infections are the most common cause of illness of the lower respiratory tract characterized by

bronchiolitis and pneumonia (Nair et al., 2010). In children (< 5 years), 33 million cases of RSV infections are estimated to occur annually worldwide, of which 10% lead to hospitalization and up to 200,000 of deaths (Jha et al., 2016). RSV infection can also pose severe lower respiratory illness in older adults or immunocompromised patients (Falsey and Walsh, 2000).

Until recently, no RSV vaccine was licensed. This was because an incident halted RSV vaccine development for over 30 years. An RSV vaccine (inactivated with formalin) developed in 1960s did not protect against a natural RSV infection but even led to increased RSV disease severity (Kapikian et al., 1969, Kim et al., 1969). This was caused by a significantly higher induction of non-neutralizing than neutralizing antibodies (Murphy et al., 1986), formation of immune complexes (Polack et al., 2002), a lack of antibody affinity maturation (Delgado et al., 2009), and strong and unbalanced cellular immune response (Openshaw et al., 2001). As alternative, a humanized monoclonal antibody targeting the RSV F (palivizumab) was developed and licensed 1999 for the European Union (EU) (IMPact-RSV-Study-Group, 1998). However, escape from palivizumab has been reported (Adams et al., 2010, Zhu et al., 2018) and the drug requires administration at 30 day intervals for 5 months (Rogovik et al., 2010). As second immunoprophylaxis in pediatric use, nirsevimab was approved 2022 in the EU. The main advantage of nirsevimab involves the higher potency and extended half-life, requiring only a single administration per RSV season (Domachowske et al., 2018, Hammitt et al., 2022). In 2023, the Food and Drug Administration (FDA) approved two recombinant subunit RSV vaccines Arexvy® (GSK) and Abrysvo® (Pfizer) for older adults 60 years of age and older, both are administered intramuscularly. Arexvy® contains the stabilized prefusion F protein (RSVPreF3 OA vaccine) and Abrysvo® a stabilized bivalent RSV-A and RSV-B prefusion F protein (RSVPreF vaccine).

In *in vitro* cell culture experiments, RSV remains highly associated to the cell membrane (~95%), hence freeze-thaw cycles, vortexing, or sonication are typically applied to increase infectious virus titers for seed virus production (Collins et al., 2013). Moreover, RSV has a low thermostability, therefore, addition of excipients (e.g.

sucrose) is beneficial to increase virus stability (Ausar et al., 2007). During RSV infection, syncytia are formed in which infected cells fuse.

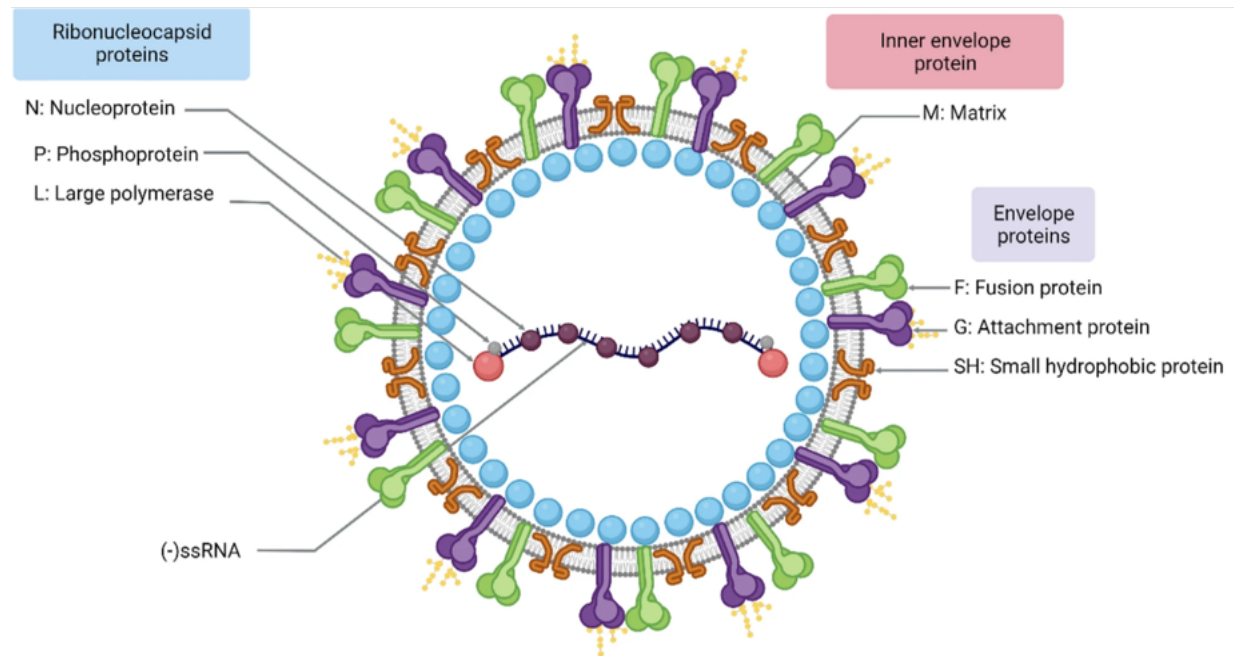


Figure 4: Structure of RSV. The RSV genome is associated with N, P, and L that form the nucleocapsid. M of RSV is located between the nucleocapsid and the lipid bilayer. Three glycoproteins are located on the surface of the RSV virus. Figure taken from (Córdova-Dávalos et al., 2022).

2.1.3. Flaviviruses - Yellow fever virus and Zika virus

The genus *Flavivirus* of the family *Flaviviridae* consists of 56, mostly arthropod-borne virus species. A large number of infections result from the yellow fever virus (YFV), Zika virus (ZIKV), Dengue virus (DENV) and Japanese encephalitis virus (JEV). YFV and ZIKV, which are in the focus of this PhD thesis, are both primarily transmitted to humans via a bite of an infected *Aedes* species mosquito. Flavivirus particles are spherical, enveloped and have a diameter of about 50 nm (Fig. 5). The positive-strand RNA genome with a size of 10.8 kb encodes for a large polyprotein precursor, which is processed into three structural (capsid (C), pre-membrane (prM)), and envelope (E) and seven non-structural proteins (Lindenbach et al., 2020). Immature flavivirus particles display prM and E on the virus surface. During the particle maturation process, prM is cleaved into the pr peptide and membrane protein of flavivirus (M') by the cellular protease furin, which is essential for the formation of an infectious virion

(Li et al., 2008, Plevka et al., 2011). Moreover, C binds to the vRNA, forming the nucleocapsid.

Illness after YFV infections in humans ranges from asymptomatic (55% of cases) or mild (33%) to severe disease (12%) (Johansson et al., 2014). The incubation time is three to seven days. When entering the first phase, fever, chills, muscle pain, headache, and myalgia occur, which disappear after 3 to 4 days. However, around 15% of infected individuals enter the second phase with high fever, vomiting, epigastric pain, and jaundice. Among patients entering the second phase, 20–50% die (Monath, 2008, Pierson et al., 2020). ZIKV infections are mostly asymptomatic, but febrile illness occurs in 25–50% of cases (Pierson et al., 2020). Symptoms of ZIKV infections most commonly include maculopapular rash, fatigue, fever, arthralgia or myalgia, and conjunctivitis (Musso et al., 2018). ZIKV infection during pregnancy can lead to virus transmission to the child (20–30%) and, thus, grave defects of the fetus and child. The congenital Zika syndrome is characterized by malformations such as microcephaly (Marbán-Castro et al., 2021).

The recent emergence of ZIKV in the South Pacific area in 2013 (Cao-Lormeau et al., 2014) and South America in 2015 (Campos et al., 2015, Zanluca et al., 2015) and re-emergence of YFV (Faria et al., 2018, Giovanetti et al., 2019) requires the development of safe and effective vaccines and antivirals. So far, no antiviral therapy against flavivirus infections has been approved. Vaccines continue to be the most cost-effective way to protect against flavivirus infections in the long-term (Dutta and Langenburg, 2023). So far, only vaccines against YFV, JEV, tick-borne encephalitis virus and tetravalent DENV have been licensed for human use. The first developed flavivirus vaccine was the live attenuated YFV-17D vaccine in 1937, which was obtained by serial passaging of the Asibi YFV strain in mouse and chicken tissue, resulting in reduced pathogenicity (Theiler and Smith, 1937). Two substrains of the YFV-17D are currently produced, the YFV-17DD (higher passage number) for Brazil and YFV-17D-204 for the other countries (de Miranda et al., 2022, Pierson et al., 2020). Since 1937, 850 million doses of the safe and effective YFV-17D have been administered demonstrating the great success of this vaccine (Kum et al., 2019).

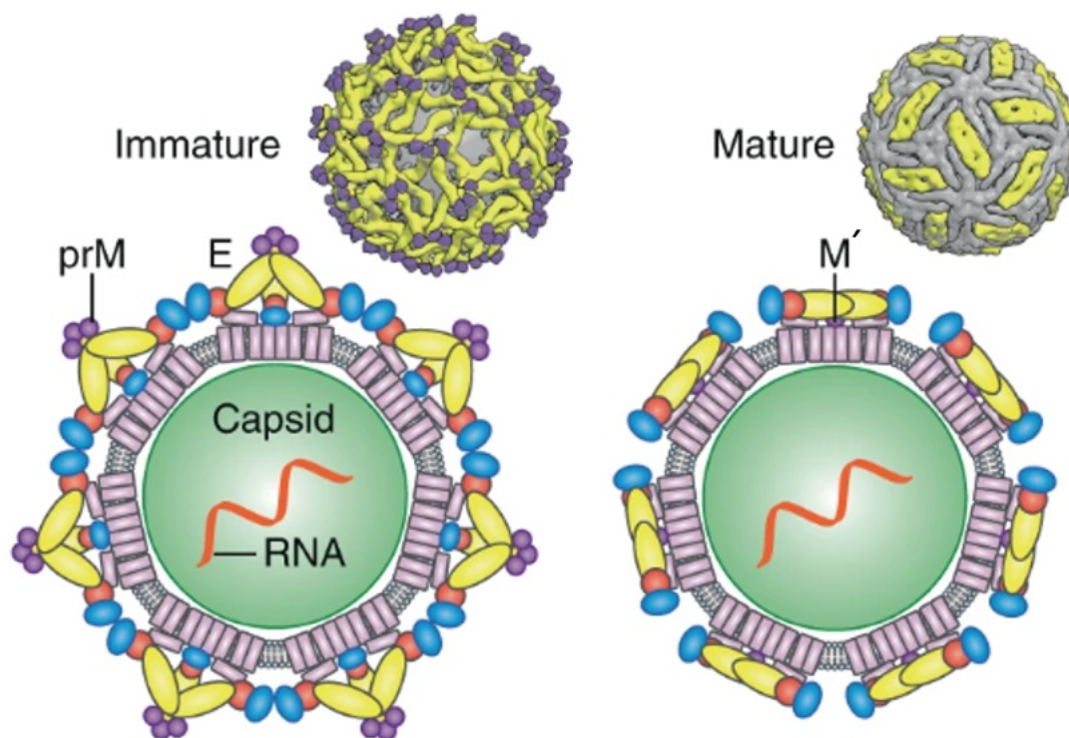


Figure 5: Structure of flaviviruses. The capsid protein binds to the positive-strand RNA genome forming the capsid, which is located in a lipid-bilayer. Flavivirus particles exist in immature and mature forms. In the immature form (left panel), the particle carries prM and E on its surface. During the maturation process, that generates the mature form (right panel), prM is cleaved into the pr peptide and M'. Image courtesy of Ethan Tyler. Figure taken from (Pierson and Diamond, 2020).

2.2. Recombinant vesicular stomatitis virus-based vectors

For both vaccines and oncolytic immunovirotherapy, recombinant vesicular stomatitis virus (rVSV)-based vectors are very promising. Important characteristics are the rapid and high-titer production in cell culture (Elahi et al., 2019, Kiesslich et al., 2021), low viral pathogenicity, and rare pre-existing anti-vector immunity in humans (Ura et al., 2021). Vesicular stomatitis virus (VSV) is a single-stranded negative-sense RNA virus and belongs to the family *Rhabdoviridae*. rVSV-based vectors are generated by replacement of its native envelope glycoprotein (VSV G) with distinct envelope proteins of a heterologous virus (Tani et al., 2011). The first rVSV-based vector vaccine against Ebola (ERVEBO[®]) has gained approval in 2019 in EU (EMA, 2019) and USA (FDA, 2019), after being tested safe and immunogenic in humans in clinical

trials (Suder et al., 2018). Vaccines based on rVSV also protected against e.g. SARS-CoV-2 (Case et al., 2020), Lassa virus (Geisbert et al., 2005), Marburg virus (Jones et al., 2005), Andes virus (Brown et al., 2011), IAV (Furuyama et al., 2020), ZIKV (Emanuel et al., 2018), and DENV (Lauretti et al., 2016) in animal models by conferring a rapid and robust immune response, and some are currently evaluated in clinical trials.

In recent years, oncolytic viruses have gained importance in cancer therapy (Bishnoi et al., 2018) as they kill tumor cells. The first product (Imlygic[®]), which is based on the herpes simplex virus type 1, has been approved by the FDA in 2015 to treat melanoma (FDA, 2023c). VSV is of special relevance for oncolytic immunovirotherapy due to its high cytotoxicity, tumor-specific cell destruction, rapid replication kinetics, low viral pathogenicity, but also its immunostimulatory effects (Bishnoi et al., 2018, Zhang and Nagalo, 2022). One promising rVSV-based vector harbors the surface protein of Newcastle disease virus (NDV) (rVSV-NDV) instead of the neurotoxic VSV G to increase safety and confer fusogenicity. The latter is required that rVSV-NDV forms syncytia and kills tumor cells through fusion that leads to intratumoral spread and induction of antitumor immune responses (Krabbe and Altomonte, 2018). In animal models, rVSV-NDV showed efficacy in cancer therapy (Abdullahi et al., 2018, Krabbe et al., 2021). In our research group at the MPI, a production process in batch and perfusion mode was developed for rVSV-NDV (Göbel et al., 2023, Göbel et al., 2022).

2.3. Defective interfering particles for IAV

Henle and Henle were the first to demonstrate that inactive viruses can interfere with the influenza virus propagation (Henle and Henle, 1943). In the end of 1940s, Preben von Magnus reported the occurrence of “incomplete forms” of influenza virus (Gard and von Magnus, 1947). These incomplete forms arose during serial passaging of IAV in embryonated chicken eggs, as indicated by a reducing ratio of infectious to total virus titer over passages (von Magnus, 1951). In 1970, Huang and Baltimore

introduced the term “defective interfering particles” and detailed their properties (Huang and Baltimore, 1970).

2.3.1. Structure and formation of DI vRNAs

DIPs are naturally occurring viral mutants that arise during virus infections. Most RNA and DNA virus families are known to form DIPs (Marriott and Dimmock, 2010, Nayak et al., 1985, Vignuzzi and Lopez, 2019, Yang et al., 2019). Structurally, DIPs are missing an important part in their vRNA genome and are, thus, unable to self-replicate. In general, DI vRNAs are formed due to an error-prone replication of the viral polymerase (Alnaji and Brooke, 2020). Upon coinfection with infectious STVs, the lacking genetic function is supplied and, thus, DIPs have the ability to replicate while interfering with STV propagation.

For the different virus families, several types of DI vRNAs have been reported including internal deletions, rearrangements, point- and hypermutations, frameshift, copy-back and snap-back as reviewed elsewhere (Vignuzzi and Lopez, 2019). IAV DIPs can harbor either DI vRNAs with an internal deletion (Alnaji et al., 2019, Davis et al., 1980, Nayak et al., 1982, Saira et al., 2013) or hypermutations (Kupke et al., 2019) in at least one of their eight vRNA segments (Fig. 6). Hence, those forms are the focus of the present work. Two models for the formation of DI vRNAs containing an internal deletion, referred to as cDIPs, have been proposed: i) looping out and ii) template translocation (Alnaji and Brooke, 2020). For the looping out model, the two sites of the deletion junction are engaged by the formation of a loop and RdRp is able to “roll over” to the opposite part, generating a truncation. The template translocation model describes that a RNA structure or basepair mismatch leads to a pausing of the strand synthesis, which starts again at a downstream point (Alnaji and Brooke, 2020). IAV cDIPs typically harbor deletion junctions on the longest vRNA Seg 1–3 (Davis and Nayak, 1979, Duhaut and Dimmock, 1998, Jennings et al., 1983, Nayak et al., 1985, Saira et al., 2013), encoding for the polymerase subunits. A prominent, well-characterized cDIP having an internal deletion in vRNA Seg 1 is “DI244”, which exhibits high antiviral efficacy *in vivo* (Dimmock et al., 2012a, Dimmock et al., 2008,

Easton et al., 2011, Hein et al., 2021a). For in-depth characterization of cDIP population, NGS is a useful tool by detecting and quantifying distinct DI vRNAs. For IAV cDIPs, an Illumina-based sequencing framework was developed recently. This allowed e.g. to identify the presence of hundreds of different DI vRNAs that arise during an IAV infection (Alnaji et al., 2019).

The truncated genome might also exclude parts required for replication and packaging. For IAV, a selective packaging of the eight different vRNAs segments have been suggested (Hutchinson et al., 2010, Noda and Kawaoka, 2010), which is governed by the segment-specific packaging signal located at the terminal ends of the respective vRNA. This packaging signal comprises the incorporation signal (NCR, including promoter region) and the bundling signal (at the terminal ends of the coding region) (Goto et al., 2013). Previous work showed that the NCR and parts of the coding region (Davis et al., 1980, Duhaut and Dimmock, 1998, Jennings et al., 1983, Nayak and Sivasubramanian, 1983, Saira et al., 2013) of naturally occurring DI vRNAs are typically retained, providing a sufficient signal for packaging (Dimmock and Easton, 2014, Hutchinson et al., 2010).

In our research group (MPI), a novel type of IAV DIP, named “OP7”, was discovered previously by single-cell analysis of adherent Madin-Darby canine kidney (MDCK) cells infected with the influenza virus strain A/PR/8/34 (H1N1), referred to as PR8. Instead of an internal deletion, OP7 has a hypermutated form of the vRNA of Seg 7 with 37 point mutations residing in the NCR (includes the promoter region), packaging signal, and coding region of the genome (Fig. 6) (Kupke et al., 2019). In cell culture-based experiments, the presence of OP7 was indicated by an over-proportional level of mutated Seg 7 of OP7 (Seg 7-OP7) vRNA relative to other segments (Hein et al., 2021c, Kupke et al., 2019). Moreover, co-infection experiments revealed a very high suppression of infectious STV formation of samples containing OP7 (Hein et al., 2021c, Kupke et al., 2019). Two nucleotide substitutions G3A/C8U were identified in the promoter region of Seg 7 vRNA, which were previously described to increase vRNA replication (Belicha-Villanueva et al., 2012, Vreede et al., 2008). The over-proportional Seg 7-OP7 vRNA in comparison to the other segments indicates the

partial absence of other vRNA segments in OP7, likely explaining the lack of viral replication.

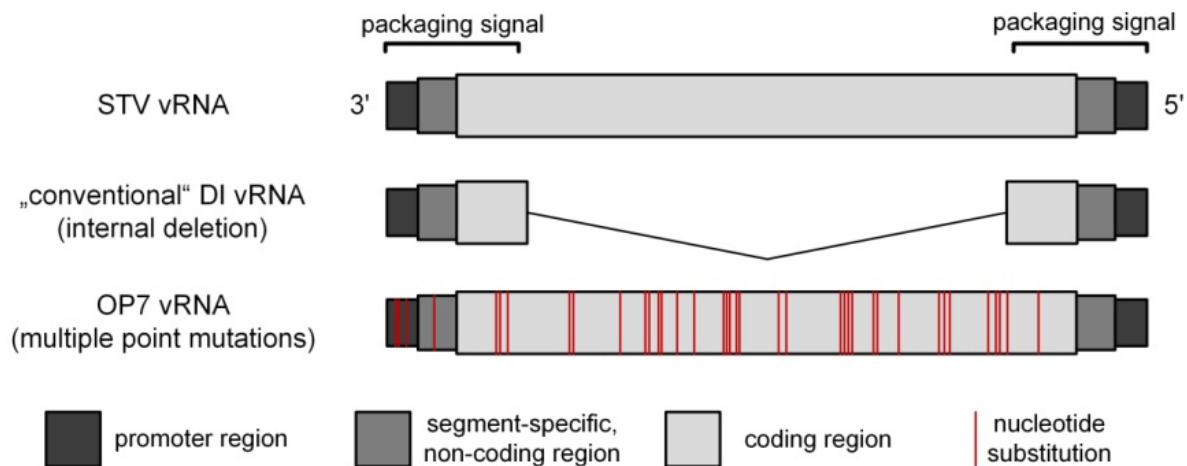


Figure 6: Genome structure of different types of DI vRNAs of IAV DIPs. STV particles carry eight vRNA segments at full-length. In contrast, cDIPs have at least one vRNA segment with a large internal deletion. OP7 vRNA of Seg 7 contains 37 point mutations affecting the promoter region, NCR and coding region. Figure taken from (Hein, 2022), which is adapted from (Kupke et al., 2019).

2.3.2. Interference mechanisms

DIPs interfere at different stages of the IAV life cycle. In co-infected cells, the shortened DI vRNA of cDIPs is preferentially replicated compared to its full-length (FL) analog (Genoyer and Lopez, 2019, Laske et al., 2016, Mendes and Russell, 2021, Nayak et al., 1985). In the case of OP7, a hypothesized “superpromotor” leads to an enhanced vRNA replication (Kupke et al., 2019). Moreover, a competition for cellular and viral proteins (RdRps, NPs, structural proteins, glycoproteins) required for encapsulation, replication, and formation of progeny virions is present (Genoyer and Lopez, 2019, Laske et al., 2016, Marriott and Dimmock, 2010, Wu et al., 2022). Thus, DIPs interfere with and hinder replication and spread of STV and thereby exert an antiviral effect. Bdeir et al. investigated the antiviral activity of DIPs containing two DI vRNAs and found no increase relative to a single DI vRNA (Bdeir et al., 2021). Other work suggested that DI vRNAs also interfere at the packaging step by inhibiting the packaging of the FL vRNA of the same (Duhaut and McCauley, 1996, Odagiri and Tashiro, 1997) or another genome segment (Ueda et al., 1980). However, recent studies proposed a disadvantage of small DI vRNAs during packaging relative to the

FL vRNA (Alnaji et al., 2021, Mendes and Russell, 2021). Furthermore, the expressed truncated protein encoded in the DI vRNA of Seg 1 further add to the antiviral effect (Ranum et al., 2024).

DIPs have also been reported to stimulate an antiviral innate (Dimmock and Easton, 2014, Frensing et al., 2014, Ho et al., 2016, Lin et al., 2022, Mendes and Russell, 2021, Rand et al., 2021, Strahle et al., 2006, Tapia et al., 2013) and adaptive immune response (Mercado-López et al., 2013) and support viral persistence (Manzoni and López, 2018, Roux and Waldvogel, 1981, Schmaljohn and Blair, 1977, Xu et al., 2017). Moreover, DIPs play an important role in modulating pathogenesis *in vivo* (Rabinowitz and Huprikar, 1979, Šantak et al., 2015, Sun et al., 2015). Due to their ability to suppress infectious STV replication and to induce an immune response, DIPs are considered as a promising antiviral agent for prophylaxis and treatment of influenza infections (Dimmock et al., 2012a, Dimmock et al., 2008, Hein et al., 2021a, Huo et al., 2020, Wu et al., 2022, Yang et al., 2019, Zhao et al., 2018), but also of unrelated virus infection (Easton et al., 2011, Rand et al., 2021, Scott et al., 2011).

2.3.3. DIPs for antiviral treatment

IAV infections can be treated prophylactically with vaccines or therapeutically with antiviral agents. However, the composition of IAV vaccines has to be reformulated annually in response to antigenic drifts, which poses the risk of vaccine mismatches (Vogel and Manicassamy, 2020). Moreover, presently available antiviral drugs have a limited efficacy. An increasing concern is that IAV strains have developed resistances to the neuraminidase inhibitors oseltamivir and zanamivir (Paules and Subbarao, 2017) or the viral endonuclease inhibitor baloxavir marboxil (O'Hanlon and Shaw, 2019). Therefore, the development of effective antiviral agents is of great urgency.

2.3.3.1. Homologous virus infections

IAV DIPs are regarded as safe and effective antiviral agents for treatment and prophylaxis of the influenza disease due to their interference with IAV replication.

Remarkably, IAV DIPs suppressed the replication of a wide range of IAV strains (homologous virus infection), that included seasonal, pandemic and highly pathogenic avian IAV (Dimmock et al., 2012b, Dimmock et al., 2008, Huo et al., 2020, Kupke et al., 2019, Zhao et al., 2018). Moreover, no DIP-resistance mutations have been identified so far and the chance of occurrence of an escape mutant is estimated to be 10^{-45} (Dimmock and Easton, 2015). IAV DIP co-treatment protected mice (Dimmock et al., 2008, Hein et al., 2021a, Hein et al., 2021c, Scott et al., 2011) and ferrets (Dimmock et al., 2012a, Dimmock et al., 2012b) from disease or death. In addition, DI244 conferred a higher antiviral effect than oseltamivir in ferrets against a pandemic IAV infection (Dimmock et al., 2012a). Moreover, the intranasal administration of DI244 and OP7 was very well tolerated, as demonstrated by an absence of body weight loss and a total survival of mice (Hein et al., 2021a, Hein et al., 2021c). Furthermore, a dual-functional peptide, which delivers three DI plasmid DNAs but simultaneously stops endosomal acidification (confers an additional antiviral effect by inhibiting the export of vRNP into the cytoplasm), demonstrated high prophylactic and therapeutic protection in mice against avian and seasonal IAV infections. A higher antiviral effect could be found for this dual-functional peptide relative to treatment with zanamivir (Zhao et al., 2018) underlining again the great potential for IAV DIPs for treatment and prophylaxis.

A therapeutic effect could also be observed when IAV DIPs were administered after an IAV infection. More specifically, intranasal administration of DI244 one day after a lethal IAV challenge rescued mice from death, weight loss and even disease. The antiviral efficacy declined when DI244 was administered two days after the challenge, but still delayed disease (Dimmock et al., 2008). Dimmock et al. investigated the duration of the prophylactic effect of IAV DIPs given prior to a lethal IAV challenge, which was found to be maintained for at least one week after administration. The DI vRNA could even be detected for up to three weeks (Dimmock et al., 2008). This indicated that a higher DI vRNA input might protect mice even longer than one week until the DI vRNA is degraded to a subprotective dose (Dimmock and Easton, 2015). The DIP/STV ratio determines the level of antiviral efficacy *in vitro* and *in vivo*. More specifically, full protection was lost when the DIP/STV ratio was lowered to below 30,000:1 for DI244 (Dimmock and Easton, 2015, Hein et al., 2021c).

Two mechanisms are involved in interference of DIPs with homologous viruses: i) “replication interference” and ii) induction of an antiviral state. IAV DIPs derived from H5N1 generated in mast cells showed protection in mice against highly pathogenic H5N1 IAV strain and multiple other IAV strains by stimulation of an innate immune response (type-II IFN) (Huo et al., 2020). IAV DIP-enriched virus stocks elicited an early type-I IFN response in mice lungs that controlled IAV infection resulting in survival of all mice and reduced weight loss (Penn et al., 2022). However, IAV DIPs also protected mice independently of type-I IFNs (Easton et al., 2011) and even of type-I and III IFNs (Wang et al., 2023). This suggests that yet unrevealed pathways may take part in the induction of IFN-stimulated genes (ISGs) independently of IFN (Arora et al., 2021, Easton et al., 2011, Wang et al., 2020). It has previously been shown that ISG expression can be stimulated without IFN signaling (Schmid et al., 2010, Wang et al., 2010). Wang and colleagues were able to identify a unique host signature in mice lacking type-I and -III IFN signaling that were protected by IAV DIPs in a homologous IAV infection (Wang et al., 2023). Penn et al. have shown that the fraction of DI vRNAs in a H5N1 seed virus that elicit an antiviral response has a critical impact on the outcome of pathogenesis in mice. More specifically, a H5N1 seed virus enriched with DIPs, reduced IAV replication by stimulating an early type-I IFN response and was nonpathogenic indicating the high antiviral effect of IAV DIPs. In contrast, a DIP depleted H5N1 seed virus, resulted in high DIP and STV accumulation, leading to increased production of proinflammatory cytokines and severe disease (Penn et al., 2022).

DIPs of other virus families have also been suggested and generated for antiviral treatment, as an antiviral activity against homologous virus infections was found *in vitro* and *in vivo* including Nipah virus (Welch et al., 2020), ZIKV (Rezelj et al., 2021), DENV (Li et al., 2021), chikungunya virus (Levi et al., 2021), SARS-CoV-2 (Chaturvedi et al., 2021, Girgis et al., 2022, Yao et al., 2021), human immunodeficiency virus (HIV) (Tanner et al., 2019), RSV (Sun et al., 2015), poliovirus (Xiao et al., 2021), Ebola virus (Smither et al., 2020), and canine distemper virus (Tilston-Lunel et al., 2021).

2.3.3.2. Unrelated virus infections

IAV DIPs confer not only an antiviral effect against the replication of IAV, but also against unrelated viruses such as SARS-CoV-2 (Rand et al., 2021), influenza B virus (IBV) (Scott et al., 2011), and pneumonia virus of mice (PVM) (Scott et al., 2011) by inducing an antiviral innate immunity. Thus, DIPs are considered as a potent countermeasure with broad-spectrum antiviral activity against various IFN-sensitive viruses. After DIP entry into host cells, pattern recognition receptors (PRR), e.g. the retinoic acid-inducible gene-I-like receptor (RIG-I), senses pathogen-associated molecular patterns (PAMPs) including the FL and DI vRNA (Baum and García-Sastre, 2011, Rehwinkel et al., 2010). This initiates signaling cascades leading to the production of IFNs and the expression of antiviral ISGs. Ultimately, the cell is brought into an antiviral state to inhibit the viral replication.

Broad-spectrum antiviral activity was also reported for DENV DIPs against SARS-CoV-2, RSV, YFV, and ZIKV (Lin et al., 2022) and different DENV subtypes (Li et al., 2021, Lin et al., 2022). In addition, poliovirus DIPs conferred protection by innate immunity activation against SARS-CoV-2, IAV and Coxsackievirus B3 (Xiao et al., 2021). The prophylactic protection against unrelated virus infections lasts shorter than against a homologous virus infection (more than one week) (Dimmock and Easton, 2014). A decrease in the prophylactic effect against unrelated PVM was observed when DIPs were administered three or more days before virus challenge (Easton et al., 2011). This indicates that rather the replication interference than the induction of an antiviral state is the crucial player in the antiviral effect of IAV DIPs (Dimmock and Easton, 2014).

Different works suggest that the mechanisms of action of IAV DIP-induced protection against unrelated and homologous virus infections (already discussed) are different (Easton et al., 2011, Wang et al., 2023). Only the protection against unrelated viruses is dependent on IFN. For instance, protection against IBV infection was decreased in type-I IFN receptor knock-out mice (Scott et al., 2011). Moreover, intranasal administration of DI244 protected wild-type (WT) mice against a lethal PVM challenge, while only 17% of type-I IFN deficient mice survived this infection. As symptoms set in

four days later in these knock-out mice, Easton and colleagues suggested that other factors than IFN might be involved to confer an antiviral activity (Easton et al., 2011).

Because of their ability to confer an antiviral effect by replication interference (homologous virus infections) and stimulation of innate immunity (homologous and unrelated virus infection), IAV DIPs are being considered for protection against respiratory virus infections (e.g. IAV, IBV, RSV, and SARS-CoV-2) in humans. IAV DIPs could be administered as nasal spray to combat those infections at the first infection site, i.e. in the nose and throat, and reduce symptoms and virus transmission. During a pandemic, IAV DIPs could be a very fast countermeasure to protect the population, when no vaccines have yet been approved and other antiviral drugs are ineffective. This applies in particular to the protection of elderly and immunocompromised individuals and persons-at risk (e.g. hospital staff).

2.4. Innate immune response

Virus infections trigger an antiviral innate immune response, an early defense barrier of the cells (Fig. 7). For this, the viral constituents are sensed, which stimulates signaling pathways leading to expression of IFNs. Activation of IFN pathways lead to the development of an antiviral state in the infected and neighboring cells. More specifically, IFNs trigger the expression of antiviral ISGs and programmed cell death to restrict viral replication (Malik and Zhou, 2020). However, IAV, RSV, YFV, and ZIKV provide different functions for evasion of innate immune responses in order to replicate.

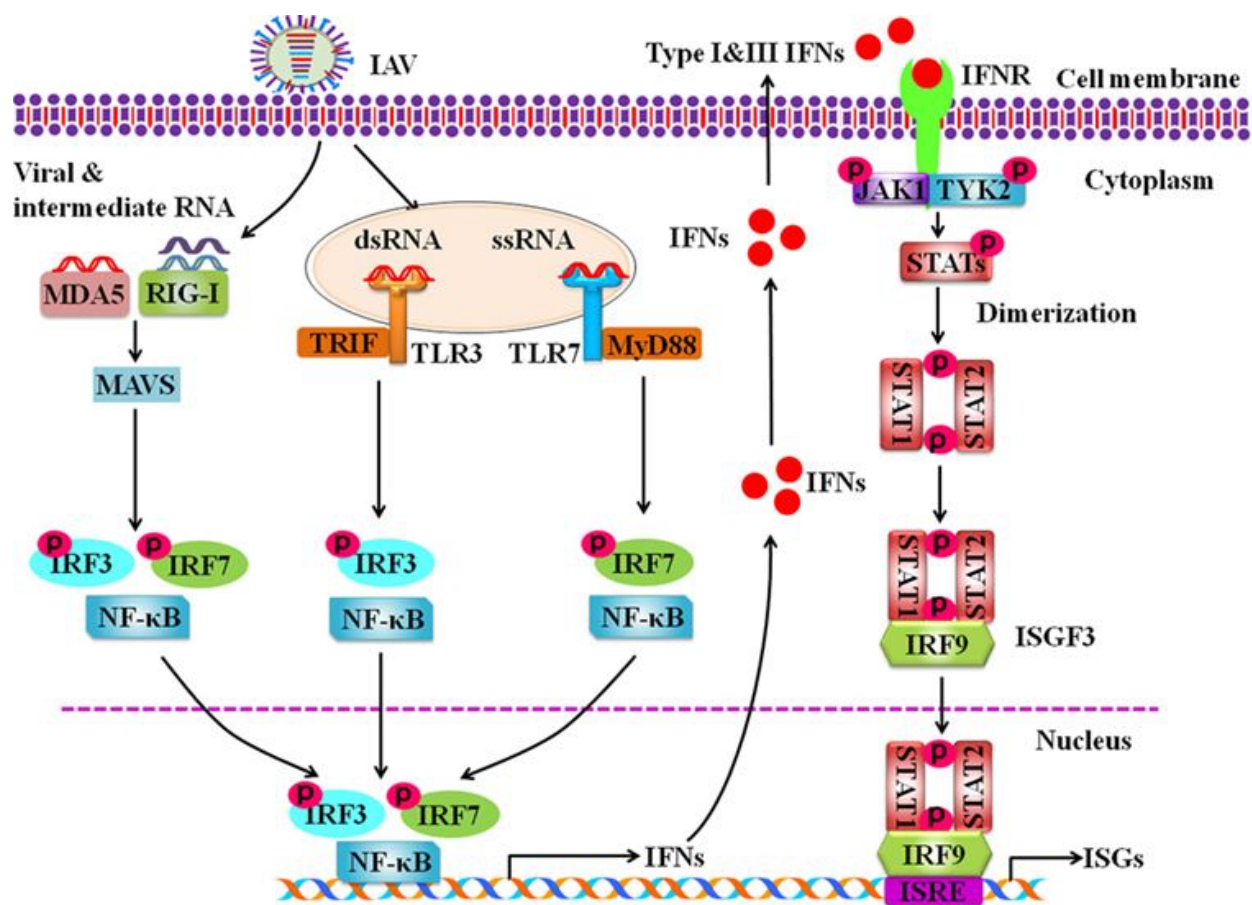


Figure 7: IAV infection stimulates an antiviral innate immune response of cells. Upon viral entry, vRNA is sensed by PRRs, which leads to the activation of IRF3, IRF7 and NF-κB and, subsequently, the expression of type-I and -III IFNs. IFNs bind to their respective IFN receptor (IFNR), resulting in the activation of JAK1 and TYK2. STAT1 and STAT2 are recruited, phosphorylated and form the ISGF3 complex together with IRF9. Ultimately, ISGF3 translocates to the nucleus, binds to ISRE, and induces the expression of ISGs, which confers an antiviral activity against IAV. Figure taken from (Chen et al., 2018b).

2.4.1. Recognition of IAV

IAV infections are recognized by the cell, which initiates an innate immune response (Fig. 7). PAMPs are conserved, small molecule motifs from the virus and enable recognition by host PRRs. Typical PRRs involved in sensing IAV infections are RIG-I-like receptors (RLR), toll-like receptors (TLR) and cyclic GMP-AMP synthase (cGas). PRRs are activated by binding to PAMPs of IAV and initiate programmed cell death, production of type-I IFNs and proinflammatory cytokines (Lee and Ryu, 2021).

The three distinct RLRs include RIG-I, melanoma differentiation-associated protein 5 (MDA5), and laboratory of genetics and physiology 2 (LGP2), which all contain a DExD/H box helicase domain (Yoneyama et al., 2005, Yoneyama et al., 2004) and are

localized in the cytoplasm. RIG-I is activated by short double-stranded RNA (dsRNA) with a 5' triphosphorylated RNA panhandle structure (Liu et al., 2015, Weber et al., 2013) and MDA5 by longer dsRNA. RIG-I does not only reside in the cytoplasm, but was recently also found in the nucleus (Liu et al., 2018). Shorter vRNAs, such as DI vRNAs, are thought to be preferentially recognized by RIG-I (Baum et al., 2010, Rehwinkel et al., 2010). On the contrary, a recent study showed that IFN production was not dependent on DI vRNA length (Mendes and Russell, 2021). This finding was rather explained that occurring deletions generate perturbations in the RNA secondary structure, which are effective RIG-I ligands, as seen for Sendai virus (Xu et al., 2015). RIG-I and MDA5 interact with MAVS, which leads to the activation of the transcription factors interferon regulatory factor (IRF) 3, IRF7, and nuclear factor kappa-light-chain-enhancer of activated B cells (NF- κ B). Finally, this leads to the expression of IFNs and proinflammatory cytokines (e.g. interleukin-6 (IL-6)) (Honda et al., 2006, Malik and Zhou, 2020).

TLRs include e.g. TLR3 (senses dsRNA), TLR7 (single-stranded (ssRNA)), and TLR8 (ssRNA) and are localized in the endosome and/or on the cell surface (Malik and Zhou, 2020). TLRs recruit an adaptor protein for signal transduction, which is myeloid differentiation primary response protein 88 (MyD88) for all TLRs except TLR3, which recruits Toll/interleukin-1 receptor domain-containing adapter inducing IFN- β (TRIF) (Matsumoto and Seya, 2008). Signaling results in the expression of IFNs and proinflammatory cytokines (Malik and Zhou, 2020). Activated RIG-I and TLR3 trigger an early type-I IFN response in epithelial cells as first line of defense (Wu et al., 2015).

2.4.2. Interferon response

IFNs are cytokines and part of the innate immune response of the cells (Fig. 7). Interference of IFNs with viral replication was originally identified by Alick Isaacs and Jean Lindenmann in 1957 (Isaacs and Lindenmann, 1957). IFNs are classified into three different types: Type-I (13 different α - and one β -isotype, several other subtypes), type-II (γ), and type-III (four λ -subtypes). All cells with a nucleus can produce type-I IFNs, but large amounts are produced by plasmacytoid dendritic cells

(pDCs) (Fitzgerald-Bocarsly and Feng, 2007). In studies of this PhD thesis, A549 cells (human lung epithelial cells, used for co-infection studies) and MDCK cells (co-infection studies and production of IAV DIPs) were used, which are both able to produce IFNs (Seitz et al., 2010, Wu et al., 2015). On the other hand, Vero cells (African green monkey kidney epithelial cells, used for co-infection studies) are deficient in producing IFNs (Emeny and Morgan, 1979, Vester et al., 2010) due to a deletion in chromosome 12 that code for multiple type-I IFN genes (Osada et al., 2014). Vero cells are, therefore, typically used as IFN-negative cell line for infection experiments. Type-I IFN response is regulated via a positive feedback loop that is directed by an interplay of IFN induction and signaling (Leviyang and Griva, 2018, Michalska et al., 2018). IFN- α and - β are the key IFNs in control of viral replication by innate immunity and in stimulating adaptive immunity (Garcia-Sastre, 2011, Le Bon and Tough, 2002).

Secreted IFNs bind to receptors in an autocrine (same cell) and paracrine (neighboring cell) manner (Michael Lavigne et al., 2021). Signaling of type-I IFNs occurs through the IFN- α/β receptor, which is present on a wide variety of human cells (de Weerd and Nguyen, 2012). IFN- γ is only secreted by immune cells (mainly by T cells and natural killer cells (Schoenborn and Wilson, 2007)), mediate adaptive immune responses and binds to the IFN- γ receptor (Green et al., 2017). IFN- λ is predominantly secreted by epithelial cells, but also by macrophages, monocytes and pDCs (Kotenko et al., 2019) and signals through the heterodimeric receptor complex, consisting of IFN- λ receptor 1 (IFN- λ R1) and interleukin-10 receptor 2 (IL-10R2). Type-III IFNs share signaling pathways and transcriptional responses with type-I IFNs (Lazear et al., 2019), but in comparison they reduce immunopathology while exerting antiviral activity primarily on mucosal surfaces (Broggi et al., 2020).

Viruses can attenuate type-I IFN responses to facilitate replication and transmission (Garcia-Sastre, 2011). For IAV, NS1 (IAV) plays a key role in inhibiting IFN production (Hale et al., 2010, Quinlivan et al., 2005, Solórzano et al., 2005). RSV infections do not induce a robust type-I IFNs response as non-structural protein 1 of RSV (NS1 (RSV)), non-structural protein 2 (NS2) and G impair IFN expression (Barik, 2013, Lo et al., 2005, Moore et al., 2008, Spann et al., 2004). For flaviviruses, the non-structural

protein 5 (NS5) has been reported to be an antagonist of type-I IFN response (Grant et al., 2016).

Treatment with recombinant type-I IFN provided antiviral activity against IAV (Kugel et al., 2009, Szretter et al., 2009), RSV (Dai et al., 1987, He et al., 2020, Sung et al., 1993), and flavivirus infections (Caine et al., 2019, Julander et al., 2007, Pires de Mello et al., 2018). In humans, pegylated IFN- α -2a has been approved to treat chronic hepatitis B (without ribavirin) and C (in combination with ribavirin) (EMA, 2023, FDA, 2023d). In type-I IFN deficient mice, the infection with avian IAV of the subtype H5N1 resulted in enhanced virulence and virus spread (Szretter et al., 2009) indicating the significant role of type-I IFNs against e.g. IAV infections. Nevertheless, recombinant type-I IFN therapies are expensive (Nguyen et al., 2019), have potential adverse effects in a dose-dependent manner including flu like symptoms, fatigue, depression, neutropenia and anemia (Borden and Parkinson, 1998, Hauschild et al., 2008, Kirkwood et al., 2002), and limitations in stability and availability (Julander et al., 2011).

2.4.3. JAK/STAT signaling pathway

An IFN response results in the activation of the Janus kinase/signal transducers and activators of transcription (JAK/STAT) signaling pathway, which is a key cascade for signal transduction from the cell membrane to the nucleus and regulates the expression of genes (Fig. 7). This signaling pathway mediates important cellular processes such as hematopoiesis, immune fitness, inflammation, tissue repair, adipogenesis, and apoptosis (Owen et al., 2019). Most of the involved molecular components were identified in the 1990s (Hu et al., 2021).

Expressed type-I and -III IFNs bind to their respective receptors on the plasma membrane. This binding leads to the activation of Janus kinase 1 (JAK1) and tyrosine kinase 2 (TYK2). Upon phosphorylation of tyrosine residues of the receptor, signal transducer and activator of transcription 1 (STAT1) and signal transducer and activator of transcription 2 (STAT2) are recruited, phosphorylated and form a heterodimer. This leads to the recruitment of IRF9 and the formation of the IFN-stimulated gene factor 3 (ISGF3) complex (contains STAT1, STAT2 and IRF9). ISGF-3 translocates to the

nucleus, binds to IFN-stimulated response elements (ISRE), and stimulates the expression of ISGs (Hu et al., 2021, Plataniias, 2005, Stanifer et al., 2019).

Ruxolitinib is a pyrazole and a potent JAK1 and Janus kinase 2 (JAK2) inhibitor, which downregulates the JAK/STAT signaling pathway. Research use of ruxolitinib allowed to demonstrate that IAV DIPs confer antiviral activity against the replication of unrelated viruses such as SARS-CoV-2, which depends on signaling through the JAK/STAT pathway (Rand et al., 2021).

2.4.4. Interferon-stimulated genes

About 450 different ISGs are expressed upon stimulation by IFNs. ISGs have a broad range of pathogen control activities such as sensing of pathogens (PRRs and IRFs), IFN desensitization and antiviral effectors functions (Schneider et al., 2014). ISGs as virus restriction factors exert an antiviral effect by targeting different stages of the viral life cycle including suppression of viral entry, translation, replication, and egress (Schneider et al., 2014, Schoggins, 2019).

2.4.4.1. Mx

ISGs include e.g. Mx genes, which are present in almost all vertebrate species and encode for family members of dynamin-like large GTPases. Induced by type-I and -III IFNs, Mx proteins provide resistance mainly against RNA viruses (Haller et al., 2007, Verhelst et al., 2013). Multiple studies show that human and murine Mx proteins are the key resistance factors against IAV infections independent of other IFN-induced factors (Haller et al., 1979, Haller et al., 1980, Haller et al., 2010, Hefti et al., 1999, Staeheli et al., 1986). Murine Mx1 protein is localized in the nucleus and is a potent resistance factor against IAV infections by interference with the assembly of the RNP complex (Verhelst et al., 2012). In contrast, the cytosolic murine Mx2 protein does not suppress IAV replication, but that of VSV (Zürcher et al., 1992). The human MxA protein is a homologue of murine Mx1 (Horisberger et al., 1990, Thimme et al., 1995). MxA is expressed in the cytoplasm and inhibits IAV infections by binding to NP and

preventing the viral transport into the nucleus (Pavlovic et al., 1992, Xiao et al., 2013). Moreover, human MxB has a cytoplasmic and nuclear form, but shows no antiviral effect against IAV but against human immunodeficiency virus type 1 (HIV-1) (Goujon et al., 2013). MDCK cells are typically used for high-titer production of IAV and encode for canine Mx1 and Mx2, which do not inhibit IAV propagation.

2.4.4.2. IFITM

IFITM genes encode for small transmembrane proteins and are mainly induced by type-I IFNs. As strong viral restriction factors, IFITM proteins suppress the infection of IAV, RSV, DENV, SARS-CoV-2, and filoviruses, among others (Huang et al., 2011, Zhang et al., 2015). Three human IFITM family members exert an antiviral effect with IFITM1, IFITM2, and IFITM3. IFITM1 is exposed on the cellular surface and contains a conserved intracellular loop domain, which is crucial for viral restriction (Smith et al., 2019). IFITM2 and IFITM3 are localized to endosomes and lysosomes (Mudhasani et al., 2013, Weston et al., 2014). The inhibition of infection occurs by targeting viral entry and replication (Zhang et al., 2015). In IFITM1-deficient mice, RSV infection led to a more severe outcome (Smith et al., 2019).

2.4.4.3. RSAD2 protein

The radical S-adenosylmethionine domain containing 2 (RSAD2) gene is also known as virus inhibitory protein, ER-associated, IFN-inducible (viperin). The induction of this ISG can occur by all three types of IFN (I, II, and III) or IFN-independent (Seo et al., 2011). RSAD2 proteins are present in the ER or in lipid droplets (Hinson and Cresswell, 2009). A broad-spectrum antiviral activity of RSAD2 protein was found against IAV, ZIKV, JEV, West Nile virus, HIV-1, hepatitis C virus, human cytomegalovirus, and herpes simplex virus 1, among others, and were, therefore, proposed as antiviral medication. The catalytic activity of RSAD2 modulates cellular metabolic pathways, which are necessary for the viral life cycle, (Honarmand Ebrahimi, 2018) leading to a restriction of viral replication processes. For instance,

interference with lipid raft metabolism was observed during IAV infection resulting in an inhibition of IAV release (Wang et al., 2007).

2.5. Viral vaccines

Viruses are used as vaccines, vectors in gene therapy, for cancer treatment (Bin Umair et al., 2022), or antiviral treatment (DIPs). In 1796, Edward Jenner observed that infection with a cowpox virus protected a human from a deadly smallpox infection (Stewart and Devlin, 2006). Finally, the vaccination resulted in the eradication of smallpox, declared by the WHO in 1980, and was the basis for the development of an increasing number of safe and effective viral vaccines. Vaccines are developed to stimulate a durable and effective humoral and cellular response of the adaptive immune system to protect against virus infections and control the spread of the virus (Feng et al., 2021, Primorac et al., 2022). Several technology platforms including virus or non-virus systems are used for production of about 966 vaccine candidates in the R&D pipeline including recombinant proteins (22%), nucleic acids (18%), inactivated viruses (14%), viral vectors (14%), conjugates (components of virus/bacteria, 11%), live attenuated viruses (9%), virus-like particles (4%), and toxoids (3%) (Yue et al., 2023).

2.5.1. Influenza vaccines

Due to the high mutation rate of IAV, changes in the HA and NA can occur, which is referred to as antigenic drift. This leads to emergence of new IAV variants, which escape the recognition by neutralizing antibodies (Han and Marasco, 2011). Therefore, continuous global influenza surveillance and annual reformulation of influenza vaccines to match circulating strains is required. This became clear when the first licensed influenza vaccine in the United States in 1945 proved to be ineffective against circulating strains during the 1947 influenza epidemic due to intrasubtypic antigenic variations (Kilbourne et al., 2002). Annual reformulation is a difficult and lengthy process and poses the risk of vaccine mismatch (Chen et al., 2021, Weir and

Gruber, 2016). Therefore, there are strong research efforts to develop an universal influenza vaccine that confer robust cross-protective immunity, and several clinical trials are currently underway (Wang et al., 2022). Typically, an annual influenza vaccine is composed of two influenza A strains (H1N1, H3N2) and one (trivalent) to two (quadrivalent) influenza B strains, with a different composition for the Northern and Southern hemisphere. Despite its moderate vaccine effectiveness, influenza vaccination is the most effective means of preventing influenza disease (Javanian et al., 2021). Currently used antiviral drugs for treatment target the viral neuraminidase (oseltamivir, zanamivir, peramivir) or the viral endonuclease (baloxavir), but increasing drug resistance occur reducing the drug efficacy (Lampejo, 2020, Sarker et al., 2022).

Most influenza vaccines are inactivated whole (treated with formaldehyde or β -propiolactone), subunit (treated with detergents) or split (treated with ethyl ether or sodium dodecyl) vaccines made from whole virus particles (Doroshenko and Halperin, 2009). Administration of inactivated influenza vaccines is typically intramuscular. Today, inactivated influenza vaccines account for 89.6% of total production capacity of seasonal influenza vaccines, while two further types with live attenuated influenza vaccines (LAIVs) (5.0%) and recombinant vaccines (5.4%) are on the market (Sparrow et al., 2021). The cold-adapted LAIV FluMist[®] replicate efficiently at lower temperatures of 25°C, but its replication is greatly reduced in the respiratory tract leading to no influenza-like illness (FDA, 2023b, Zhou et al., 2016). This vaccine is administered as nasal spray and additionally triggers mucosal and cell-mediated immunity leading to a broader protection against different influenza virus variants (Belshe et al., 2000, Mendelman et al., 2004, Subbarao, 2021). The recombinant influenza vaccine (Flublok[®]) is produced in insect cells using the baculovirus expression vector system and administered intramuscularly (Cox and Hollister, 2009). Influenza vaccines based on the mRNA technology are an additional option and a clinical study for a universal vaccine is currently conducted (FDA, 2023a).

2.6. Production of influenza vaccines

Since the 1940s, the traditional production process involves embryonated chicken eggs, but cell culture-based or recombinant influenza vaccines produced in insect cells were also established. Embryonated chicken eggs are still heavily used for production of seasonal influenza vaccines (84.5%) relative to virus grown in cell culture (15.5%) (Sparrow et al., 2021).

2.6.1. Egg-based production

The production in embryonated chicken eggs is a standardized and low cost procedure and egg-based vaccines have a long proven history of safety (Hegde, 2015). The seed virus used for egg-based production can be isolated from clinical samples and passaged in eggs. However, reassorting is necessary when the virus cannot be grown to high titers. In this process, the new influenza strain is recombined in a co-infection scenario or by using reverse genetics with a well growing laboratory adapted virus (PR8) (Fulvini et al., 2011). Subsequently, the virus variants with the donor antigens (HA and NA) are selected with antibodies. This results in a seed virus that yields high titers during production and harbors the antigenic determinants of the donor strain (Fulvini et al., 2011, Rajaram et al., 2020, Robertson et al., 1992). There are numerous disadvantages of the labor-intensive egg-based production compared to cell culture. One to two eggs are needed to manufacture one influenza vaccine dose (Manini et al., 2017), which means that need for eggs is very high. Moreover, sterility is a challenge for this way of influenza vaccine production using more than 100 million embryonated chicken eggs (Rajaram et al., 2020). Moreover, eggs harbor avian receptors (α 2,3-linked sialic acid), but human influenza vaccines bind preferentially to a different receptor (α 2,6-linked sialic acid) present on mammalian cells (Rajaram et al., 2020). Therefore, a process called egg adaptation is required for preferential binding to the avian receptor and, thus, ensuring growth in eggs. The gained egg-adaptive mutations can alter antigenicity of HA (Liang et al., 2022), which might reduce the vaccine effectiveness (Kodihalli et al., 1995, Rajaram et al., 2020, Zost et al.,

2017). Cell culture-based influenza vaccines do not require egg adaptation and might be more effective than egg-based vaccines (Rajaram et al., 2020).

2.6.2. Cell culture-based production

Commercial cell culture-based influenza vaccine manufacturing uses MDCK cells growing in suspension culture (Flucelvax[®] (Seqirus, 2023)). In addition, several other suspension cell lines such as the human cell lines PER.C6 (Pau et al., 2001), CAP (Genzel et al., 2013), and human embryonic kidney cell line HEK293-SF (Petiot et al., 2011), the avian cell lines AGE1.CR and AGE1.CR.pIX (Lohr et al., 2009), the duck embryonic stem cell line EB66 (Naruse et al., 2015), and the porcine kidney cell line PBG.PK2.1 (Gränicher et al., 2019) were described for high titer production of IAV. So far, all could not reach the maximum cell-specific virus yields (CSVYs) exceeding 12,000 (virions/cell) for MDCK cells reported in research use (Bissinger et al., 2019). For live attenuated influenza vaccine production, adherent MDCK and Vero cells have been reported to be high producers (George et al., 2010, Ghendon et al., 2005, Liu et al., 2009). Relative to egg-based virus growth, cell culture-based production offers i) improved process control, ii) low sterility risks, iii) more flexibility in scaling up by using suspension cells, iv) shorter production and supply times, v) moderately more effective vaccines, and vi) no risk regarding loss of eggs during bird flu outbreaks.

First developed (large-scale) influenza vaccine production processes in bioreactors involved the use of adherent cells growing on microcarriers (Genzel et al., 2006, Kistner et al., 1998). Baxter Vaccines established a cell culture-based manufacturing process for human influenza vaccines with adherent Vero cells in 1998. In 2001, a first influenza vaccine (Influvac[®]TC) manufactured in adherent MDCK cells (American-Type Culture Collection (ATCC), CCL-34) was licensed for Solvay Biologicals in the Netherlands, but never brought to market (Doroshenko and Halperin, 2009). Vaccines produced in Vero cells were licensed for EU in 2009 (Celvapan[®]) and 2010 (Preflucel[®]) for Baxter, but were dropped in 2012 at the latest due to the risk of negative side effects (Pérez Rubio and Eiros, 2018).

Cultivations with adherent cells pose limitations in scale-up, which is limited by the surface area rather than on volume as for suspension cells. Moreover, handling adherent cells is more labor intense as e.g. cell detachment is required. Therefore, production in suspension cells is preferred over adherent cells due to a better process control and the possibility of intensified virus production in perfusion mode (see 2.8). Therefore, the adherent MDCK cell line CCL-34 was adapted to grow in suspension culture (MDCK 33016) in 1997 (Gröner and Vorlop, 1997) and used as cell substrate for the production of Optaflu[®] by Novartis, which was approved 2007 (Doroshenko and Halperin, 2009). Currently, this cell line is used for the production of quadrivalent Flucelvax[®] Tetra (Europe) and Flucelvax[®] Quadrivalent (United States) licensed for Seqirus (Lamb, 2019). MDCK cell lines for scientific use are either derived from ATCC or European Collection of Authenticated Cell Cultures (ECACC). Initial suspension growth adapted MDCK cell lines grown in the chemically defined medium Smif8 showed only moderate cell growth with doubling times of 26 h, maximum VCC (VCC_{max}) of $4-8 \times 10^6$ cells/mL and maximum total virus yields of $3.3 \log_{10}(\text{HAU}/100 \mu\text{L})$. Moreover, cell aggregation was observed (Bissinger, 2020). Adaptation to an optimized chemically defined medium (Xeno[™], Shanghai BioEngine Sci-Tech) resulted in suspension MDCK cell lines (MDCK(sus) derived from ECACC, and MDCK(sus).A derived from ATCC) growing as single cells with doubling times of 21–22 h, VCC_{max} of $8-12 \times 10^6$ cells/mL and maximum total virus yields of $3.6 \log_{10}(\text{HAU}/100 \mu\text{L})$ in batch mode in shake flasks (Bissinger, 2020). Further process intensification by operation of STR in perfusion mode enabled cell growth up to 50×10^6 cells/mL and a maximum HA titer of $4.4 \log_{10}(\text{HAU}/100 \mu\text{L})$ (Wu et al., 2021). Recent efforts focused on the establishment of a monoclonal MDCK suspension culture using an automated single-cell cloning approach (Zinnecker et al., 2024). Moreover, MDCK cells were engineered to enhance the isolation rates and propagation of human influenza viruses (Matrosovich et al., 2003, Oh et al., 2008, Takada et al., 2019). For instance, MDCK-SIAT1 cells overexpress the human α -2,6-sialtransferase (SIAT1), which results in higher levels of α -2,6-linked sialic acid receptors (Byrd-Leotis et al., 2022, Matrosovich et al., 2003), which are present on mammalian cells.

The upstream process for suspension cell culture-based production of influenza vaccines consists of two phases. First, the production bioreactor is inoculated with cells, which were previously expanded during the seed train. Cells are, then, exponentially grown to a certain VCC, typically between $1\text{--}4 \times 10^6$ cells/mL, at predefined optimal cultivation conditions (e.g. temperature, pH, aeration). Addition of fresh medium to the production bioreactor can help to supplement cells with limiting substrates (e.g. glucose, glutamine) and dilute toxic byproducts such as ammonium and lactate inhibiting cell growth and virus production (Schneider et al., 1996). Furthermore, a temperature decrease from 37°C to $32\text{--}33^\circ\text{C}$ prior to infection was reported to be beneficial for IAV propagation (Hein et al., 2021b, Wu et al., 2021). Subsequently, cells are infected with influenza virus at low multiplicity of infection (MOI) to minimize the volume of seed virus material required. For virus propagation, trypsin addition is required to facilitate the activation of influenza viruses by proteolytic cleavage of HA (Seitz et al., 2012). After virus harvest at optimal time point, virus broth is clarified by e.g. centrifugation and depth/micro filtration, DNA is digested, infectious viruses are chemically inactivated, the virus is disrupted in the case of subunit or split influenza vaccines, the material is purified and the vaccine is formulated (Milian and Kamen, 2015).

2.7. Production of defective interfering particles

2.7.1. Influenza A virus

DIPs are deficient in replication and can only replicate in co-infection with infectious STVs by complementation of the missing gene function. At low MOI, only a low number of co-infection events occur, preventing the propagation of DIPs, while STVs can grow unhindered leading to high STV concentrations. High MOI scenarios increases the chance for co-infection, which favors a fast accumulation of DIPs (Frensing, 2015). Concurrently, as DIPs possess a replication advantage relative to STVs (Laske et al., 2016, Marriott and Dimmock, 2010, Nayak et al., 1985), STV propagation is inhibited, which leads to a reduction of infectious virus titers. Serial passaging of IAV led to

periodic oscillations in infectious and total virus titers over time, confirming the “von Magnus effect”, with infectious virus titers dropping first (Bangham and Kirkwood, 1990, Kirkwood and Bangham, 1994).

Historically, multiple serial passages of IAV STVs at high MOI were conducted to generate and accumulate IAV DIPs in embryonated chicken eggs (Dimmock et al., 1986). Time points with a low ratio of infectious to total virus titer indicated the presence of a high fraction of DIPs within the virus population. Moreover, UV irradiation of the DIP material was needed to inactivate the infectious STVs prior to testing in mice (Dimmock et al., 1986). However, the serial passaging approach led to undefined DIP harvests due to the occurrence of a large variety of different DI vRNAs (Davis and Nayak, 1979, Duhaut and Dimmock, 1998, Jennings et al., 1983). Therefore, it was not possible to study the antiviral effect of one single DI vRNA *in vitro* or *in vivo*.

The generation of well-defined IAV DIP seeds by using reverse genetics, originally developed for IAV STV (Hoffmann et al., 2000, Neumann et al., 2000), circumvented this problem (Duhaut and Dimmock, 2003, Fodor et al., 1999). To generate IAV DIPs, Vero cells were transfected with a plasmid encoding for the DI vRNA and 17 plasmids for the STV (A/WSN, H1N1) needed for DIP propagation. An additional passage in embryonated chicken eggs after rescue was performed to boost DIP production (Duhaut and Dimmock, 2003). In the following years, a transfection system for IAV DIPs derived from PR8, was established (Dimmock et al., 2008, Subbarao et al., 2003), a virus backbone also used for high-titer viral vaccine production (Harvey et al., 2010). This transfection system included plasmids encoding for the eight genomic segments, expression plasmids for PB2, PB1, PA, and NP, one additional plasmid for the defective interfering (DI) genome, the use of human embryonic kidney cells, containing the SV40 large T antigen (HEK-293T) for transfection, and adherent MDCK cells to increase virus titers. Again, supernatant was passaged two times in embryonated chicken eggs still resulting in a large variety of different DI vRNAs (Dimmock et al., 2008, Wasik et al., 2018). To improve process control, scalability, sterility, and flexibility, our research group at the MPI developed a cell culture-based production process for DI244 in the presence of STVs in batch mode using suspension

AGE1.CR.pIX cells. The use of a seed virus depleted in DI vRNAs, which was generated by several low MOI passages, reduced the variability of DI vRNAs present in the DIP harvest (Wasik et al., 2018). Moreover, production of DI244 in continuous mode (two-stage bioreactor system) was demonstrated (Tapia et al., 2019). Nevertheless, the presence of infectious STVs would raise safety and concerns for the regulatory authorities, and the required UV inactivation reduced interfering efficacy of produced DIP materials (Hein et al., 2021c).

Therefore, a genetically engineered cell-based production system for generation of purely clonal cDIPs, harboring a deletion in vRNA of Seg 1 (e.g. DI244), without addition of STVs was developed (Bdeir et al., 2019, Hein et al., 2021a). For this, adherent HEK-293T and MDCK cells were transduced by a retrovirus for stable expression of the missing PB2 (deleted in corresponding cDIPs) to complement for the defect in viral replication (Bdeir et al., 2019, Yamagata et al., 2019). Upon transfection of HEK-293T-PB2(adh) and MDCK-PB2(adh) with one plasmid encoding for the DI vRNA and seven plasmids encoding for the remaining full-length vRNAs (eight-plasmid reverse genetics system (Bdeir et al., 2019, Hoffmann et al., 2000)), purely clonal DI244 was generated (Bdeir et al., 2019). To enhance DIP production and scalability, suspension MDCK cells growing in Xeno™ stably expressing PB2 were generated, in the following referred to as MDCK-PB2(sus) (Hein et al., 2021a). Production and interfering efficacy of DI244 in MDCK-PB2(sus) in shake flasks was strongly dependent on the multiplicity of DIP (MODIP). The optimized DI244 production process in batch mode was transferred to a STR and a steric exclusion-based chromatographic purification train was developed with a product yield of 92% (Hein et al., 2021a). Subsequent process intensification in perfusion mode with perfusion rate control enabled very high-titer production of DI244 at more than 20×10^6 cells/mL (Hein et al., 2021b). Importantly, the process yielded in reproducible product quality as no apparent contamination with DI vRNAs other than DI244 in all eight segments was achieved. Furthermore, innocuity assays demonstrated the absence of infectious STVs after two passages of purely clonal DI244 in adherent MDCK cells (Hein et al., 2021a). The production strategy to produce Seg 1 cDIPs in the absence of infectious STVs has been adopted by other research groups for IAV DIPs (Alnaji et al., 2021, Wang et al., 2020, Wang et al., 2023).

For OP7, no production system free of infectious STVs was available so far. Cell culture-based production of OP7 in MDCK(sus) cells in shake flasks still relied on co-infection with STVs and subsequent UV inactivation (Hein et al., 2021c). As OP7 seed virus (PR8), a single-cell virus isolate was used (Kupke et al., 2019). Moreover, OP7 production yields and interfering efficacy again showed a dependency on MOI of STVs. As OP7 suppressed viral replication, lower virus titers were achieved at higher MOIs. On the contrary, lower MOIs led to higher virus titers due to a decreased chance for co-infection and, thus, reduced OP7 replication. Optimal OP7 production was achieved at an intermediate MOI of 10^{-2} as the highest concentration of OP7 and interfering efficacy of the material was obtained (Hein et al., 2021c).

2.7.2. Other viruses

Initially, DIPs were mainly studied to understand their formation and their role within the virus population rather than to produce them for antiviral therapy *in vivo* (Vignuzzi and Lopez, 2019). Typically, STVs were passaged at high MOI in cell culture to force the generation and accumulation of DIPs as shown for RSV (Sun and Lopez, 2016), VSV (Stauffer Thompson et al., 2009) and measles virus (Calain and Roux, 1988, Hall et al., 1974). DIP separation/purification was often performed by gradient centrifugation when DIPs have a lower density than the corresponding STVs (Hall et al., 1974, Stauffer Thompson et al., 2009, Sun and Lopez, 2016). Yet, loss of RSV infectivity was reported for ultracentrifugation in sucrose matrix (Gias et al., 2008, Trépanier et al., 1981). Further developed molecular and genetic tools made it possible to produce first clonal DI genomes and DIPs including Sendai virus (Calain et al., 1992), mouse hepatitis virus (Groot et al., 1992), classical swine fever virus (Meyers et al., 1996), and Semliki forest virus (Thomson et al., 1998).

In the upcoming years, interest in DIP studies increased, i.e. as an option for antiviral therapy. In 2016, the INTERfering and Co-Evolving Prevention and Therapy (INTERCEPT) program was initiated by Defense Advanced Research Projects Agency (DARPA) of the United States Department of Defense. This program aimed to develop platforms to produce safe and efficacious DIPs against multiple viral diseases

caused by ZIKV (Rezelj et al., 2021), Chikungunya virus (Levi et al., 2021), poliovirus (Xiao et al., 2021), Nipah virus (Welch et al., 2022, Welch et al., 2020), IAV (Hein et al., 2021a, Hein et al., 2021b), HIV (Tanner et al., 2019), and SARS-CoV-2 (Chaturvedi et al., 2021). Serial passaging of STVs was typically conducted to generate and select highly competitive DI genomes in a virus population, which were considered to possess a high interfering efficacy. Subsequently, novel sequencing (e.g. Illumina sequencing) and computational tools enabled the detection and quantification of distinct DI vRNAs (Rezelj et al., 2021). Instead of selecting DI genomes by viral evolution, studies also reported on artificial designs (Chaturvedi et al., 2021, Tanner et al., 2019, Yao et al., 2021). Several biological production systems were developed for STV-free DIP production including packaging DI genomes in virus-like particles (VLPs) (Chaturvedi et al., 2021, Rezelj et al., 2021), packaging cell lines (Xiao et al., 2021), cell lines continuously producing DIPs (Li et al., 2021, Lin et al., 2022), and *in vitro*-transcription of RNA with packaging into lipid nanoparticles (LNPs) (Chaturvedi et al., 2021). More specifically, a VLP-production system for ZIKV DIPs was developed in which plasmids encoding for a DI genome, the structural proteins C, PrM, E and the non-structural protein 1 of ZIKV (NS1 (ZIKV)) were transfected to HEK-293T (Rezelj et al., 2021). The packaging cell line approach for poliovirus DIPs included the electroporation of *in vitro* transcribed DI genomes into a HeLa S3 cell line stably expressing the precursor of the poliovirus capsid (Xiao et al., 2021). A HEK-293T cell line was designed to continuously produce DENV DIPs upon lentiviral and retroviral transduction that express structural, non-structural proteins and the DI genome (Li et al., 2021). The suspension adapted producer cell line was used to produce DENV DIPs in a bioreactor and a purification process by column chromatography was developed (Lin et al., 2022). For SARS-CoV-2 DIPs, packaged RNA into LNPs enabled efficient RNA delivery into lungs upon intranasal administration (Chaturvedi et al., 2021) and protected RNA from degradation by ribonucleases (Eygeris et al., 2022).

2.8. Process intensification by perfusion culture

In recent years, identification of a producer cell line (MDCK), its adaptation to suspension growth in chemically-defined medium, its genetic engineering for STV-free production of cDIPs and the implementation of reverse genetics to generate DIP seeds have greatly increased VCC_{max} to $>10 \times 10^6$ cells/mL in batch mode, CSVY and product quality (purely clonal DIPs) for cell culture-based IAV DIP production. In the case of a pandemic scenario, there is a very high demand for vaccines and viral vectors. Gene therapies also depend on very large quantities of viral vectors, and several of those have been approved and many are currently in clinical development (Zhao et al., 2022). Optimization of the batch mode production can be carried out by identification of optimal production conditions (temperature, pH, dissolved oxygen (DO), stirring speed), infection conditions (MOI, time of infection (TOI), temperature shift), trypsin concentration, and time of harvest (Pelz et al., 2022). To increase virus yields, multiple batch mode bioreactors can be operated in parallel. Yet, more cost-efficient and flexible strategies for production of biopharmaceuticals are desired today (Chen et al., 2018a). Process intensification can be applied for an efficient production by increasing space-time yield (STY) or even the volumetric virus productivity (VVP). This can decrease the size of bioreactors and facility footprint (Chen et al., 2018a).

2.8.1. Cultivation at high viable cell concentrations

Process intensification is enabled by perfusion cultivation at high VCC to produce significantly more virus while maintaining or even enhancing CSVY (Gallo-Ramirez et al., 2015). In a perfusion cultivation, a cell retention device is coupled to a bioreactor. At a constant bioreactor working volume spent medium is removed while retaining the cells and addition of fresh medium. Thereby, cells are provided with sufficient substrates and only low levels of inhibitory metabolites accumulate. VCC_{max} in the range of $10\text{--}160 \times 10^6$ cells/mL have been reported for high-titer virus production (Coronel et al., 2019, Coronel et al., 2020, Genzel et al., 2014, Göbel et al., 2023, Gränicher et al., 2021, Gränicher et al., 2019, Gränicher et al., 2020, Hein et al., 2021b, Nikolay et al., 2018, Petiot et al., 2011, Tran and Kamen, 2022, Wu et al.,

2021). Various cell retention devices have been described for perfusion cultivation including membrane-based systems, acoustic filters, inclined settlers, centrifuges, and hydrocyclones. Pharmaceutical industry also started to consider the use of perfusion cultures as a process option of the future (Bielser et al., 2018). However, the introduction of perfusion technologies for industrial virus production is slow and mainly used in academia. Next to production at high VCC, perfusion can also be used for cell banking to start from a higher initial cell number upon thawing (Tao et al., 2011) and for the last seed train step previous to the production bioreactor (Bielser et al., 2018, Woodgate, 2018), which is implemented for large-scale recombinant protein production.

2.8.1.1. Membrane-based perfusion systems

Membranes are frequently used as cell retention device owing to their scalability, ease of use, and high cell retention efficiency (Nikolay et al., 2020). Membrane-based perfusion systems include alternating tangential flow filtration (ATF), tangential flow filtration (TFF), TFDF, hollow fiber bioreactors, and spin filters. One major drawback of using membranes for perfusion is filter fouling indicated by increased transmembrane pressure (Voisard et al., 2003). A system designed to decrease the risk of filter fouling is the TFF system. A centrifugal or peristaltic pump (Wang et al., 2017) is connected to a membrane (typically a hollow fiber membrane) and the bioreactor within a recirculation loop as illustrated in Fig. 8. The flow of the cell suspension is unidirectional and tangential across the membrane at positive pressure. Cell-free supernatant is removed by a peristaltic pump. Retention of recombinant proteins was observed in the membrane for the TFF system (Karst et al., 2016). The ATF system consists of a diaphragm pump and a filter housing for the membrane (Fig. 8). An alternating flow of cell suspension is generated across the membrane between the bioreactor and the diaphragm pump by an exhaust and pressure cycle. The pulsating flow during the exhaust cycle creates a self-cleaning backflush from the permeate side, which reduces filter fouling and, thus, decreases or prevents retention of e.g. recombinant proteins (Clincke et al., 2013, Karst et al., 2016, Schwarz et al., 2020).

Typically, hollow fiber membranes with a cut-off of 0.2–0.65 μm are used, which often leads to retention of viruses inside the bioreactor, despite the self-cleaning backflush of the ATF or the tangential flow of the TFF (Genzel et al., 2014, Hein et al., 2021b, Nikolay et al., 2020, Vázquez-Ramírez et al., 2019, Wu et al., 2021). In virus retention, structural and physicochemical characteristics of the membrane play an important role (Nikolay et al., 2020). Recently, the introduction of a new tubular membrane (pore size $\sim 10 \mu\text{m}$) allowed for continuous virus harvesting of DI244 and murine leukemia virus (MLV) vectors by using the ATF system (Hein et al., 2021b, Hein et al., 2023). Similarly, continuous virus harvesting of lentiviral vectors (LV) (Tona et al., 2023, Tran and Kamen, 2022), adeno-associated viruses (AAV) (Mendes et al., 2022) and IAV (Silva et al., 2023) was possible by using a TDF system, which is operated similarly to a TFF system but relies on a depth filter (pore size 2–5 μm) for cell retention. Continuous virus harvesting was also shown for non-membrane-based retention devices, more specifically acoustic filters (Göbel et al., 2023, Gränicher et al., 2020, Manceur et al., 2017) and inclined settlers (Coronel et al., 2020). However, both systems have limited scalability, lower cell retention efficiency and a higher residence time of cells and viruses (Coronel et al., 2020, Gränicher et al., 2020). Continuous virus harvesting through membranes would allow direct virus harvest cooling, which typically increases virus stability and, thus, virus yields and productivity. Moreover, integration of upstream and downstream processing could be realized to increase cost-effectiveness, productivity, flexibility, and product quality (Bielser et al., 2018, Gränicher et al., 2021).

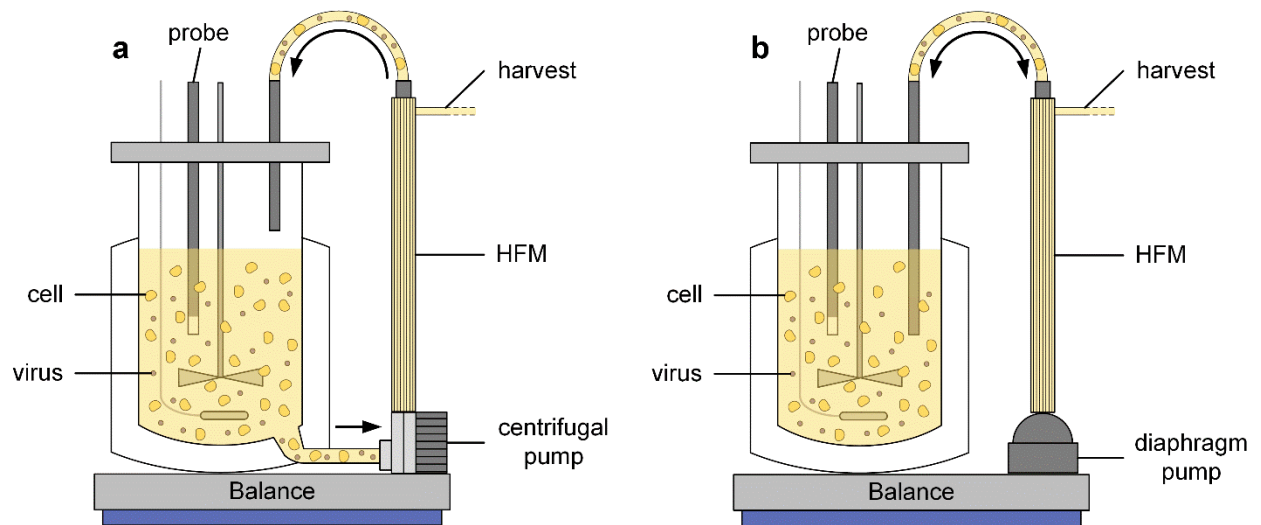


Figure 8: Schematic illustration of perfusion systems comprising a TFF (a) and ATF (b) device. Both perfusion systems consist of a pump, which drives the cell suspension across the hollow fiber membrane (HFM) between the bioreactor and the pump. In the TFF system, the centrifugal or peristaltic pump is operated in unidirectional flow. For the ATF system, an alternating flow is created by a diaphragm pump. For TFF and ATF, cell-free harvest is removed by a peristaltic pump (not shown). Figure taken from (Hein, 2022).

3. Manuscripts

This cumulative dissertation comprises six manuscripts, which are presented in the following. The manuscripts cover the objectives listed in the introduction and include the main results of the doctoral thesis project. All relevant topics were covered in the theoretical background. The manuscripts were developed in collaboration with various partners. Therefore, the initiation and management of these collaborations was an important part of the doctoral thesis.

3.1. First Manuscript

In the study of the first manuscript, data obtained from NGS shed light on characteristics of the DIP population in a semi-continuous culture. Moreover, novel cDIP candidates with improved antiviral activity compared to known IAV DIPs are screened, produced free of infectious STVs, and evaluated for efficacious antiviral therapy.

Pelz, Lars*; Rüdiger, Daniel*; Dogra, Tanya*; Alnaji, Fadi G.; Genzel, Yvonne; Brooke, Christopher B.; Kupke, Sascha Y.; Reichl, Udo

*Shared first authorship

Semi-continuous propagation of influenza A virus and its defective interfering particles: Analyzing the dynamic competition to select candidates for antiviral therapy

Journal of Virology, 2021

(Pelz et al., 2021)

Reproduced with permission from American Society for Microbiology.

No changes were made.



<https://creativecommons.org/licenses/by/4.0/>

Individual contribution:

In the study of the first manuscript, I carried out the semi-continuous propagation of IAV and DIPs (Figure 1), multiplication of new candidate Seg 1 DIPs in MDCK-PB2(sus) cells and interference assay (Figure 7). In addition, I investigated the processed NGS data for Figure 2, 3, 4, 5, 6 with Daniel Rüdiger, who performed the computational data analysis. Moreover, I wrote major parts of the manuscript.



Semi-continuous Propagation of Influenza A Virus and Its Defective Interfering Particles: Analyzing the Dynamic Competition To Select Candidates for Antiviral Therapy

Lars Pelz,^a Daniel Rüdiger,^a Tanya Dogra,^a Fadi G. Alnaji,^b Yvonne Genzel,^a  Christopher B. Brooke,^b  Sascha Y. Kupke,^a Udo Reichl^{a,c}

^aMax Planck Institute for Dynamics of Complex Technical Systems, Bioprocess Engineering, Magdeburg, Germany

^bUniversity of Illinois at Urbana-Champaign, Department of Microbiology, Urbana, Illinois, USA

^cOtto-von-Guericke-University Magdeburg, Bioprocess Engineering, Magdeburg, Germany

Lars Pelz, Daniel Rüdiger, and Tanya Dogra contributed equally to this work. Author order was determined by a throw of the dice.

ABSTRACT Defective interfering particles (DIPs) of influenza A virus (IAV) are naturally occurring mutants that have an internal deletion in one of their eight viral RNA (vRNA) segments, rendering them propagation-incompetent. Upon coinfection with infectious standard virus (STV), DIPs interfere with STV replication through competitive inhibition. Thus, DIPs are proposed as potent antivirals for treatment of the influenza disease. To select corresponding candidates, we studied *de novo* generation of DIPs and propagation competition between different defective interfering (DI) vRNAs in an STV coinfection scenario in cell culture. A small-scale two-stage cultivation system that allows long-term semi-continuous propagation of IAV and its DIPs was used. Strong periodic oscillations in virus titers were observed due to the dynamic interaction of DIPs and STVs. Using next-generation sequencing, we detected a predominant formation and accumulation of DI vRNAs on the polymerase-encoding segments. Short DI vRNAs accumulated to higher fractions than longer ones, indicating a replication advantage, yet an optimum fragment length was observed. Some DI vRNAs showed breaking points in a specific part of their bundling signal (belonging to the packaging signal), suggesting its dispensability for DI vRNA propagation. Over a total cultivation time of 21 days, several individual DI vRNAs accumulated to high fractions, while others decreased. Using reverse genetics for IAV, purely clonal DIPs derived from highly replicating DI vRNAs were generated. We confirm that these DIPs exhibit a superior *in vitro* interfering efficacy compared to DIPs derived from lowly accumulated DI vRNAs and suggest promising candidates for efficacious antiviral treatment.

IMPORTANCE Defective interfering particles (DIPs) emerge naturally during viral infection and typically show an internal deletion in the viral genome. Thus, DIPs are propagation-incompetent. Previous research suggests DIPs as potent antiviral compounds for many different virus families due to their ability to interfere with virus replication by competitive inhibition. For instance, the administration of influenza A virus (IAV) DIPs resulted in a rescue of mice from an otherwise lethal IAV dose. Moreover, no apparent toxic effects were observed when only DIPs were administered to mice and ferrets. IAV DIPs show antiviral activity against many different IAV strains, including pandemic and highly pathogenic avian strains, and even against nonhomologous viruses, such as SARS-CoV-2, by stimulation of innate immunity. Here, we used a cultivation/infection system, which exerted selection pressure toward accumulation of highly competitive IAV DIPs. These DIPs showed a superior interfering efficacy *in vitro*, and we suggest them for effective antiviral therapy.

KEYWORDS influenza A virus, defective interfering particles, antiviral, next-generation sequencing, continuous virus production

Citation Pelz L, Rüdiger D, Dogra T, Alnaji FG, Genzel Y, Brooke CB, Kupke SY, Reichl U. 2021. Semi-continuous propagation of influenza A virus and its defective interfering particles: analyzing the dynamic competition to select candidates for antiviral therapy. *J Virol* 95: e01174-21. <https://doi.org/10.1128/JVI.01174-21>.

Editor Stacey Schultz-Cherry, St. Jude Children's Research Hospital

Copyright © 2021 Pelz et al. This is an open-access article distributed under the terms of the [Creative Commons Attribution 4.0 International license](https://creativecommons.org/licenses/by/4.0/).

Address correspondence to Sascha Y. Kupke, kupke@mpi-magdeburg.mpg.de.

Received 12 July 2021

Accepted 19 September 2021

Accepted manuscript posted online 22 September 2021

Published 23 November 2021

Yearly, on average, 400,000 people globally die from an infection with seasonal influenza A virus (IAV) (1). Moreover, the potential emergence of pandemic strains is a major threat to public health (2). The most effective prevention of the influenza disease is vaccination with tri- or quadrivalent formulations, which provide protection against different influenza virus strains (3, 4). However, influenza vaccines have to be reformulated annually as a result of antigenic drifts (5). This is associated with a potential decrease in vaccine efficacy due to false predictions and a vaccine mismatch to circulating strains (6). Furthermore, antiviral drugs targeting the viral neuraminidase (oseltamivir, zanamivir) (7) or the viral endonuclease (baloxavir) (8) may also be used. However, circulating strains have already shown resistance against available antivirals (9–11). Therefore, the development of effective prophylactic and therapeutic treatment options is urgently needed.

One promising approach for antiviral therapy is the application of defective interfering particles (DIPs) (12–16). These naturally occurring viral mutants feature an internal deletion in one of their eight viral RNA (vRNA) segments, which renders them defective in virus replication. In addition, a new species of IAV DIPs that showed point mutations on segment (Seg) 7 vRNA was discovered recently (17). DIPs can only replicate in a coinfection with infectious standard virus (STV), which complements the respective defect in the replication of the DIPs. These viral mutants are believed to interfere by preferential and faster replication of the defective interfering (DI) vRNA in comparison to the full-length (FL) vRNA, thereby drawing away cellular and viral resources required for STV growth (18–20). Furthermore, interference was shown at the packaging step, as DI vRNAs can selectively outcompete FL vRNA packaging (21, 22). Notably, in mouse and ferret models, the administration of DIPs resulted in a pronounced antiviral effect against IAV infection (13, 14, 23–26). Furthermore, IAV DIP treatment also resulted in protection against heterologous interferon (IFN)-sensitive respiratory virus infections (27, 28), including SARS-CoV-2 infection (29), by the ability of DIPs to enhance stimulation of innate immunity upon coinfection.

Recently, we established a two-stage bioreactor system for cell culture-based production of IAV (for vaccine manufacturing) (30) and production of a prototypic, well-characterized DIP (“DI244”) (23, 24, 27, 31). Here, uninfected cells (first bioreactor) were continuously fed to a second bioreactor that contained virus-infected cells. However, in such a continuous culture, the coinfection of STVs and DIPs typically results in periodic oscillations of virus titers due to their dynamic interactions. Moreover, *de novo* generation and accumulation of numerous DI vRNAs was observed (30, 31).

In the present study, a simplified, semi-continuous setup was used to thoroughly investigate the generation and growth competition between DIPs during 21 days of IAV infection. Assuming that DIPs showing exceptional propagation also show high interfering efficacies, we anticipated identification of potent candidates for antiviral therapy. For detection and quantification of the different deletion junction on the IAV vRNA level, we used a recently published next-generation sequencing (NGS) framework (32). We observed a small subset of highly accumulated DI vRNAs after 21 days postinfection (dpi), while other deletion junctions showed a pronounced decrease in their fractions in the same time frame. To generate corresponding purely clonal DIPs harboring the promising candidate DI vRNAs, we used reverse genetics for IAV. Indeed, these DIPs displayed a superior *in vitro* interfering efficacy compared to DIPs derived from lowly replicating DI vRNAs, indicating their potential for antiviral therapy.

RESULTS

Semi-continuous production of IAV results in periodic oscillations of virus titers and strong accumulation of DIPs. In order to induce *de novo* generation and accumulation of DIPs, an IAV strain, A/PR/8/34, of the subtype H1N1 (PR8, provided by Robert Koch Institute, Berlin, Germany) was propagated in a semi-continuous small-scale two-stage cultivation system (Fig. 1B). For infection, we used a seed virus that was depleted in DI vRNAs as shown by segment-specific reverse transcription-PCR (RT-PCR) (Fig. 1A). Madin-Darby canine kidney (MDCK) cells growing in suspension culture (MDCK[sus]) were seeded into the cell seeding shake flask (CSS) and virus shake flasks (VS) at a viable cell concentration (VCC) of 0.6×10^6 cells/ml and grown in batch mode

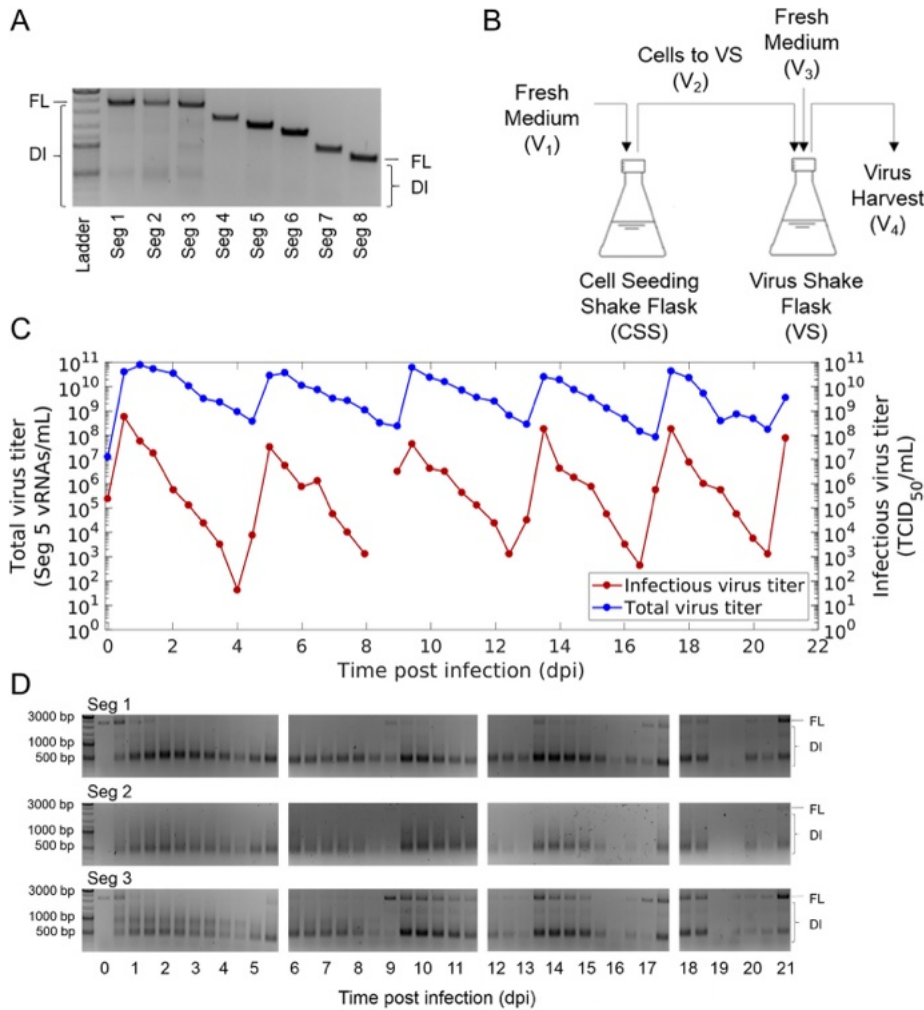


FIG 1 Semi-continuous propagation of influenza A virus and DIPs. (A) PR8 seed virus depleted in DI vRNAs was used for infection. Results of segment-specific RT-PCR for Seg 1 to 8 followed by agarose gel electrophoresis are shown. Signals corresponding to FL and DI vRNAs are indicated. The upper, middle, and lower thick bands of the DNA ladder indicate 3,000, 1,000, and 500 bp, respectively. (B) Experimental setup of the small-scale two-stage cultivation system in shake flasks (scheme adapted from Tapia et al. [68]). MDCK(sus) cells were grown in the CSS and VS. After an initial batch and semi-continuous phase (CSS and VS not coupled), the cells in the VS were infected with the seed virus (A) at an MOI of 0.1. The semi-continuous production mode was initiated 0.5 dpi, where cells were transferred from the CSS into the VS (V₂) at regular time intervals, while fresh medium was added (V₁ or V₃) and virus harvest was taken for monitoring (V₄). (C) Periodic oscillations of total and infectious virus titers during the production. The vRNA level of Seg 5 (indicating total virus particle concentration) was quantified by real-time RT-qPCR and infectious virus titer by TCID₅₀ assay. (D) Accumulation of DI vRNAs over the semi-continuous production time of 21 days. Results of the segment-specific RT-PCR are shown for Seg 1, 2, and 3. Signals corresponding to FL and DI vRNAs are indicated. The illustration includes the results of one experiment.

to about 3.0×10^6 cells/ml (−1.6 days postinfection [dpi]) (data not shown). Subsequently, for both shake flasks, a calculated volume of cell suspension was discarded, and fresh medium was added at regular time intervals (both shake flasks not yet connected in series). This resulted in a residence time (RT) of 38.3 h for both vessels. Note that preliminary studies showed a steady state in the VCC for this RT (data not shown). Once the steady state was reached, cells in the VS were infected with PR8 at a multiplicity of infection (MOI) of 0.1. At 0.5 dpi, both vessels were connected in series, and from there on, cells were transferred semi-continuously from the CSS to the VS (V₂). In addition, fresh medium was added to both shake flasks (V₁ or V₃) and virus

harvest was taken (V_4). The RT chosen was 38.3 h and 22.0 h for CSS and VS, respectively, as this previously resulted in pronounced titer fluctuations and strong accumulation of DIPs (31). Over the production time of 21 dpi, the steady state in the CSS was kept with an average VCC of 2.6×10^6 cells/ml (standard deviation [SD] of $\pm 0.2 \times 10^6$ cells/ml) (data not shown).

Strong periodic oscillations in the infectious virus titers (quantified by 50% tissue culture infective dose [TCID₅₀] assay) and in the extracellular vRNA level of Seg 5 (quantified by real-time reverse transcription-quantitative PCR [RT-qPCR]) were observed in the VS (Fig. 1C). The extracellular vRNA level of Seg 5 was taken as a measure of the total virus concentration. DI vRNAs are mostly located on polymerase-encoding segments (20, 33–36), so the occurrence of DIPs should not affect the detection of Seg 5 vRNA. Shortly after infection at 0.5 dpi, a maximum infectious virus titer of 5.6×10^8 TCID₅₀/ml was reached. Here, high concentrations of STV (complying with a high MOI) increased the chance for coinfections with DIPs. Thus, a strong DIP propagation likely occurred early in cultivation, impeding STV propagation. Therefore, infectious virus titers decreased from 0.5 dpi onward. Eventually, the declining infectious virus titers led to fewer coinfections. Thus, DIP replication decreased, and the total virus particle concentration dropped as well. Additionally, DIPs were out-diluted because of the semi-continuous feeding strategy. Then, at a low infectious virus concentration (complying with a low MOI condition, ~4.0 dpi), the chance of DIP coinfections was supposedly significantly reduced. Under these conditions, STVs could accumulate again as indicated by increasing virus titers toward 5 dpi. In the following, further periodic oscillations in virus titers occurred based on the DIP/STV interaction described above.

The dynamics in virus titers were well in agreement with results of the segment-specific RT-PCR (indicating FL and DI vRNAs) (Fig. 1D). A rapid accumulation of DI vRNAs occurred already at 0.5 dpi. Furthermore, the FL vRNA signal gradually dropped between 1 dpi and 2.5 dpi, suggesting the preferential production of DI vRNAs. Subsequently, DI vRNA replication decreased and DI vRNAs were washed out, as indicated by weaker band intensities of DI vRNAs (e.g., at 8.5 dpi). Next, in agreement with the increase of infectious viral titers (STVs), FL vRNA bands were visible again (e.g., at 9 dpi). Moreover, agarose gels indicated the presence of DI vRNA bands at the end of cultivation that may have been already present in the seed virus, suggesting that some DI vRNAs were preserved. In addition, weak DI vRNA bands as well as undefined, blurred bands emerged during the course of IAV replication, suggesting the formation and accumulation of *de novo*-generated DI vRNAs.

In summary, the semi-continuous production of IAV using a seed virus depleted in DI vRNAs led to the accumulation of DIPs. Thus, strong periodic oscillations in the total concentration of virions and infectious virus titers were observed due to the dynamic interaction of STVs and DIPs. Moreover, in the course of production, DIPs were exposed to high- and low-MOI conditions that likely resulted in alternating selection pressures, suitable for potential selection toward accumulation of highly interfering DIPs.

Next-generation sequencing results indicate predominant *de novo* formation and accumulation of deletion junctions on polymerase-encoding segments. Segment-specific RT-PCR does not enable the detection and quantification of individual deletion junctions. Therefore, to study the diversity of DI vRNAs generated during semi-continuous IAV propagation, samples were subjected to Illumina-based NGS and processed by a bioinformatics pipeline (32). In doing so, sequences of vRNAs from the produced progeny virions were obtained. Reads including a deletion junction (DI vRNA reads) do not align to the corresponding reference genome. These NGS reads were processed by the ViReMa algorithm to identify the position of individual deletion junctions (37).

The highest variation (i.e., number of different deletion junctions) was found on the polymerase-encoding segments 1 to 3, which encode the polymerase basic protein 2 (PB2) and 1 (PB1) and polymerase acidic protein (PA), respectively (Fig. 2A). Figure 2B shows the fraction of all deletion junctions located on a genome segment over time. Here, polymerase-encoding segments showed the highest fraction. In contrast, deletion junctions of non-polymerase-encoding segments showed a significantly lower fraction, which increased slightly toward the end of cultivation but always remained

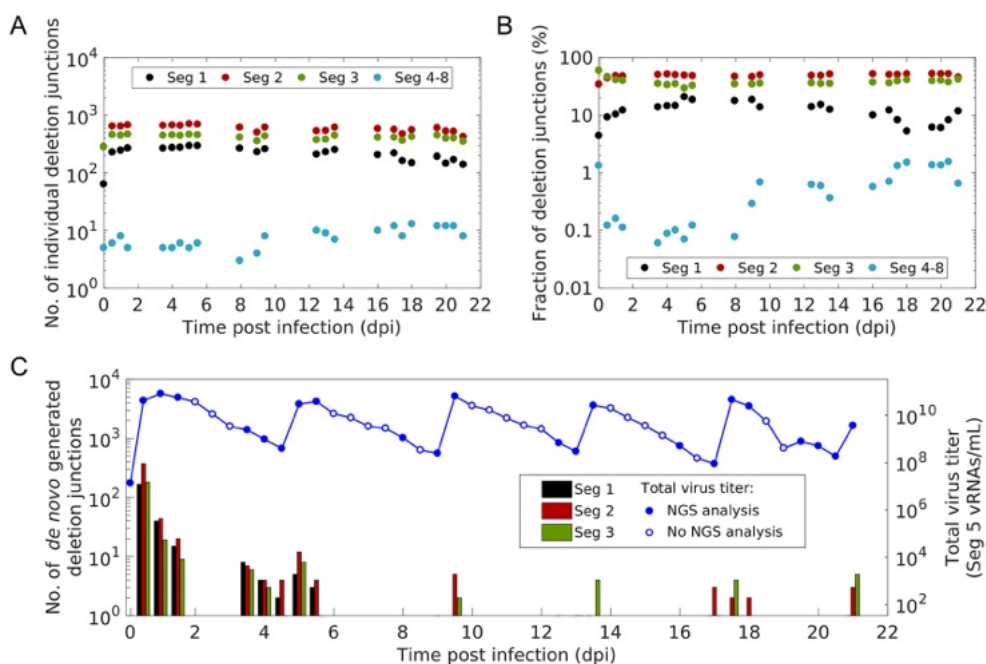


FIG 2 Diversity, distribution and *de novo* generation of deletion junctions during semi-continuous propagation of IAV. Deletion junctions were identified by Illumina-based NGS and subsequent analysis via the ViReMa algorithm (32). (A) Number of different deletion junctions located on the respective genome segment(s). (B) Fraction of all deletion junctions located on the respective genome segment(s). This fraction describes the ratio of the total number of detected deletion junctions for one segment to the total number of deletion junctions on all genome segments. (C) *De novo* formation of deletion junctions. The vRNA level of Seg 5 (indicating total virus particle concentration, as shown in Fig. 1C) was quantified by real-time RT-qPCR. Samples not analyzed by NGS are indicated by open circles. The illustration includes the results of one experiment.

below 2%. As non-polymerase segment deletion junctions occurred only in negligible numbers, they were not considered any further in subsequent analyses.

Next, we investigated the *de novo* formation of DI vRNAs over the course of the cultivation. Figure 2C shows, at specific time intervals, the number of *de novo*-generated deletion junctions. *De novo* formation occurred mainly on the polymerase-encoding segments. Interestingly, most *de novo* formations occurred within the first 1.5 dpi. In addition, a considerable number of *de novo* DI vRNAs were detected between 3.5 and 5.5 dpi. However, *de novo* formation was significantly lower at later time points. Moreover, an increase in the number of new deletions was highly correlated with an increase in the total virus particle concentration (indicated by the vRNA level of Seg 5) (Fig. 2C). This is consistent with a fast STV replication and, thus, likely with a higher occurrence of the *de novo* formation of DI vRNAs due to the error-prone nature of the replication of the IAV RNA-dependent RNA polymerase.

In sum, our results show that DI vRNAs are predominantly *de novo* formed and accumulated on the polymerase-encoding segments during semi-continuous IAV infection.

Short DI vRNAs tend to accumulate to higher fractions than longer ones; yet intermediate-length optima were observed as well. It was reported that DI vRNA accumulation surpasses that of FL vRNAs due to their shorter length resulting in a supposedly faster replication (12, 20). Therefore, we speculated that shorter DI vRNAs may also accumulate to higher abundances than longer DI vRNAs. Figure 3 shows the fraction of all individual deletion junctions and their corresponding DI vRNA length. Indeed, a bias toward accumulation of shorter DI vRNAs was observed, with short DI vRNAs showing overall higher fractions than longer ones during semi-continuous IAV production (Fig. 3). However, the highest fractions were not found for the shortest DI vRNAs. Rather, it appeared that the highest fractions were distributed around a length optimum. To visualize this optimum, we fitted a normal distribution function to the DI

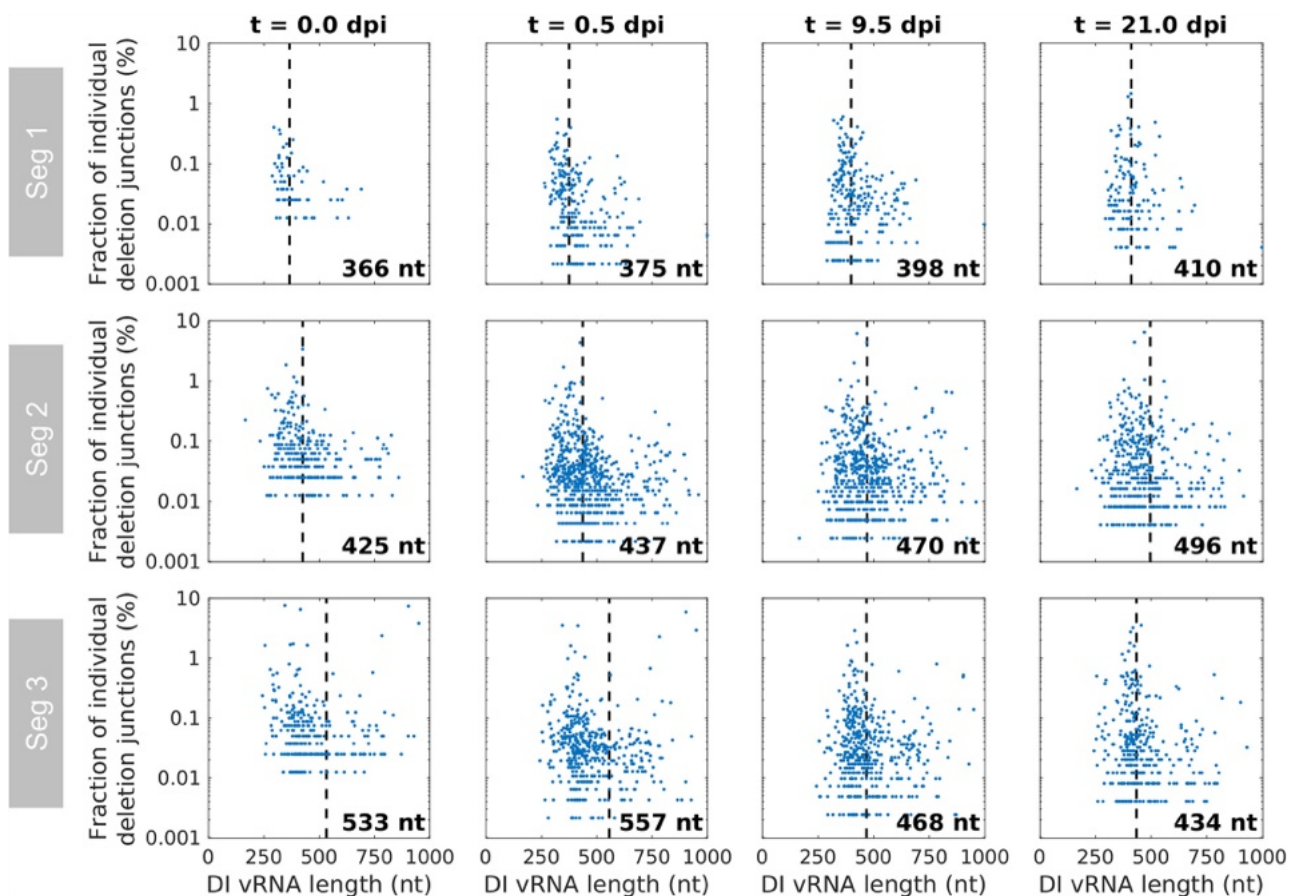


FIG 3 Dependency of the length of DI vRNAs on their accumulation during semi-continuous propagation of IAV. Deletion junctions were identified by Illumina-based NGS and subsequently analyzed via the ViReMa algorithm (32). Fractions of individual deletion junctions were calculated based on the ratio of the number of NGS reads of one individual deletion junction to the number of NGS reads of all deletion junctions located on all eight segments. The means of DI vRNA length (calculated by fitting a normal distribution function) are indicated by dashed vertical lines, and the corresponding lengths are shown. Representative time points are illustrated. The illustration includes the results of one experiment.

vRNA length and plotted the resulting mean as a dashed vertical line (Fig. 3). Over the whole cultivation, the mean DI vRNA length ranged between 366 and 414 nucleotides (nt), from 425 and 534 nt, and from 434 and 557 nt for Seg 1, 2, and 3, respectively.

Moreover, a few larger DI vRNAs (comprising a sequence length of up to 1,000 nt) accumulated to high fractions, suggesting that the sequence and the position of the deletion junction may be another factor to consider for replication of a DIP (Fig. 3). Note that Fig. 3 only shows DI vRNAs up to 1,000 nt in length, although we also detected very long DI vRNAs (>2,000 nt) (data not shown). These DI vRNAs with very short deletions may either not result in a defective vRNA, comprise two deletions, or represent technical artifacts. Due to their unknown origin and function and a lack of description in the literature, defective vRNAs larger than 85% of their respective FL length were excluded from analysis in this work.

Taken together, shorter DI vRNAs showed an overall stronger accumulation than longer DI vRNAs. However, highest fractions were distributed around an optimum length, indicating advantages for efficient DI vRNA replication and spreading.

The incorporation signal but not the entire bundling signal appears to be required for propagation of DIPs. We next examined the position of the breaking points of DI vRNAs. Figure 4 illustrates the position of individual deletion junctions, as indicated by the number of retained nucleotides prior to (DI vRNA 3' length) and after (DI vRNA 5' length) the deletion junction site. In the course of the semi-continuous

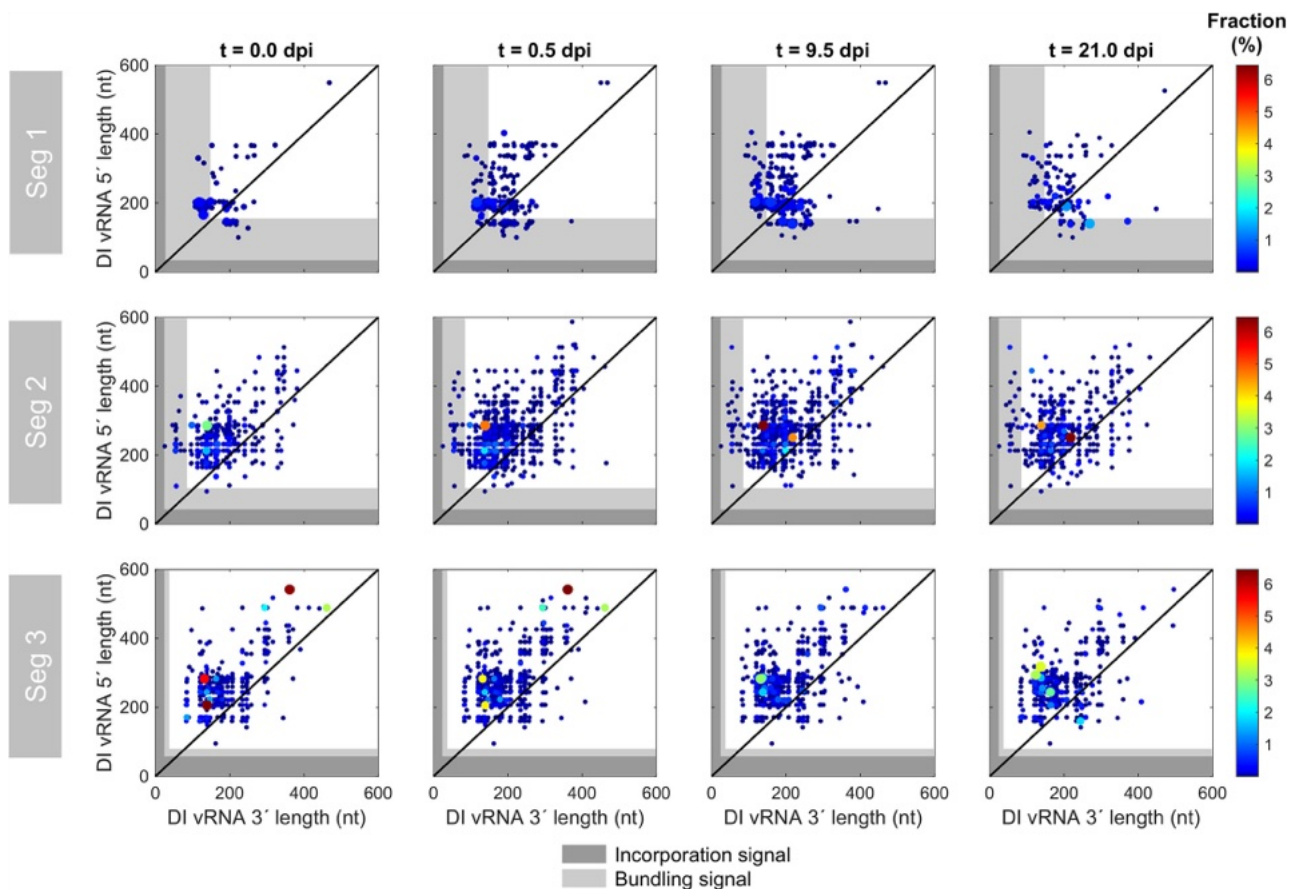


FIG 4 Deletion junction sites of DI vRNAs during semi-continuous propagation of IAV. Deletion junctions were identified by Illumina-based NGS and subsequently analyzed via the ViReMa algorithm (32). DI vRNA 3' and 5' lengths indicate the number of retained nucleotides prior to and after the deletion junction, respectively, at the corresponding vRNA ends. The packaging signal is indicated as gray areas and is divided into the incorporation signal (dark gray area) and bundling signal (light gray area). Representative time points are illustrated. The color code from red to blue shown on the right denotes the fraction of the individual deletion junction, which was calculated based on the ratio of the number of NGS reads of one individual deletion junction to the number of NGS reads of all deletion junctions located on all eight segments. Additionally, the circle radii increase with higher fractions. The diagonal black line indicates equal DI vRNA 3' and 5' lengths. The illustration includes the results of one experiment.

cultivation, breaking points were mostly located in proximity to both ends of vRNA (Fig. 4). This finding is in line with our observation of the predominant accumulation of short DI vRNAs (Fig. 3). We also observed highly abundant medium-sized DI vRNAs on Seg 3 in the seed virus (0.0 dpi), yet, the fraction of DI vRNAs carrying these deletions decreased, or even disappeared, toward the end of cultivation (Fig. 3). Again, this indicates that shorter DI vRNAs replicate faster and may outcompete longer ones. Additionally, the 3' length of the DI vRNA largely did not correlate with the 5' length, suggesting that deletion junctions are not preferably symmetrical.

While the lengths of the 3' and 5' ends ranged from below 100 nt to over 500 nt, specific minimum lengths were retained in the DI vRNAs (Fig. 4). We then asked whether the complete packaging signal (situated at the terminal ends of vRNA), which is important for organized packaging into progeny virions (38), was unaffected by deletions. A small percentage of breaking points was located in the packaging signal (on Seg 1 and 2), yet the majority of the deletion junction sites were located outside it, which is in line with the observation of an optimum in DI vRNA length (Fig. 3). For a more thorough investigation of deletion junctions in the packaging signal, we highlighted the positions of the incorporation signal (noncoding region [NCR], including the promoter region) and the bundling signal (terminal ends of the coding region) (39). The incorporation signal was reported to lead the packaging of the vRNA in which

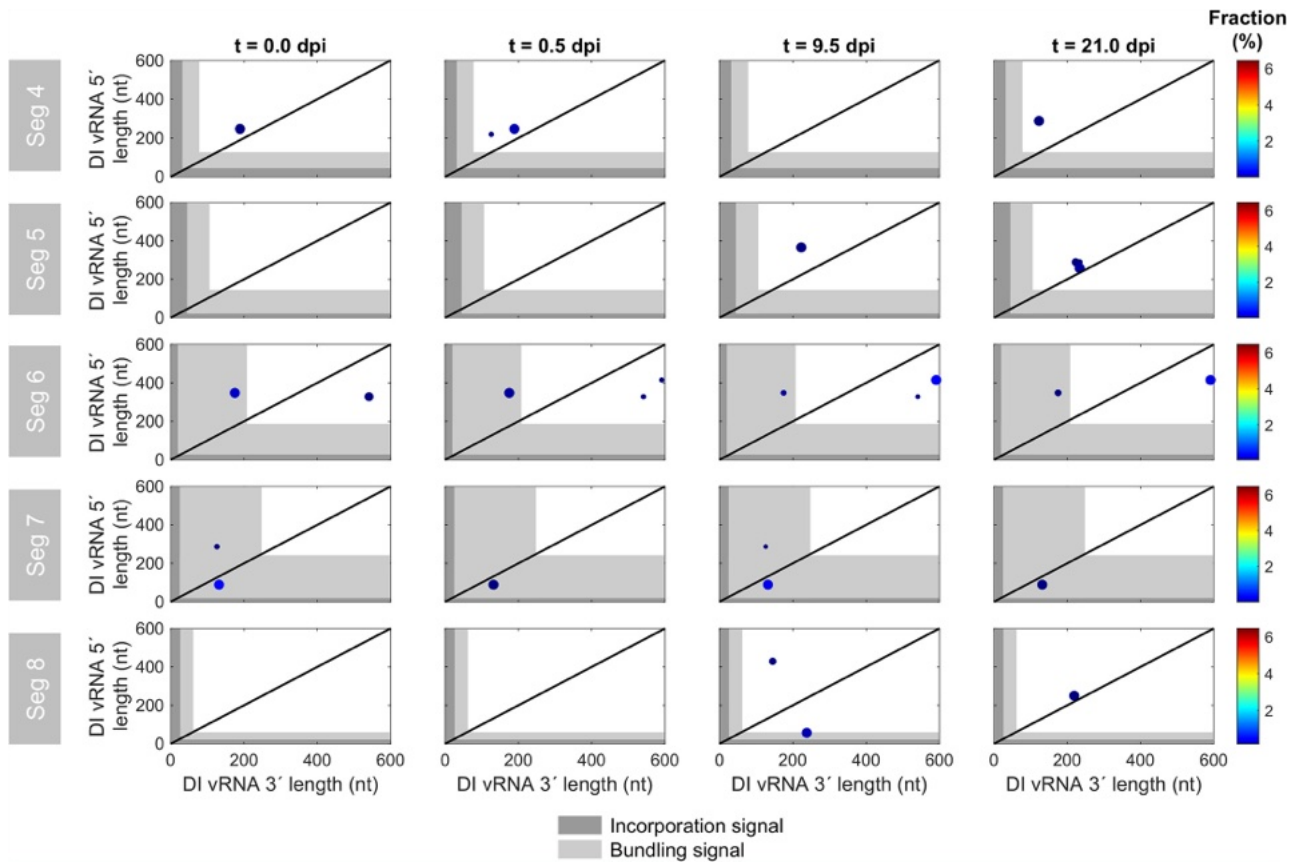


FIG 5 Deletion junction sites of DI vRNAs on non-polymerase-encoding segments during semi-continuous propagation of IAV. Deletion junctions were identified by Illumina-based NGS and subsequently analyzed via the ViReMa algorithm (32). DI vRNA 3' and 5' lengths indicate the number of retained nucleotides prior to and after the deletion junction, respectively, at the corresponding vRNA ends. The packaging signal is indicated as gray areas and is divided into the incorporation signal (dark gray area) and bundling signal (light gray area). Representative time points are illustrated. The color code from red to blue shown on the right denotes the fraction of the individual deletion junction, which was calculated based on the ratio of the number of NGS reads of one individual deletion junction to the number of NGS reads of all deletion junctions located on all eight segments. For graphs where no breaking points are shown, no DI vRNAs were detected at the selected time points. Additionally, the circle radii increase with higher fractions. The diagonal black line indicates equal DI vRNA 3' and 5' lengths. The illustration includes the results of one experiment.

the signal is found. The second part of the packaging signal is the bundling signal, which confers the selective packaging of all the eight different segments together (39). We checked which part of the sequence at both ends was retained to infer a minimum sequence length for functional replication and packaging of the truncated vRNAs, assuming that only propagation-competent DI vRNAs can be detected. No deletion junctions in the incorporation signal for the polymerase-encoding segments or for Seg 4 to 8 were identified (Fig. 4 and 5, respectively). Therefore, we suggest that the preservation of the entire incorporation signal is crucial for the propagation of DIPs.

Interestingly, deletion junctions in the bundling signal (on Seg 1 and 2) could be detected, indicating that the entire bundling signal of these segments is most likely not required for propagation of DIPs. In particular, clusters of DI vRNA breaking points in the bundling signal were stable and present over the complete course of the semi-continuous cultivation. In contrast, Seg 3 did not show any breaking points in both signals. We found a minimum sequence length of 84 nt (3' end) and 100 nt (5' end), 25 nt and 95 nt, and 82 nt and 95 nt for Seg 1, 2, and 3, respectively. Figure 5 shows the position of deletion junction sites in Seg 4 to 8. Notably, although only very few individual deletion junctions were detected, breaking points were found in the bundling signal on Seg 6 (3' end), Seg 7 (both ends), and Seg 8 (5' end) as well.

In summary, our results indicate that the complete incorporation signal is crucial for

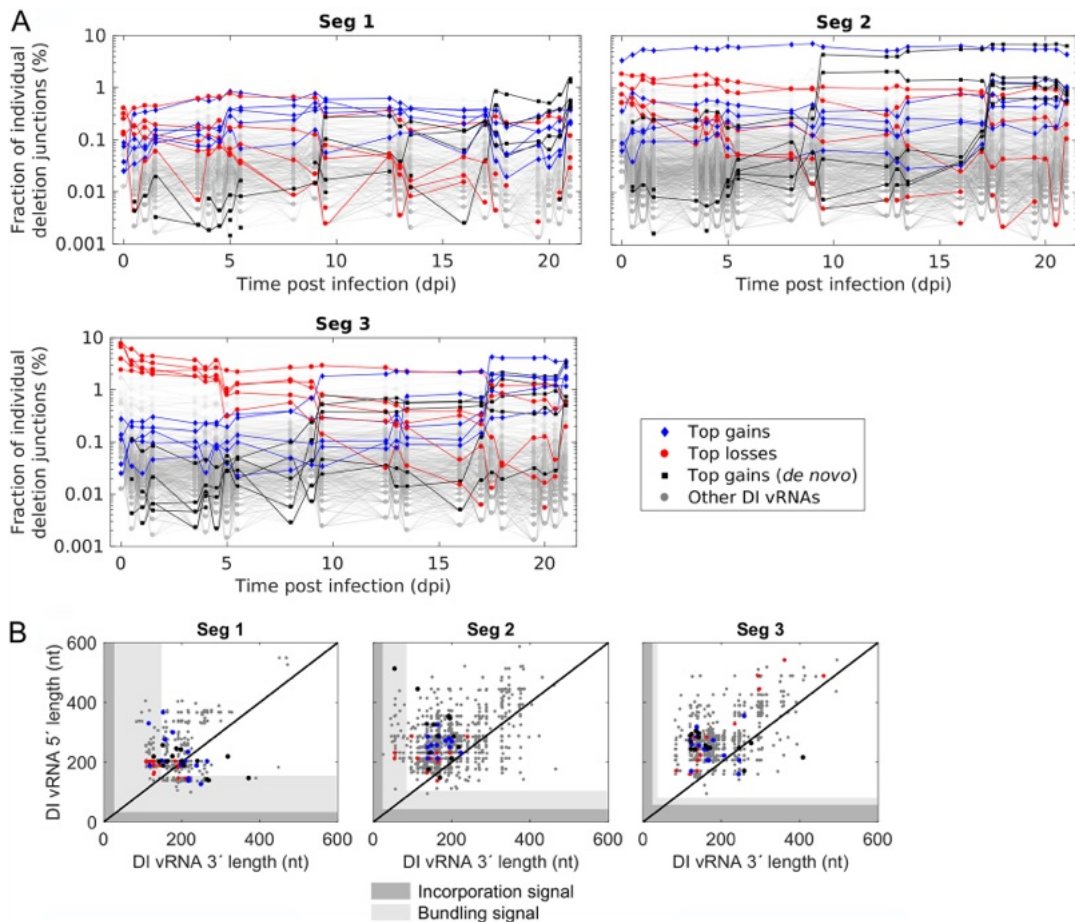


FIG 6 Propagation of DI vRNAs showing the highest gains or losses in their fractions during semi-continuous propagation of IAV. Deletion junctions were identified by Illumina-based NGS and subsequently analyzed via the ViReMa algorithm (32). Fractions of individual deletion junctions were calculated based on the ratio of the number of NGS reads of one individual deletion junction to the number of NGS reads of all deletion junctions located on all eight segments. (A) Fraction of individual DI vRNAs belonging to the group of top five gains, losses, and gains (*de novo*) of the fraction over cultivation time. Top gains (*de novo*) indicate newly formed deletion junctions with the highest fraction at the end of cultivation. (B) Deletion junction position of the top 15 gains, losses, and gains (*de novo*). DI vRNA 3' and 5' lengths indicate the number of retained nucleotides prior and after the deletion junction, respectively, at the corresponding vRNA ends. The packaging signal is indicated as gray areas and is divided into the incorporation signal (dark gray area) and bundling signal (light gray area). The illustration includes the results of one experiment.

propagation of DIPs, yet only a part of the bundling signal in Seg 1 and 2 seems to be required for DIP spreading.

Dynamic competition in propagation between DI vRNAs leads to selection toward accumulation of highly interfering DIPs.

In order to elucidate whether the various DI vRNAs show differences in their propagation, we next studied the composition of deletion junctions over cultivation time. More specifically, we determined the fraction of each individual deletion junction over time. Figure 6A shows these fractions and highlights the top five deletion junctions that showed the highest gain or largest loss in their fraction from the seed virus (0.0 dpi) to the end of cultivation (21 dpi). Likewise, the top five gains of *de novo*-formed DI vRNAs are indicated. Interestingly, differences between gains and losses were very pronounced, with a decreasing fraction of the top five losses, while the top five gains (including *de novo*) showed a strong accumulation. These trends were most prominent for Seg 3. Of note is also one deletion junction on Seg 2 that was present at a very high fraction in the seed virus and throughout the whole cultivation. Furthermore, pronounced shifts in the composition of deletion junctions were found for 9 to 9.5 and 17 to 17.5 dpi, at best visible for Seg 3. The occurrence of DI vRNAs that accumulate faster and achieve higher fractions

TABLE 1 Generated Seg 1 candidate DIPs and the respective deletion junction positions in the 5' to 3' cDNA sequence

DIP	5' Fragment size (bp)	3' Fragment size (bp)	DIP fragment size (bp)
Loss	129	166	295
Gain	217	138	355
Gain (<i>de novo</i>)	269	140	409

than other DI vRNAs suggests that there was a dynamic competition in the propagation between individual DI vRNAs.

Moreover, we examined whether top gains (including *de novo*) and losses show differences in the deletion junction position (Fig. 6B). To obtain a better overview, we expanded the number of the top candidates in each category to 15. However, it appeared that no clear differences between the groups were present. For both gains and losses, few deletion junction sites were located in the bundling signal for Seg 1 and 2 (although most were found outside [Fig. 6B]), but none for Seg 3. Therefore, even for competitive DIPs (which require an efficient packaging process), we found a shorter packaging signal than that of the FL vRNA on Seg 1 (both ends) and on Seg 2 (3' end). Please also note a few DI vRNAs (belonging to the top 15 losses) on Seg 3 showing a medium-sized DI vRNA length (~900 nt) (Fig. 6B, upper right corner), which is in line with our observation that long DI vRNAs accumulate to low fractions (Fig. 3). However, we also found two top 15 gains (*de novo*) on Seg 2 with a very long DI vRNA (1,905 nt and 1,628 nt) (data not shown). This finding might suggest that not only the sequence length but also the breaking point position and probably further unknown regulatory effects are crucial for the efficient propagation of DI vRNAs.

In order to test the hypothesis, that fast-propagating DI vRNAs show a higher interfering efficacy than slow-propagating ones, we reconstituted the corresponding DIPs and tested them in an *in vitro* interference assay. More specifically, we rescued purely clonal DIPs (in the absence of STV) harboring either the top gain, top loss, or top gain (*de novo*) DI vRNA of Seg 1 (Table 1) using a modified reverse genetics system for IAV DIPs (25, 40). Next, we propagated these selected DIPs in genetically engineered MDCK-PB2(sus) cells, expressing PB2, to allow multiplication of these DIPs (harboring a deletion in Seg 1) without STV through complementation. Almost complete absence of contamination with other DI vRNAs was confirmed by results of segment-specific RT-PCR (data not shown).

In the *in vitro* interference assay (Fig. 7), adherent MDCK cells (MDCK[adh]) cells were infected with STV at an MOI of 0.01 and coinfecting with the different DIPs to evaluate the inhibition of STV replication compared to infection with STV alone (NC). Here, the DIP input for the interference assay was normalized through dilution based on the concentration of DIPs to ensure a direct comparison between the DIPs. In addition, we compared the interfering efficacy to a prototypic, well-characterized DIP named DI244 (23–25, 27). Indeed, the DIPs derived from the top gains (including *de novo*) showed the highest interfering efficacy. The top gain (*de novo*) DIP reduced the infectious virus release by more than 5 orders of magnitude, the top gain by 5 logs, while top loss and DI244 showed a reduction of only 4 orders of magnitudes (Fig. 7A). Reduction of the total virus particle release, indicated by the hemagglutination (HA) titer, showed a similar trend (Fig. 7B).

In summary, our results indicate that the semi-continuous propagation of IAV led to a dynamic competition in propagation between different DI vRNAs. We demonstrate that DI vRNAs showing the highest increase in the fraction over the cultivation period result in the formation of DIPs that show a superior interfering efficacy compared to DIPs containing slowly propagating DI vRNAs. These DIPs are, thus, promising candidates for antiviral therapy.

DISCUSSION

IAV DIPs have been proposed as an effective antiviral agent for the influenza disease. In this study, we investigated the *de novo* generation and the competition in the

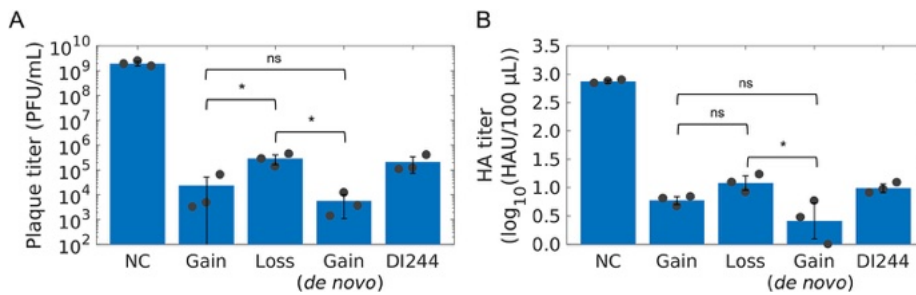


FIG 7 Interfering efficacy of DIPs derived from DI vRNAs showing the highest gain, loss, or gain (*de novo*) in their fraction during semi-continuous propagation of IAV. Purely clonal DIPs containing a deletion in Seg 1 (derived from DI vRNAs showing the top gains and top loss) were generated using a modified reverse genetics methodology for reconstitution of purely clonal IAV DIPs (40). Next, DIPs were multiplied in genetically engineered MDCK-PB2(sus) cells (expressing PB2) in a shake flask at a multiplicity of DIP (MODIP). (A and B) Interference assay. MDCK(adh) cells were infected with STV only at an MOI of 0.01 (NC) or coinfecting with the corresponding DIP, resulting in a DIP/STV ratio of 3,224 (number of DIPs, 4.25×10^8 virions; number of STVs, 1.32×10^5 virions, derived from the HA titer). For comparison, DI244, a prototypic, well-characterized DIP (23–25, 27), was used. (A) Infectious virus release, quantified by plaque assay. (B) Total virus particle release, measured by HA assay. The illustration includes the results of three independent experiments ($n = 3$). Error bars indicate the SD. One-way analysis of variance (ANOVA) followed by Tukey's multiple-comparison test (*, $P < 0.05$; ns, $P > 0.05$, not significant) was used to determine significance.

growth between a diversity of DIPs during long-term semi-continuous IAV infection in order to identify strong candidates for antiviral therapy. In general, DIPs and STVs are in a competition for cellular and viral resources in a coinfection scenario (19, 41). Due to the replication advantage of DIPs, suppression of and interference with STV replication occurs (18–20). Moreover, it was shown that DIPs interfere with STV propagation at the packaging step, as preferential incorporation of DI vRNAs over FL vRNAs was observed (21, 22). We thus hypothesized that DI vRNAs showing the strongest accumulation during long-term coinfection possess the highest interference efficacy with STV replication. In our experiments, a small subset of individual DI vRNAs was observed that showed a pronounced accumulation, while the fractions of some other DI vRNAs strongly decreased (Fig. 6A). Next, DIPs harboring the most competitive DI vRNAs on Seg 1 were generated, and we showed that these DIPs exhibit a higher interfering efficacy than slowly propagating ones (Fig. 7). Strikingly, the interfering efficacy was also higher in comparison to DI244, a prototypic and well-characterized DIP (23–25), suggesting a huge potential of these candidates for antiviral treatment.

The antiviral mechanisms of IAV DIPs comprise (i) competitive inhibition during replication, i.e., “replication interference,” and (ii) inhibition of STV replication by the enhanced stimulation of innate immunity upon DIP coinfection (12, 42). Regarding the latter mechanism, the myxovirus resistance proteins (Mx) are thought to be a key player in the IFN-induced antiviral activity (43). However, in the present study, MDCK cells were used, where the canine Mx1 and Mx2 were shown to lack IFN-induced antiviral activity against IAV replication (44). In addition, trypsin (required for proteolytic activation of the viral hemagglutinin, enabling efficient multicycle replication) was used for virus propagation, yet it was shown that trypsin also strongly inhibits IFN signaling by proteolytic degradation of secreted IFNs (45). Therefore, the IFN response has presumably not significantly contributed to the oscillating virus replication in the present study. Our cultivation system has, rather, allowed for selection toward accumulation of DIPs showing a high “replication interference.” In the context of a potential antiviral treatment *in vivo*, note that retinoic acid-inducible gene I (RIG-I) preferentially associates with DI vRNAs over FL vRNAs (46), eventually resulting in an enhanced stimulation of the IFN response (47). We expect high DI vRNA accumulation in a coinfection with highly competitive DIPs (identified in this study), which may also result in a stronger stimulation of an antiviral innate immune response (besides their stronger “replication interference”) than coinfections with lowly accumulated DIPs. Corresponding experiments (*in vitro* and *in vivo*) are the subject of ongoing studies.

Our data show that the most competitive DI vRNAs are derived from the polymerase-encoding segments. Further, we found the highest variation, accumulation, and *de novo* formation of DI vRNAs on these segments (Fig. 2A, B, and C, respectively). This confirms previous studies which showed that DI vRNAs are predominantly found on Seg 1, 2, and 3 (20, 33–36). In agreement with this, a bias toward the emergence of DI vRNAs on the polymerase-encoding segments was observed during production of IAV over 17 days in a fully continuous two-stage bioreactor system (30). Mathematical modeling of the intracellular replication during STV and DIP coinfection also suggested that DI vRNAs located on the polymerase-encoding segments are more competitive than DI vRNAs on other segments (18). In particular, they even yielded high progeny numbers in less advantageous infection scenarios, i.e., when STV coinfection was delayed by several hours. Accordingly, in *in vivo* studies, DI244 containing a deletion on Seg 1, or DI vRNAs carrying a deletion in Seg 1, 2, or 3 showed a pronounced antiviral effect upon administration against IAV replication in mice and in ferrets (14, 23–25).

Our results show that short DI vRNAs tended to accumulate to higher fractions than longer DI vRNAs (Fig. 3). In general, it is believed that the shorter length of DI vRNAs (in comparison to FL vRNAs) leads to a replication advantage (18–20), which supports our findings. However, our observation of a length optimum also indicates that specific DI vRNA lengths are beneficial for DIP replication and spreading (Fig. 3). In agreement with this, the highly potent DI244 (395 nt) shows a similar DI vRNA length (Fig. 3) (23–25, 27). Other studies reported a similar mean DI vRNA length of 400 to 500 nt for Seg 1, 2, and 3 (12, 34). For DIPs originating from clinical isolates, similar mean DI vRNA lengths of 377 nt (Seg 1), 390 nt (Seg 2), and 490 nt (Seg 3) were found (36). Another investigation confirmed the finding of a replication advantage toward shorter vRNAs but additionally suggested that the sequence (untranscribed regions [UTRs] and coding region) may also have an influence on vRNA competition (41). This is consistent with previous work proposing that not only the length, but also the sequence (or the deletion junction position) may drive the replication advantage of DI vRNAs (20). This may explain our observation of few larger DI vRNAs up to 1,000 nt, which accumulated to high fractions (Fig. 3). In addition, two very long DI vRNAs (1,905 nt and 1,628 nt) were included in the top 15 gains (*de novo*) of DI vRNAs (data not shown). In further agreement, the *in vivo* interfering efficacy of three clonal DIPs containing DI vRNAs with a similar length (but diverse deletion junctions) differed significantly from each other (24). We found no clear patterns between the deletion junction positions of top gains (including *de novo*) and losses (Fig. 6B). These results may support the hypothesis that not only the DI vRNA length, but also the deletion junction site and further unknown regulatory effects are decisive factors for competitive DI vRNAs.

The packaging of progeny virions of IAV is a complex process. The leading packaging model postulates selective packaging of the eight different vRNA genome segments (48, 49). Decisive for correct and efficient packaging is a special vRNA sequence (packaging signal), which was discovered using reverse genetics approaches (38). As DIPs include a truncated segment, this packaging signal might equally be affected. However, it was suggested that this packaging signal in the shortened segment typically remains intact (12, 48). The packaging signal is divided into two parts, the incorporation signal (NCR, including promoter region) and the bundling signal (located at the terminal ends of the coding region). Our results show that the incorporation signal is crucial for DIP propagation, as it was unaffected by deletions (Fig. 4). However, several deletion junction sites were located in the bundling signal (Fig. 4, 6B, and 5). Therefore, we suggest that DIPs require only a part of the bundling signal for efficient replication and spreading. This finding does not agree with a previous study, which implied that the entire packaging signal is crucial for DI vRNA stability (50) and for high interference (51), yet only a few deletions were tested. The new insights obtained by our approach can be explained (i) by the significantly higher throughput of DI vRNA identification (in sum, on the order of 1,000) and (ii) by DIPs being challenged by alternating high- and low-MOI conditions for 21 days, which allowed extensive *de novo* generation and accumulation of new DIPs.

Previous work showed that DI vRNAs interfere with FL vRNAs during the packaging process, by selectively suppressing the packaging of either the parent segment (21, 22) or the FL vRNA of another genome segment (52). However, one recent study showed the opposite, in which DI vRNA were packaged less frequently than FL vRNA (previously posted on a preprint server [53]). Furthermore, differences in the packaging rates were found between individual DI vRNAs (21, 51). Thus, the highly abundant DI vRNAs found in the present study may have an advantage in the entire propagation process over others, including both replication and packaging. However, further in-depth studies are required to better characterize the interference of DI vRNAs at the virus assembly step.

Taken together, our findings show that DIPs containing DI vRNAs with a superior propagation rate also show a superior capacity to interfere with STV replication. These DIPs are very interesting candidates for antiviral treatment. The highly competitive DI vRNAs are predominantly located on the polymerase-encoding segments, display an optimal DI vRNA length, and conserve the incorporation signal but do not require the entire bundling signal. In addition, yet unidentified sequence motifs certainly also play an additional role during DI vRNA propagation. Due to the complex features of highly competitive DIPs, the best candidates for antiviral therapy are probably challenging to design *in silico*. Thus, evolution studies are a more convenient screening tool as shown for DIPs of other virus families (54–56).

MATERIALS AND METHODS

Cells and viruses. MDCK(adh) cells (ECACC, No. 84121903) were adapted in previous works to grow in suspension culture (57) and then in chemically defined Xeno medium (58), in this work referred to as MDCK(sus) cells. Further, this cell line was engineered to stably express the PB2 for the production of purely clonal DIPs harboring a DI vRNA in Seg 1 (25, 40) and is denoted MDCK-PB2(sus). Cultivation of both cell lines was conducted in shake flasks at a working volume of 50 ml (125-ml baffled Erlenmeyer flask; Thermo Fisher Scientific, 4116-0125) using an orbital shaker (Multitron Pro, Infors HT; 50 mm shaking orbit) at 185 rpm and 37°C in a 5% CO₂ environment. The medium was supplemented with 8 mM glutamine. For MDCK-PB2(sus) cells, puromycin (Thermo Fisher Scientific, no. A1113803) was added at a final concentration of 0.5 μg/ml. Quantification of VCC, viability, and diameter were performed using a cell counter (Vi-Cell XR; Beckman Coulter, no. 731050). MDCK(adh) cells were maintained in Glasgow minimum essential medium (GMEM; Thermo Fisher Scientific, no. 221000093) supplemented with 10% fetal bovine serum and 1% peptone at 37°C and 5% CO₂. The corresponding adherent MDCK cell line that stably expressed PB2 [MDCK-PB2(adh)] (40) was maintained in the presence of 1.5 μg/ml puromycin. Adherent PB2-expressing HEK-293T (HEK-293T-PB2) cells (40) were maintained in Dulbecco's modified Eagle medium (DMEM; Gibco, no. 41966029) supplemented with 10% fetal bovine serum, 1% penicillin streptomycin (10,000 units/ml penicillin and 10,000 μg/ml streptomycin; Gibco, no. 15140122), and 1 μg/ml puromycin at 37°C and 5% CO₂.

For virus infection during semi-continuous cultivation, PR8 (provided by the Robert Koch Institute, Berlin, Germany) was used (58). The strain was adapted to MDCK(sus) cells, and depletion of DI vRNAs was carried out over five passages at a very low MOI of 10⁻⁵. For the interference assay in MDCK(adh) cells, the same PR8 strain, but adapted to adherent MDCK cells, was used. In addition, we generated candidate DIPs containing a deletion in Seg 1 using reverse genetics as described in "Generation of Purely Clonal DIPs Containing a Deletion in Seg 1," below.

Small-scale two-stage cultivation system for semi-continuous STV/DIP propagation. For the semi-continuous propagation of PR8, a two-stage cultivation system was used, which consisted of two baffled shake flasks (250-ml baffled Erlenmeyer flask; Thermo Fisher Scientific, 4116-0250) connected in series (Fig. 1B). The CSS and the VS were operated at a working volume of 90.00 ml and 77.52 ml, respectively. MDCK(sus) cells in the exponential growth phase were seeded at a VCC of 0.6 × 10⁶ cells/ml and were cultivated in batch mode at 185 rpm and 37°C in a 5% CO₂ environment for 2 days. When the VCC reached approximately 3.0 × 10⁶ cells/ml, at -1.6 dpi, a calculated volume of cell suspension was harvested every 12 h, while prewarmed fresh medium was added manually to obtain an RT (inverse of the dilution rate) of 38.3 h (both CSS and VS). Please note that both shake flasks were not yet connected in series. After steady state was achieved, the cells in the VS were infected with PR8 at an MOI of 0.1, and trypsin (Thermo Fisher Scientific, no. 27250-018) was added (final activity of 20 U/ml). At 12 h postinfection (hpi), semi-continuous production was started by transferring cells from the CSS to the VS (V₂). Furthermore, virus was harvested (V₄), and both shake flasks were filled with prewarmed fresh medium (V₁ or V₃) to obtain an RT of 38.3 h and 22.0 h for CSS and VS, respectively. It is important that the fresh medium, which was added to the VS, contained 60 U/ml trypsin to reach 20 U/ml in the VS. The respective transferred volumes are indicated (equations 1 to 4). The RT of 22.0 h for the VS was chosen, as previously published data showed a pronounced DIP/STV replication dynamic (31). In addition, samples were taken from the virus harvest at every volume transfer for analysis. Cell-free supernatants (300 × g, 4°C, 5 min) were stored at -80°C for further analysis.

TABLE 2 Primers used for segment-specific RT-PCR

Reaction	Target	Primer name	Sequence (5'→3')
RT	All segments	Uni 12	AGCAAAAGCAGG
PCR	Segment 1	S1 Uni for	AGCGAAAGCAGGTCAATTAT
		S1 Uni rev	AGTAGAAACAAGGTCGTTTTTAAAC
	Segment 2	S2 Uni for	AGCGAAAGCAGGCAAACCAT
		S2 Uni rev	AGTAGGAACAAGGCATTTTTTCATG
	Segment 3	S3 Uni for	AGCGAAAGCAGGTAAGTATCC
		S3 Uni rev	AGTAGAAACAAGGTAAGTTTTTGG
	Segment 4	S4 Uni for	AGCAAAAGCAGGGGAA
		S4 Uni rev	AGTAGAAACAAGGGTGTTC
	Segment 5	S5 Uni for	AGCAAAAGCAGGGTAGATAATC
		S5 Uni rev	AGTAGAAACAAGGGTATTTTTTC
	Segment 6	S6 Uni for	AGCGAAAGCAGGGGTTAAAATG
		S6 Uni rev	AGTAGAAACAAGGAGTTTTTTGAAC
	Segment 7	S7 Uni for	AGCGAAAGCAGGTAGATATTG
		S7 Uni rev	AGTAGAAACAAGGTAGTTTTTTAC
	Segment 8	S8 Uni for	AGAAAAGCAGGGTGACAAA
		S8 Uni rev	AGTAGAAACAAGGGTGTTC

$$V_1 = (t_n - t_{n-1}) \cdot V_{CSS} \cdot D_{CSS} \quad (1)$$

$$V_2 = V_1 = (t_n - t_{n-1}) \cdot V_{CSS} \cdot D_{CSS} \quad (2)$$

$$V_3 = (t_n - t_{n-1}) \cdot (V_{VS} \cdot D_{VS} - V_{CSS} \cdot D_{CSS}) \quad (3)$$

$$V_4 = (t_n - t_{n-1}) \cdot D_{VS} \cdot V_{VS} \quad (4)$$

where t_n denotes the sample time point, and t_{n-1} , the previous sample time point. V_{CSS} is the volume of the CSS, V_{VS} is the volume of VS, D_{CSS} is the dilution rate of CSS, and D_{VS} is the dilution rate of VS. V_{CSS} , D_{CSS} , and D_{VS} were predefined as mentioned above. V_3 was set as $0.5 \times V_2$ to ensure a sufficient volume of fresh medium in the VS. This assumption was applied to calculate the volume of V_{VS} .

Virus quantification. Quantification of the infectious virus titer was performed by TCID₅₀ assay as described previously (59) with a measurement error of $\pm 0.3 \log_{10}$ (60). The active DIP titer (required for calculation of a multiplicity of DIP [MODIP] for production of candidate DIPs in shake flasks; see "Rescue and Production of DIPs," below) was quantified by plaque assay using MDCK-PB2(adh) cells (measurement error of $\pm 0.2 \log_{10}$) (25). To determine the infectious virus titers in the interference assay ("Interference Assay," below), MDCK(adh) cells were deployed in the same plaque assay (25). In addition, an HA assay was used to quantify the total number of virions in the supernatant with a measurement error of $\pm 0.15 \log_{10}$ (HAU/100 μ l) (61). The concentration of DIPs (c_{DIP}) and concentration of STVs (c_{STV}) were derived from the HA titer and determined according to equation 5, where c_{RBC} denotes the concentration of red blood cells (2.0×10^7 cells/ml).

$$c_{DIP} = 10^{\frac{\log_{10} HA}{100 \mu l}} \cdot c_{RBC} \quad (5)$$

PCR measurements. Genomic vRNA in progeny virions was examined using PCR. In brief, isolation of vRNA from 150 μ l cell-free supernatants was carried out with the NucleoSpin RNA virus kit (Macherey-Nagel, 740956) as described in the manufacturer's instructions. In order to analyze the presence of FL vRNA and DI vRNA (truncated form), a segment-specific RT-PCR was performed (see "Segment-Specific RT-PCR," below). Real-time RT-qPCR was applied for absolute quantification of Seg 5 vRNA from the progeny virions (see "Real-Time RT-qPCR," below).

Segment-specific RT-PCR. A recently described method was utilized for segment-specific RT-PCR (17, 30). In brief, isolated vRNA was reverse transcribed into cDNA using universal primers that bind at the conserved terminal regions of all eight IAV genome segments (Table 2). Subsequently, segment-specific primers were used for amplification of the respective genome segment sequence by PCR (Table 2). Finally, PCR products were analyzed by agarose gel electrophoresis.

Real-time RT-qPCR. A recently reported method for the specific detection and quantification of influenza viral RNA segments using real-time RT-qPCR was employed (17, 62, 63). Briefly, RNA refer-

TABLE 3 Primers used for reference standard generation

Target	Primer name	Sequence (5'→3')
Seg 5	S5 uni for	AGCAAAAGCAGGGTAGATAATC
	S5 uni T7 rev	TAATACGACTCACTATAGGGAGTAGAAACAAGGGTATTTTTTC

TABLE 4 Primers used for RT

Target	Primer name	Sequence (5' → 3')
Seg 5	S5 tagRT for	ATTTAGGTGACACTATAGAAGCGAGTGATTATGAGGGACGGTTGAT

ence standards were *in vitro* synthesized for absolute quantification (primers required for generation are listed in Table 3). Isolated vRNA of the samples was used for reverse transcription, along with a dilution series of the reference standards (primers listed in Table 4), followed by real-time qPCR (primer sequence in Table 5). Calculation for absolute quantification of vRNA of Seg 5 was conducted as previously described (17, 63).

NGS and data processing. Sample preparation, NGS library preparation, and sequencing analysis of deletion junctions was performed according to a recently published study (32).

Analysis of deletion junctions. Deletion junctions refer to the DI vRNAs in the viral population, while deletion junction sites refer to the start and end position of the breaking points in the viral genome. Deletion junctions that did not accumulate to levels above 14 NGS reads in at least one sampling time point were removed from the data set for higher accuracy (32). Furthermore, defective vRNAs that showed more than 85% of the length of FL vRNA were excluded from analysis in this work. DI vRNA 3' and 5' length indicated the number of retained nucleotides prior and after the deletion junction at the respective vRNA end. Of note is that the DI vRNA sequence was reported in negative-sense and 3' to 5' orientation. The calculation of the DI vRNA length comprised the following sequence lengths: Seg 1 (2,341 nucleotides [nt]), Seg 2 (2,341 nt), Seg 3 (2,233 nt), Seg 4 (1,775 nt), Seg 5 (1,565 nt), Seg 6 (1,413 nt), Seg 7 (1,027 nt), and Seg 8 (890 nt). The number of nucleotides of the incorporation signal (NCR) and the bundling signal (terminal ends of coding region), which together form the packaging signal, were taken from a recent review (64).

Generation of purely clonal DIPs containing a deletion in Seg 1. To generate purely clonal Seg 1-derived DIPs (top gain, loss, gain [*de novo*]) in the absence of STV, we used a previously established plasmid-based reverse-genetics system (40). More specifically, to complement the missing PB2 to allow DIP production without STV, we used a coculture of HEK-293T-PB2 cells and MDCK-PB2(adh) cells for reconstitution.

Generation of plasmids. Plasmids harboring specific deletions were generated as described previously (40). In brief, pHW191 encoding the PR8-derived PB2 gene (65) was used as a template for PCR amplification (Phusion Hot Start II DNA polymerase; Thermo Fisher, no. F549L). Here, the desired 5' fragment (containing overhangs complementary to the 3' fragment) of a specified deletion junction (Table 1) was amplified, using a 5'-specific forward and reverse primer set (Table 6). Similarly, a set of 3'-specific primers were used to amplify the desired 3' fragment (containing overhangs complementary to the 5' fragment) of a specified deletion junction from the pHW191 template DNA. Next, the 5' fragments hybridized with the overlapping 3' fragments, resulting in PCR products with the individual deletion junctions (splice-overlapped products) after subsequent amplification cycles at an annealing temperature of 62°C. Lastly, the internally spliced PB2 sequence was inserted in pHW2000-GGAar1 using Golden Gate cloning (66, 67). All plasmids were sequenced to confirm the generated deletion junctions.

Rescue and production of DIPs. For rescue of purely clonal DIPs containing a deletion in Seg 1 (40), we cotransfected a coculture of adherent HEK-293T-PB2 cells (0.2×10^6 cells/well) and MDCK-PB2(adh) cells (0.2×10^6 cells/well) with corresponding plasmids harboring a deletion in the PB2 sequence (50 ng) and 1 μ g of each pHW192-pHW198 plasmid (encoding the remaining gene segments of PR8 IAV) using the calcium phosphate method in a 6-well format. DIP-containing supernatants were harvested at 4, 6, 8, 10, and 12 days posttransfection and stored at -80°C for further use. Larger stocks (seed viruses) of purely clonal Seg 1 DIPs were generated in MDCK-PB2(sus) cells in shake flasks.

The production of Seg 1 DIPs in MDCK-PB2(sus) cells was conducted according to a recently published paper (25). In brief, MDCK-PB2(sus) cells cultivated in shake flasks were centrifuged ($300 \times g$, 5 min, room temperature) and used to inoculate a new shake flask at 2.0×10^6 cells/ml with fresh medium and trypsin (final activity of 20 U/ml). Subsequently, cells were infected at an MOI of E-2. Cell-free supernatants ($3,000 \times g$, 4°C , 10 min) were stored at -80°C for further analysis.

Interference assay. To measure the efficacy of DIPs to suppress STV replication, we performed an *in vitro* coinfection assay in MDCK(adh) cells following a previously published description (26). To summarize, MDCK(adh) cells, cultivated in 6-well plates, were washed twice with phosphate-buffered saline (PBS). Next, cells were either infected with STV only (MOI of 0.01, based on the TCID₅₀ titer) or coinfecting with STV and 125 μ l of the produced DIP material (diluted for normalization). Wells were filled up to 250 μ l with infection medium (GMEM; 1% peptone, 5 U/ml trypsin), and incubation was conducted for 1 h at 37°C and 5% CO₂. Subsequently, the inoculum was aspirated, the cells washed with PBS, and 2 ml

TABLE 5 Primers used for real-time qPCR

Target	Primer name	Sequence (5' → 3')
Introduced tag sequence	vRNA tagRealtime for	ATTTAGGTGACACTATAGAAGCG
Seg 5	Seg 5 Realtime rev	CGCACTGGGATGTTCTTC

TABLE 6 Splice overlap extension PCR primers

Target	Primer name	Sequence (5'→3')	Annealing temp for overlap PCR (°C)
Gain 5' fragment	For	CGGTCACCTGCCAGTGGGAGCGAAAGCA	66
	Rev	ACGTCTCCTTGCCCAATTATCCTCTTGTCTGCTGTA	
Gain 3' fragment	For	TACAGCAGACAAGAGGATAATTGGGCAAGGAGACGT	
	Rev	CCCACCTGCGCGCTATTAGTAGAAACAAGGTCGTTTTAACTATT	
Loss 5' fragment	For	CCCACCTGCCAGTGGGAGCGAAAGCAG	67
	Rev	GCCTTCTCTCTTTCGCGTACTTCTTGATTATGGCCA	
Loss 3' fragment	For	TGGCCATAATCAAGAAGTACGCGAAAGGAGAGAAGGC	
	Rev	CCCACCTGCGCGCTATTAGTAGAAACAAGGTCGTTTTAACTA	
Gain (<i>de novo</i>) 5' fragment	For	CAGTCACCTGCCGATGGGAGCGAAAGCAGGT	67
	Rev	CCACGTCTCCTTGCCCAATTATTTACTCCATAAAGTTTGCCTTGC	
Gain (<i>de novo</i>) 3' fragment	For	GCAAGGACAACCTTTATGGAGTAAATAATTGGGCAAGGAGACGTGG	
	Rev	CCCACCTGCTTTTTATTAGTAGAAACAAGGTCGTTTTAACTATT	

of infection medium was added. Cells were incubated for 24 h at 37°C and 5% CO₂. The supernatant was harvested and stored at –80°C until further analysis by plaque assay and HA assay.

Data availability. The reference sequence of the PR8 genome used for alignment can be found under the following NCBI accession numbers: [AF389115.1](https://.ncbi.nlm.nih.gov/nucl/AF389115.1) (PB2), [AF389116.1](https://.ncbi.nlm.nih.gov/nucl/AF389116.1) (PB2), [AF389117.1](https://.ncbi.nlm.nih.gov/nucl/AF389117.1) (PA), [AF389118.1](https://.ncbi.nlm.nih.gov/nucl/AF389118.1) (HA), [AF389119.1](https://.ncbi.nlm.nih.gov/nucl/AF389119.1) (NP), [AF389120.1](https://.ncbi.nlm.nih.gov/nucl/AF389120.1) (NA), [AF389121.1](https://.ncbi.nlm.nih.gov/nucl/AF389121.1) (M), [AF389122.1](https://.ncbi.nlm.nih.gov/nucl/AF389122.1) (NS). The complete NGS data set is available under the BioProject accession number [PRJNA743179](https://www.ncbi.nlm.nih.gov/bioproject/PRJNA743179).

ACKNOWLEDGMENTS

Special thanks go to Claudia Best and Nancy Wynserski for their outstanding technical support. We thank Thomas Bissinger for providing the seed virus and Marc Hein for valuable discussions. The authors appreciate the sequencing work of Alvaro Hernandez, Christy Wright, and the staff at the Roy. J. Carver Biotechnology Center, University of Illinois. We thank the St. Jude Children's Research Hospital, Memphis, USA, for providing pHW2000 plasmids. Furthermore, a special thank you is directed to Stefan Pöhlmann, Prerna Arora, and Najat Bdeir of the German Primate Center, Göttingen, Germany, for providing plasmids and cell lines for rescue of DIP candidates and helpful discussions. We thank Shanghai BioEngine Sci-Tech and Wen-Song Tan from the East China University of Science and Technology for supplying the Xeno medium.

The work was supported by the Defense Advanced Research Projects Agency (<https://www.darpa.mil/program/intercept>) INTERCEPT program under cooperative agreements W911NF-17-2-0012 and DARPA-16-35-INTERCEPT-FP-018.

A patent for the use of OP7 (a DIP containing point mutations instead of a deletion in Seg 7) as an antiviral agent for treatment of IAV infection is pending. The patent holders are S.Y.K. and U.R. Another patent for the use of DI244 and OP7 as an antiviral agent for treatment of coronavirus infection is pending. The patent holders are S.Y.K., U.R.

Conceptualization: L.P., D.R., T.D., Y.G., C.B.B., S.Y.K., and U.R.; formal analysis: L.P., D.R., F.G.A., and S.Y.K.; funding acquisition: C.B.B. and U.R.; investigation: L.P., D.R., T.D., and F.G.A.; project administration: L.P. and S.Y.K.; supervision: Y.G., C.B.B., S.Y.K., and U.R.; visualization: L.P., D.R., and S.Y.K.; writing – original draft: L.P., T.D., and S.Y.K.; writing – review and editing: L.P., D.R., T.D., F.G.A., Y.G., C.B.B., S.Y.K., and U.R.

REFERENCES

- Paget J, Spreeuwenberg P, Charu V, Taylor RJ, Iuliano AD, Bresee J, Simonsen L, Viboud C, Global Seasonal Influenza-Associated Mortality Collaborator Network and GLaMOR Collaborating Teams. 2019. Global mortality associated with seasonal influenza epidemics: new burden estimates and predictors from the GLaMOR Project. *J Glob Health* 9:e020421. <https://doi.org/10.7189/jogh.09.020421>.
- Taubenberger JK, Morens DM. 2020. The 1918 influenza pandemic and its legacy. *Cold Spring Harb Perspect Med* 10:a038695. <https://doi.org/10.1101/cshperspect.a038695>.
- Moa AM, Chughtai AA, Muscatello DJ, Turner RM, MacIntyre CR. 2016. Immunogenicity and safety of inactivated quadrivalent influenza vaccine in adults: a systematic review and meta-analysis of randomised controlled trials. *Vaccine* 34:4092–4102. <https://doi.org/10.1016/j.vaccine.2016.06.064>.
- Samson SI, Leventhal PS, Salamand C, Meng Y, Seet BT, Landolfi V, Greenberg D, Hollingsworth R. 2019. Immunogenicity of high-dose trivalent inactivated influenza vaccine: a systematic review and meta-analysis. *Expert Rev Vaccines* 18:295–308. <https://doi.org/10.1080/14760584.2019.1575734>.

5. Vogel OA, Manicassamy B. 2020. Broadly protective strategies against influenza viruses: universal vaccines and therapeutics. *Front Microbiol* 11: 135. <https://doi.org/10.3389/fmicb.2020.00135>.
6. Tricco AC, Chit A, Soobiah C, Hallett D, Meier G, Chen MH, Tashkandi M, Bauch CT, Loeb M. 2013. Comparing influenza vaccine efficacy against mismatched and matched strains: a systematic review and meta-analysis. *BMC Med* 11:153. <https://doi.org/10.1186/1741-7015-11-153>.
7. Paules C, Subbarao K. 2017. Influenza. *Lancet* 390:697–708. [https://doi.org/10.1016/S0140-6736\(17\)30129-0](https://doi.org/10.1016/S0140-6736(17)30129-0).
8. O'Hanlon R, Shaw ML. 2019. Baloxavir marboxil: the new influenza drug on the market. *Curr Opin Virol* 35:14–18. <https://doi.org/10.1016/j.coviro.2019.01.006>.
9. Hurt AC, Ernest J, Deng YM, Iannello P, Besselaar TG, Birch C, Buchy P, Chittaganpitch M, Chiu SC, Dwyer D, Guigon A, Harrower B, Kei IP, Kok T, Lin C, McPhie K, Mohd A, Olveda R, Panayotou T, Rawlinson W, Scott L, Smith D, D'Souza H, Komadina N, Shaw R, Kelso A, Barr IG. 2009. Emergence and spread of oseltamivir-resistant A(H1N1) influenza viruses in Oceania, South East Asia and South Africa. *Antiviral Res* 83:90–93. <https://doi.org/10.1016/j.antiviral.2009.03.003>.
10. Hayden FG, Sugaya N, Hirotsu N, Lee N, de Jong MD, Hurt AC, Ishida T, Sekino H, Yamada K, Portsmouth S, Kawaguchi K, Shishido T, Arai M, Tsuchiya K, Uehara T, Watanabe A, Baloxavir Marboxil Investigators Group. 2018. Baloxavir marboxil for uncomplicated influenza in adults and adolescents. *N Engl J Med* 379:913–923. <https://doi.org/10.1056/NEJMoa1716197>.
11. Jones JC, Kumar G, Barman S, Najera I, White SW, Webby RJ, Govorkova EA. 2018. Identification of the I38T PA substitution as a resistance marker for next-generation influenza virus endonuclease inhibitors. *mBio* 9: e00430-18. <https://doi.org/10.1128/mBio.00430-18>.
12. Dimmock NJ, Easton AJ. 2014. Defective interfering influenza virus RNAs: time to reevaluate their clinical potential as broad-spectrum antivirals? *J Virol* 88:5217–5227. <https://doi.org/10.1128/JVI.03193-13>.
13. Huo C, Cheng J, Xiao J, Chen M, Zou S, Tian H, Wang M, Sun L, Hao Z, Hu Y. 2020. Defective viral particles produced in mast cells can effectively fight against lethal influenza A virus. *Front Microbiol* 11:553274. <https://doi.org/10.3389/fmicb.2020.553274>.
14. Zhao H, To KKW, Chu H, Ding Q, Zhao X, Li C, Shuai H, Yuan S, Zhou J, Kok KH, Jiang S, Yuen KY. 2018. Dual-functional peptide with defective interfering genes effectively protects mice against avian and seasonal influenza. *Nat Commun* 9:2358. <https://doi.org/10.1038/s41467-018-04792-7>.
15. Yang Y, Lyu T, Zhou R, He X, Ye K, Xie Q, Zhu L, Chen T, Shen C, Wu Q, Zhang B, Zhao W. 2019. The antiviral and antitumor effects of defective interfering particles/genomes and their mechanisms. *Front Microbiol* 10: 1852. <https://doi.org/10.3389/fmicb.2019.01852>.
16. Vignuzzi M, Lopez CB. 2019. Defective viral genomes are key drivers of the virus-host interaction. *Nat Microbiol* 4:1075–1087. <https://doi.org/10.1038/s41564-019-0465-y>.
17. Kupke SY, Riedel D, Frensing T, Zmora P, Reichl U. 2019. A novel type of influenza A virus-derived defective interfering particle with nucleotide substitutions in its genome. *J Virol* 93:e01786-18. <https://doi.org/10.1128/JVI.01786-18>.
18. Laske T, Heldt FS, Hoffmann H, Frensing T, Reichl U. 2016. Modeling the intracellular replication of influenza A virus in the presence of defective interfering RNAs. *Virus Res* 213:90–99. <https://doi.org/10.1016/j.virusres.2015.11.016>.
19. Marriott AC, Dimmock NJ. 2010. Defective interfering viruses and their potential as antiviral agents. *Rev Med Virol* 20:51–62. <https://doi.org/10.1002/rmv.641>.
20. Nayak DP, Chambers TM, Akkina RK. 1985. Defective-interfering (DI) RNAs of influenza viruses: origin, structure, expression, and interference. *Curr Top Microbiol Immunol* 216:103–151. https://doi.org/10.1007/978-3-642-70227-3_3.
21. Duhaut SD, McCauley JW. 1996. Defective RNAs inhibit the assembly of influenza virus genome segments in a segment-specific manner. *Virology* 216:326–337. <https://doi.org/10.1006/viro.1996.0068>.
22. Odagiri T, Tashiro M. 1997. Segment-specific noncoding sequences of the influenza virus genome RNA are involved in the specific competition between defective interfering RNA and its progenitor RNA segment at the virion assembly step. *J Virol* 71:2138–2145. <https://doi.org/10.1128/JVI.71.3.2138-2145.1997>.
23. Dimmock NJ, Dove BK, Meng B, Scott PD, Taylor I, Cheung L, Hallis B, Marriott AC, Carroll MW, Easton AJ. 2012. Comparison of the protection of ferrets against pandemic 2009 influenza A virus (H1N1) by 244 DI influenza virus and oseltamivir. *Antiviral Res* 96:376–385. <https://doi.org/10.1016/j.antiviral.2012.09.017>.
24. Dimmock NJ, Rainsford EW, Scott PD, Marriott AC. 2008. Influenza virus protecting RNA: an effective prophylactic and therapeutic antiviral. *J Virol* 82:8570–8578. <https://doi.org/10.1128/JVI.00743-08>.
25. Hein MD, Arora P, Marichal-Gallardo P, Winkler M, Genzel Y, Pohlmann S, Schughart K, Kupke SY, Reichl U. 2021. Cell culture-based production and in vivo characterization of purely clonal defective interfering influenza virus particles. *BMC Biol* 19:91. <https://doi.org/10.1186/s12915-021-01020-5>.
26. Hein MD, Kollmus H, Marichal-Gallardo P, Puttker S, Benndorf D, Genzel Y, Schughart K, Kupke SY, Reichl U. 2021. OP7, a novel influenza A virus defective interfering particle: production, purification, and animal experiments demonstrating antiviral potential. *Appl Microbiol Biotechnol* 105: 129–146. <https://doi.org/10.1007/s00253-020-11029-5>.
27. Easton AJ, Scott PD, Edworthy NL, Meng B, Marriott AC, Dimmock NJ. 2011. A novel broad-spectrum treatment for respiratory virus infections: influenza-based defective interfering virus provides protection against pneumovirus infection in vivo. *Vaccine* 29:2777–2784. <https://doi.org/10.1016/j.vaccine.2011.01.102>.
28. Scott PD, Meng B, Marriott AC, Easton AJ, Dimmock NJ. 2011. Defective interfering influenza A virus protects in vivo against disease caused by a heterologous influenza B virus. *J Gen Virol* 92:2122–2132. <https://doi.org/10.1099/vir.0.034132-0>.
29. Rand U, Kupke SY, Shkarlet H, Hein MD, Hirsch T, Marichal-Gallardo P, Cicin-Sain L, Reichl U, Bruder D. 2021. Antiviral activity of influenza A virus defective interfering particles against SARS-CoV-2 replication in vitro through stimulation of innate immunity. *Cells* 10:1756. <https://doi.org/10.3390/cells10071756>.
30. Frensing T, Heldt FS, Pflugmacher A, Behrendt I, Jordan I, Flockerzi D, Genzel Y, Reichl U. 2013. Continuous influenza virus production in cell culture shows a periodic accumulation of defective interfering particles. *PLoS One* 8:e72288. <https://doi.org/10.1371/journal.pone.0072288>.
31. Tapia F, Laske T, Wasik MA, Rammhold M, Genzel Y, Reichl U. 2019. Production of defective interfering particles of influenza A virus in parallel continuous cultures at two residence times—insights from qPCR measurements and viral dynamics modeling. *Front Bioeng Biotechnol* 7:275. <https://doi.org/10.3389/fbioe.2019.00275>.
32. Alnaji FG, Holmes JR, Rendon G, Vera JC, Fields CJ, Martin BE, Brooke CB. 2019. Sequencing framework for the sensitive detection and precise mapping of defective interfering particle-associated deletions across influenza A and B viruses. *J Virol* 93:e00354-19. <https://doi.org/10.1128/JVI.00354-19>.
33. Davis AR, Nayak DP. 1979. Sequence relationships among defective interfering influenza viral RNAs. *Proc Natl Acad Sci U S A* 76:3092–3096. <https://doi.org/10.1073/pnas.76.7.3092>.
34. Duhaut SD, Dimmock NJ. 1998. Heterologous protection of mice from a lethal human H1N1 influenza A virus infection by H3N8 equine defective interfering virus: comparison of defective RNA sequences isolated from the DI inoculum and mouse lung. *Virology* 248:241–253. <https://doi.org/10.1006/viro.1998.9267>.
35. Jennings PA, Finch JT, Winter G, Robertson JS. 1983. Does the higher order structure of the influenza virus ribonucleoprotein guide sequence rearrangements in influenza viral RNA? *Cell* 34:619–627. [https://doi.org/10.1016/0092-8674\(83\)90394-x](https://doi.org/10.1016/0092-8674(83)90394-x).
36. Saira K, Lin X, DePasse JV, Halpin R, Twaddle A, Stockwell T, Angus B, Cozzi-Lepri A, Delfino M, Dugan V, Dwyer DE, Freiberg M, Horban A, Lusso M, Lynfield R, Wentworth DN, Holmes EC, Davey R, Wentworth DE, Ghedin E, Group IFS, INSIGHT FLU002 Study Group, INSIGHT FLU003 Study Group. 2013. Sequence analysis of in vivo defective interfering-like RNA of influenza A H1N1 pandemic virus. *J Virol* 87:8064–8074. <https://doi.org/10.1128/JVI.00240-13>.
37. Routh A, Johnson JE. 2014. Discovery of functional genomic motifs in viruses with ViReMa—a Virus recombination mapper—for analysis of next-generation sequencing data. *Nucleic Acids Res* 42:e11. <https://doi.org/10.1093/nar/gkt916>.
38. Fujii Y, Goto H, Watanabe T, Yoshida T, Kawaoka Y. 2003. Selective incorporation of influenza virus RNA segments into virions. *Proc Natl Acad Sci U S A* 100:2002–2007. <https://doi.org/10.1073/pnas.0437721000>.
39. Goto H, Muramoto Y, Noda T, Kawaoka Y. 2013. The genome-packaging signal of the influenza A virus genome comprises a genome incorporation signal and a genome-bundling signal. *J Virol* 87:11316–11322. <https://doi.org/10.1128/JVI.01301-13>.
40. Bdeir N, Arora P, Gartner S, Hoffmann M, Reichl U, Pohlmann S, Winkler M. 2019. A system for production of defective interfering particles in the

- absence of infectious influenza A virus. *PLoS One* 14:e0212757. <https://doi.org/10.1371/journal.pone.0212757>.
41. Widjaja I, de Vries E, Rottier PJ, de Haan CA. 2012. Competition between influenza A virus genome segments. *PLoS One* 7:e47529. <https://doi.org/10.1371/journal.pone.0047529>.
 42. Dimmock NJ, Easton AJ. 2015. Cloned defective interfering influenza RNA and a possible pan-specific treatment of respiratory virus diseases. *Viruses* 7:3768–3788. <https://doi.org/10.3390/v7072796>.
 43. Pavlovic J, Haller O, Staeheli P. 1992. Human and mouse Mx proteins inhibit different steps of the influenza virus multiplication cycle. *J Virol* 66: 2564–2569. <https://doi.org/10.1128/JVI.66.4.2564-2569.1992>.
 44. Seitz C, Frensing T, Hoper D, Kochs G, Reichl U. 2010. High yields of influenza A virus in Madin-Darby canine kidney cells are promoted by an insufficient interferon-induced antiviral state. *J Gen Virol* 91:1754–1763. <https://doi.org/10.1099/vir.0.020370-0>.
 45. Seitz C, Isken B, Heynisch B, Rettkowski M, Frensing T, Reichl U. 2012. Trypsin promotes efficient influenza vaccine production in MDCK cells by interfering with the antiviral host response. *Appl Microbiol Biotechnol* 93: 601–611. <https://doi.org/10.1007/s00253-011-3569-8>.
 46. Baum A, García-Sastre A. 2011. Differential recognition of viral RNA by RIG-I. *Virulence* 2:166–169. <https://doi.org/10.4161/viru.2.2.15481>.
 47. Rehwinkel J, Tan CP, Goubau D, Schulz O, Pichlmair A, Bier K, Robb N, Vreede F, Barclay W, Fodor E, Reis e Sousa C. 2010. RIG-I detects viral genomic RNA during negative-strand RNA virus infection. *Cell* 140: 397–408. <https://doi.org/10.1016/j.cell.2010.01.020>.
 48. Hutchinson EC, von Kirchbach JC, Gog JR, Digard P. 2010. Genome packaging in influenza A virus. *J Gen Virol* 91:313–328. <https://doi.org/10.1099/vir.0.017608-0>.
 49. Noda T, Kawaoka Y. 2010. Structure of influenza virus ribonucleoprotein complexes and their packaging into virions. *Rev Med Virol* 20:380–391. <https://doi.org/10.1002/rmv.666>.
 50. Duhaut S, Dimmock NJ. 2000. Approximately 150 nucleotides from the 5' end of an influenza A segment 1 defective virion RNA are needed for genome stability during passage of defective virus in infected cells. *Virology* 275:278–285. <https://doi.org/10.1006/viro.2000.0502>.
 51. Duhaut SD, Dimmock NJ. 2002. Defective segment 1 RNAs that interfere with production of infectious influenza A virus require at least 150 nucleotides of 5' sequence: evidence from a plasmid-driven system. *J Gen Virol* 83:403–411. <https://doi.org/10.1099/0022-1317-83-2-403>.
 52. Ueda M, Nakajima K, Sugiura A. 1980. Extra RNAs of von Magnus particles of influenza virus cause reduction of particular polymerase genes. *J Virol* 34:1–8. <https://doi.org/10.1128/JVI.34.1.1-8.1980>.
 53. Alnajj FG, Reiser WK, te Velthuis A, Brooke CB. 2021. Influenza A virus defective viral genomes are inefficiently packaged into virions relative to wild-type genomic RNAs. *bioRxiv* <https://doi.org/10.1101/2021.05.13.444068>; 2021.05.13.444068.
 54. Levi LI, Rezelj VV, Henrion-Lacritick A, Erazo D, Boussier J, Vallet T, Bernhauerova V, Suzuki Y, Carrau L, Weger-Lucarelli J, Saleh MC, Vignuzzi M. 2021. Defective viral genomes from chikungunya virus are broad-spectrum antivirals and prevent virus dissemination in mosquitoes. *PLoS Pathog* 17:e1009110. <https://doi.org/10.1371/journal.ppat.1009110>.
 55. Rezelj VV, Carrau L, Merwaiss F, Levi LI, Erazo D, Tran QD, Henrion-Lacritick A, Gausson V, Suzuki Y, Shengjuler D, Meyer B, Vallet T, Weger-Lucarelli J, Bernhauerova V, Titievsky A, Sharov V, Pietropaoli S, Diaz-Salinas MA, Legros V, Pardigon N, Barba-Spaeth G, Brodsky L, Saleh MC, Vignuzzi M. 2021. Defective viral genomes as therapeutic interfering particles against flavivirus infection in mammalian and mosquito hosts. *Nat Commun* 12:2290. <https://doi.org/10.1038/s41467-021-22341-7>.
 56. Welch SR, Tilston NL, Lo MK, Whitmer SLM, Harmon JR, Scholte FEM, Spengler JR, Duprex WP, Nichol ST, Spiropoulou CF. 2020. Inhibition of Nipah virus by defective interfering particles. *J Infect Dis* 221:S460–S470. <https://doi.org/10.1093/infdis/jiz564>.
 57. Lohr V, Genzel Y, Behrendt I, Scharfenberg K, Reichl U. 2010. A new MDCK suspension line cultivated in a fully defined medium in stirred-tank and wave bioreactor. *Vaccine* 28:6256–6264. <https://doi.org/10.1016/j.vaccine.2010.07.004>.
 58. Bissinger T, Fritsch J, Mihut A, Wu Y, Liu X, Genzel Y, Tan WS, Reichl U. 2019. Semi-perfusion cultures of suspension MDCK cells enable high cell concentrations and efficient influenza A virus production. *Vaccine* 37: 7003–7010. <https://doi.org/10.1016/j.vaccine.2019.04.054>.
 59. Genzel Y, Reichl U. 2007. Vaccine production, p 457–473. *In* Pörtner R (ed), *Animal cell biotechnology*. Humana Press, Totowa, NJ. https://doi.org/10.1007/978-1-59745-399-8_21.
 60. Genzel Y, Rödig J, Rapp E, Reichl U. 2014. Vaccine production: upstream processing with adherent or suspension cell lines, p 371–393. *In* Pörtner R (ed), *Animal cell biotechnology*. Humana Press, Totowa, NJ.
 61. Kalbfuss B, Knochlein A, Krober T, Reichl U. 2008. Monitoring influenza virus content in vaccine production: precise assays for the quantitation of hemagglutination and neuraminidase activity. *Biologicals* 36:145–161. <https://doi.org/10.1016/j.biologics.2007.10.002>.
 62. Kawakami E, Watanabe T, Fujii K, Goto H, Watanabe S, Noda T, Kawaoka Y. 2011. Strand-specific real-time RT-PCR for distinguishing influenza vRNA, cRNA, and mRNA. *J Virol Methods* 173:1–6. <https://doi.org/10.1016/j.jviromet.2010.12.014>.
 63. Frensing T, Kupke SY, Bachmann M, Fritzsche S, Gallo-Ramirez LE, Reichl U. 2016. Influenza virus intracellular replication dynamics, release kinetics, and particle morphology during propagation in MDCK cells. *Appl Microbiol Biotechnol* 100:7181–7192. <https://doi.org/10.1007/s00253-016-7542-4>.
 64. Breen M, Nogales A, Baker SF, Martinez-Sobrido L. 2016. Replication-competent influenza A viruses expressing reporter genes. *Viruses* 8:179. <https://doi.org/10.3390/v8070179>.
 65. Hoffmann E, Neumann G, Kawaoka Y, Hobom G, Webster RG. 2000. A DNA transfection system for generation of influenza A virus from eight plasmids. *Proc Natl Acad Sci U S A* 97:6108–6113. <https://doi.org/10.1073/pnas.100133697>.
 66. Andreou AI, Nakayama N. 2018. Mobius assembly: a versatile Golden-Gate framework towards universal DNA assembly. *PLoS One* 13:e0189892. <https://doi.org/10.1371/journal.pone.0189892>.
 67. Engler C, Gruetner R, Kandzia R, Marillonnet S. 2009. Golden Gate shuffling: a one-pot DNA shuffling method based on type IIs restriction enzymes. *PLoS One* 4:e5553. <https://doi.org/10.1371/journal.pone.0005553>.
 68. Tapia F, Jordan I, Genzel Y, Reichl U. 2017. Efficient and stable production of Modified Vaccinia Ankara virus in two-stage semi-continuous and in continuous stirred tank cultivation systems. *PLoS One* 12:e0182553. <https://doi.org/10.1371/journal.pone.0182553>.

3.2. Second Manuscript

In the study of the second manuscript, the replication of IAV DIPs and STVs for a broad range of DIP and STV inputs is analyzed. This helps to assess the impact on virus-induced apoptosis and to calibrate a mathematical multiscale model of IAV and STV infection enabling the prediction of optimal dosing ratio for IAV DIPs.

Rüdiger, Daniel*; **Pelz, Lars***; Hein, Marc D.; Kupke, Sascha Y.; Reichl, Udo

*Shared first authorship

Multiscale model of defective interfering particle replication for influenza A virus infection in animal cell culture

PLoS Computational Biology, 2021

(Rüdiger et al., 2021)

Reproduced with permission from PLOS.

No changes were made.

<https://creativecommons.org/licenses/by/2.0/>

Individual contribution:

In the study of the second manuscript, I generated data for mathematical modeling that includes performing infection experiments and quantification of “active DIP titer” by plaque assay (both together with Marc Hein), analyzing real-time RT-qPCR data and conducting of imaging flow cytometry. Moreover, I wrote corresponding parts of the materials & methods section.

RESEARCH ARTICLE

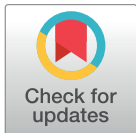
Multiscale model of defective interfering particle replication for influenza A virus infection in animal cell culture

Daniel Rüdiger¹*, Lars Pelz¹, Marc D. Hein², Sascha Y. Kupke^{1*}, Udo Reichl^{1,2}

1 Max Planck Institute for Dynamics of Complex Technical Systems, Magdeburg, Germany, **2** Chair of Bioprocess Engineering, Institute of Process Engineering, Faculty of Process & Systems Engineering, Otto-von-Guericke University, Magdeburg, Germany

* These authors contributed equally to this work.

* ruedigerd@mpi-magdeburg.mpg.de (DR); kupke@mpi-magdeburg.mpg.de (SYK)



Abstract

Cell culture-derived defective interfering particles (DIPs) are considered for antiviral therapy due to their ability to inhibit influenza A virus (IAV) production. DIPs contain a large internal deletion in one of their eight viral RNAs (vRNAs) rendering them replication-incompetent. However, they can propagate alongside their homologous standard virus (STV) during infection in a competition for cellular and viral resources. So far, experimental and modeling studies for IAV have focused on either the intracellular or the cell population level when investigating the interaction of STVs and DIPs. To examine these levels simultaneously, we conducted a series of experiments using highly different multiplicities of infections for STVs and DIPs to characterize virus replication in Madin-Darby Canine Kidney suspension cells. At several time points post infection, we quantified virus titers, viable cell concentration, virus-induced apoptosis using imaging flow cytometry, and intracellular levels of vRNA and viral mRNA using real-time reverse transcription qPCR. Based on the obtained data, we developed a mathematical multiscale model of STV and DIP co-infection that describes dynamics closely for all scenarios with a single set of parameters. We show that applying high DIP concentrations can shut down STV propagation completely and prevent virus-induced apoptosis. Interestingly, the three observed viral mRNAs (full-length segment 1 and 5, defective interfering segment 1) accumulated to vastly different levels suggesting the interplay between an internal regulation mechanism and a growth advantage for shorter viral RNAs. Furthermore, model simulations predict that the concentration of DIPs should be at least 10000 times higher than that of STVs to prevent the spread of IAV. Ultimately, the model presented here supports a comprehensive understanding of the interactions between STVs and DIPs during co-infection providing an ideal platform for the prediction and optimization of vaccine manufacturing as well as DIP production for therapeutic use.

OPEN ACCESS

Citation: Rüdiger D, Pelz L, Hein MD, Kupke SY, Reichl U (2021) Multiscale model of defective interfering particle replication for influenza A virus infection in animal cell culture. *PLoS Comput Biol* 17(9): e1009357. <https://doi.org/10.1371/journal.pcbi.1009357>

Editor: Rustom Antia, Emory University, UNITED STATES

Received: April 1, 2021

Accepted: August 18, 2021

Published: September 7, 2021

Peer Review History: PLOS recognizes the benefits of transparency in the peer review process; therefore, we enable the publication of all of the content of peer review and author responses alongside final, published articles. The editorial history of this article is available here: <https://doi.org/10.1371/journal.pcbi.1009357>

Copyright: © 2021 Rüdiger et al. This is an open access article distributed under the terms of the [Creative Commons Attribution License](https://creativecommons.org/licenses/by/4.0/), which permits unrestricted use, distribution, and reproduction in any medium, provided the original author and source are credited.

Data Availability Statement: The experimental data are within the manuscript and its [Supporting Information](#) files. The code for model simulation

and optimization is available at https://github.com/ModIAV/STV_DIP_Coinfection.

Funding: This work was partially supported by the Defense Advanced Research Project Agency INTERCEPT program (<https://www.darpa.mil/program/intercept>) under Cooperative Agreement W911NF-17-2-0012 (LP). The funders had no role in study design, data collection and analysis, decision to publish, or preparation of the manuscript.

Competing interests: I have read the journal's policy and the authors of this manuscript have the following competing interests: A patent for the use of OP7 (a DIP containing point mutations instead of a deletion in viral genome segment 7) as an antiviral agent for treatment of IAV infection is pending. Patent holders are S.Y.K. and U.R. Another patent for the use of DI244 and OP7 as an antiviral agent for treatment of coronavirus infection is pending. Patent holders are S.Y.K., U.R. and M.D.H. The remaining authors declare no conflict of interest.

Author summary

Influenza viruses replicate inside their hosts after infection. Along with the release of wild-type standard virus (STV), they can also generate specific kinds of particles that have deletions in their genome. These so-called “defective interfering particles” (DIPs) are unable to replicate on their own. However, during co-infection with STV they can interfere with the viral life cycle suppressing STV production and instead release a large number of progeny DIPs. Recent studies have shown promising results regarding their potential as antiviral agents. To characterize the interactions between STVs and DIPs during co-infections, we infected animal cell cultures using 12 different multiplicities of infection for STVs and DIPs, respectively. We measured intra- and extracellular infection dynamics and show that STV replication can be suppressed completely using high amounts of DIPs. Then, we developed a mathematical model that describes co-infection dynamics closely using a single set of parameters. We used this model to predict optimal dosing ratios for DIPs to suppress STV infections and for cell culture-derived production of DIPs for antiviral therapy.

Introduction

Infectious diseases continue to pose significant and unpredictable risks for human and animal life despite enormous preventive and therapeutic efforts taken over the last 100 years. The current COVID-19 pandemic clearly demonstrates that newly emerging viruses can lead to millions of deaths and severe impacts on the global economy [1]. Influenza A virus (IAV) has the potential to produce equally dangerous epi- and pandemics due to its high mutation rate and a natural reservoir in various species [2,3]. Prevention and treatment strategies focus mostly on vaccination and the administration of antiviral drugs. However, emerging resistances to current antivirals may limit treatment approaches [4,5], which emphasizes the need for an improvement and expansion of the therapeutic catalogue.

Defective interfering particles (DIPs) are structurally similar to their corresponding standard virus (STV), but replication-incompetent due to a large internal deletion in at least one of their eight viral genome segments [6–10]. During co-infection with the STV, which acts as a helper virus by providing the missing genomic information, they can generate progeny DIPs as well as reduce production and release of STV particles strongly. The decrease in STV production was theorized to be related to a growth advantage of the defective interfering (DI) genome over its full-length (FL) counterpart [7,11,12]. Currently, the shorter length of DI RNA is a prominent hypothesis for the source of this advantage [7], however, the underlying mechanisms are still not understood completely. Besides IAV, nearly all RNA viruses produce DIPs [8,13]. Based on their inhibiting effect during co-infection, DIPs are considered promising candidates for antiviral therapy. Previous animal studies showed that the administration of DIPs could successfully prevent and treat IAV infections in mice and ferrets [14–18]. However, the exact mechanisms of DIP interference, the structural requirements for a potent inhibition of IAV infection and the selection of an optimal dose for therapeutic application remain elusive. In addition, the design and optimization of the production of DIP preparations for manufacturing of antivirals is a challenge. Therefore, a comprehensive mathematical model describing the interplay between STVs and DIPs in cell culture during co-infection on a systems level could support further research into these areas.

Previous model-based studies of DIP infection examined mostly *in vitro* virus propagation on the cell population level [19–22]. However, the competition for cellular resources and inhibition of STV production and release occurs during intracellular virus replication. While few

studies also focused specifically on the effect of DIPs on the intracellular level [23,24], the spreading of DIPs in cell populations was not taken into account. Finally, some previously developed models considered both levels of infection [25,26]. However, these contained rather basic representations of the intracellular virus replication dynamics. A general outcome of model-based DIP infection studies was the impact of the ratio between STVs and DIPs for inhibition, i.e., the applied multiplicity of infection (MOI) and multiplicity of DIPs (MODIP).

Besides DIP production-related issues, a better understanding of the interaction between these two virus populations could also contribute to the development of innovative therapeutic approaches. Applying different MOIs and MODIPs for an infection of animal cells can influence the dynamics of virus propagation significantly. Using vast amounts of both STVs and DIPs leads to more co-infections, which favor DIP production. In contrast, for low MOI and MODIP conditions, only few co-infections occur and, consequently, the STVs can replicate unhindered and overcome inhibition by DIPs. In addition, the MOI can change drastically during the course of an infection as more and more virions are released [27], which is expected to also apply to the MODIP. Therefore, the interplay between the infection conditions on the cell population level and the resulting effects on intracellular replication could be a key factor to understand DIP inhibition dynamics.

To elucidate the complex interactions between STVs and DIPs, we conducted a comprehensive set of experiments using various combinations of MOI and MODIP, and analyzed the infection dynamics on the intracellular and population level in Madin-Darby Canine Kidney suspension (MDCKsus) cells. In addition, we developed a multiscale model for STV and DIP co-infection on the cellular and the population level. As a starting point we considered two previously published models; one focusing on virus replication at the single-cell level [23], the other describing STV replication and propagation for different MOIs [27]. We introduced populations of cells infected only by DIPs and co-infected cells on the population level as well as specific viral mRNA regulations and viral genomic RNA synthesis suppression dynamics on the intracellular level. Then, we utilized the obtained experimental data to calibrate the multiscale model and to predict the impact of different MOI/MODIP conditions on the infection dynamics.

Results

High DIP loads suppress STV infection and prevent virus-induced apoptosis

To examine how a variation of MOI and MODIP affects the overall replication dynamics during STV and DIP co-infection, we infected MDCKsus cells with different combinations of STV (A/PR/8/34, H1N1) and purely clonal DIP input. We selected MOIs of 10^{-3} , 3, 30 and MODIPs of 0, 10^{-3} , 3, 30 to create 12 different infection conditions (Fig 1A). For our experiments, we used a prototypic, well-characterized DIP referred to as DI244 [28]. DI244 particles contain a deletion on the virus genome segment 1 encoding for polymerase basic protein 2 (PB2). The applied MOIs and MODIPs ranged over four orders of magnitude to cover highly different infection scenarios.

For all 12 infection conditions (Fig 1A), we measured the dynamics of viral mRNA and genomic viral RNA (vRNA) on the intracellular level (Figs 2 and S5–S10) using real-time reverse transcription qPCR (real-time RT-qPCR). On the extracellular level, we determined the yield of infectious particles (quantified by plaque assay) and the total yield of STVs and DIPs (quantified by real-time RT-qPCR). Furthermore, we measured the fraction of infected and apoptotic cells using imaging flow cytometry (S3 and S4 Figs).

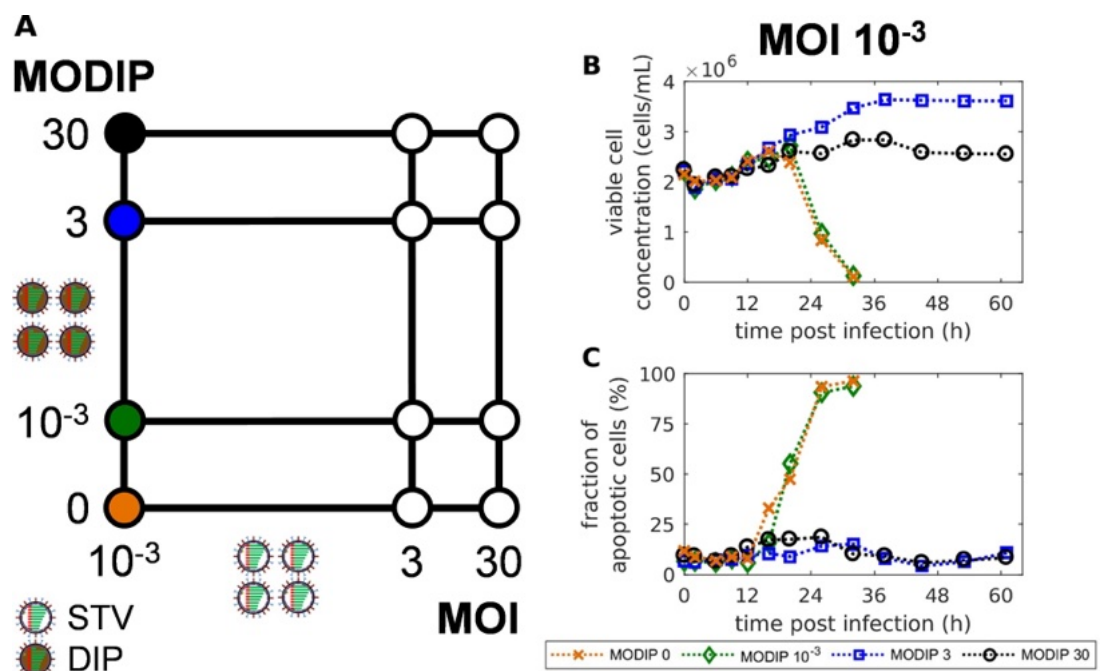


Fig 1. Addition of defective interfering particles (DIPs) can prevent virus-induced apoptosis and protect MDCKsus cells from standard virus (STV) infection. (A) Schematic depiction of the 12 different MOI and MODIP conditions used for infection experiments. (B) Viable cell concentration and (C) the fraction of apoptotic cells for infections with MOI 10^{-3} and MODIPs of 0, 10^{-3} , 3 and 30. Results for all infection conditions are shown in S1 Fig.

<https://doi.org/10.1371/journal.pcbi.1009357.g001>

Our experimental results show that MDCKsus cells were protected from virus-induced cell death when infected at a low MOI of 10^{-3} combined with MODIPs of 3 and 30 (Fig 1B). These two infection conditions will from here on be referred to as L3 (MOI 10^{-3} + MODIP 3) and L30 (MOI 10^{-3} + MODIP 30). For L3, the cells continued to grow until 38 hours post infection (hpi), while for L30 less cell growth occurred which seemed to be affected by the higher concentration of DIPs (Fig 1B). In contrast, all other infection conditions lead to virus-induced apoptosis and cell death after addition of STVs (S1 Fig). Interestingly, for L3 and L30 conditions, the apoptosis level stayed below 20% (Fig 1C) although the cells were infected by high amounts of DIPs. This is likely caused by a significant reduction of intracellular virus replication, especially the low accumulation of vRNAs (Fig 2), whereby apoptotic processes are not triggered.

Both infectious and total virus titers were reduced significantly for L3 and L30 (S3 Fig). Virus replication still occurred on a low level, however, compared to the other conditions a reduction of the infectious virus titer at 26 hpi by five to six orders of magnitude was observed in L3 and L30, respectively.

In sum, the addition of high amounts of DIPs during a STV infection at a low MOI can protect cells from virus-induced cell death and reduce viral titers severely.

DIP infection leads to considerable viral mRNA transcription even in the absence of co-infections

On the intracellular level, we focused on the dynamics of viral RNAs. Negative-sense vRNAs contain the genomic information and enter the cellular nucleus during infection. There, they

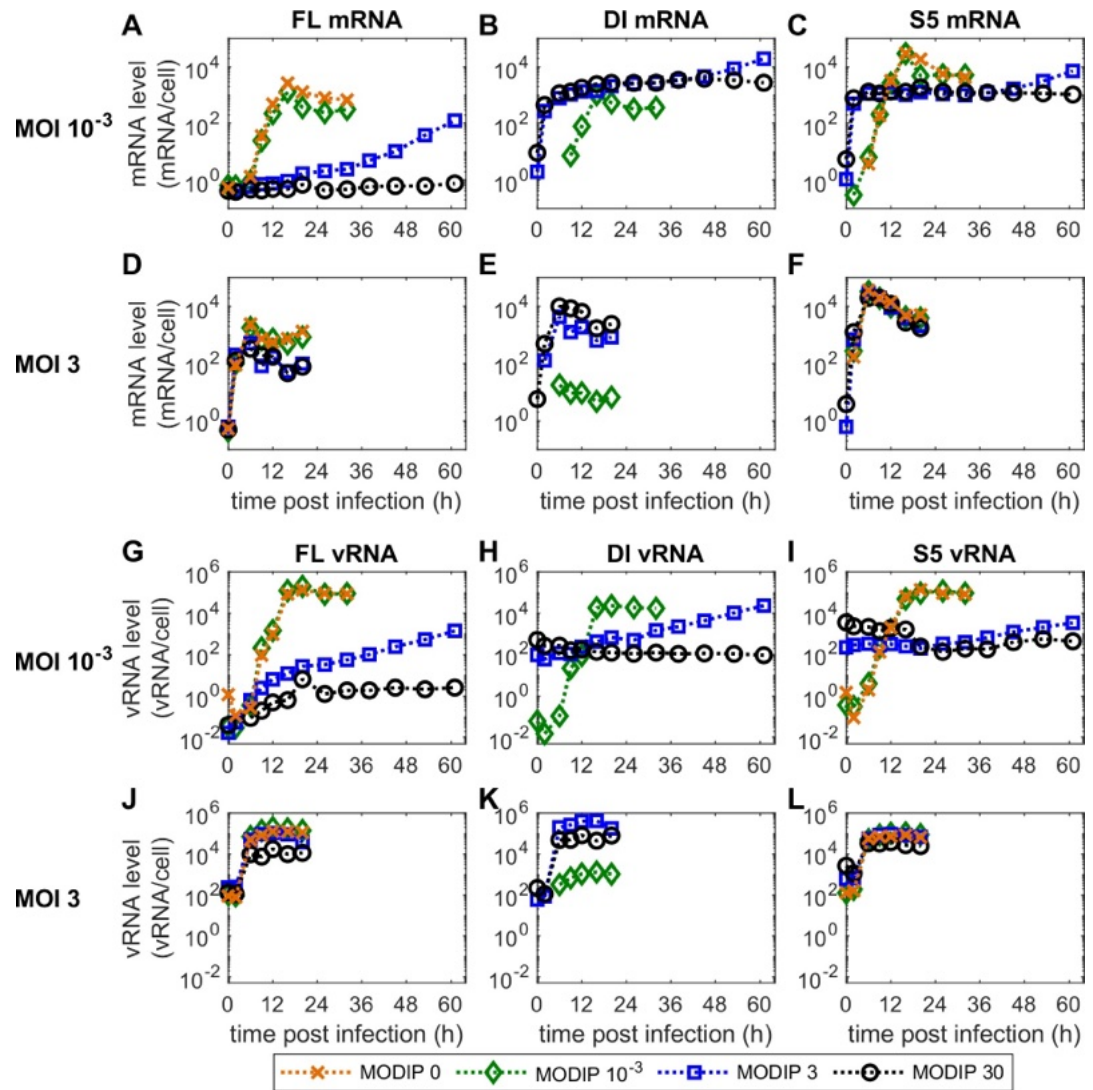


Fig 2. Viral RNA dynamics in infected MDCKsus cells are strongly influenced by the applied concentrations of STVs and DIPs. Real-time RT-qPCR measurements of (A-F) viral mRNA and (G-L) vRNA levels for different infection conditions. The results for (left) FL segment 1, (middle) DI segment 1 and (right) FL segment 5 are shown. Results for the remaining infection conditions are presented in S5–S7 Figs.

<https://doi.org/10.1371/journal.pcbi.1009357.g002>

act as templates for the synthesis of two positive-sense RNAs, i.e., viral mRNA and complementary RNA (cRNA). The former is required to perform viral protein translation and the latter is a replicative intermediate that can be transcribed to produce progeny vRNAs. We measured the levels of vRNA and viral mRNA for three different genome segments, i.e., the FL segment 1, the truncated DI244 segment 1 and segment 5 (S5).

The maximum levels of viral mRNA show clear differences between the three measured segments. S5 mRNA reaches the highest levels and FL mRNA levels are reduced by over one order of magnitude (Fig 2). DI mRNA achieves levels between the other two segments. This

implies that there is a fundamental mechanism that regulates the mRNA accumulation of different segments as this behavior is replicated over all infection conditions (S5–S7 Figs).

The levels of viral mRNA are reduced strongly for the low MOI, high MODIP conditions L3 and L30. FL mRNA is not produced in L30 (Fig 2A) and increases slowly over time in L3. Interestingly, DI and S5 mRNA initially accumulate to similar levels as for other infection conditions using high MOI or MODIP until 2 hpi. Then, their increase stagnates and they stay at this level until at least 45 hpi. Due to the low MOI and high MODIP for conditions L3 and L30, the vast majority of cells were infected only by DIPs and not by STVs. Therefore, the observed levels of DI and S5 mRNA were generated by DIP-only infected cells and did not require a co-infection by STVs providing missing genomic information.

The accumulation of vRNA for all three observed segments is suppressed completely for L30 but shows a slow and steady increase for L3 (Fig 2). Because of the defective genome in DI244, PB2 cannot be produced in cells only infected by DIPs. PB2 is a subunit of the viral RNA-dependent RNA polymerase (RdRp) which is essential for virus replication. Therefore, in cells only infected by a DIP and no STV, the synthesis of progeny vRNA is prevented. For the other conditions, FL and S5 vRNA show typical accumulation dynamics. However, both vRNA and viral mRNA trend towards reduced levels with increasing MODIPs.

Taken together, the DI244 used in our experiments is capable of viral mRNA transcription at considerable levels without the STV functioning as a helper virus.

Developing a multiscale model of STV and DIP co-infection

The mathematical model presented comprises basic aspects of two of our previously published models but expands their scope by including viral RNA replication phenomena observed for DIP propagation in this study. The model structure is based on an MOI-sensitive multiscale model of STV infection in animal cell culture [27]. For the description of the data obtained in our experiments, we expanded this model by considering the dynamics of DIPs on the cell population level and the intracellular level using an adapted model of intracellular DIP replication [23].

To this end, we introduced cells only infected by DIPs (I_{DIP}) and co-infected cells (I_{CO}) to the existing uninfected (T), STV-only infected (I_{STV}), uninfected apoptotic (T_A) and infected apoptotic cells (I_A) on the population level (Fig 3, Eqs (11)–(16)). We assumed that DIP-only infected cells are incapable to produce progeny virions due to missing genomic information and, therefore, neglected virus entry, replication and release on their intracellular level. On the other hand, co-infected cells release both progeny STVs and DIPs. In accordance with the description of STV-only infected cells (Eq (13)), co-infected cells were also represented as an age-segregated population $I_{CO}(t, \tau)$ (Eq (14)). Additionally, DIPs themselves (D) as well as their different binding and endocytosis states, i.e., attached DIPs (D_n^{Att}) and DIPs in endosomes (D^{En}), were implemented analogous to STV particles (Eqs (S59)–(S69)).

On the intracellular level the DIP entry and nuclear import, the replication of the DI segment and the release of progeny DIPs were considered. We modified the model structure slightly in accordance with specific assumptions used in the original multiscale model [27]. Therefore, we modified the STV and DIP release kinetics by including a maximum release rate of infected cells (Eqs (7)–(10)).

The fraction of infectious virions released (FIVR, F_{Par}) by infected cells was crucial in the development of the original multiscale model as it determined how rapidly an infection can spread when low MOI concentrations are used [27]. In the original model, the FIVR had to be adjusted for application for different infection conditions as it showed a reduced value for high MOI ($F_{Par} = 0.034$) compared to low MOI scenarios ($F_{Par} = 0.26$). We speculated that this

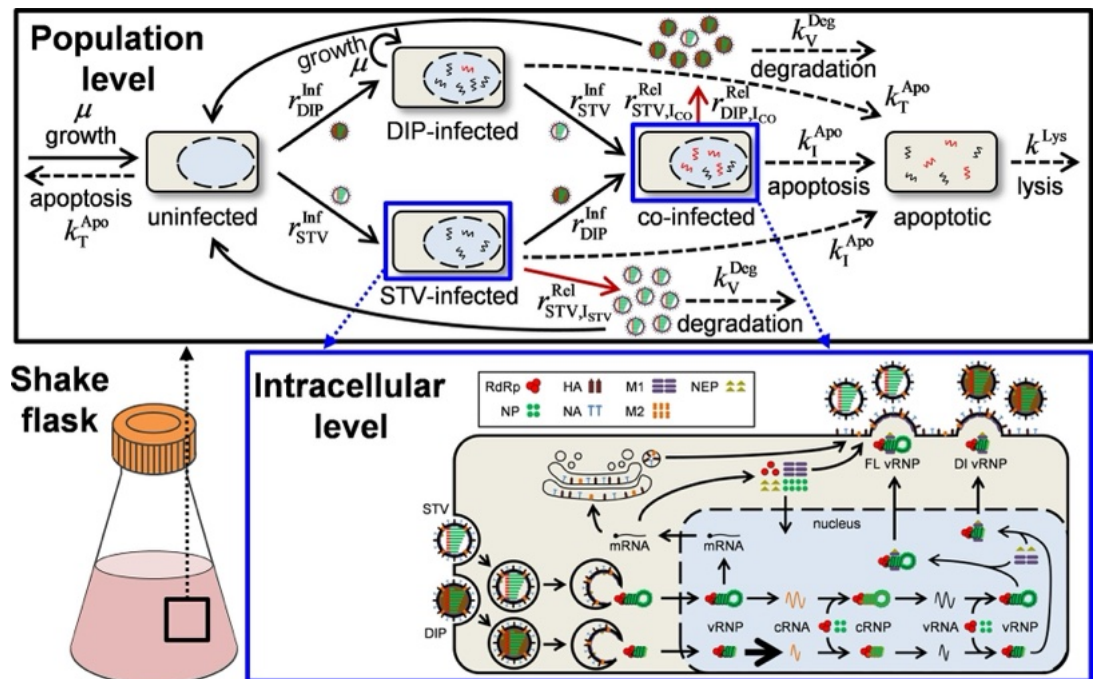


Fig 3. Schematic depiction of the multiscale STV and DIP co-infection model. (Top) The population level of infection describes growth and apoptosis of uninfected cells, their infection by either STVs or DIPs, the co-infection of STV-only infected and DIP-only infected cells, virus-induced apoptosis of all infected cells and the lysis of apoptotic cells. STVs are released from STV-only infected and co-infected cells, DIPs are only released from co-infected cells and both are cleared via virus degradation. (Bottom) Virus entry, nuclear import, viral RNA and protein synthesis, nuclear export and progeny virion release in STV-only infected cells and co-infected cells is simulated using the same intracellular model. Figure adapted from [29].

<https://doi.org/10.1371/journal.pcbi.1009357.g003>

variation was most likely induced by DIPs, which affect STV replication more strongly in high MOI conditions. For the development of our model of STV and DIP co-infection, we applied a single value for the FIVR, because the impact of DIP interference was implemented in the model itself.

To take into account the specific impact of MOI and MODIP conditions as well as their dynamics over time, we consider the current virus concentrations explicitly when calculating intracellular dynamics. In the original multiscale model, the initial conditions for the simulation of the intracellular level were based solely on the MOI at time of infection. For the model developed in this study, we use varying initial conditions, which are adapted to the current concentrations of STVs and DIPs in the cell culture to simulate intracellular dynamics. While this increases computational burden, it considers the dynamic changes of MOI and MODIP during infection.

The original multiscale model [27] relied on experimental data obtained from a different cellular system (adherent MDCK cells). The seed virus used in this study, however, was adapted to MDCKsus cells that show overall faster infection dynamics. Therefore, a re-evaluation of various process parameters that may have been affected by this change in the cell line was required. Additionally, the model was adapted to utilize infectious STV titer measurements obtained via plaque assay (PFU/mL) instead of the previously used tissue culture infection dose (TCID₅₀) assay [30] that typically results in higher titers.

The basic model of STV and DIP co-infection was calibrated to the intra- and extracellular data of 12 infection conditions (Figs 1 and 2). However, for most infection conditions, model simulations showed large deviations to the measured values (S2 Fig). Especially for low MOI conditions, large deviations for the observed intracellular properties were apparent (S11 Fig). Therefore, we were not able to obtain a set of parameters describing all measured dynamics simultaneously. Most likely, this is due to the inherent complexity of the interaction of STVs and DIPs during infection.

In sum, we established a mathematical multiscale model of STV and DIP co-infection by taking into account DIP replication and spreading on the intracellular and cell population level, respectively, to describe the infection dynamics observed in our experiments (Fig 1). However, estimating a set of parameters that describes all infection conditions could not be achieved with this basic model.

Extension of the basic model of STV and DIP co-infection

To address the observed discrepancies between our basic model and the measured dynamics during STV and DIP co-infection in animal cell culture, we implemented several targeted changes to the model equations.

First, we wanted to address the discrepancies observed between the levels of the three different viral mRNAs (Fig 4A). Although the overall dynamics of viral mRNA accumulation could be captured, the levels of FL and DI mRNA were overestimated, while the levels of S5 mRNA were underestimated. Previously, a clear distinction was postulated for segments encoding for proteins of the viral polymerase RdRp, i.e., segment 1 to 3, and the other segments 4 to 8 [31–33]. The polymerase segments seemed to accumulate to significantly lower levels. Therefore, we decided to implement this effect by a simple parameter f_M that reduces mRNA transcription in polymerase segments including the DI segment (Eq (2)). This clearly improved the description of our experimental data compared to the basic model and enabled the representation of the different levels of accumulated viral mRNA (Figs 4B and S5–S7).

Another significant deviation between the simulation of the basic model and the experimental data could be observed for the levels of DI and S5 mRNA in low MOI, high MODIP conditions L3 and L30 (Fig 4C). These two mRNAs still accumulated to considerable numbers, although nearly all infected cells should have been infected with a DIP but no STV as a helper virus. We assumed initially that cells just infected by DIPs do not produce any viral RNAs. Yet, previous IAV infection studies showed that the “primary transcription” of viral mRNAs by incoming parental vRNAs can lead to significant levels [34–36].

To implement this hypothesis, we used a modified version of the intracellular equation describing viral mRNA kinetics (Eq (1)) for DIP-only infected cells. In this simplified equation (Eq (3)), the negative feedback induced by RdRp is removed, because cells only infected by DI244 cannot synthesize functional PB2, which is essential for RdRp formation. Furthermore, the primary transcription now depends on the raw input of viral ribonucleoprotein (vRNP) templates per cell from the initial infection. Using this simple description, we can capture the level of viral mRNA accumulation in L30 closely (Figs 4D and S5–S7). For L3, the combination of primary transcription and the regular viral mRNA generation in co-infected cells also describes the initial plateau and the following increase.

Then, we focused on the vRNA dynamics, which were not represented completely (S11 Fig). Therefore, we fixed every model parameter except k_V^{Syn} , which describes the rate of vRNA synthesis, and calibrated the model to the experimental data. Thus, we identified that k_V^{Syn} was estimated to very similar values for low initial DIP concentrations, i.e., MODIP 0 and 10^{-3} , but showed a clear reduction when MODIP 3 and 30 were used for infection (Fig 4E). Specifically,

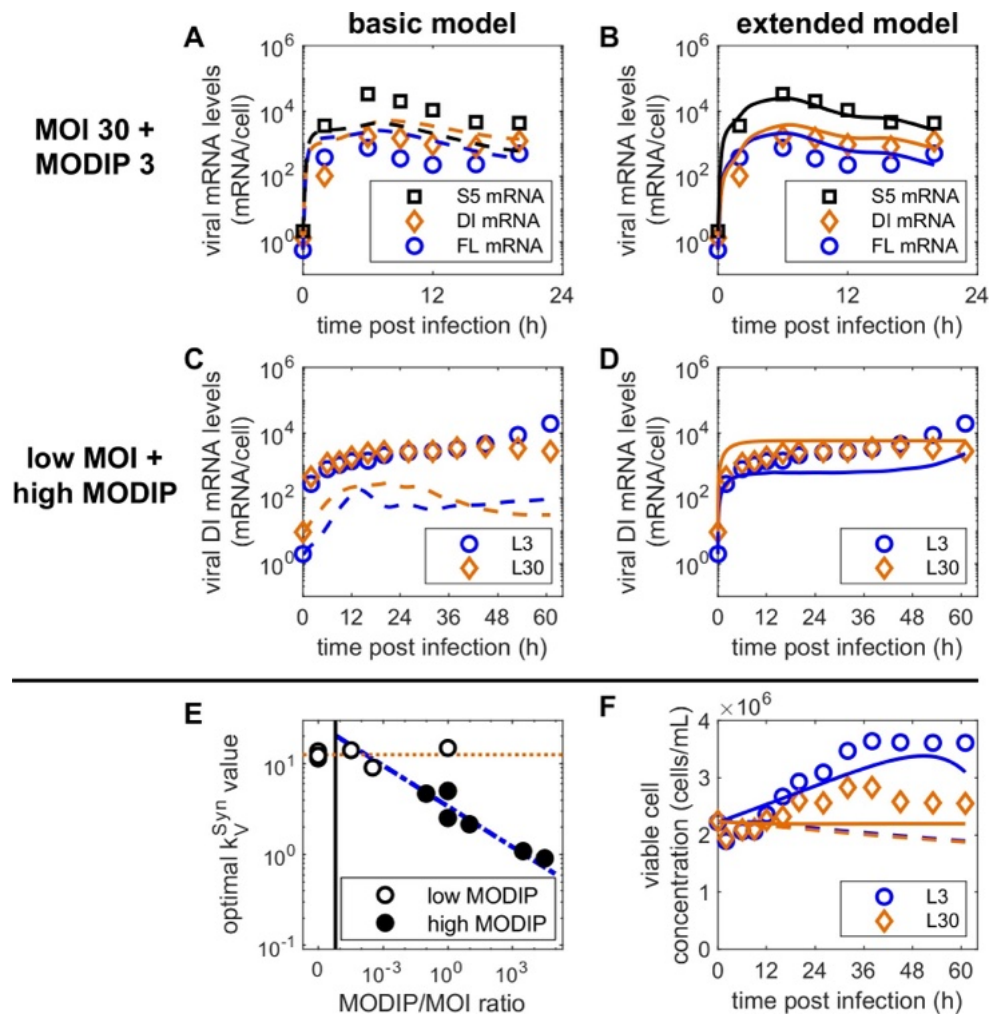


Fig 4. Adaptations of viral RNA synthesis and cell growth mechanisms of the basic model improve the description of observed infection dynamics. (A+C+F) Dashed lines show model simulations of the basic model fitted to experimental data, (B+D+F) solid lines depict simulations of the extended model calibrated to the same measurements. (A+B) Dynamics of viral mRNA for segment 5, full-length segment 1 and defective interfering segment 1 using MOI 30 and MODIP 3. (C+D) Accumulation of viral DI mRNA for conditions L3 (MOI 10⁻³ and MODIP 3) and L30 (MOI 10⁻³ and MODIP 30). (E) Estimated values for the parameter k_v^{Syn} describing vRNA synthesis for different infection scenarios based on the applied MODIP-to-MOI ratio. The orange dotted line depicts the average k_v^{Syn} value for low MODIP infections (empty circles) and the blue dash-dotted line represents the dependency of k_v^{Syn} on the MODIP-to-MOI ratio for high MODIP conditions (full circles). The vertical black line separates infections only using STVs from infections with MODIP > 0. (F) Dynamics of the viable cell concentration for low MOI, high MODIP conditions L3 and L30. Experimental data for all other infection conditions are shown in S1 and S3–S10 Figs.

<https://doi.org/10.1371/journal.pcbi.1009357.g004>

we observed a direct relation of the parameter value to the applied ratio of MODIP to MOI. Consequently, we introduced a dependency of the parameter k_v^{Syn} on the MODIP-to-MOI ratio used during infection (Eq (4)). Fortunately, this modification to the model did not only enable the description of STV and DIP co-infection for all conditions using a single set of parameters, but also improved the description of our experimental data considerably (S2–S10 Figs).

Additionally, we considered that the cell growth observed for low MOI, high MODIP conditions L3 and L30 seemed to be lower with increased MODIP (Figs 1B and S1). Therefore, we introduced a factor f_{μ} that reduces the specific cell growth rate during infection depending on the initial DIP concentration (Eq (19)). While the fraction of apoptotic cells did not increase when infected with a large quantity of DIPs (Fig 1C), they nevertheless showed an impaired cell growth. By using this additional factor, we were able to describe the differing growth dynamics for conditions L3 and L30 (Fig 4F).

Finally, the extended model of STV and DIP co-infection (Eqs (S1)-(S74)) was fitted to measurements from 12 different combinations of MOI and MODIP conditions (Table 1). Model simulations capture experimental data on the intracellular and cell population level closely (Figs 5 and S3-S10). Especially the effects of STV suppression for low MOI, high MODIP conditions L3 and L30 can be described well (Fig 5L). On the intracellular level, the balance between vRNA and viral mRNA can be captured for nearly all conditions. Furthermore, viral titers and cell population dynamics are described well. The extended model comprises 132 ODEs and 73 parameters (basic model: 130 ODEs, 68 parameters). For 8 out of 12 experiments fitted, the extended model showed lower values for the Akaike information criterion (S1 Table) and is, therefore, preferable [37]. This applies, in particular, for MOI 10^{-3} combined with a low MODIP, where the experimental data could not be described using the basic model (S11 Fig). Furthermore, for high MOI combined with high MODIP conditions the data is fitted better by the extended model. Overall, while the basic model displays a certain advantage to describe some infection conditions, the extended model is able to capture all conditions simultaneously.

In summary, we extended our basic model of STV and DIP co-infection by considering (I) segment-specific viral mRNA production, (II) the primary transcription of viral mRNA in DIP-only infected cells, (III) a reduction of vRNA synthesis depending on the applied

Table 1. Parameters estimated from the experimental data in S1 and S3-S10 Figs.

Parameter	Value	Confidence interval (95%) ^a
$F_{Par}(0)$ (-)	3.6×10^{-3}	$(0.3-48.9) \times 10^{-3}$
F_{Adv} (-)	0.32	0.07-0.84
F_M (-)	0.12	0.006-0.53
F_{μ} (-)	0.63	0.2-1
k_T^{Apo} (h^{-1})	1.18×10^{-2}	$(0.1-1.3) \times 10^{-2}$
k^{Fus} (h^{-1})	58.3	9.5-258.8
K_I (h^{-1})	0.27	0.05-0.35
k^{Lys} (h^{-1})	0.16	0.02-0.5
K_R (molecules)	7.8×10^3	$(1.1-30.9) \times 10^3$
k_{Red}^{Rel} (h^{-1})	4.1×10^{-4}	$(0.7-16.1) \times 10^{-4}$
k^{Rel} (virions $\cdot h^{-1}$)	6.15×10^3	$(0.9-19.3) \times 10^3$
K_V (h^{-1})	20.1	4.7-78.5
$K_{V,Red}$ (virions)	1.8	0.3-6.8
τ_{Apo} (h)	6.65	5.0-18.0
v_1 (-)	5.2	2.0-47.7
v_2 (-)	0.1	0.002-0.23 ^b

^a 95% confidence intervals were obtained from the Q0.025 and Q0.975 quantiles of 1250 bootstrap iterations [38].

^b Estimates reached lower bootstrap parameter bounds.

<https://doi.org/10.1371/journal.pcbi.1009357.t001>

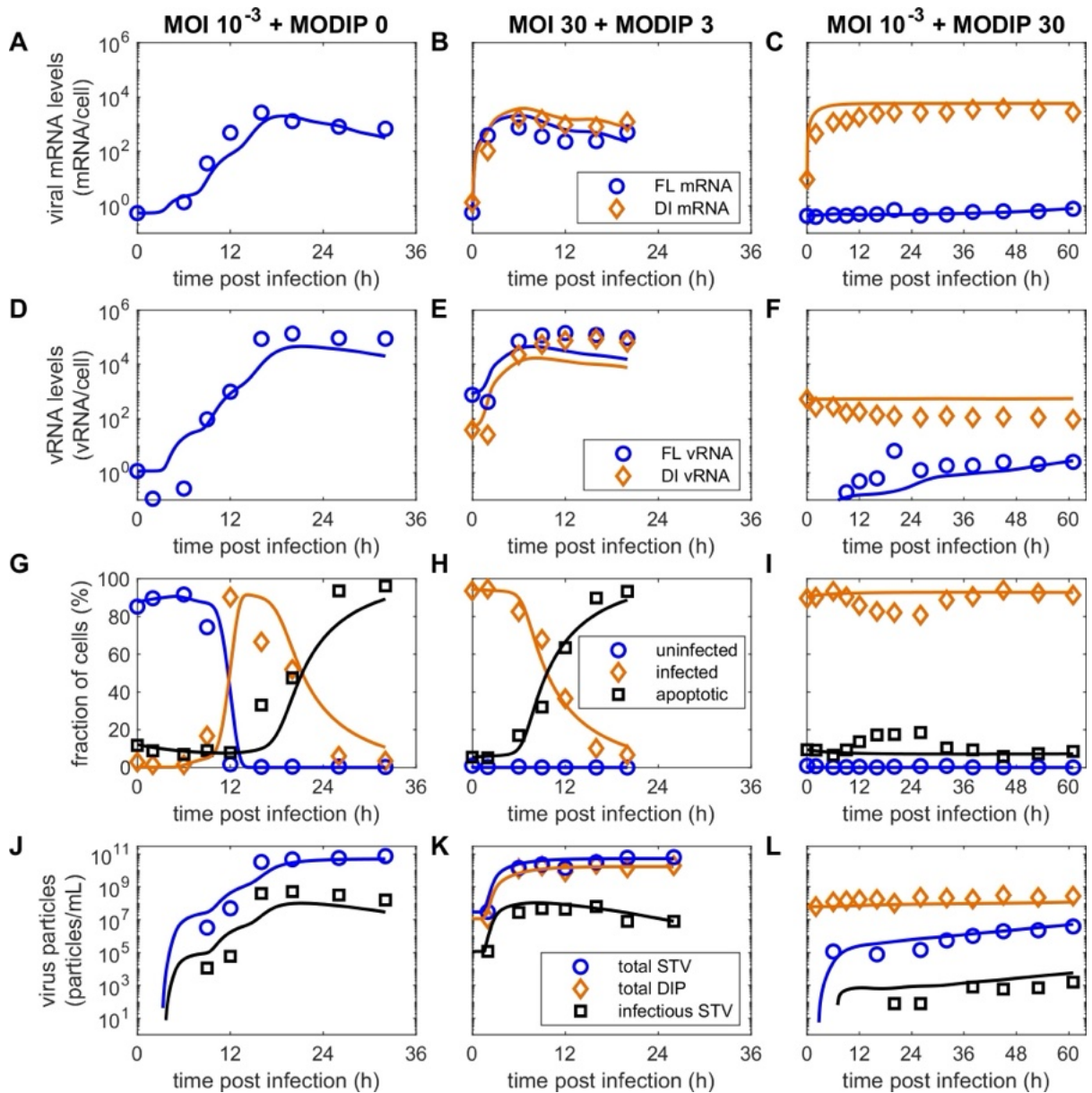


Fig 5. The extended multiscale model captures infection dynamics on the intracellular and cell population level for all measured infection conditions. Curves depict simulations of the extended model fitted to (A-C) cell-specific viral mRNA, (D-F) cell-specific vRNA, (G-I) cell population and (J-L) extracellular virus titers measured in MDCKsus cell cultures infected with different amounts of influenza A/PR/8/34 (H1N1) and defective interfering particles (DI244). Results for MOI 10^{-3} and MODIP 0 (first column), 30 and 3 (second column), and 10^{-3} and 30 (third column) are shown. The figures presenting cell population dynamics (G-I) show fits to uninfected non-apoptotic, infected non-apoptotic, as well as the sum of uninfected and infected apoptotic cells. The extended model is based on Rüdiger et al. [27] and Laske et al. [23], but additionally considers primary transcription of viral mRNA, segment-specific viral mRNA production, a reduced vRNA synthesis for high MODIP conditions and a DIP-induced reduction of cell growth. Simulation results for all other infection conditions are shown in S3–S10 Figs.

<https://doi.org/10.1371/journal.pcbi.1009357.g005>

MODIP-to-MOI ratio, and (IV) DIP-induced cell growth reduction. The extended model describes all examined infection conditions using a single set of parameters.

Model simulations predict the ratio of MODIP to MOI required to reduce infectious STV titers significantly

In a next step, the extended model was used to predict the optimal infection conditions for the successful suppression of STV propagation and the generation of large DIP quantities. These two scenarios are especially relevant regarding the production of DIPs for antiviral therapy and their potential application against STV infection.

Generally, high doses of DIPs are required for strong inhibition of STV infection (Fig 6A). However, also low doses of DIPs can show an inhibiting effect when the MOI is significantly lower than the MODIP. Our simulations predict that using ratios of MODIP to MOI of 1:1 enables a reduction of infectious STV titers by a factor of 10 compared to a DIP-free infection. To induce a strong reduction of infectious virus titers, i.e., by at least four orders of magnitude, a ratio of $10^4:1$ is required.

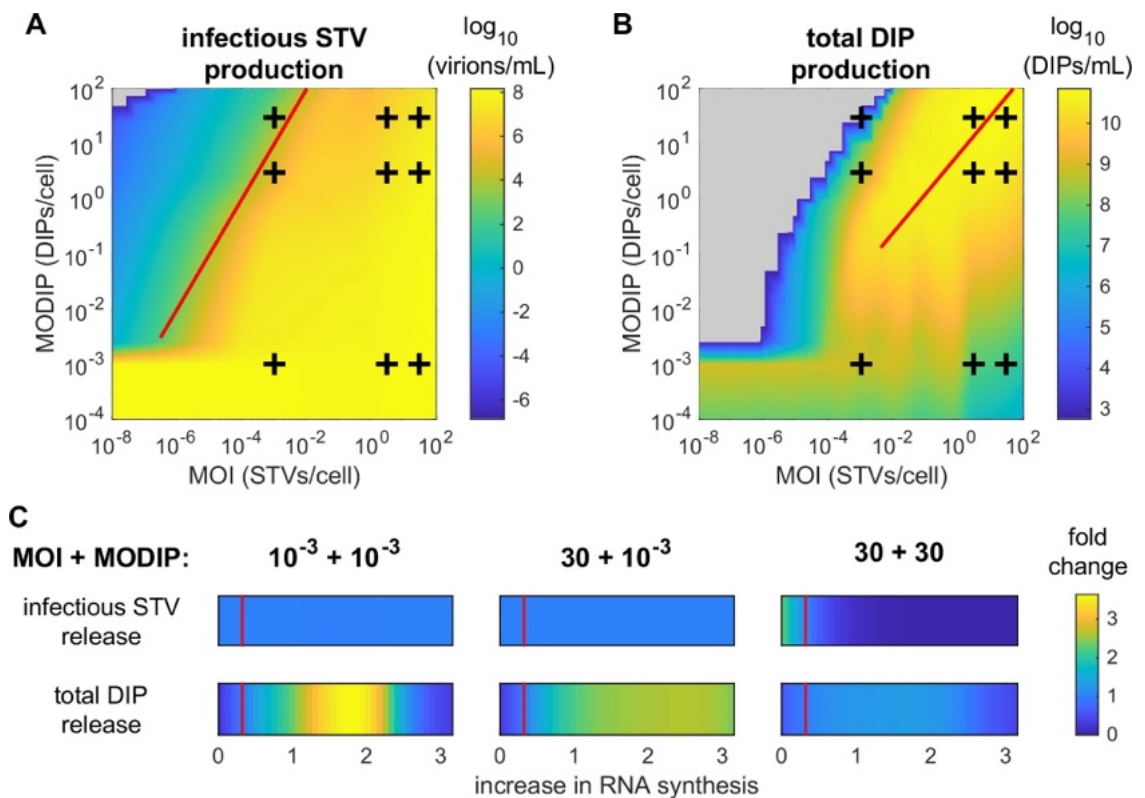


Fig 6. STV infection suppression and DIP production are strongly affected by the infection conditions. (A+B) Infections of MDCK_{SUS} cells were simulated with the extended model using MOIs and MODIPs in the range of 10^{-8} – 10^2 and 10^{-4} – 10^2 , respectively. The predicted concentrations of (A) infectious STVs and (B) total DIPs at 48 hpi determine the color of the heat map. The experimentally observed infection scenarios (+) are depicted. The solid red line indicates (A) an MODIP-to-MOI ratio of $10^4:1$ and (B) the optimal multiplicity ratios for DIP production. For the switch between regular and reduced vRNA synthesis for low and high initial DIP concentrations a threshold value of $F_{MODIP} = 10^{-3}$ was used. Grey areas indicate that no production of either STVs or DIPs did occur. (C) The predicted fold-change for yields of infectious STVs and total DIPs at 24 hpi depending on a reduction or increase in the replication advantage of DI cRNAs over their FL counterpart is presented. The parameter F_{Adv} was varied in the range of 0 to 1000% of its estimated value. The vertical red line indicates the replication advantage estimated during model calibration, i.e., $F_{Adv} = 0.32$.

<https://doi.org/10.1371/journal.pcbi.1009357.g006>

Our model predicts that the highest DIP amount can be produced using large quantities of both MOI and MODIP during infection (Fig 6B). However, this would require a lot of virus seed material for infection, rendering this option unattractive for large scale DIP manufacturing. Very good yields could also be achieved by lower virus input, i.e., an MOI of 0.01 and an MODIP of 0.25, which reaches over 50% of the predicted maximum DIP production using a 150 times lower seed virus concentrations for infection. In general, applying slightly higher DIP than STV concentrations during infection resulted in the best results for DIP production.

Furthermore, we investigated the effect of the intracellular parameter F_{Adv} , the replication advantage of DI cRNA over its FL counterpart, on infectious STV inhibition and DIP propagation. For an MODIP of 10^{-3} , no significant impact of this parameter on infectious STV titers (Fig 6C) could be determined. When combining high STV and DIP concentrations, an increase of the parameter F_{Adv} could lead to decreased infectious STV titers. A reduction of the replication advantage would in turn lead to improved STV production in this scenario. The release of DIPs could be improved when the parameter F_{Adv} is increased, however, after reaching an optimal value the model predicts a decrease for higher values (Fig 6C). For equimolar virus particle concentrations, i.e., when both MOI and MODIP are either 10^{-3} or 30, this optimal value regarding DIP production is $F_{Adv} = 1.8$. Using MOI 30 and MODIP 10^{-3} , $F_{Adv} = 2.5$ is predicted to be optimal for DIP production.

Taken together, the extended multiscale model of STV and DIP co-infection predicts that a MODIP-to-MOI ratio of about $10^4:1$ has to be used to restrict STV production and spreading significantly. Furthermore, an increase of the replication advantage of DI cRNAs could improve both the suppression of STV release and the production of DIPs.

Discussion

IAV infection is an intricate biological process in which the virus and the host cell interact on multiple levels. Typically, only STV replication is considered but the influence of DIPs present at time of infection or emerging continuously adds an additional layer of complexity to the underlying system. Current experimental and computational techniques facilitate a profound investigation of such processes. In this study, we conducted a series of STV and DIP co-infection experiments and developed a mathematical multiscale model, which captures the measured intra- and extracellular dynamics closely. We used this model to predict virus propagation for a wide range of infection conditions and estimated optimal settings for STV suppression and DIP production.

Our experiments with different MOIs and MODIPs show that STV production can be reduced significantly for specific infection conditions. Additionally, the fraction of apoptotic cells for low MOI and high MODIP scenarios remained at a very low level and cells survived for over 60 hpi. Interestingly, even the generation of over 10^3 viral mRNAs per cell and the putative translation of viral proteins in DIP-only infected cells did not lead to an augmented cell death response. Therefore, another trigger has to cause this cellular defense mechanism against infection. As discussed in [39], previous studies clearly suggested that the intracellular concentration of vRNA is a critical factor for apoptosis induction. Our experimental results support these findings and indicate that only the replication of large amounts of viral genomes in the nucleus, i.e., vRNA, will lead to virus-induced apoptosis in MDCKsus cells.

Furthermore, the wide range of applied infection conditions enables a comprehensive characterization of the effect of MOI and MODIP on virus production. In a recent study, Martin et al. [40] showed that the MOI strongly affects dynamics of STV replication in adherent MDCK cells. They observed higher virus titers and an earlier onset of virus particle release with increasing MOIs. While our experimental results of MDCKsus cell infections support a

faster release of both STVs and DIPs with higher MOIs (S3 Fig), we did not observe an overall improvement of virus titers using a larger STV input. The highest concentrations of infectious and total STV were achieved in low MOI conditions (S3A and S3B Fig). Similar results have been reported previously for adherent MDCK cells [41,42]. The maximum DIP titers in our experiments were found for an equimolar STV and DIP input (S3G and S3L Fig). This indicates that the ratio between MOI and MODIP might play a larger role than the total virus input for optimal DIP production conditions.

By measuring STV and DIP co-infection kinetics on the intracellular and cell population level for 12 different infection conditions, we obtained a multitude of experimental data, which provides a deep look into the interaction between these two viruses. However, to describe the dynamics of all observed infection conditions with a single set of parameters, we had to extend the initially developed basic multiscale model of STV and DIP co-infection by considering various steps of viral mRNA synthesis in more detail. Specifically, we introduced an internal regulation between segments, i.e., a lower transcription rate for segments encoding for RdRp-related proteins compared to structural proteins, as observed in previous replication studies [31–33]. Interestingly, for infection conditions using equal amounts of STVs and DIPs, the DI mRNA levels are exactly between FL and S5 mRNA levels (Fig 4B). This indicates that due to the replication advantage of DIPs their viral mRNA can overcome their STV counterpart, but not reach the levels of S5 and potentially other segments.

Furthermore, our experiments show that cells only infected by DIPs are able to produce high concentrations of viral mRNA for scenarios with very few co-infections, i.e., low MOI conditions. A baseline level of viral mRNA was detected, which correlates with a primary transcription mediated only by the infecting DIP. However, since segment 1 encoding for a subunit of RdRp is defective (DI244), the replication of vRNA and with that the amplification of the viral genome did not occur. A highly interesting aspect in this regard is, if cells are capable to perform vRNA replication in case that they are solely infected by DIPs with deletions in segments not encoding for RdRp. In a recent study, Phan et al. [33] investigated the levels of viral RNAs during infection for two different defective influenza viruses in A549 cells. One of them was lacking FL segment 2, which encodes for a subunit of RdRp, and showed an accumulation of viral mRNA but no replication of vRNA similar to our experimental results for condition L30. An infection with the second virus, which was lacking FL segment 4 encoding for the structural protein hemagglutinin, resulted in vRNA and viral mRNA levels similar to a wild-type infection. This indicates that the *de novo* synthesis of RdRp is critical for virus replication, while the genome-bound RdRp provided by virions entering during initial infection is sufficient for viral mRNA transcription.

The extended model was calibrated to measurements on the intracellular and cell population level simultaneously and was able to capture the observed dynamics closely (S3–S10 Figs). An important factor to capture all infection dynamics simultaneously was the introduction of an MODIP-to-MOI ratio-dependent rate of vRNA synthesis resulting in a reduction of vRNA levels in the presence of high DIP concentrations. Experimental data clearly demonstrated that higher MODIPs lead to a reduction of vRNA levels (S8 and S10 Figs). This interaction could describe a “self-interference” that has been reported previously [25,43] and was also predicted by mathematical modeling [23]. Specifically, due to high DIP levels, the viral replication is restricted and, thus, the amplification of both STVs and DIPs is affected. However, the exact mechanism of this effect and the factors involved in such a reduction cannot be clarified using a mathematical model. Our hypothesis regarding the underlying interactions is that viral replication is limited due to a strong competition for viral proteins caused by high DIP concentrations. If DI genomes occupy most RdRp, the transcription of FL mRNA could be reduced significantly and fewer functional viral proteins would be synthesized. This would ultimately

lead to a reduction of viral replication for both STVs and DIPs. To elucidate such interdependencies, further experiments focusing on the effect of high DIP levels on viral RNA replication are required.

In our model prediction, we showed that an MODIP-to-MOI ratio of at least 10^4 :1 is required to reduce STV titers by over four orders of magnitude and enable a suppression of STV infection in MDCKsus cells (Fig 6A). In line with our model prediction, recent infection experiments in mice using varying STV and DIP concentrations provided similar results [16,44]. In these studies, the complete protection induced by DIP administration was overcome when the MODIP-to-MOI ratio was reduced from 3.4×10^4 :1 to 3.4×10^3 :1 and from 4.4×10^4 :1 to 2.2×10^4 :1, respectively.

For infections in humans, about 0.6 to 3 infectious units were reported for successful airborne transmissions [44]. Extrapolating our findings from cell culture experiments, the administration of 3×10^4 DIPs, e.g. via nasal spray, could be sufficient to limit infection spread severely. However, as the preferred target tissues of IAV in humans do not correspond to a well-mixed cultivation system, the administration of higher doses is likely necessary. If we assume that the complete respiratory tract consists of about 4×10^8 cells [45] and that at least an MODIP of 10^{-1} should be achieved to induce strong infection suppression at such low MOIs, 4×10^7 DIPs would be required for a strong inhibiting effect. This amount of DIPs would also theoretically protect against up to 4000 infectious units, which is 1300 times the airborne infectious dose. However, if we consider an advanced infection already subject to strong virus replication, high MOI conditions could be induced. Assuming MOIs of 1 or above, at least 4×10^{12} DIPs would be necessary to achieve a strong inhibition according to our predicted MODIP-to-MOI ratio. Most likely, the application of such high DIP doses would not be reasonable due to safety concerns. Therefore, the use of DIP preparations shows the biggest promise shortly after infection or for prophylaxis. Previous *in vivo* experiments, which administered DIPs to mice at varying times before and after infection, support this hypothesis [28].

In addition, the innate immune response induced by DIPs was shown to play a major role for their therapeutic effect [46]. This concerns, in particular, their antiviral activity against influenza B virus [47], pneumovirus [48] and SARS-CoV-2 [49]. Obviously, DIPs could also improve the defense against STVs by other means than high DI RNA replication rates and competition for intracellular resources. To evaluate such effects, a different cell line should be used. While MDCK cells show a strong interferon response following STV infection, the subsequently produced myxovirus resistance protein 1 shows a lack of activity against the human IAV due to its canine origin [50]. Moreover, it was reported that the trypsin added to the cultivation medium to facilitate the IAV entry into the cells also degrades interferon [51].

Lastly, the model predicts that for the cell culture-based production of large amounts of DIPs relatively low amounts of virus material are sufficient for infection. As long as STVs and DIPs are provided in more or less equimolar concentrations and the initial MODIP is kept above 0.1, high levels of DIPs are obtained (Fig 6B). Generally, the predicted DIP production was highest when slightly more DIPs than STVs were provided. An additional factor that should be considered for the generation of higher DIP titers in co-infections is the replication advantage of DI over FL genomes [7]. By using an optimal factor for this advantage, which is implemented as an increased synthesis rate of DI cRNA over its FL counterpart in our model, up to 3.6 times more total DIPs could be produced in simulations (Fig 6C). Furthermore, model predictions suggest a more prominent replication advantage could also improve STV titer reduction in high virus concentration scenarios. A potential strategy to obtain DIPs with higher advantages over the STV is the selection of strongly accumulating DIPs from long-term continuous bioreactor cultivations [52]. Such DIPs consistently replicated at high levels indicating an increased advantage over their competition, i.e., other emerging DIPs.

Further model extension towards description of *in vivo* infections could support the exploration of strategies to prevent virus spreading in tissues and organs. To achieve such goals, the model would require an expansion to describe virus spread in the second or third spatial dimension. Additionally, the immune system, especially the innate immune response, would need to be considered explicitly. Finally, the multiscale model developed in this study is well calibrated to optimize cell culture-based DIP production and provides a solid basis for the analysis of DIP application strategies for prophylaxis and treatment of IAV infections.

Materials and methods

Model of the intracellular level

The description of the intracellular dynamics of STV and DIP co-infection is based on a model developed recently in our group [23]. Briefly, this model consists of a set of ordinary differential equations that represent virus entry, viral mRNA and protein synthesis, virus genome replication, packaging of viral genomes and progeny virion release for STVs and DIPs (Eqs (S1)-(S45)). To link this model with the model established on the cell population level and to capture the infection dynamics observed in cell cultures closely, we modified various equations in the original intracellular model. For the complete set of equations see [S1 Appendix](#).

First, we incorporated additional regulation mechanisms during viral mRNA synthesis, i.e., (I) the inhibition of mRNA transcription activity by RdRp as suggested in [53,54], and (II) a reduction of RdRp-related viral mRNA transcription as shown in [31–33]. To that end, we adjusted the viral mRNA dynamics to

$$\frac{dR_i^M}{dt} = f_M \frac{k_M^{Syn} V p_i^{Nuc}}{L_i \left(1 + \frac{P_{RdRp}}{K_R}\right)} - k_M^{Deg} R_i^M \tag{1}$$

with

$$f_M = \begin{cases} F_M, & i \in \{1, 2, 3, 9\}, \\ 1, & i \in \{4, \dots, 8\}, \end{cases} \tag{2}$$

with F_M as a reduction factor for RdRp-related viral mRNA synthesis, the concentration of unbound viral polymerase P_{RdRp} and K_R denoting the amount of free viral polymerase required to reduce mRNA transcription by 50%. Viral ribonucleoprotein $V p^{Nuc}$ is the template for transcription and L_i represents the length of the viral mRNA for segment i . The DI segment is referred to as segment $i = 9$. Viral mRNA synthesis and degradation rates are described by k_M^{Syn} and k_M^{Deg} , respectively.

In our experiments, we unexpectedly observed the significant accumulation of viral mRNA in cells only infected by DIPs for low MOI, high MODIP conditions L3 and L30 (Fig 4C). To describe these dynamics, we implemented primary viral transcription events, discussed in [34–36], for DIP-only infected cells on the population level. Therefore, we assume that the viral vRNAs entering the nucleus during initial infection enable the production of large amounts of viral mRNA. However, as we used a DIP with a deletion in a genome segment related to RdRp, the replication of vRNA cannot take place (Fig 2). We implemented the primary viral mRNA transcription similar to Eq (1) as

$$\frac{dR_{i,DIP}^M}{dt} = f_M \frac{k_M^{Syn}}{L_i} \frac{D(t_I)}{C_{Tot}(t_I)} - k_M^{Deg} R_{i,DIP}^M, \quad i = 2, \dots, 9 \tag{3}$$

where f_M is the reduction factor for RdRp-related viral mRNA synthesis (Eq (2)). Here, the

templates for transcription in an individual cell $\frac{D(t_I)}{C_{Tot}(t_I)}$ are the DIPs provided at the time of initial infection t_I . The inhibition of mRNA synthesis by RdRp is not applied in these equations, because we used a DIP containing a deletion in segment 1 encoding for PB2.

Additionally, we introduced a regulatory mechanism that affects vRNA synthesis depending on the MODIP-to-MOI ratio. Experimental results indicated a clear reduction of vRNA levels when high DIP concentrations were used for infection while no such effect could be detected when using low DIP concentrations (Fig 4E). Therefore, we modified the parameter k_V^{Syn} , which is used in Eq (S17) and describes the synthesis rate of vRNA, to

$$k_V^{Syn}(t_I) = \frac{K_V}{f_{D,V}(t_I)} \tag{4}$$

with a dependency on the MODIP-to-MOI ratio described by

$$f_{D,V}(t_I) = \begin{cases} v_1 \left(\frac{D(t_I)}{V(t_I)} \right)^{v_2}, & \frac{D(t_I)}{C_{Tot}(t_I)} \geq F_{MODIP}, \\ 1, & \frac{D(t_I)}{C_{Tot}(t_I)} < F_{MODIP}, \end{cases} f_{D,V}(t_I) \geq 1 \tag{5}$$

where K_V denotes the maximum vRNA synthesis rate and t_I describes the time point at which a cell got infected. The parameters v_1 and v_2 describe the effect of the MODIP-to-MOI ratio $\frac{D(t_I)}{V(t_I)}$ on the parameter $k_V^{Syn}(t_I)$. To calculate the MODIP-to-MOI ratio, the extracellular concentrations of STV ($V(t_I)$) and DIPs ($D(t_I)$) at the time of infection are utilized. If the MODIP is above a threshold value F_{MODIP} when a cell is infected, the vRNA synthesis is reduced. Based on our experiments, we determined this value to be in the range of 10^{-3} to 3. For model prediction in Fig 6 we assumed a value of $F_{MODIP} = 10^{-3}$.

Furthermore, the virus release kinetics were adjusted to bring them in line with the model of the population level [27] and to consider non-infectious virus particles. To enable the description of the infectious and total amount of virus particles, we introduced the FIVR $F_{Par}(\tau)$, which describes what percentage of released virions has the capacity to infect new cells. It is defined as

$$\frac{dF_{Par}}{dt} = -k_{Red}^{Rel} F_{Par} \tag{6}$$

with k_{Red}^{Rel} denoting the decrease of infectious virus particle release over the life span of an infected cell. In [27] the FIVR needed to be changed depending on the infection conditions decreasing with higher MOIs. Here, we apply the same FIVR for all 12 infection conditions. Using the FIVR, we adjust the equations for infectious virions released from either STV- or co-infected cells to

$$\frac{dV_m^{Rel}}{dt} = r_{STV,m}^{Rel}(\tau) = F_{Par} k^{Rel} \frac{V_{Cplx}^{Cyt}}{V_{Cplx}^{Cyt} + D_{Cplx}^{Cyt} + K_{V^{Rel}}} \prod_j \frac{P_j}{P_j + N_{P_j} K_{V^{Rel}}} \tag{7}$$

$$\frac{dD_m^{Rel}}{dt} = r_{DIP,m}^{Rel}(\tau) = F_{Par} k^{Rel} \frac{D_{Cplx}^{Cyt}}{V_{Cplx}^{Cyt} + D_{Cplx}^{Cyt} + K_{V^{Rel}}} \prod_j \frac{P_j}{P_j + N_{P_j} K_{V^{Rel}}} \tag{8}$$

and introduce the total virus particle release

$$\frac{dV_{m,Tot}^{Rel}}{dt} = r_{STV,m,Tot}^{Rel}(\tau) = k^{Rel} \frac{V_{Cplx}^{Cyt}}{V_{Cplx}^{Cyt} + D_{Cplx}^{Cyt} + K_{V^{Rel}}} \prod_j \frac{P_j}{P_j + N_{P_j} K_{V^{Rel}}} \tag{9}$$

$$\frac{dD_{m, \text{Tot}}^{\text{Rel}}}{dt} = r_{\text{DIP}, m, \text{Tot}}^{\text{Rel}}(\tau) = k^{\text{Rel}} \frac{D_{\text{Cplx}}^{\text{Cyt}}}{V_{\text{Cplx}}^{\text{Cyt}} + D_{\text{Cplx}}^{\text{Cyt}} + K_{V^{\text{Rel}}}} \prod_j \frac{P_j}{P_j + N_{P_j} K_{V^{\text{Rel}}}} \tag{10}$$

where $j \in \{\text{HA}, \text{NA}, \text{M1}, \text{M2}\}$, $m \in \{I_{\text{STV}}, I_{\text{CO}}\}$ represents the type of cells which release virus particles, and P_j denotes the available viral proteins. The amount of vRNP-complexes for either STVs ($V_{\text{Cplx}}^{\text{Cyt}}$) or DIPs ($D_{\text{Cplx}}^{\text{Cyt}}$) determines the release of progeny virions. The infection age of a cell, which represents the time that has passed since cells were infected, is described by τ . The parameters $K_{V^{\text{Rel}}}$ and N_{P_j} denote the amount of viral complexes necessary to achieve half the maximum virus release rate and the number of viral proteins required for the formation of virus particles, respectively. Therefore, the parameter k^{Rel} acts as a maximum value for the rate of virus release. Using these equations, we can describe the dynamics of infectious virions, total STVs and total DIPs released during the infection of an animal cell culture.

Model of the population level

The extracellular kinetics describing STV and DIP co-infection are based on a recently published multiscale model of IAV infection [27], which expanded conventional cell population dynamics by using a logistic infection age-dependent apoptosis rate. In short, a set of ordinary differential equation is coupled with integro-partial differential equations to describe infection dynamics on the cell population level. This model describes (I) growth, infection and apoptosis of uninfected cells, (II) infection-induced apoptosis of infected cells, and (III) attachment, endocytosis, production and degradation of virus particles (Eqs (S47)-(S74)). To describe the interactions of DIPs with the STV dynamics, we expanded this model by introducing DIP-related cell and virus populations. For a detailed description of the population dynamics, the reader is referred to [S1 Appendix](#).

Based on the original model, ODEs describing the time course of uninfected target cells T , STV-only infected cells I_{STV} and their apoptotic forms T_A and I_A , respectively, were expanded to handle DIP-only infected I_{DIP} and co-infected cells I_{CO}

$$\frac{dT}{dt} = \mu T - r_{\text{STV}}^{\text{Inf}} T - r_{\text{DIP}}^{\text{Inf}} T - k_T^{\text{Apo}} T \tag{11}$$

$$\frac{dI_{\text{DIP}}}{dt} = r_{\text{DIP}}^{\text{Inf}} T + \mu I_{\text{DIP}} - r_{\text{STV}}^{\text{Inf}} I_{\text{DIP}} - k_T^{\text{Apo}} I_{\text{DIP}} \tag{12}$$

$$\frac{\partial I_{\text{STV}}}{\partial t} + \frac{\partial I_{\text{STV}}}{\partial \tau} = -[r_{\text{DIP}}^{\text{Inf}} + k_I^{\text{Apo}}(\tau)] I_{\text{STV}}(t, \tau) \tag{13}$$

$$\frac{\partial I_{\text{CO}}}{\partial t} + \frac{\partial I_{\text{CO}}}{\partial \tau} = -k_I^{\text{Apo}}(\tau) I_{\text{CO}}(t, \tau) \tag{14}$$

$$\frac{dT_A}{dt} = k_T^{\text{Apo}} T - r_{\text{STV}}^{\text{Inf}} T_A - r_{\text{DIP}}^{\text{Inf}} T_A - k^{\text{Lys}} T_A \tag{15}$$

$$\frac{dI_A}{dt} = \int_0^\infty k_I^{\text{Apo}}(\tau) [I_{\text{STV}}(t, \tau) + I_{\text{CO}}(t, \tau)] d\tau + k_T^{\text{Apo}} I_{\text{DIP}} + r_{\text{STV}}^{\text{Inf}} T_A + r_{\text{DIP}}^{\text{Inf}} T_A - k^{\text{Lys}} I_A \tag{16}$$

$$C_{\text{Tot}}(t) = T(t) + T_A(t) + I_{\text{DIP}}(t) + \int_0^\infty I_{\text{STV}}(t, \tau) d\tau + \int_0^\infty I_{\text{CO}}(t, \tau) d\tau + I_A(t) \tag{17}$$

with

$$\mu(t) = \left(f_\mu \frac{\mu_{\text{Max}}}{T_{\text{Max}}} [T_{\text{Max}} - C_{\text{Tot}}(t)] \right)_+ \tag{18}$$

and

$$f_\mu = \begin{cases} F_\mu, [V(0) + D(0)]C_{\text{Tot}}(0)^{-1} \geq 6, \\ 1, [V(0) + D(0)]C_{\text{Tot}}(0)^{-1} < 6, \end{cases} \tag{19}$$

Uninfected and DIP-only infected cells get apoptotic with the same rate k_T^{Apo} and grow with the specific rate μ , with a maximum value μ_{Max} . This specific rate is affected by very high virus concentrations during infection via the factor F_μ . While suspension cell growth is generally not restricted severely by the available space in a vessel, we utilized the maximum cell concentration $T_{\text{Max}} = 10^7$ cells/mL measured in our experiments as an upper limit. The infection of cells by STVs and DIPs is described by the rates $r_{\text{STV}}^{\text{Inf}}$ and $r_{\text{DIP}}^{\text{Inf}}$, respectively. Target cells and their apoptotic counterpart can get infected by either STVs or DIPs, however, re-infection of STV- and DIP-only infected cells is only possible by the opposing virus particle. Additionally, STV-only infected cells are protected from re-infection after reaching an infection age of 3 h to consider superinfection exclusion, which is mediated by neuraminidase [55,56]. Following the implementations in [29] and [27], the infection age τ of STV- and co-infected cells is considered and both populations undergo apoptosis with an infection age-dependent apoptosis rate $k_I^{\text{Apo}}(\tau)$. Cell lysis of apoptotic target and apoptotic infected cells is described by the rate k^{Lys} .

Furthermore, we added DIPs on the population level following the description of STVs and defined them as

$$\frac{dD}{dt} = \int_0^\infty [r_{\text{DIP,STV}}^{\text{Rel}}(\tau)I_{\text{STV}}(t, \tau) + r_{\text{DIP,ICO}}^{\text{Rel}}(\tau)I_{\text{CO}}(t, \tau)]d\tau - k_D^{\text{Deg}}D + \sum_n (k_n^{\text{Dis}}D_n^{\text{Att}} - k_{cn}^{\text{Att}}B_n^D D) \tag{20}$$

with $r_{\text{DIP,m}}^{\text{Rel}}(\tau)$ as the age-dependent DIP release rate of $m \in \{\text{STV}, \text{ICO}\}$ cells. The age-segregated cell populations $I_{\text{STV}}(t, \tau)$ and $I_{\text{ICO}}(t, \tau)$ can both produce DIPs and degradation occurs with a rate of k_D^{Deg} . The dissociation and association of DIPs from cells is described by k_n^{Dis} and k_n^{Att} with $n \in \{\text{hi}, \text{lo}\}$, respectively. B_n^D refers to the amount of virus binding sites on the cell surface to which DIPs can attach. DIPs attached to cells (D_n^{Att}) and inside cellular endosomes (D^{En}) were implemented analogous to the corresponding STV versions (Eqs (S66)-(S69)).

Simulation approach and parameter estimation

Generally, model simulation was performed based on previously published multiscale models [27,29]. However, the intracellular and population model are not decoupled anymore, because we assume that the extracellular level has an impact on intracellular events. As before, the intracellular and population models are linked by the virus release rates, i.e., $r_{\text{STV}}^{\text{Rel}}$ and $r_{\text{DIP}}^{\text{Rel}}$. These rates are calculated on the intracellular level depending on the infection age τ and determine virus release on the population level (Eqs (S42)-(S45)). In addition, we assume that the current number of STVs ($V(t)$, $V_n^{\text{Att}}(t)$, $V^{\text{En}}(t)$) and DIPs ($D(t)$, $D_n^{\text{Att}}(t)$, $D^{\text{En}}(t)$) on the extracellular level dictates the initial conditions for cells infected at this specific time t . In contrast to the previous approaches, we did not utilize a reduced intracellular model and simulated the intracellular model directly based on the state of the population level. This change increased computational burden considerably, however, it also enables the representation of infections with highly dynamic virus concentrations.

The intracellular model (Eqs (S1)-(S45)) was solved numerically using the CVODE routine from SUNDIALS [57] on a Linux-based system. The Systems Biology Toolbox 2 [58] was employed in MATLAB (version 9.2.0.556344, R2017a) to process model files and experimental data. The population model (Eqs (S47)-(S74)) and Eq (S46) were calculated using Euler's method with a step size $dt = 0.1$ h. In case this step size lead to rapidly oscillating behavior, e.g. when the concentration of uninfected target cells reached values close to zero, it was reduced to $dt = 0.02$ h. The integrals in Eqs (S55)-(S56), (S59)-(S60), (S62), (S64)-(S65), (S71) and (S73) were calculated by substituting Eq (S51) for $I_{STV}(t, \tau)$, Eq (S52) for $I_{CO}(t, \tau)$ and applying the rectangle rule to approximate results.

As in [27], we assume that cells are infected in the moment a virus genome enters their cytoplasm and that at least one complete STV or DIP is required for infection. Therefore, the initial values for $V^{Cyt}(0)$ and $D^{Cyt}(0)$, which describe the amount of STVs and DIPs in the cytoplasm before nuclear import, are set to 1 for simulation of the intracellular model. The other initial conditions, i.e., viral species $V^{Ex}(0)$, $V_n^{Att}(0)$, $V^{En}(0)$, $D^{Ex}(0)$, $D_n^{Att}(0)$ and $D^{En}(0)$, are taken from the current state of the population model. For simulation of cells only infected by STVs, all DIP-related initial values are set to 0.

Furthermore, we assume that the minimum release from an infected cell is one complete virus particle. To that end, all values in the infection age-dependent release rates $r_{STV}^{Rel}(\tau)$, $r_{STV,Tot}^{Rel}(\tau)$, $r_{DIP}^{Rel}(\tau)$, and $r_{DIP,Tot}^{Rel}(\tau)$ that are below 1 are set to 0. This introduces a certain delay between the infection of cells and the subsequent release of virions, which prevents an unreasonably rapid virus spread in short time intervals, especially for low MOI conditions.

For parameter calibration, the intracellular and the population model were fitted simultaneously to experimental data from all 12 infection conditions (S1 and S3–S10 Figs). On the intracellular level, we obtained vRNA and viral mRNA measurements. Cell population dynamics and viral titers for infectious STVs, total STVs and total DIPs were determined on the extracellular level. To estimate a single set of parameters, which enables the description of all infection conditions at the same time, we used the evolutionary optimization algorithm CMA-ES [59]. During model calibration, intermediate estimation results were assessed by normalizing errors to their respective maximum measurement value. Then, the SSRs determined on the intracellular and population level were divided by the corresponding number of data points and added to evaluate the quality of fits. For simulated values of vRNAs and viral mRNAs, the first measured data point was added as an offset to accommodate for a background signal in the real-time RT-qPCR analysis.

The final parameter values are presented in S2 Table and S3 Table. An overview of the local sensitivity for all model parameters, which was calculated based on Heldt et al. [60], is provided in S4 Table. The confidence intervals shown in Table 1 were calculated using a bootstrapping method [38] considering a standard deviation of 55% for qPCR measurements and a standard deviation of 40% for cell population data based on experiments from [61]. Additionally, an error of 40% for the infectious STV titer was applied based on test runs using the PFU assay.

Model prediction

For the prediction of infectious STV and total DIP release for various infection conditions (Fig 6), we simulated the extended multiscale model using the parameters calibrated to our experimental data. The amount of initially available STVs and DIPs on the population level was adjusted to the intended values by multiplying the corresponding MOI and MODIP with a viable cell concentration of $T(0) = 2.2 \times 10^6$ cells/mL. The values in Fig 6 show the maximum concentration of progeny STVs and DIPs on the population level until 48 hpi.

To evaluate the impact of the replication advantage of DI cRNA on STV and DIP release, we simulated the multiscale model using adjusted parameter values (Fig 6C). Therefore, we varied the parameter F_{Adv} between 0 and 1000% of its estimated value and performed model

simulations for different MOI and MODIP conditions. The fold-change shown in Fig 6C was calculated by comparing the resulting virus titers at 24 hpi with simulation outcomes obtained by using the unmodified parameter $F_{Adv} = 0.32$.

Cells and viruses

An adherent Madin-Darby Canine Kidney (MDCK) cell line (ECACC, No. 84121903), adapted first to growth in suspension [62] and subsequently to growth in the chemically defined medium Xeno [63], in the following referred to as MDCKsus cells, was used. The medium was supplemented with 8 mM glutamine. Cells were cultivated in shake flasks (125 mL baffled Erlenmeyer Flask, Thermo Fisher Scientific, 4116-0125) at a working volume of 50 mL in an orbital shaker (Multitron Pro, Infors HT; 50 mm shaking orbit) at 185 rpm, 37°C, 5% CO₂. The parental adherent MDCK cells (“MDCKadh”, ECACC, No. 84121903) used for determination of infectious STV titers (PFU/mL, see below) were cultured in Glasgow minimum essential medium (GMEM, Thermo Fisher Scientific, #221000093) containing 1% peptone and 10% fetal bovine serum at 37°C and 5% CO₂.

For STV infection, an influenza A virus strain A/PR/8/34 of subtype H1N1 (PR8) (provided by Robert Koch Institute, Berlin, Germany), adapted to MDCKsus cells and Xeno medium [63] was used. Infectious virus titer (0.8×10^9 TCID₅₀/mL) of the seed virus was quantified via TCID₅₀ assay [30]. Generation of purely clonal DI244 was conducted according to [64] and production as specified in [15]. “Active DIP titer” of the seed virus (1.5×10^8 PFU/mL) was determined as described in [15]. Depletion of DIPs in the seed virus was controlled by segment-specific PCR according to [20,65].

Infection

MDCKsus cells were infected with different STV doses (corresponding to MOIs of 10^{-3} , 3, 30) and DI244 doses (MODIPs of 0, 10^{-3} , 3, 30), as shown in Fig 1. We calculated the MOIs based on the TCID₅₀ titer, while MODIPs were calculated based on the “active DIP titer” as described in [15]. For infection, we added trypsin at a final activity of 20 U/mL. After inoculation with virus, cells were washed at 0.75 hpi with pre-warmed phosphate-buffered saline (PBS) (300×g, 5 min, room temperature), and cells were provided with fresh infection medium containing trypsin for subsequent cultivation.

Sampling for analytics

For sampling at indicated time points post infection, viable cell concentration was measured via a cell counter (Vi-Cell XR, Beckman coulter, #731050). Next, 1×10^6 cells were centrifuged (300×g, 5 min, 4°C), and supernatant was discarded. Cell pellets were lysed with 350 μL lysis buffer “RA1” (from “NucleoSpin RNA” kit, Macherey-Nagel, 740955) supplemented with 1% (v/v) β-mercaptoethanol and stored at -80°C until real-time RT-qPCR analytics. In addition, aliquots of cell suspensions were centrifuged (300×g, 5 min, 4°C) and supernatants were stored at -80°C until virus titration or real-time RT qPCR analytics. The remaining cell pellet was fixed with paraformaldehyde (1% (w/v)), and processed according to a previously published protocol for cell sampling required for imaging flow cytometry analysis [61,65].

Plaque assay

Quantification of the “active DIP titer” of the DI244 seed virus by plaque assay followed an established protocol [15]. Furthermore, the plaque assay using MDCKadh cells was applied to determine the course of STV titers.

Real-time RT-qPCR

vRNAs in supernatants were isolated using the “NucleoSpin RNA virus” kit (Macherey-Nagel, 740956), and vRNAs in cell pellets utilizing the “NucleoSpin RNA” kit (Macherey-Nagel, 740955) according to the manufacturers’ instructions. A previously published method [61,65,66] was used for the absolute quantification of vRNAs and mRNAs using real-time reverse transcription qPCR (real-time RT-qPCR). Primers for reference standard generation and specific detection of FL segment 1 and DI244 vRNA [67], and S5 vRNA and viral mRNA [61,65] were used. Primers of FL segment 1 and DI244 vRNA and viral mRNA are listed in S5 Table and S6 Table.

Imaging flow cytometry

An established protocol for imaging flow cytometric analysis of cells was utilized [61,65]. In brief, cells were stained for NP using a monoclonal mouse anti-NP mAb61A5 (provided by Fumitaka Momose) at a dilution of 1:100 and a secondary antibody Alexa Fluor 647-conjugated polyclonal goat anti-mouse (Thermo Fisher, #A21235) at a dilution of 1:500. DAPI was added for nuclear staining. Acquisition of 10,000 single cells for each sample was performed using the ImageStream X Mark II (Luminex). For data analysis, IDEAS software was utilized. vRNP positive cells (infected cells) were determined based on a gate set on mock infected cells (1% threshold). Apoptotic cells were detected based on image analysis, evaluating chromatin condensation, nuclear fragmentation and cell shrinkage [61,65,68]. Furthermore, we determined fractions of the whole cell population that were (I) infected and apoptotic, (II) infected and non-apoptotic, (III) non-infected and apoptotic, and (IV) non-infected and non-apoptotic [27,29].

Supporting information

S1 Appendix. Full list of equations for the multiscale model.
(DOCX)

S1 Data. Experimental data used for model calibration.
(XLSX)

S1 Fig. Cell concentration and fraction of apoptotic cells for all MOI and MODIP conditions. Measurements of (A-C) viable cell concentration and (D-F) the fraction of apoptotic cells for infections with MOI 10^{-3} , 3 and 30 using different MODIPs.
(TIF)

S2 Fig. Model extension significantly improves description of experimental measurements. The sum of squared residuals for each individual measured property is depicted. Logarithmic errors of each variable were normalized to the respective maximum measurement value. The (A) basic model and the (B) extended model were calibrated to a wide range of experimental data. Measured properties include vRNA and mRNA of full-length (FL) segment 1, defective-interfering (DI) segment 1 and segment 5 (S5), the concentration of uninfected, infected and apoptotic cells, total and standard virus (STV) titers as well as DIP titers.
(TIF)

S3 Fig. Experimental data and model simulations for virus titers. Model fits to measurements of the infectious STV titer, the total amount of STVs and the total amount of DIPs for MDCKsus infections with MOI 10^{-3} , 3 and 30 using different MODIPs.
(TIF)

S4 Fig. Experimental data and model simulations for cell populations. Model fits to measurements of the fraction of uninfected, uninfected and apoptotic, infected, infected and apoptotic cells for MDCKsus infections with MOI 10^{-3} , 3 and 30 using different MODIPs. (TIF)

S5 Fig. Experimental data and model simulations for FL mRNA dynamics. Model fits to measurements of the intracellular levels of FL mRNA for MDCKsus infections with MOI 10^{-3} , 3 and 30 using different MODIPs. (TIF)

S6 Fig. Experimental data and model simulations for DI mRNA dynamics. Model fits to measurements of the intracellular levels of DI mRNA for MDCKsus infections with MOI 10^{-3} , 3 and 30 using different MODIPs. (TIF)

S7 Fig. Experimental data and model simulations for segment 5 mRNA dynamics. Model fits to measurements of the intracellular levels of segment 5 mRNA for MDCKsus infections with MOI 10^{-3} , 3 and 30 using different MODIPs. (TIF)

S8 Fig. Experimental data and model simulations for FL vRNA dynamics. Model fits to measurements of the intracellular levels of FL vRNA for MDCKsus infections with MOI 10^{-3} , 3 and 30 using different MODIPs. (TIF)

S9 Fig. Experimental data and model simulations for DI vRNA dynamics. Model fits to measurements of the intracellular levels of DI vRNA for MDCKsus infections with MOI 10^{-3} , 3 and 30 using different MODIPs. (TIF)

S10 Fig. Experimental data and model simulations for segment 5 vRNA dynamics. Model fits to measurements of the intracellular levels of segment 5 vRNA for MDCKsus infections with MOI 10^{-3} , 3 and 30 using different MODIPs. (TIF)

S11 Fig. The basic model fails to describe virus replication and propagation dynamics for all infection conditions. Curves represent model simulations of the basic model calibrated to (A-C) cell-specific vRNA, (D-F) cell-specific viral mRNA, (G-I) cell population and (J-L) virus titer data measured in MDCK suspension cell cultures infected with different amounts of influenza A/PR/8/34 (H1N1) and defective interfering particles (DI244). Results from MOIs and MODIPs of 10^{-3} and 0 (first column), 30 and 3 (second column), 10^{-3} and 30 (third column) are shown. The basic model describes IAV and DIP replication and propagation based on Rüdiger et al. [5] and Laske et al. [1] without considering additional model adaptations. (TIF)

S1 Table. Evaluation of the model fits performed for the basic and the extended model for individual infection conditions. (DOCX)

S2 Table. Parameters of the intracellular model. (DOCX)

S3 Table. Parameters of the cell population model. (DOCX)

S4 Table. Sensitivity of intracellular and cell population model parameters.
(DOCX)

S5 Table. Primers used for real-time RT qPCR of mRNA.
(DOCX)

S6 Table. Primers used for reference standard generation of mRNA.
(DOCX)

Acknowledgments

We thank Nancy Wynserski and Claudia Best for excellent technical assistance and Tanja Laske for critical comments on the manuscript.

Author Contributions

Conceptualization: Daniel Rüdiger, Lars Pelz, Sascha Y. Kupke, Udo Reichl.

Data curation: Lars Pelz, Marc D. Hein.

Formal analysis: Daniel Rüdiger, Lars Pelz, Marc D. Hein.

Funding acquisition: Udo Reichl.

Investigation: Daniel Rüdiger, Lars Pelz, Marc D. Hein.

Methodology: Daniel Rüdiger, Lars Pelz, Marc D. Hein, Sascha Y. Kupke.

Project administration: Sascha Y. Kupke, Udo Reichl.

Software: Daniel Rüdiger.

Supervision: Sascha Y. Kupke, Udo Reichl.

Validation: Daniel Rüdiger, Lars Pelz, Sascha Y. Kupke.

Visualization: Daniel Rüdiger, Lars Pelz.

Writing – original draft: Daniel Rüdiger, Lars Pelz, Sascha Y. Kupke.

Writing – review & editing: Daniel Rüdiger, Lars Pelz, Marc D. Hein, Sascha Y. Kupke, Udo Reichl.

References

1. OECD. Global financial markets policy responses to COVID-19. 2020 March [cited 28 January 2021]. Available from: <https://www.oecd.org/coronavirus/policy-responses/global-financial-markets-policy-responses-to-covid-19-2d98c7e0/>
2. Carrat F, Flahault A. Influenza vaccine: the challenge of antigenic drift. *Vaccine*. 2007; 25(39–40):6852–6862. <https://doi.org/10.1016/j.vaccine.2007.07.027> PMID: 17719149
3. Webster RG, Govorkova EA. Continuing challenges in influenza. *Annals of the New York Academy of Sciences*. 2014; 1323(1):115–139. <https://doi.org/10.1111/nyas.12462> PMID: 24891213
4. Lackenby A, Thompson CI, Democratis J. The potential impact of neuraminidase inhibitor resistant influenza. *Current Opinion in Infectious Diseases*. 2008; 21(6):626–638. <https://doi.org/10.1097/QCO.0b013e3283199797> PMID: 18978531
5. Imai M, Yamashita M, Sakai-Tagawa Y, Iwatsuki-Horimoto K, Kiso M, Murakami J. Influenza A variants with reduced susceptibility to baloxavir isolated from Japanese patients are fit and transmit through respiratory droplets. *Nature Microbiology*. 2020; 5(1):27–33. <https://doi.org/10.1038/s41564-019-0609-0> PMID: 31768027

6. Huang AS, Baltimore D. Defective viral particles and viral disease processes. *Nature*. 1970; 226(5243):325–327. <https://doi.org/10.1038/226325a0> PMID: 5439728
7. Marriott AC, Dimmock NJ. Defective interfering viruses and their potential as antiviral agents. *Reviews in Medical Virology*. 2010; 20(1):51–62. <https://doi.org/10.1002/rmv.641> PMID: 20041441
8. Dimmock NJ, Easton AJ. Defective interfering influenza virus RNAs: time to reevaluate their clinical potential as broad-spectrum antivirals? *Journal of Virology*. 2014; 88(10):5217–5227 <https://doi.org/10.1128/JVI.03193-13> PMID: 24574404
9. Yang Y, Lyu T, Zhou R, He X, Ye K, Xie Q. The Antiviral and Antitumor Effects of Defective Interfering Particles/Genomes and Their Mechanisms. *Frontiers in Microbiology*. 2019; 10:1852. <https://doi.org/10.3389/fmicb.2019.01852> PMID: 31447826
10. Kupke SY, Ly LH, Börno ST, Ruff A, Timmermann B, Vingron M, et al. Single-Cell Analysis Uncovers a Vast Diversity in Intracellular Viral Defective Interfering RNA Content Affecting the Large Cell-to-Cell Heterogeneity in Influenza A Virus Replication. *Viruses*. 2020; 12(1):71. <https://doi.org/10.3390/v12010071> PMID: 31936115
11. Nayak DP, Chambers TM, Akkina RK. Defective-interfering (DI) RNAs of influenza viruses: origin, structure, expression, and interference. *Current Topics in Microbiology and Immunology*. 1985; 114:103–151. https://doi.org/10.1007/978-3-642-70227-3_3 PMID: 3888540
12. Duhaut SD, McCauley JW. Defective RNAs inhibit the assembly of influenza virus genome segments in a segment-specific manner. *Virology*. 1996; 216(2):326–337. <https://doi.org/10.1006/viro.1996.0068> PMID: 8607262
13. Vignuzzi M, López CB. Defective viral genomes are key drivers of the virus-host interaction. *Nat Microbiol*. 2019; 4(7):1075–1087. <https://doi.org/10.1038/s41564-019-0465-y> PMID: 31160826
14. Dimmock NJ, Dove BK, Meng B, Scott PD, Taylor I, Cheung L. Comparison of the protection of ferrets against pandemic 2009 influenza A virus (H1N1) by 244 DI influenza virus and oseltamivir. *Antiviral Research*. 2012; 96(3):376–385. <https://doi.org/10.1016/j.antiviral.2012.09.017> PMID: 23041142
15. Hein MD, Arora P, Marichal-Gallardo P, Winkler M, Genzel Y, Pöhlmann S, et al. Cell culture-based production and in vivo characterization of purely clonal defective interfering influenza virus particles. *BMC Biology*. 2021; 19(1):91. <https://doi.org/10.1186/s12915-021-01020-5> PMID: 33941189
16. Hein MD, Kollmus H, Marichal-Gallardo P, Püttker S, Benndorf D, Genzel Y. OP7, a novel influenza A virus defective interfering particle: production, purification, and animal experiments demonstrating antiviral potential. *Applied Microbiology and Biotechnology*. 2021; 105(1):129–146. <https://doi.org/10.1007/s00253-020-11029-5> PMID: 33275160
17. Zhao H, To KKW, Chu H, Ding Q, Zhao X, Li C. Dual-functional peptide with defective interfering genes effectively protects mice against avian and seasonal influenza. *Nature Communications*. 2018; 9(1):2358. <https://doi.org/10.1038/s41467-018-04792-7> PMID: 29907765
18. Huo C, Tian J, Cheng J, Xiao J, Chen M, Zou S, et al. Safety, Immunogenicity, and Effectiveness of Defective Viral Particles Arising in Mast Cells Against Influenza in Mice. *Frontiers in Immunology*. 2020; 11:585254. <https://doi.org/10.3389/fimmu.2020.585254> PMID: 33304349
19. Kirkwood TB, Bangham CR. Cycles, chaos, and evolution in virus cultures: a model of defective interfering particles. *Proceedings of the National Academy of Sciences of the United States of America*. 1994; 91(18):8685–8689. <https://doi.org/10.1073/pnas.91.18.8685> PMID: 8078942
20. Frensing T, Heldt FS, Pflugmacher A, Behrendt I, Jordan I, Flockerzi D, et al. Continuous influenza virus production in cell culture shows a periodic accumulation of defective interfering particles. *PLOS One*. 2013; 8(9):e72288. <https://doi.org/10.1371/journal.pone.0072288> PMID: 24039749
21. Liao LE, Iwami S, Beauchemin CA. (In)validating experimentally derived knowledge about influenza A defective interfering particles. *Journal of the Royal Society Interface*. 2016; 13(124):20160412. <https://doi.org/10.1098/rsif.2016.0412> PMID: 27881801
22. Tapia F, Laske T, Wasik MA, Rammhold M, Genzel Y, Reichl U. Production of Defective Interfering Particles of Influenza A Virus in Parallel Continuous Cultures at Two Residence Times-Insights From qPCR Measurements and Viral Dynamics Modeling. *Frontiers in Bioengineering and Biotechnology*. 2019; 7:275. <https://doi.org/10.3389/fbioe.2019.00275> PMID: 31681751
23. Laske T, Heldt FS, Hoffmann H, Frensing T, Reichl U. Modeling the intracellular replication of influenza A virus in the presence of defective interfering RNAs. *Virus Research*. 2016; 213:90–99. <https://doi.org/10.1016/j.virusres.2015.11.016> PMID: 26592173
24. Shirogane Y, Rousseau E, Voznica J, Xiao Y, Su W, Catching A. Experimental and mathematical insights on the interactions between poliovirus and a defective interfering genome. *BioRxiv [Preprint]*. 2021 bioRxiv 2021.01.11.426198 [posted 2021 Jan 11; cited 2021 Mar 10]: [50 p.]. Available from: <https://www.biorxiv.org/content/10.1101/2021.01.11.426198v1>

25. Akpinar F, Timm A, Yin J. High-Throughput Single-Cell Kinetics of Virus Infections in the Presence of Defective Interfering Particles. *Journal of Virology*. 2015; 90(3):1599–1612. <https://doi.org/10.1128/JVI.02190-15> PMID: 26608322
26. Akpinar F, Inankur B, Yin J. Spatial-Temporal Patterns of Viral Amplification and Interference Initiated by a Single Infected Cell. *Journal of Virology*. 2016; 90(16):7552–7566. <https://doi.org/10.1128/JVI.00807-16> PMID: 27279621
27. Rüdiger D, Kupke SY, Laske T, Zmora P, Reichl U. Multiscale modeling of influenza A virus replication in cell cultures predicts infection dynamics for highly different infection conditions. *PLOS Computational Biology*. 2019; 15(2):e1006819. <https://doi.org/10.1371/journal.pcbi.1006819> PMID: 30779733
28. Dimmock NJ, Rainsford EW, Scott PD, Marriott AC. Influenza virus protecting RNA: an effective prophylactic and therapeutic antiviral. *Journal of Virology*. 2008; 82(17):8570–8578. <https://doi.org/10.1128/JVI.00743-08> PMID: 18579602
29. Heldt FS, Frensing T, Pflugmacher A, Gröpler R, Peschel B, Reichl U. Multiscale modeling of influenza A virus infection supports the development of direct-acting antivirals. *PLOS Computational Biology*. 2013; 9(11):e1003372. <https://doi.org/10.1371/journal.pcbi.1003372> PMID: 24278009
30. Genzel Y, Reichl U. Vaccine production—state of the art and future needs in upstream processing. In: Poertner R, editor. *Animal cell biotechnology: methods and protocols*. Humana Press; 2007. pp. 457–473.
31. Enami M, Fukuda R, Ishihama A. Transcription and replication of eight RNA segments of influenza virus. *Virology*. 1985; 142(1):68–77. [https://doi.org/10.1016/0042-6822\(85\)90423-4](https://doi.org/10.1016/0042-6822(85)90423-4) PMID: 2997982
32. Hatada E, Hasegawa M, Mukaigawa J, Shimizu K, Fukuda R. Control of influenza virus gene expression: quantitative analysis of each viral RNA species in infected cells. *Journal of Biochemistry*. 1989; 105(4):537–546. <https://doi.org/10.1093/oxfordjournals.jbchem.a122702> PMID: 2760014
33. Phan T, Fay EJ, Lee Z, Aron S, Hu WS, Langlois RA. Segment-specific kinetics of mRNA, cRNA and vRNA accumulation during influenza infection. *Journal of Virology*. 2021; 95(10):e02102–20. <https://doi.org/10.1128/JVI.02102-20> PMID: 33658346
34. Hay AJ, Lomniczi B, Bellamy AR, Skehel JJ. Transcription of the influenza virus genome. *Virology*. 1977; 83(2):337–355. [https://doi.org/10.1016/0042-6822\(77\)90179-9](https://doi.org/10.1016/0042-6822(77)90179-9) PMID: 929980
35. Bean WJ Jr, Simpson RW. Primary transcription of the influenza virus genome in permissive cells. *Virology*. 1973; 56(2):646–651. [https://doi.org/10.1016/0042-6822\(73\)90067-6](https://doi.org/10.1016/0042-6822(73)90067-6) PMID: 4796552
36. Cheung TK, Poon LL. Biology of influenza A virus. *Annals of the New York Academy of Sciences*. 2007; 1102:1–25. <https://doi.org/10.1196/annals.1408.001> PMID: 17470908
37. Akaike H. A new look at the statistical model identification. *IEEE Transactions on Automatic Control*. 1974; 19(6):716–723.
38. Efron B, Tibshirani R. Bootstrap methods for standard errors, confidence intervals, and other measures of statistical accuracy. *Statistical Science*. 1986; 1:54–75.
39. Shim JM, Kim J, Tenson T, Min JY, Kainov DE. Influenza Virus Infection, Interferon Response, Viral Counter-Response, and Apoptosis. *Viruses*. 2017; 9(8):223.
40. Martin BE, Harris JD, Sun J, Koelle K, Brooke CB. Cellular co-infection can modulate the efficiency of influenza A virus production and shape the interferon response. *PLoS Pathogens*. 2020; 16(10):e1008974. <https://doi.org/10.1371/journal.ppat.1008974> PMID: 33064776
41. Aggarwal K, Jing F, Maranga L, Liu J. Bioprocess optimization for cell culture based influenza vaccine production. *Vaccine*. 2011; 29(17):3320–3328. <https://doi.org/10.1016/j.vaccine.2011.01.081> PMID: 21335031
42. Isken B, Genzel Y, Reichl U. Productivity, apoptosis, and infection dynamics of influenza A/PR/8 strains and A/PR/8-based reassortants. *Vaccine*. 2012; 30(35):5253–5261. <https://doi.org/10.1016/j.vaccine.2012.05.065> PMID: 22698452
43. Sekellick MJ, Marcus PI. Viral interference by defective particles of vesicular stomatitis virus measured in individual cells. *Virology*. 1980; 104(1):247–252. [https://doi.org/10.1016/0042-6822\(80\)90385-2](https://doi.org/10.1016/0042-6822(80)90385-2) PMID: 6249028
44. Dimmock NJ, Easton AJ. Cloned Defective Interfering Influenza RNA and a Possible Pan-Specific Treatment of Respiratory Virus Diseases. *Viruses*. 2015; 7(7):3768–3788. <https://doi.org/10.3390/v7072796> PMID: 26184282
45. Baccam P, Beauchemin CAA, Macken CA, Hayden FG, Perelson AS. Kinetics of influenza A virus infection in humans. *Journal of Virology*. 2006; 80:7590–7599. <https://doi.org/10.1128/JVI.01623-05> PMID: 16840338
46. López CB. Defective viral genomes: critical danger signals of viral infections. *Journal of Virology*. 2014; 88(16):8720–8723. <https://doi.org/10.1128/JVI.00707-14> PMID: 24872580

47. Scott PD, Meng B, Marriott AC, Easton AJ, Dimmock NJ. Defective interfering influenza A virus protects *in vivo* against disease caused by a heterologous influenza B virus. *Journal of General Virology*. 2011; 92(9):2122–2132. <https://doi.org/10.1099/vir.0.034132-0> PMID: 21632569
48. Easton AJ, Scott PD, Edworthy NL, Meng B, Marriott AC, Dimmock NJ. A novel broad-spectrum treatment for respiratory virus infections: influenza-based defective interfering virus provides protection against pneumovirus infection *in vivo*. *Vaccine*. 2011; 29(15):2777–2784. <https://doi.org/10.1016/j.vaccine.2011.01.102> PMID: 21320545
49. Rand U, Kupke SY, Shkarlet H, Hein MD, Hirsch T, Marichal-Gallardo P, et al. Antiviral activity of influenza A virus defective interfering particles against SARS-CoV-2 replication *in vitro* through stimulation of innate immunity. *Cells*. 2021; 10(7):1756. <https://doi.org/10.3390/cells10071756> PMID: 34359926
50. Seitz C, Frensing T, Höper D, Kochs G, Reichl U. High yields of influenza A virus in Madin-Darby canine kidney cells are promoted by an insufficient interferon-induced antiviral state. *J Gen Virol*. 2010; 91(Pt 7):1754–1763. <https://doi.org/10.1099/vir.0.020370-0> PMID: 20357039
51. Seitz C, Isken B, Heynisch B, Rettkowski M, Frensing T, Reichl U. Trypsin promotes efficient influenza vaccine production in MDCK cells by interfering with the antiviral host response. *Applied Microbiology and Biotechnology*. 2012; 93(2):601–611. <https://doi.org/10.1007/s00253-011-3569-8> PMID: 21915610
52. Pelz L, Rüdiger D, Alnaji FG, Genzel Y, Brooke CB, Kupke SY, et al. Semi-continuous propagation of influenza A virus and its defective interfering particles: analyzing the dynamic competition to select candidates for antiviral therapy. *BioRxiv* [Preprint]. 2021 bioRxiv 2021.02.08.430251 [posted 2021 Feb 08; cited 2021 Mar 10]: [33 p.]. Available from: <https://www.biorxiv.org/content/10.1101/2021.02.08.430251v1>
53. Rodriguez A, Pérez-González A, Nieto A. Influenza virus infection causes specific degradation of the largest subunit of cellular RNA polymerase II. *Journal of Virology*. 2007; 81(10):5315–5324. <https://doi.org/10.1128/JVI.02129-06> PMID: 17344288
54. Martínez-Alonso M, Hengrung N, Fodor E. RNA-free and ribonucleoprotein-associated influenza virus polymerases directly bind the serine-5-phosphorylated carboxyl-terminal domain of host RNA polymerase II. *Journal of Virology*. 2016; 90(13):6014–6021. <https://doi.org/10.1128/JVI.00494-16> PMID: 27099314
55. Huang IC, Li W, Sui J, Marasco W, Choe H, Farzan M. Influenza A virus neuraminidase limits viral superinfection. *Journal of Virology*. 2008; 82(10):4834–4843. <https://doi.org/10.1128/JVI.00079-08> PMID: 18321971
56. Dou D, Hernández-Neuta I, Wang H, Östbye H, Qian X, Thiele S. Analysis of IAV Replication and Co-infection Dynamics by a Versatile RNA Viral Genome Labeling Method. *Cell Reports*. 2017; 20(1):251–263. <https://doi.org/10.1016/j.celrep.2017.06.021> PMID: 28683318
57. Cohen SD, Hindmarsh AC. CVODE, a stiff/nonstiff ODE solver in C. *Computers in Physics*. 1996; 10:138–143.
58. Schmidt H, Jirstrand M. Systems Biology Toolbox for MATLAB: a computational platform for research in systems biology. *Bioinformatics*. 2006; 22:514–515. <https://doi.org/10.1093/bioinformatics/bti799> PMID: 16317076
59. Hansen N, Ostermeier A. Completely Derandomized Self-Adaptation in Evolution Strategies. *Evolutionary Computation*. 2001; 9(2):159–195. <https://doi.org/10.1162/106365601750190398> PMID: 11382355
60. Heldt FS, Frensing T, Reichl U. Modeling the intracellular dynamics of influenza virus replication to understand the control of viral RNA synthesis. *Journal of Virology*. 2012; 86(15):7806–7817. <https://doi.org/10.1128/JVI.00080-12> PMID: 22593159
61. Frensing T, Kupke SY, Bachmann M, Fritzsche S, Gallo-Ramirez LE, Reichl U. Influenza virus intracellular replication dynamics, release kinetics, and particle morphology during propagation in MDCK cells. *Applied Microbiology and Biotechnology*. 2016; 100(16):7181–7192. <https://doi.org/10.1007/s00253-016-7542-4> PMID: 27129532
62. Lohr V, Genzel Y, Behrendt I, Scharfenberg K, Reichl U. A new MDCK suspension line cultivated in a fully defined medium in stirred-tank and wave bioreactor. *Vaccine*. 2010; 28(38):6256–64. <https://doi.org/10.1016/j.vaccine.2010.07.004> PMID: 20638458
63. Bissinger T, Fritsch J, Mihut A, Wu Y, Liu X, Genzel Y. Semi-perfusion cultures of suspension MDCK cells enable high cell concentrations and efficient influenza A virus production. *Vaccine*. 2019; 37(47):7003–7010. <https://doi.org/10.1016/j.vaccine.2019.04.054> PMID: 31047676
64. Bdeir N, Arora P, Gärtner S, Hoffmann M, Reichl U, Pöhlmann S. A system for production of defective interfering particles in the absence of infectious influenza A virus. *PLOS One*. 2019; 14(3):e0212757. <https://doi.org/10.1371/journal.pone.0212757> PMID: 30822349
65. Kupke SY, Riedel D, Frensing T, Zmora P, Reichl U. A Novel Type of Influenza A Virus-Derived Defective Interfering Particle with Nucleotide Substitutions in Its Genome. *Journal of Virology*. 2019; 93(4):e01786–18. <https://doi.org/10.1128/JVI.01786-18> PMID: 30463972

66. Kawakami E, Watanabe T, Fujii K, Goto H, Watanabe S, Noda T. Strand-specific real-time RT-PCR for distinguishing influenza vRNA, cRNA, and mRNA. *Journal of Virology Methods*. 2011; 173(1):1–6.
67. Wasik MA, Eichwald L, Genzel Y, Reichl U. Cell culture-based production of defective interfering particles for influenza antiviral therapy. *Applied Microbiology and Biotechnology*. 2018; 102(3):1167–1177. <https://doi.org/10.1007/s00253-017-8660-3> PMID: 29204901
68. Maguire O, Collins C, O'Loughlin K, Miecznikowski J, Minderman H. Quantifying nuclear p65 as a parameter for NF- κ B activation: Correlation between ImageStream cytometry, microscopy, and Western blot. *Cytometry A*. 2011; 79(6):461–469. <https://doi.org/10.1002/cyto.a.21068> PMID: 21520400

3.3. Third Manuscript

The study of the third manuscript describes the investigation of the ability of IAV DIPs as a broad-spectrum antiviral agent and identifies the mechanism of protection against unrelated virus infections. For this, the antiviral activity of IAV DIPs is studied *in vitro* in co-infection experiments against the replication of IFN-sensitive RSV, YFV, and ZIKV.

Pelz, Lars; Piagnani, Elena; Marsall, Patrick; Wynserski, Nancy; Hein, Marc D.;
Marichal-Gallardo, Pavel; Kupke, Sascha Y.; Reichl, Udo

Broad-spectrum antiviral activity of influenza A defective interfering particles against
respiratory syncytial, yellow fever, and Zika virus replication *in vitro*

Viruses, 2023

(Pelz et al., 2023)

Reproduced with permission from MDPI.

No changes were made.

<https://creativecommons.org/licenses/by/4.0/>

Individual contribution:

The study of the third manuscript comprises parts of the supervised Master's theses of Elena Piagnani (RSV) and Patrick Marsall (YFV) and experiments carried out by Nancy Wynserski (ZIKV). I designed experiments, analyzed and visualized data, and wrote the manuscript.

Article

Broad-Spectrum Antiviral Activity of Influenza A Defective Interfering Particles against Respiratory Syncytial, Yellow Fever, and Zika Virus Replication In Vitro

Lars Pelz ¹, Elena Piagnani ¹, Patrick Marsall ¹, Nancy Wynserski ¹, Marc Dominique Hein ², Pavel Marichal-Gallardo ¹, Sascha Young Kupke ^{1,*} and Udo Reichl ^{1,2}

¹ Bioprocess Engineering, Max Planck Institute for Dynamics of Complex Technical Systems, 39106 Magdeburg, Germany

² Bioprocess Engineering, Otto von Guericke University Magdeburg, 39106 Magdeburg, Germany

* Correspondence: kupke@mpi-magdeburg.mpg.de

Abstract: New broadly acting and readily available antiviral agents are needed to combat existing and emerging viruses. Defective interfering particles (DIPs) of influenza A virus (IAV) are regarded as promising options for the prevention and treatment of IAV infections. Interestingly, IAV DIPs also inhibit unrelated viral infections by stimulating antiviral innate immunity. Here, we tested the ability of IAV DIPs to suppress respiratory syncytial, yellow fever and Zika virus infections in vitro. In human lung (A549) cells, IAV DIP co-infection inhibited the replication and spread of all three viruses. In contrast, we observed no antiviral activity in Vero cells, which are deficient in the production of interferon (IFN), demonstrating its importance for the antiviral effect. Further, in A549 cells, we observed an enhanced type-I and type-III IFN response upon co-infection that appears to explain the antiviral potential of IAV DIPs. Finally, a lack of antiviral activity in the presence of the Janus kinase 1/2 (JAK1/2) inhibitor ruxolitinib was detected. This revealed a dependency of the antiviral activity on the JAK/signal transducers and activators of transcription (STAT) signaling pathway. Overall, this study supports the notion that IAV DIPs may be used as broad-spectrum antivirals to treat infections with a variety of IFN-sensitive viruses, particularly respiratory viruses.

Keywords: respiratory syncytial virus; yellow fever virus; Zika virus; defective interfering particles; broad-spectrum antiviral



Citation: Pelz, L.; Piagnani, E.; Marsall, P.; Wynserski, N.; Hein, M.D.; Marichal-Gallardo, P.; Kupke, S.Y.; Reichl, U. Broad-Spectrum Antiviral Activity of Influenza A Defective Interfering Particles against Respiratory Syncytial, Yellow Fever, and Zika Virus Replication In Vitro. *Viruses* **2023**, *15*, 1872. <https://doi.org/10.3390/v15091872>

Academic Editor: Ayato Takada

Received: 8 August 2023

Revised: 25 August 2023

Accepted: 1 September 2023

Published: 4 September 2023



Copyright: © 2023 by the authors. Licensee MDPI, Basel, Switzerland. This article is an open access article distributed under the terms and conditions of the Creative Commons Attribution (CC BY) license (<https://creativecommons.org/licenses/by/4.0/>).

1. Introduction

Viral infections pose a serious health burden. Respiratory syncytial virus (RSV) infections represent the second-most common cause of infant death [1] but can also result in considerable disease in older adults [2,3]. For prophylaxis, two vaccines based on the RSV prefusion F protein are recommended for elderly people [4], and one is recommended for infants [5]. However, only antivirals can be used to treat acute infections. For instance, the small-molecule drug ribavirin is applied for the treatment of severe RSV infections in high-risk immunocompromised infants [6]. However, ribavirin is associated with a low antiviral effect, high costs, possible toxicity in patients, and risks for health care workers [6–10]. Infections with flaviviruses are another concern as they can result in high morbidity and mortality. Furthermore, as vector-borne RNA viruses that can emerge unexpectedly in human populations, they constitute a serious global health challenge. Most infections are caused by yellow fever virus (YFV), Zika virus (ZIKV), dengue virus (DENV), and West Nile virus, which are primarily transmitted via mosquitoes to humans [11]. Vaccines are only approved for YFV, DENV, and Japanese encephalitis virus. No small molecule antiviral agents have been approved to treat acute flavivirus infections so far [12]. In a mouse infection model, the antibiotic fidaxomicin [13], which binds and inhibits the ZIKV polymerase, was shown to

suppress ZIKV propagation. In addition, it was demonstrated that the nucleoside analog ribavirin [14] could be of potential use for treatment of humans.

Interferons (IFNs) of type-I (e.g., IFN- α and - β) and type-III (e.g., IFN- λ) are considered an option to inhibit flavivirus and RSV infections [15,16]. For instance, the treatment with type-I and -III IFNs resulted in inhibition of ZIKV infections [17]. In addition, treatment with type-I IFN negatively correlated with disease severity for RSV [16], raising the potential for antiviral treatment. Nevertheless, recombinant type-I IFN therapies are costly [18] and pose the risk of adverse effects [19–21]. Therefore, the development of new antivirals with broad-spectrum activity which are safe, effective, and affordable is in high demand.

One such option is the use of defective interfering particles (DIPs) [22–25]. DIPs are naturally arising viral mutants that are found in a variety of RNA viruses [26–37], including influenza A viruses (IAV) [38–48]. Conventional IAV DIPs have a large internal deletion in one of their eight viral RNA (vRNA) segments, leading to a defect in virus replication. Furthermore, IAV DIPs inhibit IAV propagation in the context of a co-infection via “replication interference”. Here, the defective interfering (DI) vRNA is preferentially replicated relative to the full-length (FL), infectious standard virus (STV) counterpart. This leads to a depletion of cellular and viral resources and results in the inhibition of STV replication [47,49–51]. As a result, IAV DIPs suppress many strains, including seasonal, pandemic, and highly pathogenic avian IAV [39,41,42,52,53].

Next to replication interference, IAV DIP infection results in the induction of an antiviral state and suppresses not only the replication of IAV [42,54,55] but also the replication of unrelated viruses including severe acute respiratory syndrome coronavirus 2 (SARS-CoV-2) [22], pneumonia virus of mice [23], and influenza B virus [24]. In line with this, DIPs of DENV have been shown to confer an antiviral effect against ZIKV, YFV, RSV, SARS-CoV-2 [25], and various DENV subtypes [56], while DIPs of poliovirus inhibited SARS-CoV-2, Coxsackievirus B3, and IAV infections [33]. In this context, it was suggested for IAV DIPs that host-cell-derived pattern recognition receptors (PRRs) recognize pathogen-associated molecular patterns (PAMPs) such as FL and DI vRNAs [57,58]. This initiates a signaling cascade that activates IFN expression. Finally, IFN-stimulated genes (ISGs) are expressed, with some of the proteins conferring antiviral activity. These include myxovirus resistance protein 1 (Mx1), radical S-adenosyl methionine domain containing 2 (RSAD2), and IFN-induced transmembrane protein 1 (IFITM1).

To investigate whether IAV DIPs can also be used to treat other relevant viral infections, we studied their antiviral activity against the replication of the IFN-sensitive RSV, YFV, and ZIKV in co-infection experiments *in vitro* in human lung cells. For this, we used the IAV DIP “DI244” [39,59], a well-characterized DIP harboring a deletion in segment (Seg) 1. In addition, we tested “OP7”, a new type of IAV DIP that shows multiple point mutations in the vRNA of Seg 7 instead of an internal deletion [52]. DIP preparations were generated in cell cultures using laboratory-scale bioreactors [38,60]. We demonstrate that IAV DIPs inhibit RSV, YFV, and ZIKV propagation *in vitro* via stimulation of the innate antiviral immunity. Our results suggest that IAV DIPs might be a promising option for use as broad-spectrum antivirals to treat infections of many different IFN-sensitive viruses.

2. Materials and Methods

2.1. Cells and Viruses

Adherent human lung epithelial (A549, American Type Culture Collection (ATCC), #CCL-185) cells were maintained at 37 °C and 5% CO₂ in Dulbecco’s Modified Eagle Medium (DMEM) supplemented with 10% fetal bovine serum (FBS, Merck, Darmstadt, Germany, #F7524). Adherent African green monkey kidney epithelial (Vero) cells (European Collection of Authenticated Cell Cultures (ECACC), #88020401) and porcine stable kidney (PS) cells (provided by M. Niedrig, Robert Koch Institute (RKI), Berlin, Germany) were routinely cultivated in Glasgow Minimum Essential Medium (GMEM) supplemented with 10% FBS and 1% peptone at 37 °C and 5% CO₂. For YFV and ZIKV seed virus generation, Vero cells were cultivated in VP-SFM (Thermo Fisher Scientific, Waltham, MA, USA, #11681020) and GMEM (10% FBS, 1% peptone), respectively. Adherent HeLa-

derived Epithelial Carcinoma (HEp-2) cells (ATCC, #CCL-23) were maintained in DMEM supplemented with 10% FBS, or without FBS (infection medium) for RSV seed virus production. Hep-2 cells were cultivated in RPMI1640 medium (Thermo Fisher Scientific, #21870084) supplemented with 2 mM L-glutamine and 10% FBS, or without FBS (infection medium) for 50% tissue culture infectious dose (TCID₅₀) assay.

For infections, live attenuated YFV-17D (provided by M. Niedrig, RKI, Berlin, Germany) was used. ZIKV, originally isolated from whole blood specimens of ZIKV-positive adults in State of Espirito Santo, Brazil, was provided by Oswaldo Cruz Foundation, Brazil. Human RSV strain A2 (RSV A2) was obtained from ATCC (#VR-1540). OP7 and DI244 preparations (active and inactive, Table 1) were produced in a cell culture-based process, as described previously [38,60]; steric exclusion chromatography was used for purification [61,62].

Table 1. IAV DIP material used for co-infection experiments.

Description	HA Titer ¹ (log ₁₀ HAU/100 µL)	DI vRNA Concentration (DI vRNAs/mL) ²
Active OP7 (8 min UV)	3.53	1.60 × 10 ¹¹
Inactive OP7 (24 min UV)	3.52	2.85 × 10 ¹⁰
Active DI244 (no UV)	3.89	8.89 × 10 ¹⁰
Inactive DI244 (24 min UV)	3.85	1.03 × 10 ⁹

¹ Hemagglutination assay (HA) [63]. ² OP7: Seg 7-OP7 vRNAs/mL, DI244: Seg 1-DI244 vRNAs/mL.

2.2. Co-Infection Experiments

A549 and Vero cells were seeded at 0.5×10^6 cells/well and 0.4×10^6 cells/well, respectively, in 6-well plates and incubated for 24 h. Cells were washed prior to infection with $1 \times$ phosphate-buffered saline (PBS). Cells were infected with indicated viruses alone at a multiplicity of infection (MOI) of 10^{-2} , or co-infected with 100 µL of active or inactive IAV DIPs (Table 1) at indicated dilutions. Cells were co-treated with ruxolitinib (Cayman Chemical, Ann Arbor, MI, USA, #11609), IFN-β-1a (PBL assay Science, Piscataway, NJ, USA, #11410), ribavirin (Cayman Chemical, #16757-5), and fidaxomicin (MedChemExpress, Monmouth Junction, NJ, USA, #HY-17580) at indicated concentrations. For RSV infection, additional pre-treatment (3 h) with ruxolitinib was conducted.

For ZIKV infections, wells were incubated with 2000 µL of serum- and sodium-bicarbonate-containing medium (A549: DMEM, 10% FBS, 1% sodium bicarbonate; Vero: GMEM, 10% FBS, 1% peptone, 5% sodium bicarbonate) containing the virus(es) and/or antivirals. YFV infections were conducted in 500 µL of serum-free medium, and incubation was performed for 4 h at 37 °C. Subsequently, YFV infected cells were washed with $1 \times$ PBS, and 2000 µL of corresponding serum-free medium was added. For YFV infections, pH was adjusted manually through the addition of 7.5% sodium bicarbonate to prevent pH from decreasing below 6.8. Supernatants were harvested at 48 h post-infection (hpi), and 72 hpi for YFV and ZIKV infections, respectively. After centrifugation at $2000 \times g$, 5 min and 4 °C, cell-free supernatants were stored at -80 °C until virus quantification.

For RSV infections, wells were incubated with 250 µL of serum-free medium containing indicated virus(es) and antivirals and incubated for 2 h. Then, 1750 µL infection medium was added. Samples were taken at 72 hpi, followed by centrifugation at $300 \times g$, 5 min, 4 °C. Next, cell-free supernatants were snap frozen in liquid nitrogen.

For intracellular RNA extraction, remaining cells were washed with $1 \times$ PBS and lysed with 350 µL of RA1 buffer (Macherey Nagel, Düren, Germany, #740961) containing 1% of β-mercaptoethanol. Purification of RNAs was conducted according to the manufacturers' instructions. RNAs were stored at -80 °C.

2.3. Virus Quantification

For experiments with YFV and ZIKV, infectious virus titers were quantified via plaque assay as described recently [64] with few modifications. In brief, PS cells (0.2×10^5 cells/well)

were added to 24-well plates two days prior to infection. Cells were infected with 170 μ L of serially diluted samples (each 1:10, two replicates per sample) and incubated for 4 h at 37 °C and 5% CO₂. Subsequently, 600 μ L of 1.6% carboxymethyl cellulose in GMEM (supplemented with 10% FBS and 1% peptone) was added to the virus-containing medium. Cells were then incubated (37 °C, 5% CO₂) for 96 h (YFV) or 64 h (ZIKV). For fixation, 300 μ L of glyoxal solution was used (15 min) and cells were stained with 300 μ L of naphthalin black solution (30–60 min). Finally, plaques were counted and infectious virus titers expressed as plaque-forming units (PFU)/mL calculated based on the Spearman and Kärber method [65].

Quantification of infectious RSV titers were conducted by TCID₅₀ assay in accordance to a previously published protocol [66] with few modifications. In brief, HEp-2 cells (0.2×10^5 cells/well) were seeded to 96-well plates two days prior to infection. For infection, cells were washed with infection medium and 25 μ L of serially diluted samples (each 1:5, eight replicates per sample) were added. After incubation (2 h, 37 °C, 5% CO₂), 75 μ L of infection medium was added to each well and cells were incubated for 96 h. Wells that showed the presence of syncytia and/or lytic cell death under the light microscope were scored positive for RSV. For detection of lytic cell death, cells were stained with 50 μ L of crystal violet solution. The infectious virus titer was determined according to the Spearman and Kärber method.

2.4. Gene Expression Analysis

To measure mRNA expression levels, a real-time reverse transcription-quantitative PCR (RT-qPCR) method was utilized [22,52]. Purified RNA was reverse transcribed using Maxima H minus reverse transcriptase (Thermo Fisher Scientific, #EP0751) and an oligo (dT) primer according to the manufacturers' instructions. Next, real-time qPCR was performed with gene-specific forward and reverse primers (Table 2) and 2 \times QuantiNova SYBR green PCR master mix (Qiagen, Hilden, Germany, #208056). The fold change in gene expression (relative to untreated, uninfected cells (mock infection control)) was calculated using the $\Delta\Delta$ Ct method [67] using the reference housekeeping gene of glyceraldehyd-3-phosphat-dehydrogenase (GAPDH).

Table 2. Primers used for real-time RT-qPCR (gene expression).

Target Gene	Primer Name	Sequence (5'→3')
RIG-I [68]	RIG-I for RIG-I rev	GGACGTGGCAAAACAAATCAG GCAATGTCAATGCCTTCATCA
IFN- β -1 [69]	IFN- β -1 for IFN- β -1 rev	CATTACCTGAAGGCCAAGGA CAGCATCTGCTGGTTGAAGA
IFN- λ -1 [69]	IFN- λ -1 for IFN- λ -1 rev	GGTGACTTTGGTGCTAGGCT TGAGTGACTCTTCCAAGGCG
Mx1 [69]	Mx1 for Mx1 rev	GTATCACAGAGCTGTTCTCCTG CTCCACTCCCTGAAATCTG
IFITM1 [70]	IFITM1 for IFITM1 rev	ATCAACATCCACAGCGAGAC CAGAGCCGAATACCAGTAACAG
RSAD2 [69]	RSAD2 for RSAD2 rev	CCCCAACCAGCGTCAACTAT TGATCTTCTCCATACCAGCTTCC
GAPDH [69]	GAPDH for GAPDH rev	CTGGCGTCTTACCACCATGG CATCACGCCACAGTTTCCCGG

RIG-I: retinoic acid-inducible gene-I.

2.5. Quantification of Intracellular IAV vRNAs

To quantify intracellular genomic vRNAs of IAV, a previously described real-time RT-qPCR method was used [22,52,60,71] with a different reagent for qPCR (2 \times QuantiNova SYBR green qPCR master mix, Qiagen, #208056). The method employs a primer system

that allows gene-specific detection of individual IAV vRNAs [72]. RNA reference standards were used to facilitate absolute quantification.

3. Results

3.1. IFN-Dependent Inhibition of YFV Propagation by IAV DIP Co-Infection

To study whether IAV DIPs suppress YFV propagation, we performed in vitro co-infection experiments in A549 (IFN-competent) and Vero cells (IFN-deficient [73–78]) (Figure 1). Cells were infected with YFV alone (untreated, UT) at a MOI of 10^{-2} or co-infected with purified and concentrated IAV DIPs (DI244 or OP7, diluted to 1:20) derived from cell culture-based production [38,60]. Co-treatment with active DIPs (aDI244 and aOP7, see Table 1) resulted in a strong inhibition of infectious YFV release in A549 cells, as no plaque titer was detected (Figure 1A). As expected, inactive DIPs (iDI244 and iOP7) conferred no apparent antiviral activity. Note that iDI244 and iOP7 were UV irradiated for 24 min, which results in an inactivation and degradation of DI vRNAs [38,60]. In Vero cells that are deficient in IFN production [74,76], co-infections with active and inactive DIPs did not display any antiviral activity (Figure 1B).

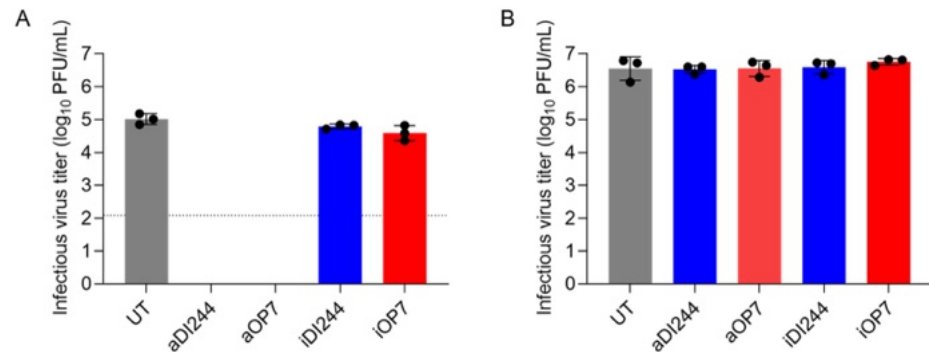


Figure 1. Inhibition of YFV replication and spread by IAV DIP co-infection in vitro in IFN-competent and -incompetent cells. Cells were infected with YFV alone at a MOI of 10^{-2} (UT, untreated) or co-infected with 100 μ L of active (a) or inactive (i) IAV DIPs DI244 or OP7. Infections in IFN-competent A549 cells (A) or IFN-deficient Vero cells (B). The DIP material used was diluted to 1:20. Infectious virus release is indicated by the YFV plaque titer (PFU/mL) at 48 hpi. The figure depicts the results of three independent experiments. Dashed horizontal line shows the limit of detection (LOD). Error bars indicate the standard deviation (SD).

We next studied host cell gene expression during inhibition of YFV replication by IAV DIP co-infection in A549 cells to identify mechanism of protection. For this, we investigated the expression of type-I and -III IFNs (IFN- β -1 and IFN- λ -1, respectively) and the ISGs Mx1 and RSAD2 using real-time RT-qPCR quantification (Figure 2). Co-treatment with active DIPs induced an increased expression of all genes at early time points (6 hpi, 24 hpi) relative to YFV infection alone (Figure 2, upper panel). The early upregulation of gene expression was independent on the infection with YFV, as infection with only IAV DIPs showed similar dynamics and levels (Figure 2, lower panel). A much less pronounced early upregulation of antiviral innate immunity was observed for infection with inactive DIPs, in agreement with the absence of inhibition by inactive DIPs (Figure 1A). For comparison, YFV infection without IAV DIPs resulted in relatively low IFN and ISG gene expression levels at early times. This suggests that the antiviral activity of IAV DIPs against YFV infection is caused by the early and strong upregulation of the type-I and -III IFN responses.

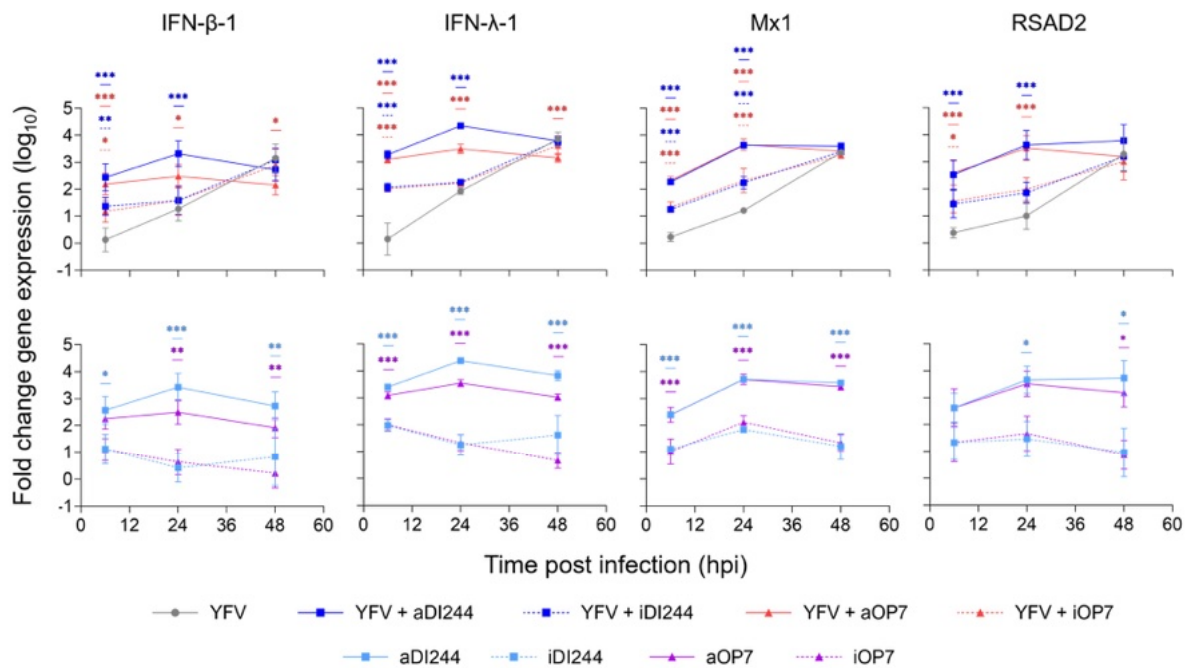


Figure 2. Induction of IFN-induced antiviral gene expression by IAV DIP infections. A549 cells were infected with YFV alone at a MOI of 10^{-2} or co-infected with 100 μ L of active (a) or inactive (i) IAV DIPs DI244 or OP7. The DIP material used was diluted to 1:20. Cells were lysed at indicated time points for subsequent intracellular RNA isolation. Gene expression was quantified using real-time RT-qPCR and expressed as fold change (relative to untreated, uninfected cells (mock infection control)). The figure depicts the results of three independent experiments. Error bars indicate the SD. Upper panel: Two-way ANOVA (or mixed-effects model for IFN- λ -1) followed by Dunnett's multiple comparison test (** $p < 0.001$; * $p < 0.01$; * $p < 0.05$; not significant, $p > 0.05$) was used to determine statistical significance compared to the untreated group. Lower panel: Two-way ANOVA followed by Tukey's multiple comparison test was used to determine statistical significance between respective active and inactive DIP material.

Next, we measured the intracellular IAV vRNA levels of the respective DI vRNA and of FL vRNA of Seg 5 and 8 in co-infections with DI244 and OP7 (Figure 3). Moreover, we measured the gene expression of RIG-I, a host-derived PRR that detects vRNA and has a crucial role in initiating a cellular innate immune response. We found high levels of DI and FL vRNAs after co-infection (Figure 3A,B) and a concurrent early upregulation of RIG-I expression (Figure 3C). At 24 hpi, we detected an increase by factors of 29 (YFV + aOP7) and 24 (YFV + aDI244) in the expression of RIG-I for IAV DIP co-infections compared to YFV infection alone. This may explain the upregulation of type-I and -III IFN response relative to the infection without IAV DIPs (as shown in Figure 2). The same upregulation of RIG-I was observed after infection with only IAV DIPs (Figure 3D). Moreover, lower vRNA levels were observed for co-infections with inactive DIPs, and no DI vRNAs could be detected for inactive DI244 co-infections (Figure 3A,B). This indicates an efficient degradation of vRNAs by UV inactivation. Accordingly, lower RIG-I expression levels were observed upon inactive IAV DIP infections (Figure 3C,D), which may explain their lack of IFN-induced antiviral activity (Figure 1A). Furthermore, we detected no increase of IAV genomic FL and DI vRNAs over time, indicating the defect in virus replication of IAV DIPs.

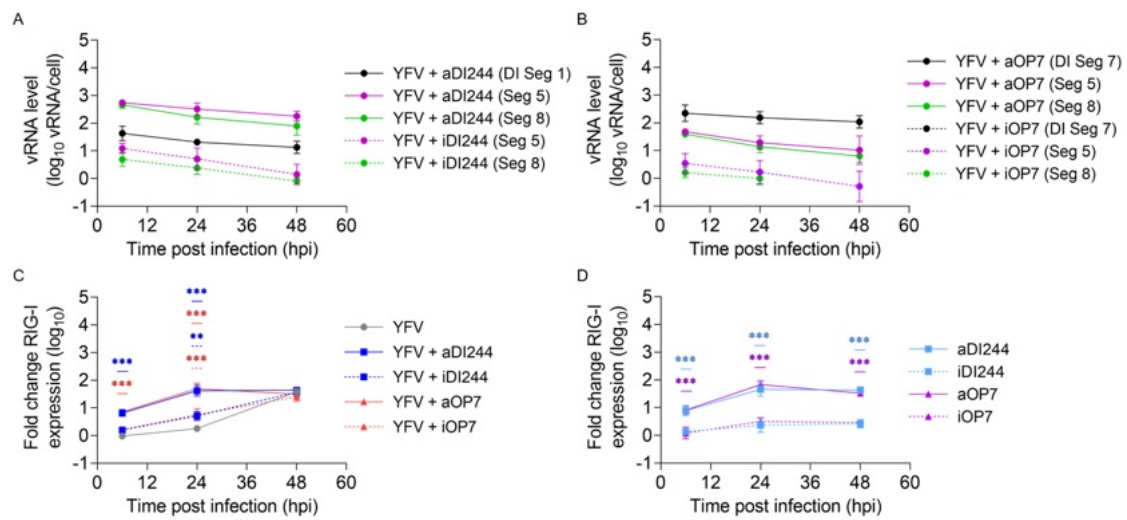


Figure 3. Intracellular levels of DI and FL vRNA and RIG-I expression after IAV DIP infections. A549 cells were infected with YFV alone at a MOI of 10^{-2} or co-infected with 100 μ L of active (a) or inactive (i) IAV DIPs DI244 (A) or OP7 (B). The DIP material used for infection was diluted to 1:20. Cells were lysed at indicated time points for subsequent intracellular RNA isolation. (A,B) DI and FL vRNA levels were quantified using real-time RT-qPCR. (C,D) Gene expression of RIG-I was quantified using real-time RT-qPCR and expressed as fold change (compared to untreated, uninfected cells (mock infection control)). The figure depicts the results of three independent experiments. Error bars indicate the SD. (C) Two-way ANOVA followed by Dunnett’s multiple comparison test (** $p < 0.001$; * $p < 0.01$; * $p < 0.05$; not significant, $p > 0.05$) was used to determine statistical significance compared to the untreated group. (D) Two-way ANOVA followed by Tukey’s multiple comparison test was used to determine statistical significance between respective active and inactive DIP material.

Taken together, IAV DIP co-infections resulted in an inhibition of YFV replication, which was dependent on the production of IFNs. Furthermore, we found that IAV DIP infection enhanced the type-I and -III IFN response, which appears to be initiated by sensing of DI and FL IAV vRNAs by RIG-I. The early and enhanced cellular innate immune response by IAV DIP infection likely explains their antiviral effect against YFV infection.

3.2. IAV DIP Infection Inhibits ZIKV Replication via JAK/STAT Signaling

Next, we investigated the inhibition of ZIKV replication by IAV DIPs (Figure 4). Therefore, we infected A549 cells and Vero cells at a MOI of 10^{-2} with ZIKV alone (UT) or co-infected with IAV DIPs. For active DIPs (aDI244, aOP7), different dilutions ranging from undiluted (1) to 1:100 dilutions were tested. Here, active DIPs showed antiviral activity against ZIKV propagation in a dose-dependent manner (Figure 4A). For instance, undiluted material of active OP7 and DI244 reduced the infectious virus titer by more than three and two orders of magnitude, respectively. The antiviral activity of IAV DIPs against ZIKV replication appeared to be lower relative to the inhibition of YFV replication (Figure 1A). This may be due to the use of a live attenuated strain YFV-17D and its increased sensitivity to IFN treatment [79]. Moreover, we found a residual antiviral activity of inactive DIPs against ZIKV replication (Figure 4A). This is likely mediated by a weak stimulation of the IFN-induced antiviral gene expression upon infection with inactive IAV DIPs only (also see Figure 2).

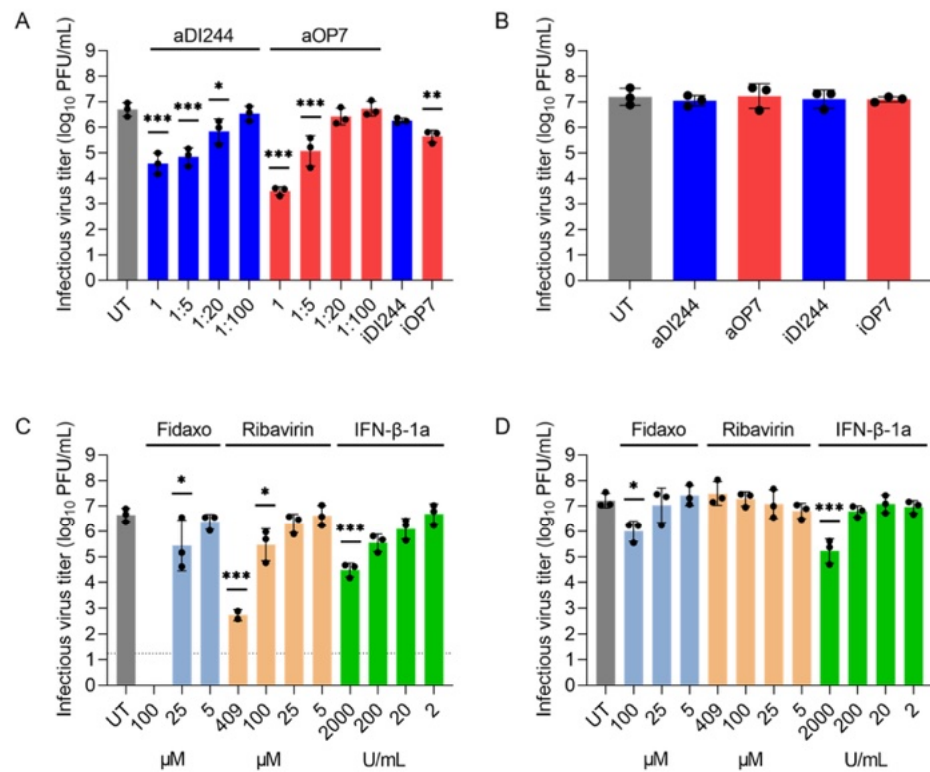


Figure 4. Inhibition of ZIKV replication and spread by IAV DIP co-infection in comparison to small molecule antiviral or IFN treatment. Infections in IFN-competent A549 cells (A,C) and in IFN-deficient Vero cells (B,D). Cells were infected with ZIKV alone at a MOI of 10^{-2} (UT, untreated), co-infected with 100 μ L of active (a) or inactive (i) IAV DIPs DI244 or OP7 at indicated dilutions (A) or without dilution (B). In addition, ZIKV-infected cells were co-treated with antiviral drugs (C,D) at indicated concentrations. Infectious virus release is indicated by the ZIKV plaque titer (PFU/mL) at 72 hpi. The figure depicts the results of three independent experiments or two experiments for ribavirin (409 μ M) in (C). Dashed horizontal line shows the LOD. Error bars indicate the SD. One-way ANOVA followed by Dunnett's multiple comparison test (** $p < 0.001$; ** $p < 0.01$; * $p < 0.05$; not significant, $p > 0.05$) was used to determine statistical significance compared to the untreated control group.

In Vero cells, co-treatment with IAV DIPs did not result in an inhibition of ZIKV replication, indicating the dependence of the antiviral effect on the production of IFN (Figure 4B). Next, we tested different relevant antivirals (i.e., fidaxomicin (Fidaxo) [13], ribavirin [14,80], and IFN- β -1a [81,82]) against ZIKV infection (Figure 4C,D). As expected, the different drugs conferred an antiviral activity in a dose-dependent manner. In A549 cells, fidaxomicin at 100 μ M showed very high inhibitory activity as no infectious virus titer could be detected anymore (Figure 4C). In comparison, a concentration of 409 μ M of ribavirin and 2000 U/mL of IFN- β -1a reduced the infectious virus titer by almost four and more than two orders of magnitude, respectively. The inhibition conferred by the three different antivirals were less pronounced in Vero relative to A549 cells, indicating a lower sensitivity to treatment of the former (Figure 4D). Although Vero cells are unable to produce IFN [74,76], we found a residual inhibition of ZIKV replication during IFN- β -1a treatment (Figure 4D). This may be explained by the fact that Vero cells bear functional IFN receptors and can, thus, respond to exogenous IFN treatment [83,84].

To confirm that the inhibition of ZIKV replication is caused by the ability of DIPs to stimulate the IFN system, we used the Janus kinase 1/2 (JAK1/2) inhibitor ruxolitinib in co-infection experiments (Figure 5). JAK1/2 is a crucial player in the JAK/STAT signaling pathway. Following binding of type-I IFNs to the IFN- α/β receptor, the associated JAK

would stimulate activation of STAT, ultimately leading to expression of antiviral ISGs. For co-treatment with ruxolitinib, we observed no inhibition of infectious ZIKV release by IAV DIPs in A549 cells. In conclusion, the inhibition of ZIKV by IAV DIPs was dependent on IFN production and on signaling through the JAK/STAT pathway.

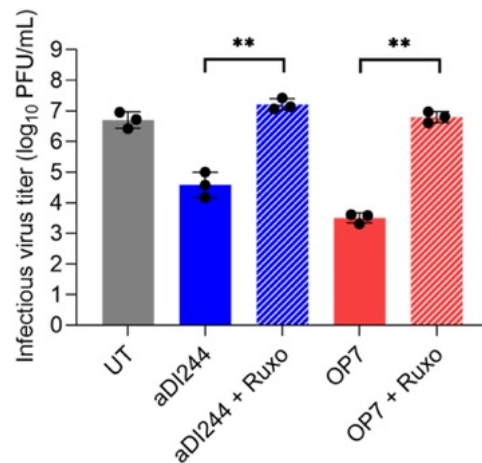


Figure 5. Antiviral activity of IAV DIPs against ZIKV propagation under JAK1/2 inhibition. A549 cells were infected with ZIKV alone at a MOI of 10^{-2} (UT, untreated) or co-infected with 100 μ L of active (a) IAV DIPs DI244 or OP7. The DIP material used was non-diluted. As indicated, co-infections were performed in the presence of ruxolitinib (2 μ M). Infectious virus release is indicated by the ZIKV plaque titer (PFU/mL) at 72 hpi. The figure depicts the results of three independent experiments. Error bars indicate the SD. One-way ANOVA followed by Tukey's multiple comparison test (** $p < 0.001$; * $p < 0.01$; * $p < 0.05$; not significant, $p > 0.05$) was used to determine statistical significance between co-infections with and without ruxolitinib.

3.3. IFN-Dependent Inhibition of RSV Replication by IAV DIPs Relies on JAK/STAT Signaling

Finally, we tested the antiviral activity of IAV DIPs against RSV replication. For this, we infected A549 cells and Vero cells at a MOI of 10^{-2} (UT) or co-infected with IAV DIPs (diluted to 1:20) (Figure 6). RSV-infected A549 cells showed an infectious virus titer of 2.6×10^5 TCID₅₀/mL at 72 hpi. Co-treatment with active DI244 (aDI244) and active OP7 (aOP7) suppressed the infectious virus release to 5.4×10^4 and 7.1×10^3 TCID₅₀/mL, respectively (Figure 6A). Furthermore, two clinically relevant antivirals, i.e., IFN- β -1a (2000 U/mL) and ribavirin (409 μ M), were tested for comparison. Treatment with IFN- β -1a showed an inhibition of infectious virus release to 1.2×10^4 TCID₅₀/mL, whereas ribavirin treatment almost shut down RSV propagation (6×10^0 TCID₅₀/mL) in A549 cells.

An early and enhanced upregulation of IFN-induced antiviral gene expression (indicated by RIG-I, IFN- β -1, Mx1, and IFITM1) was observed in A549 cells for the treatment with DIPs only and the co-infection with RSV in comparison to infection with RSV only (Figure 7). The residual antiviral activity of inactive DIPs against RSV infection (Figure 6A) may be explained by the intermediate upregulation of IFN and ISGs (Figure 7).

Next, we tested the inhibitory activity of IAV DIPs in Vero cells (Figure 6B). As expected, no suppression of the infectious virus titer was found for active or inactive IAV DIPs. However, treatment with IFN- β -1a led to a reduction in infectious virus titers from 4.9×10^5 TCID₅₀/mL (UT) to 2.3×10^4 TCID₅₀/mL, as Vero cells still express an IFN receptor. Further, a lower inhibition (compared to A549 cells, Figure 6A) was observed for ribavirin treatment (reduction to 1.9×10^5 TCID₅₀/mL).

To investigate whether the inhibition of RSV infection by active IAV DIPs is dependent on signaling through the JAK/STAT pathway, A549 cells were co-infected with aDI244 or aOP7 in the presence or absence of the JAK1/2 inhibitor ruxolitinib (Ruxo) (Figure 8). No suppression of the infectious virus titer was found in presence of ruxolitinib. Taken together,

we show that IAV DIPs inhibit RSV propagation in an IFN-dependent manner. Moreover, the antiviral activity was promoted via signaling through the JAK/STAT pathway, which results in IFN-induced antiviral gene expression.

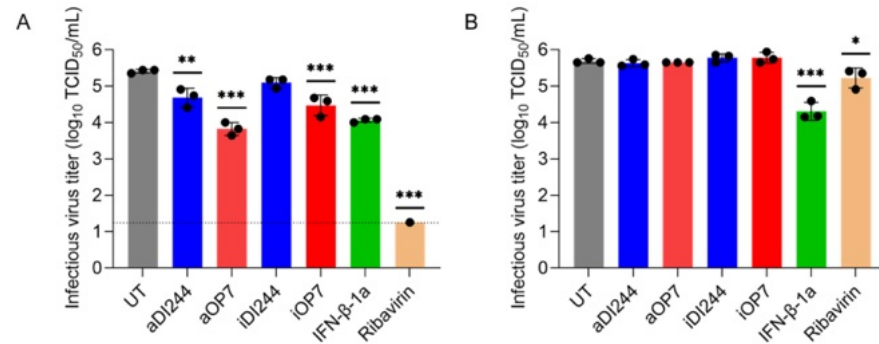


Figure 6. Inhibition of RSV replication and spread by IAV DIP co-infection in comparison to ribavirin or IFN treatment. Infections in IFN-competent A549 cells (A) or IFN-deficient Vero cells (B). Cells were infected with RSV alone at a MOI of 10⁻² (UT, untreated), co-infected with 100 μL of active (a) or inactive (i) IAV DIPs DI244 or OP7. In addition, RSV-infected cells were co-treated with antiviral drugs (IFN-β-1a (2000 U/mL) or ribavirin (409 μM)). The DIP material used was diluted to 1:20. Infectious virus release is indicated by the RSV TCID₅₀ titer (TCID₅₀/mL) at 72 hpi. The figure depicts the results of three independent experiments. Dashed horizontal line shows the LOD. Error bars indicate the SD. One-way ANOVA followed by Dunnett’s multiple comparison test (***) *p* < 0.001; ** *p* < 0.01; * *p* < 0.05; not significant, *p* > 0.05) was used to determine statistical significance compared to the untreated group.

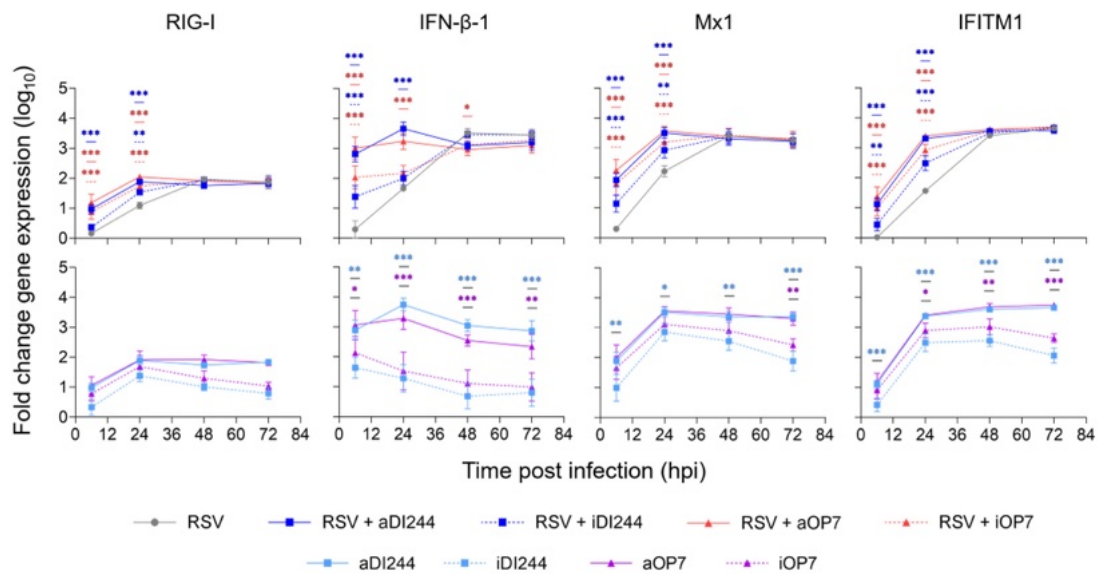


Figure 7. Induction of IFN-induced antiviral gene expression by IAV DIP infections. A549 cells were infected with RSV alone at a MOI of 10⁻² or co-infected with 100 μL of active (a) or inactive (i) IAV DIPs DI244 or OP7. The DIP material used was diluted to 1:20. Cells were lysed at indicated time points for subsequent intracellular RNA isolation. Gene expression was quantified using real-time RT-qPCR and expressed as fold change (relative to untreated, uninfected cells (mock infection control)). The figure depicts the results of three independent experiments. Error bars indicate the SD. Upper panel: Two-way ANOVA followed by Dunnett’s multiple comparison test (***) *p* < 0.001; ** *p* < 0.01; * *p* < 0.05; not significant, *p* > 0.05) was used to determine statistical significance compared to the untreated group. Lower panel: Two-way ANOVA followed by Tukey’s multiple comparison test was used to determine statistical significance between respective active and inactive DIP material.

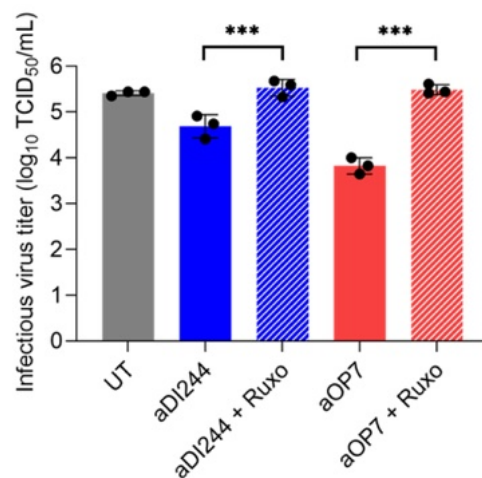


Figure 8. Antiviral activity of IAV DIPs against RSV propagation under JAK1/2 inhibition. A549 cells were infected with RSV alone at a MOI of 10^{-2} (UT, untreated) or co-infected with 100 μ L of active (a) IAV DIPs DI244 or OP7. The DIP material used was diluted to 1:20. As indicated, co-infections were performed in the presence of ruxolitinib (2 μ M, after pre-treatment for 3 h). Infectious virus release is indicated by the RSV TCID₅₀ titer (TCID₅₀/mL) at 72 hpi. The figure depicts the results of three independent experiments. Error bars indicate the SD. One-way ANOVA followed by Tukey's multiple comparison test (** $p < 0.01$; * $p < 0.05$; not significant, $p > 0.05$) was used to determine statistical significance between co-infections with and without ruxolitinib.

4. Discussion

IAV DIPs are considered for use as broad-spectrum antiviral agents to treat not only infections of different IAV strains [39,41,42,52,53] but also those of unrelated viruses [22–24]. Our study shows that IAV DIPs also inhibit the replication of IFN-sensitive RSV, YFV, and ZIKV infections *in vitro* by their ability to upregulate the IFN response that acts antivirally. The availability of such broadly acting antivirals may increase our pandemic preparedness.

Our study supports other work that suggests that IFN induction is a key player for the antiviral activity of DIPs against the replication of unrelated viruses [22–25,33,42,54,55]. IAV DIPs showed a lower antiviral activity against ZIKV than for YFV replication. In our study, we used YFV-17D, a live-attenuated vaccine strain, and wild-type (WT) ZIKV. Previously, it has been shown that in type-I IFN-deficient mice, type-II IFN restricted the replication of YFV-17D, but not that of WT YFV [79], suggesting that YFV-17D is more sensitive to IFN treatment than WT YFV. With respect to the present study, this may explain the higher antiviral activity of IAV DIPs against YFV-17D compared to antiviral activity against WT ZIKV replication, a phylogenetically related virus. Accordingly, other viruses that demonstrate higher IFN antagonism ability (like the more virulent WT YFV [79]) should be less susceptible to inhibition by IAV DIPs.

DI and FL vRNAs of IAV DIPs are potent RIG-I ligands [43,57], which is a cytosolic PRR that can initiate an IFN response. In line with this, we observed an upregulation of RIG-I upon infection with IAV DIPs, consistent with previous reports [22]. We also tested infections with IAV DIPs that were inactivated by UV light, which results in photodimeric lesions [85] or unspecific chain breaks [86,87] of their vRNAs. Here, we observed no or a very weak antiviral effect, likely due to the reduced activation of RIG-I. Accordingly, the residual antiviral activity of inactive IAV DIPs against ZIKV replication may be explained by the weak stimulation of the IFN response observed in our studies.

Next, we showed that the antiviral effect against ZIKV and RSV was dependent on an IFN-induced innate immune response that involved the JAK/STAT pathway, confirming previous IAV DIP co-infection studies with SARS-CoV-2 [22]. Furthermore, the ISGs Mx1, RSAD2, and IFITM1 were upregulated early after infection with IAV DIPs compared to

infections with YFV or RSV only. This early stimulation of an antiviral state likely explains the antiviral effect of IAV DIPs against unrelated viruses, as suggested previously [22], and also for DENV DIPs [25].

In agreement with this body of evidence, we observed an absence of antiviral activity against RSV, YFV, and ZIKV in Vero cells, which are deficient in IFN production [74,76] due to a deleted region in chromosome 12 encoding for numerous type-I IFN genes [78]. Previously, Easton et al. showed that mice were protected from death after administration of DI244 and an otherwise lethal dose of pneumonia virus of mice. In type-I IFN deficient mice, only 17% survived, but a delayed onset of symptoms was observed [23]. Moreover, a reduced protection in type-I IFN-deficient mice was found against influenza B virus infection [24]. Nevertheless, yet unidentified pathways may also be involved for IAV DIPs inducing an antiviral state in an IFN-independent manner [23], as also speculated by others [88,89].

The inhibition of infectious RSV and ZIKV release by IAV DIPs was comparable to IFN- β -1a treatment. With respect to clinical studies, partial positive effects of type-I IFN treatment on RSV infection were observed [90,91], but other studies resulted in no effects [92,93]. For RSV A2 infections, little inhibition by IFN treatment was observed [94]. Inhibition of ZIKV replication by exogenous IFN- β and - λ -1 treatment in human vaginal and cervical epithelial cells was modest [17]. Disadvantages involved in the therapy with recombinant type-I IFN are the high costs [18] and the risk of adverse effects such as flu-like symptoms, fatigue, depression, neutropenia, and anemia [19–21]. Compared to treatment with recombinant IFN, it is suggested that IAV DIPs can stimulate a more physiological IFN response in target tissues [22]. In line with this, the administration of IAV DIPs is typically very well tolerated in mice, resulting in no apparent adverse or toxic effects [38,39,60]. Furthermore, high-yield, cell culture-based production and purification of IAV DIPs is feasible [38,60,95]. This suggests that IAV DIPs can be produced in an economical manner, and thus, we anticipate relatively low prices per dose.

In our experiments, we observed that the small molecule antivirals ribavirin (in ZIKV and RSV infection) and fidaxomicin (ZIKV infection) conferred a higher antiviral activity than IAV DIPs. However, ribavirin approved for treatment of RSV infection in humans is associated with high costs and possible toxic effects [8,10]. Moreover, fidaxomicin and ribavirin are not approved for treatment of humans infected with ZIKV. Next, we showed that ribavirin and fidaxomicin treatment resulted in higher antiviral effects in A549 cells than in Vero cells. For ZIKV infection, no antiviral effect was observed for ribavirin treatment of Vero cells. These results suggest that Vero cells are less sensitive to antiviral treatment, as already reported for ribavirin for suppression of ZIKV replication [13]. This cell-dependent antiviral activity underlines the importance of the selected testing system concerning the antiviral effect observed *in vitro*. However, this may not necessarily represent the degree of inhibition *in vivo* and thus may not allow for a relevant comparison of different antivirals considered for human use. Therefore, it is mandatory to perform additional studies to compare the tested antiviral agents, including the IAV DIPs, in animal models and carefully designed clinical trials. In this manner, the antiviral activity and side effects at different doses with different routes and times of administration can be investigated to draw conclusions about their comparability and applicability.

The main application of IAV DIPs could be the intranasal application to treat IFN-sensitive respiratory virus infections, including that of IAV [39,96], SARS-CoV-2 [22] and RSV (this study). For instance, in mice and ferrets, this route of administration resulted in an antiviral effect against IAV [38,39,53,60]. The inhibition of YFV and ZIKV as shown in the present study may be regarded as a result from an *in vitro* model that indicates that IAV DIPs also exhibit antiviral activity against the replication of other IFN-sensitive viruses. The optimal route of administration of IAV DIPs and antiviral efficacy in animal experiments against such systemic viral infections, however, remain to be elucidated.

In the future, the availability of broadly acting antivirals like IAV DIPs could allow for a rapid countermeasure to protect susceptible people and persons at risk and help to

contain the spread of newly emerging IFN-sensitive viruses in case of a pandemic, when vaccines or other antivirals are not available yet.

5. Patents

A patent for the use of OP7 as antiviral agent for treatment of IAV infection is approved for USA and pending for European Union and Japan. Patent holders are S.Y.K. and U.R. Another patent for the use of DI244 and OP7 as an antiviral agent for treatment of coronavirus infection is pending. Patent holders are S.Y.K., U.R., and M.D.H.

Supplementary Materials: The following supporting information can be downloaded at: <https://www.mdpi.com/article/10.3390/v15091872/s1>.

Author Contributions: Conceptualization, L.P., S.Y.K. and U.R.; formal analysis, L.P.; investigation, L.P., E.P., P.M., N.W., M.D.H. and P.M.-G.; writing—original draft preparation, L.P.; writing—review and editing, L.P., E.P., P.M., N.W., M.D.H., P.M.-G., S.Y.K. and U.R.; visualization, L.P.; supervision, S.Y.K. and U.R.; project administration, L.P. and S.Y.K. All authors have read and agreed to the published version of the manuscript.

Funding: Part of the work was supported by the Defense Advanced Research Projects Agency (<https://www.darpa.mil/program/intercept>) INTERCEPT program under cooperative agreements W911NF-17-2-0012.

Institutional Review Board Statement: Not applicable.

Informed Consent Statement: Not applicable.

Data Availability Statement: The data presented in this study are available in Supplemental Table S1.

Acknowledgments: The authors thank Piotr Janas and Jürgen Schwarze from the University of Edinburgh, Scotland for helpful comments regarding the RSV propagation.

Conflicts of Interest: Besides the patents mentioned above, the authors declare no conflict of interest.

References

1. Lozano, R.; Naghavi, M.; Foreman, K.; Lim, S.; Shibuya, K.; Aboyans, V.; Abraham, J.; Adair, T.; Aggarwal, R.; Ahn, S.Y.; et al. Global and regional mortality from 235 causes of death for 20 age groups in 1990 and 2010: A systematic analysis for the Global Burden of Disease Study 2010. *Lancet* **2012**, *380*, 2095–2128. [[CrossRef](#)]
2. Ackerson, B.; Tseng, H.F.; Sy, L.S.; Solano, Z.; Slezak, J.; Luo, Y.; Fischetti, C.A.; Shinde, V. Severe Morbidity and Mortality Associated with Respiratory Syncytial Virus Versus Influenza Infection in Hospitalized Older Adults. *Clin. Infect. Dis.* **2019**, *69*, 197–203. [[CrossRef](#)] [[PubMed](#)]
3. Falsey, A.R.; Hennessey, P.A.; Formica, M.A.; Cox, C.; Walsh, E.E. Respiratory Syncytial Virus Infection in Elderly and High-Risk Adults. *N. Engl. J. Med.* **2005**, *352*, 1749–1759. [[CrossRef](#)] [[PubMed](#)]
4. PATH. RSV Vaccine and mAB Snapshot. Available online: <https://www.path.org/resources/rsv-vaccine-and-mab-snapshot/> (accessed on 10 July 2023).
5. EMA. Available online: <https://www.ema.europa.eu/en/medicines/human/summaries-opinion/abrysv0> (accessed on 31 July 2023).
6. Simões, E.A.F.; Bont, L.; Manzoni, P.; Fauroux, B.; Paes, B.; Figueras-Aloy, J.; Checchia, P.A.; Carbonell-Estrany, X. Past, Present and Future Approaches to the Prevention and Treatment of Respiratory Syncytial Virus Infection in Children. *Infect. Dis. Ther.* **2018**, *7*, 87–120. [[CrossRef](#)] [[PubMed](#)]
7. Trang, T.P.; Whalen, M.; Hiltz-Horeczko, A.; Doernberg, S.B.; Liu, C. Comparative effectiveness of aerosolized versus oral ribavirin for the treatment of respiratory syncytial virus infections: A single-center retrospective cohort study and review of the literature. *Transpl. Infect. Dis.* **2018**, *20*, e12844. [[CrossRef](#)]
8. Devincenzo, J.P. Therapy of respiratory syncytial virus infection. *Pediatr. Infect. Dis. J.* **2000**, *19*, 786–790. [[CrossRef](#)]
9. Guerguerian, A.-M.; Gauthier, M.; Lebel, M.H.; Farrell, C.A.; Lacroix, J. Ribavirin in Ventilated Respiratory Syncytial Virus Bronchiolitis. *Am. J. Respir. Crit. Care Med.* **1999**, *160*, 829–834. [[CrossRef](#)]
10. Domachowski, J.B.; Anderson, E.J.; Goldstein, M. The Future of Respiratory Syncytial Virus Disease Prevention and Treatment. *Infect. Dis. Ther.* **2021**, *10*, 47–60. [[CrossRef](#)]
11. Daep, C.A.; Muñoz-Jordán, J.L.; Eugenin, E.A. Flaviviruses, an expanding threat in public health: Focus on dengue, West Nile, and Japanese encephalitis virus. *J. NeuroVirol.* **2014**, *20*, 539–560. [[CrossRef](#)]
12. Chong, H.Y.; Leow, C.Y.; Abdul Majeed, A.B.; Leow, C.H. Flavivirus infection—A review of immunopathogenesis, immunological response, and immunodiagnosis. *Virus Res.* **2019**, *274*, 197770. [[CrossRef](#)]

13. Yuan, J.; Yu, J.; Huang, Y.; He, Z.; Luo, J.; Wu, Y.; Zheng, Y.; Wu, J.; Zhu, X.; Wang, H.; et al. Antibiotic fidaxomicin is an RdRp inhibitor as a potential new therapeutic agent against Zika virus. *BMC Med.* **2020**, *18*, 204. [[CrossRef](#)] [[PubMed](#)]
14. Kamiyama, N.; Soma, R.; Hidano, S.; Watanabe, K.; Umekita, H.; Fukuda, C.; Noguchi, K.; Gendo, Y.; Ozaki, T.; Sonoda, A.; et al. Ribavirin inhibits Zika virus (ZIKV) replication in vitro and suppresses viremia in ZIKV-infected STAT1-deficient mice. *Antivir. Res.* **2017**, *146*, 1–11. [[CrossRef](#)]
15. Ngono, A.E.; Shresta, S. Immune Response to Dengue and Zika. *Annu. Rev. Immunol.* **2018**, *36*, 279–308. [[CrossRef](#)]
16. Hijano, D.R.; Vu, L.D.; Kauvar, L.M.; Tripp, R.A.; Polack, F.P.; Cormier, S.A. Role of Type I Interferon (IFN) in the Respiratory Syncytial Virus (RSV) Immune Response and Disease Severity. *Front. Immunol.* **2019**, *10*, 566. [[CrossRef](#)] [[PubMed](#)]
17. Caine, E.A.; Scheaffer, S.M.; Arora, N.; Zaitsev, K.; Artyomov, M.N.; Coyne, C.B.; Moley, K.H.; Diamond, M.S. Interferon lambda protects the female reproductive tract against Zika virus infection. *Nat. Commun.* **2019**, *10*, 280. [[CrossRef](#)] [[PubMed](#)]
18. Nguyen, H.A.; Cooke, G.S.; Day, J.N.; Flower, B.; Phuong, L.T.; Hung, T.M.; Dung, N.T.; Khoa, D.B.; Hung, L.M.; Kestelyn, E.; et al. The direct-medical costs associated with interferon-based treatment for Hepatitis C in Vietnam. *Wellcome Open Res.* **2019**, *4*, 129. [[CrossRef](#)]
19. Kirkwood, J.M.; Bender, C.; Agarwala, S.; Tarhini, A.; Shipe-Spotloe, J.; Smelko, B.; Donnelly, S.; Stover, L. Mechanisms and management of toxicities associated with high-dose interferon alfa-2b therapy. *J. Clin. Oncol. Off. J. Am. Soc. Clin. Oncol.* **2002**, *20*, 3703–3718. [[CrossRef](#)]
20. Borden, E.C.; Parkinson, D. A perspective on the clinical effectiveness and tolerance of interferon-alpha. *Semin. Oncol.* **1998**, *25*, 3–8.
21. Hauschild, A.; Gogas, H.; Tarhini, A.; Middleton, M.R.; Testori, A.; Dréno, B.; Kirkwood, J.M. Practical guidelines for the management of interferon-alpha-2b side effects in patients receiving adjuvant treatment for melanoma: Expert opinion. *Cancer* **2008**, *112*, 982–994. [[CrossRef](#)]
22. Rand, U.; Kupke, S.Y.; Shkarlet, H.; Hein, M.D.; Hirsch, T.; Marichal-Gallardo, P.; Cicin-Sain, L.; Reichl, U.; Bruder, D. Antiviral Activity of Influenza A Virus Defective Interfering Particles against SARS-CoV-2 Replication In Vitro through Stimulation of Innate Immunity. *Cells* **2021**, *10*, 1756. [[CrossRef](#)] [[PubMed](#)]
23. Easton, A.J.; Scott, P.D.; Edworthy, N.L.; Meng, B.; Marriott, A.C.; Dimmock, N.J. A novel broad-spectrum treatment for respiratory virus infections: Influenza-based defective interfering virus provides protection against pneumovirus infection in vivo. *Vaccine* **2011**, *29*, 2777–2784. [[CrossRef](#)] [[PubMed](#)]
24. Scott, P.D.; Meng, B.; Marriott, A.C.; Easton, A.J.; Dimmock, N.J. Defective interfering influenza A virus protects in vivo against disease caused by a heterologous influenza B virus. *J. Gen. Virol.* **2011**, *92*, 2122–2132. [[CrossRef](#)] [[PubMed](#)]
25. Lin, M.H.; Li, D.; Tang, B.; Li, L.; Suhrbier, A.; Harrich, D. Defective Interfering Particles with Broad-Acting Antiviral Activity for Dengue, Zika, Yellow Fever, Respiratory Syncytial and SARS-CoV-2 Virus Infection. *Microbiol. Spectr.* **2022**, *10*, e0394922. [[CrossRef](#)] [[PubMed](#)]
26. Vignuzzi, M.; Lopez, C.B. Defective viral genomes are key drivers of the virus-host interaction. *Nat. Microbiol.* **2019**, *4*, 1075–1087. [[CrossRef](#)] [[PubMed](#)]
27. Meir, M.; Harel, N.; Miller, D.; Gelbart, M.; Eldar, A.; Gophna, U.; Stern, A. Competition between social cheater viruses is driven by mechanistically different cheating strategies. *Sci. Adv.* **2020**, *6*, eabb7990. [[CrossRef](#)]
28. Ziegler, C.M.; Botten, J.W. Defective Interfering Particles of Negative-Strand RNA Viruses. *Trends Microbiol.* **2020**, *28*, 554–565. [[CrossRef](#)]
29. Levi, L.I.; Rezelj, V.V.; Henrion-Lacritick, A.; Erazo, D.; Boussier, J.; Vallet, T.; Bernhauerova, V.; Suzuki, Y.; Carrau, L.; Weger-Lucarelli, J.; et al. Defective viral genomes from chikungunya virus are broad-spectrum antivirals and prevent virus dissemination in mosquitoes. *PLoS Pathog.* **2021**, *17*, e1009110. [[CrossRef](#)]
30. Rezelj, V.V.; Carrau, L.; Merwaiss, F.; Levi, L.I.; Erazo, D.; Tran, Q.D.; Henrion-Lacritick, A.; Gausson, V.; Suzuki, Y.; Shengjuler, D.; et al. Defective viral genomes as therapeutic interfering particles against flavivirus infection in mammalian and mosquito hosts. *Nat. Commun.* **2021**, *12*, 2290. [[CrossRef](#)]
31. Sun, Y.; Jain, D.; Koziol-White, C.J.; Genoyer, E.; Gilbert, M.; Tapia, K.; Panettieri, R.A., Jr.; Hodinka, R.L.; Lopez, C.B. Immunostimulatory Defective Viral Genomes from Respiratory Syncytial Virus Promote a Strong Innate Antiviral Response during Infection in Mice and Humans. *PLoS Pathog.* **2015**, *11*, e1005122. [[CrossRef](#)]
32. Welch, S.R.; Tilston, N.L.; Lo, M.K.; Whitmer, S.L.M.; Harmon, J.R.; Scholte, F.E.M.; Spengler, J.R.; Duprex, W.P.; Nichol, S.T.; Spiropoulou, C.F. Inhibition of Nipah Virus by Defective Interfering Particles. *J. Infect. Dis.* **2020**, *221*, S460–S470. [[CrossRef](#)]
33. Xiao, Y.; Lidsky, P.V.; Shirogane, Y.; Aviner, R.; Wu, C.T.; Li, W.; Zheng, W.; Talbot, D.; Catching, A.; Doitsh, G.; et al. A defective viral genome strategy elicits broad protective immunity against respiratory viruses. *Cell* **2021**, *184*, 6037–6051.e14. [[CrossRef](#)] [[PubMed](#)]
34. Yao, S.; Narayanan, A.; Majowicz, S.A.; Jose, J.; Archetti, M. A synthetic defective interfering SARS-CoV-2. *PeerJ* **2021**, *9*, e11686. [[CrossRef](#)] [[PubMed](#)]
35. Felt, S.A.; Sun, Y.; Jozwik, A.; Paras, A.; Habibi, M.S.; Nickle, D.; Anderson, L.; Achouri, E.; Feemster, K.A.; Cardenas, A.M.; et al. Detection of respiratory syncytial virus defective genomes in nasal secretions is associated with distinct clinical outcomes. *Nat. Microbiol.* **2021**, *6*, 672–681. [[CrossRef](#)] [[PubMed](#)]
36. Girgis, S.; Xu, Z.; Oikonomopoulos, S.; Fedorova, A.D.; Tchesnokov, E.P.; Gordon, C.J.; Schmeing, T.M.; Götte, M.; Sonenberg, N.; Baranov, P.V.; et al. Evolution of naturally arising SARS-CoV-2 defective interfering particles. *Commun. Biol.* **2022**, *5*, 1140. [[CrossRef](#)] [[PubMed](#)]

37. Wang, S.; Chan, K.W.K.; Naripogu, K.B.; Swarbrick, C.M.D.; Aaskov, J.; Vasudevan, S.G. Subgenomic RNA from Dengue Virus Type 2 Suppresses Replication of Dengue Virus Genomes and Interacts with Virus-Encoded NS3 and NS5 Proteins. *ACS Infect. Dis.* **2020**, *6*, 436–446. [[CrossRef](#)]
38. Hein, M.D.; Arora, P.; Marichal-Gallardo, P.; Winkler, M.; Genzel, Y.; Pöhlmann, S.; Schughart, K.; Kupke, S.Y.; Reichl, U. Cell culture-based production and in vivo characterization of purely clonal defective interfering influenza virus particles. *BMC Biol.* **2021**, *19*, 91. [[CrossRef](#)]
39. Dimmock, N.J.; Rainsford, E.W.; Scott, P.D.; Marriott, A.C. Influenza virus protecting RNA: An effective prophylactic and therapeutic antiviral. *J. Virol.* **2008**, *82*, 8570–8578. [[CrossRef](#)]
40. Yang, Y.; Lyu, T.; Zhou, R.; He, X.; Ye, K.; Xie, Q.; Zhu, L.; Chen, T.; Shen, C.; Wu, Q.; et al. The Antiviral and Antitumor Effects of Defective Interfering Particles/Genomes and Their Mechanisms. *Front. Microbiol.* **2019**, *10*, 1852. [[CrossRef](#)]
41. Zhao, H.; To, K.K.W.; Chu, H.; Ding, Q.; Zhao, X.; Li, C.; Shuai, H.; Yuan, S.; Zhou, J.; Kok, K.H.; et al. Dual-functional peptide with defective interfering genes effectively protects mice against avian and seasonal influenza. *Nat. Commun.* **2018**, *9*, 2358. [[CrossRef](#)]
42. Huo, C.; Cheng, J.; Xiao, J.; Chen, M.; Zou, S.; Tian, H.; Wang, M.; Sun, L.; Hao, Z.; Hu, Y. Defective Viral Particles Produced in Mast Cells Can Effectively Fight Against Lethal Influenza A Virus. *Front. Microbiol.* **2020**, *11*, 553274. [[CrossRef](#)]
43. Mendes, M.; Russell, A.B. Library-based analysis reveals segment and length dependent characteristics of defective influenza genomes. *PLoS Pathog.* **2021**, *17*, e1010125. [[CrossRef](#)] [[PubMed](#)]
44. Alnaji, F.G.; Brooke, C.B. Influenza virus DI particles: Defective interfering or delightfully interesting? *PLoS Pathog.* **2020**, *16*, e1008436. [[CrossRef](#)] [[PubMed](#)]
45. Wu, M.; Zhou, E.; Sheng, R.; Fu, X.; Li, J.; Jiang, C.; Su, W. Defective Interfering Particles of Influenza Virus and Their Characteristics, Impacts, and Use in Vaccines and Antiviral Strategies: A Systematic Review. *Viruses* **2022**, *14*, 2773. [[CrossRef](#)] [[PubMed](#)]
46. Alnaji, F.G.; Reiser, W.K.; Rivera-Cardona, J.; Velthuis, A.J.W.t.; Brooke, C.B. Influenza A Virus Defective Viral Genomes Are Inefficiently Packaged into Virions Relative to Wild-Type Genomic RNAs. *mBio* **2021**, *12*, e0295921. [[CrossRef](#)]
47. Rüdiger, D.; Pelz, L.; Hein, M.D.; Kupke, S.Y.; Reichl, U. Multiscale model of defective interfering particle replication for influenza A virus infection in animal cell culture. *PLoS Comput. Biol.* **2021**, *17*, e1009357. [[CrossRef](#)]
48. Rüdiger, D.; Kupke, S.Y.; Laske, T.; Zmora, P.; Reichl, U. Multiscale modeling of influenza A virus replication in cell cultures predicts infection dynamics for highly different infection conditions. *PLoS Comput. Biol.* **2019**, *15*, e1006819. [[CrossRef](#)]
49. Nayak, D.P.; Chambers, T.M.; Akkina, R.K. Defective-Interfering (DI) RNAs of Influenza Viruses: Origin, Structure, Expression, and Interference. In *Current Topics in Microbiology and Immunology*; Cooper, M., Eisen, H., Goebel, W., Hofschneider, P.H., Koprowski, H., Melchers, F., Oldstone, M., Rott, R., Schweiger, H.G., Vogt, P.K., et al., Eds.; Springer: Berlin/Heidelberg, Germany, 1985; pp. 103–151.
50. Marriott, A.C.; Dimmock, N.J. Defective interfering viruses and their potential as antiviral agents. *Rev. Med. Virol.* **2010**, *20*, 51–62. [[CrossRef](#)]
51. Laske, T.; Heldt, F.S.; Hoffmann, H.; Frensing, T.; Reichl, U. Modeling the intracellular replication of influenza A virus in the presence of defective interfering RNAs. *Virus Res.* **2016**, *213*, 90–99. [[CrossRef](#)] [[PubMed](#)]
52. Kupke, S.Y.; Riedel, D.; Frensing, T.; Zmora, P.; Reichl, U. A Novel Type of Influenza A Virus-Derived Defective Interfering Particle with Nucleotide Substitutions in Its Genome. *J. Virol.* **2019**, *93*, e01786–18. [[CrossRef](#)]
53. Dimmock, N.J.; Dove, B.K.; Scott, P.D.; Meng, B.; Taylor, I.; Cheung, L.; Hallis, B.; Marriott, A.C.; Carroll, M.W.; Easton, A.J. Cloned defective interfering influenza virus protects ferrets from pandemic 2009 influenza A virus and allows protective immunity to be established. *PLoS ONE* **2012**, *7*, e49394. [[CrossRef](#)]
54. Frensing, T.; Pflugmacher, A.; Bachmann, M.; Peschel, B.; Reichl, U. Impact of defective interfering particles on virus replication and antiviral host response in cell culture-based influenza vaccine production. *Appl. Microbiol. Biotechnol.* **2014**, *98*, 8999–9008. [[CrossRef](#)] [[PubMed](#)]
55. Penn, R.; Tregoning, J.S.; Flight, K.E.; Baillon, L.; Frise, R.; Goldhill, D.H.; Johansson, C.; Barclay, W. Levels of Influenza A Virus Defective Viral Genomes Determine Pathogenesis in the BALB/c Mouse Model. *J. Virol.* **2022**, *96*, e0117822. [[CrossRef](#)] [[PubMed](#)]
56. Li, D.; Lin, M.H.; Rawle, D.J.; Jin, H.; Wu, Z.; Wang, L.; Lor, M.; Hussain, M.; Aaskov, J.; Harrich, D. Dengue virus-free defective interfering particles have potent and broad anti-dengue virus activity. *Commun. Biol.* **2021**, *4*, 557. [[CrossRef](#)]
57. Baum, A.; García-Sastre, A. Differential recognition of viral RNA by RIG-I. *Virulence* **2011**, *2*, 166–169. [[CrossRef](#)] [[PubMed](#)]
58. Rehwinkel, J.; Tan, C.P.; Goubau, D.; Schulz, O.; Pichlmair, A.; Bier, K.; Robb, N.; Vreede, F.; Barclay, W.; Fodor, E.; et al. RIG-I Detects Viral Genomic RNA during Negative-Strand RNA Virus Infection. *Cell* **2010**, *140*, 397–408. [[CrossRef](#)]
59. Dimmock, N.J.; Dove, B.K.; Meng, B.; Scott, P.D.; Taylor, I.; Cheung, L.; Hallis, B.; Marriott, A.C.; Carroll, M.W.; Easton, A.J. Comparison of the protection of ferrets against pandemic 2009 influenza A virus (H1N1) by 244 DI influenza virus and oseltamivir. *Antivir. Res.* **2012**, *96*, 376–385. [[CrossRef](#)]
60. Hein, M.D.; Kollmus, H.; Marichal-Gallardo, P.; Püttker, S.; Benndorf, D.; Genzel, Y.; Schughart, K.; Kupke, S.Y.; Reichl, U. OP7, a novel influenza A virus defective interfering particle: Production, purification, and animal experiments demonstrating antiviral potential. *Appl. Microbiol. Biotechnol.* **2021**, *105*, 129–146. [[CrossRef](#)]

61. Marichal-Gallardo, P.; Pieler, M.M.; Wolff, M.W.; Reichl, U. Steric exclusion chromatography for purification of cell culture-derived influenza A virus using regenerated cellulose membranes and polyethylene glycol. *J. Chromatogr. A* **2017**, *1483*, 110–119. [[CrossRef](#)]
62. Marichal-Gallardo, P.; Börner, K.; Pieler, M.M.; Sonntag-Buck, V.; Obr, M.; Bejarano, D.; Wolff, M.W.; Krausslich, H.G.; Reichl, U.; Grimm, D. Single-Use Capture Purification of Adeno-Associated Viral Gene Transfer Vectors by Membrane-Based Steric Exclusion Chromatography. *Hum. Gene Ther.* **2021**, *32*, 959–974. [[CrossRef](#)]
63. Kalbfuss, B.; Knöchlein, A.; Kröber, T.; Reichl, U. Monitoring influenza virus content in vaccine production: Precise assays for the quantitation of hemagglutination and neuraminidase activity. *Biologicals* **2008**, *36*, 145–161. [[CrossRef](#)]
64. Nikolay, A.; Castilho, L.R.; Reichl, U.; Genzel, Y. Propagation of Brazilian Zika virus strains in static and suspension cultures using Vero and BHK cells. *Vaccine* **2018**, *36*, 3140–3145. [[CrossRef](#)] [[PubMed](#)]
65. Hierholzer, J.; Killington, R. Virus isolation and quantitation. In *Virology Methods Manual*; Elsevier: Amsterdam, The Netherlands, 1996; pp. 25–46.
66. Sun, Y.; Lopez, C.B. Preparation of Respiratory Syncytial Virus with High or Low Content of Defective Viral Particles and Their Purification from Viral Stocks. *Bio Protoc.* **2016**, *6*, e1820. [[CrossRef](#)]
67. Livak, K.J.; Schmittgen, T.D. Analysis of relative gene expression data using real-time quantitative PCR and the 2-(Delta Delta C(T)) Method. *Methods* **2001**, *25*, 402–408. [[CrossRef](#)]
68. Jiang, J.; Li, J.; Fan, W.; Zheng, W.; Yu, M.; Chen, C.; Sun, L.; Bi, Y.; Ding, C.; Gao, G.F.; et al. Robust Lys63-Linked Ubiquitination of RIG-I Promotes Cytokine Eruption in Early Influenza B Virus Infection. *J. Virol.* **2016**, *90*, 6263–6275. [[CrossRef](#)] [[PubMed](#)]
69. Busnadiego, I.; Fernbach, S.; Pohl, M.O.; Karakus, U.; Huber, M.; Trkola, A.; Stertz, S.; Hale, B.G. Antiviral Activity of Type I, II, and III Interferons Counterbalances ACE2 Inducibility and Restricts SARS-CoV-2. *mBio* **2020**, *11*, e01928-20. [[CrossRef](#)] [[PubMed](#)]
70. Wang, H.; Chen, L.; Luo, J.; He, H. NP and NS1 proteins of H5N1 virus significantly upregulated IFITM1, IFITM2, and IFITM3 in A549 cells. *Afr. Health Sci.* **2019**, *19*, 1402–1410. [[CrossRef](#)]
71. Frensing, T.; Kupke, S.Y.; Bachmann, M.; Fritzsche, S.; Gallo-Ramirez, L.E.; Reichl, U. Influenza virus intracellular replication dynamics, release kinetics, and particle morphology during propagation in MDCK cells. *Appl. Microbiol. Biotechnol.* **2016**, *100*, 7181–7192. [[CrossRef](#)] [[PubMed](#)]
72. Kawakami, E.; Watanabe, T.; Fujii, K.; Goto, H.; Watanabe, S.; Noda, T.; Kawaoka, Y. Strand-specific real-time RT-PCR for distinguishing influenza vRNA, cRNA, and mRNA. *J. Virol. Methods* **2011**, *173*, 1–6. [[CrossRef](#)] [[PubMed](#)]
73. Diaz, M.O.; Ziemin, S.; Le Beau, M.M.; Pitha, P.; Smith, S.D.; Chilcote, R.R.; Rowley, J.D. Homozygous deletion of the alpha- and beta 1-interferon genes in human leukemia and derived cell lines. *Proc. Natl. Acad. Sci. USA* **1988**, *85*, 5259–5263. [[CrossRef](#)]
74. Vester, D.; Rapp, E.; Kluge, S.; Genzel, Y.; Reichl, U. Virus–host cell interactions in vaccine production cell lines infected with different human influenza A virus variants: A proteomic approach. *J. Proteom.* **2010**, *73*, 1656–1669. [[CrossRef](#)] [[PubMed](#)]
75. Chew, T.; Noyce, R.; Collins, S.E.; Hancock, M.H.; Mossman, K.L. Characterization of the interferon regulatory factor 3-mediated antiviral response in a cell line deficient for IFN production. *Mol. Immunol.* **2009**, *46*, 393–399. [[CrossRef](#)] [[PubMed](#)]
76. Emeny, J.M.; Morgan, M.J. Regulation of the interferon system: Evidence that Vero cells have a genetic defect in interferon production. *J. Gen. Virol.* **1979**, *43*, 247–252. [[CrossRef](#)]
77. Desmyter, J.; Melnick, J.L.; Rawls, W.E. Defectiveness of interferon production and of rubella virus interference in a line of African green monkey kidney cells (Vero). *J. Virol.* **1968**, *2*, 955–961. [[CrossRef](#)]
78. Osada, N.; Kohara, A.; Yamaji, T.; Hirayama, N.; Kasai, F.; Sekizuka, T.; Kuroda, M.; Hanada, K. The genome landscape of the african green monkey kidney-derived vero cell line. *DNA Res.* **2014**, *21*, 673–683. [[CrossRef](#)]
79. Lam, L.K.M.; Watson, A.M.; Ryman, K.D.; Klimstra, W.B. Gamma-interferon exerts a critical early restriction on replication and dissemination of yellow fever virus vaccine strain 17D-204. *NPJ Vaccines* **2018**, *3*, 5. [[CrossRef](#)] [[PubMed](#)]
80. Bernatchez, J.A.; Yang, Z.; Coste, M.; Li, J.; Beck, S.; Liu, Y.; Clark, A.E.; Zhu, Z.; Luna, L.A.; Sohl, C.D.; et al. Development and Validation of a Phenotypic High-Content Imaging Assay for Assessing the Antiviral Activity of Small-Molecule Inhibitors Targeting Zika Virus. *Antimicrob. Agents Chemother.* **2018**, *62*, e00725-18. [[CrossRef](#)] [[PubMed](#)]
81. Frumence, E.; Roche, M.; Krejbich-Trotot, P.; El-Kalamouni, C.; Nativel, B.; Rondeau, P.; Misse, D.; Gadea, G.; Viranaicken, W.; Despres, P. The South Pacific epidemic strain of Zika virus replicates efficiently in human epithelial A549 cells leading to IFN-beta production and apoptosis induction. *Virology* **2016**, *493*, 217–226. [[CrossRef](#)]
82. Hamel, R.; Dejarnac, O.; Wichit, S.; Ekchariyawat, P.; Neyret, A.; Luplertlop, N.; Perera-Lecoin, M.; Surasombattana, P.; Talignani, L.; Thomas, F.; et al. Biology of Zika Virus Infection in Human Skin Cells. *J. Virol.* **2015**, *89*, 8880–8896. [[CrossRef](#)] [[PubMed](#)]
83. Cinatl, J.; Morgenstern, B.; Bauer, G.; Chandra, P.; Rabenau, H.; Doerr, H.W. Treatment of SARS with human interferons. *Lancet* **2003**, *362*, 293–294. [[CrossRef](#)]
84. Pires de Mello, C.P.; Drusano, G.L.; Rodriguez, J.L.; Kaushik, A.; Brown, A.N. Antiviral Effects of Clinically-Relevant Interferon-alpha and Ribavirin Regimens against Dengue Virus in the Hollow Fiber Infection Model (HFIM). *Viruses* **2018**, *10*, 317. [[CrossRef](#)]
85. Remsen, J.F.; Miller, N.; Cerutti, P.A. Photohydration of Uridine in the RNA of Coliphage R17, II. The Relationship between Ultraviolet Inactivation and Uridine Photohydration. *Proc. Natl. Acad. Sci. USA* **1970**, *65*, 460–466. [[CrossRef](#)]
86. Coahran, D.R.; Buzzell, A.; Lauffer, M.A. The effect of ultraviolet irradiation on nucleic acid isolated from tobacco mosaic virus. *Biochim. Et. Biophys. Acta* **1962**, *55*, 755–767. [[CrossRef](#)]

87. Jericevic, Z.; Kucan, I.; Chambers, R.W. Photochemical cleavage of phosphodiester bonds in oligoribonucleotides. *Biochemistry* **1982**, *21*, 6563–6567. [[CrossRef](#)] [[PubMed](#)]
88. Wang, C.; Forst, C.V.; Chou, T.W.; Geber, A.; Wang, M.; Hamou, W.; Smith, M.; Sebra, R.; Zhang, B.; Zhou, B.; et al. Cell-to-Cell Variation in Defective Virus Expression and Effects on Host Responses during Influenza Virus Infection. *mBio* **2020**, *11*, e02880-19. [[CrossRef](#)]
89. Wang, C.; Honce, R.; Salvatore, M.; Chow, D.; Randazzo, D.; Yang, J.; Twells, N.M.; Mahal, L.K.; Schultz-Cherry, S.; Ghedin, E. Influenza Defective Interfering Virus Promotes Multiciliated Cell Differentiation and Reduces the Inflammatory Response in Mice. *J. Virol.* **2023**, *97*, e0049323. [[CrossRef](#)] [[PubMed](#)]
90. Dai, J.-X.; You, C.-H.; Qi, Z.-T.; Wang, X.-M.; Sun, P.-Q.; Bi, W.-S.; Qian, Y.; Ding, R.-L.; Du, P.; He, Y. Children's respiratory viral diseases treated with interferon aerosol. *Chin. Med. J.* **1987**, *100*, 162–166. [[CrossRef](#)] [[PubMed](#)]
91. Sung, R.Y.; Yin, J.; Oppenheimer, S.J.; Tam, J.S.; Lau, J. Treatment of respiratory syncytial virus infection with recombinant interferon alfa-2a. *Arch. Dis. Child.* **1993**, *69*, 440–442. [[CrossRef](#)]
92. Chipps, B.E.; Sullivan, W.F.; Portnoy, J.M. Alpha-2A-interferon for treatment of bronchiolitis caused by respiratory syncytial virus. *Pediatr. Infect. Dis. J.* **1993**, *12*, 653–658. [[CrossRef](#)]
93. Higgins, P.G.; Barrow, G.I.; Tyrrell, D.A.J.; Isaacs, D.; Gauci, C.L. The efficacy of intranasal interferon α -2a in respiratory syncytial virus infection in volunteers. *Antivir. Res.* **1990**, *14*, 3–10. [[CrossRef](#)]
94. Atreya, P.L.; Kulkarni, S. Respiratory Syncytial Virus Strain A2 Is Resistant to the Antiviral Effects of Type I Interferons and Human MxA. *Virology* **1999**, *261*, 227–241. [[CrossRef](#)]
95. Hein, M.D.; Chawla, A.; Cattaneo, M.; Kupke, S.Y.; Genzel, Y.; Reichl, U. Cell culture-based production of defective interfering influenza A virus particles in perfusion mode using an alternating tangential flow filtration system. *Appl. Microbiol. Biotechnol.* **2021**, *105*, 7251–7264. [[CrossRef](#)] [[PubMed](#)]
96. Dimmock, N.J.; Easton, A.J. Cloned Defective Interfering Influenza RNA and a Possible Pan-Specific Treatment of Respiratory Virus Diseases. *Viruses* **2015**, *7*, 3768–3788. [[CrossRef](#)] [[PubMed](#)]

Disclaimer/Publisher's Note: The statements, opinions and data contained in all publications are solely those of the individual author(s) and contributor(s) and not of MDPI and/or the editor(s). MDPI and/or the editor(s) disclaim responsibility for any injury to people or property resulting from any ideas, methods, instructions or products referred to in the content.

3.4. Fourth Manuscript

In the study of the fourth manuscript, a cell culture-based production system for OP7 chimera DIPs free of STVs is optimized regarding virus titers, OP7 chimera DIP fractions (as OP7 chimera DIPs and cDIPs are present), and interfering efficacy. In addition, material for subsequent testing in animals regarding tolerability and antiviral efficacy is generated.

Dogra, Tanya; **Pelz, Lars**; Böhme, Julia D.; Kuchler, Jan; Kershaw, Olivia; Marichal-Gallardo, Pavel; Bälkner, Maike; Hein, Marc D.; Gruber, Achim D.; Benndorf, Dirk; Genzel, Yvonne; Bruder, Dunja; Kupke, Sascha Y.; Reichl, Udo

Generation of “OP7 chimera” defective interfering influenza A particle preparations free of infectious virus that show antiviral efficacy in mice

Scientific Reports, 2023

(Dogra et al., 2023)

Reproduced with permission from Springer Nature.

No changes were made.

<https://creativecommons.org/licenses/by/4.0/>

Individual contribution:

In the study of the fourth manuscript, I carried out the cell culture-based production for Figure 2, 3, and 4, and performed the *in vitro* interference assay shown in Figure 4. Moreover, I produced OP7 chimera DIP material in shake flasks for testing in animals shown in Figure 5 and 6. In addition, I analyzed and visualized data, wrote results section, and minor parts of materials & methods and discussion sections.



OPEN Generation of “OP7 chimera” defective interfering influenza A particle preparations free of infectious virus that show antiviral efficacy in mice

Tanya Dogra¹, Lars Pelz¹, Julia D. Boehme^{2,3}, Jan Kuechler¹, Olivia Kershaw⁴, Pavel Marichal-Gallardo¹, Maïke Baelkner^{2,3}, Marc D. Hein⁵, Achim D. Gruber⁴, Dirk Benndorf^{1,5}, Yvonne Genzel¹, Dunja Bruder^{2,3}, Sascha Y. Kupke^{1✉} & Udo Reichl^{1,5}

Influenza A virus (IAV) defective interfering particles (DIPs) are considered as new promising antiviral agents. Conventional DIPs (cDIPs) contain a deletion in the genome and can only replicate upon co-infection with infectious standard virus (STV), during which they suppress STV replication. We previously discovered a new type of IAV DIP “OP7” that entails genomic point mutations and displays higher antiviral efficacy than cDIPs. To avoid safety concerns for the medical use of OP7 preparations, we developed a production system that does not depend on infectious IAV. We reconstituted a mixture of DIPs consisting of cDIPs and OP7 chimera DIPs, in which both harbor a deletion in their genome. To complement the defect, the deleted viral protein is expressed by the suspension cell line used for production in shake flasks. Here, DIP preparations harvested are not contaminated with infectious virions, and the fraction of OP7 chimera DIPs depended on the multiplicity of infection. Intranasal administration of OP7 chimera DIP material was well tolerated in mice. A rescue from an otherwise lethal IAV infection and no signs of disease upon OP7 chimera DIP co-infection demonstrated the remarkable antiviral efficacy. The clinical development of this new class of broad-spectrum antiviral may contribute to pandemic preparedness.

Influenza A virus (IAV) is a major human pathogen. Infections cause annual epidemics, which lead to excessive morbidity and mortality¹. When novel strains emerge, IAV infections may result in a severe pandemic, which is considered an imminent threat. For instance, more than 40 million deaths were reported during the “Spanish flu” in 1918². Annual prophylactic vaccination is the most effective measure to prevent seasonal influenza infection³. Yet, the selection of strains as well as the manufacturing and release of seasonal vaccines requires several months. Thus, small-molecule drug antivirals are also used, for instance, to treat acute infections¹. However, circulating human IAV strains have acquired resistance against many current antivirals⁴. Therefore, new broadly-acting antiviral treatment options should be considered not only to complement annual vaccination schemes but also to act as a first line of defense for pandemic preparedness.

Defective interfering particles (DIPs) are regarded as a promising new class of antivirals^{4–17}. In particular, DIPs resulted in a high tolerability and antiviral efficacy in animal studies^{5,16,18–25}, and were therefore proposed as prophylactic and therapeutic antivirals^{16,25–27}. IAV DIPs typically contain a large internal deletion in one of the eight genomic viral RNA (vRNA) segments^{4,10,16,22,25,26,28–30}. The missing genomic information results in the expression of a truncated viral protein³¹. Therefore, DIPs are defective in virus replication and cannot propagate in mammalian cells. In a co-infection with an infectious standard virus (STV), however, the missing gene

¹Max Planck Institute for Dynamics of Complex Technical Systems, Bioprocess Engineering, Magdeburg, Germany. ²Institute of Medical Microbiology, Infection Prevention and Control, Infection Immunology Group, Health Campus Immunology, Infectiology and Inflammation, Otto Von Guericke University Magdeburg, Magdeburg, Germany. ³Immune Regulation Group, Helmholtz Centre for Infection Research, Braunschweig, Germany. ⁴Department of Veterinary Pathology, Freie Universität Berlin, Berlin, Germany. ⁵Bioprocess Engineering, Otto Von Guericke University Magdeburg, Magdeburg, Germany. ✉email: kupke@mpi-magdeburg.mpg.de

function (i.e., the full-length (FL) protein) is provided, and DIPs can propagate. Interestingly, this results in a strong interference with STV replication. With respect to this antiviral effect, it is suggested that the short defective interfering (DI) vRNAs replicate faster and accumulate to higher levels than the FL vRNAs. Thereby, cellular and viral resources are depleted, which suppresses infectious virus replication^{32–34}. DIP co-infections also result in a strong induction of the interferon (IFN) system^{35–38}, and it was shown that this stimulation of the innate immunity also contributes to their antiviral effect^{25,26,35,37}. As a consequence, IAV DIPs display a broad-spectrum antiviral activity that is not only directed against a wide range of IAV strains^{16,21,25,39,40}, but even against unrelated viruses, including SARS-CoV-2^{37,38,41,42}.

Previously, we developed a cell culture-based production process^{18,43} for a well-known DIP called “DI244” that harbors a deletion in segment 1 (Seg 1)^{25,26}. DI244 is unable to express the viral polymerase basic protein 2 (PB2, encoded from Seg 1) and can be propagated in genetically engineered PB2-expressing Madin-Darby canine kidney (MDCK) suspension (MDCK-PB2(sus)) cells^{18,43,44}. In addition, using a modified reverse genetics workflow for IAV that is specific for DIP rescue, clonal DI244 without STVs could be reconstituted for production⁴⁴. Therefore, considering the use of DIPs as an antiviral, the absence of infectious STVs is expected to alleviate potential safety and regulatory concerns.

We previously discovered a new type of IAV DIP, called “OP7” that contains multiple point substitutions on segment 7 (Seg 7) vRNA instead of a large internal deletion³⁹. OP7 showed a higher antiviral activity compared to Seg 1 conventional DIPs (cDIPs) including DI244 as shown in *in vitro* and *in vivo* experiments^{18,19,37}. As the source of the defect in virus replication of OP7 is yet unknown, designing a cell line that could complement the defect of OP7 was not feasible, so far. Instead, we recently established a cell culture-based production process for OP7 in the presence of infectious STVs to complement the unknown defect¹⁹. However, infectious STVs had to be UV-inactivated, which also reduced the antiviral activity of OP7. Moreover, even after UV treatment, the risk of contamination with residual STVs should raise safety concerns concerning medical application.

In the present study, we devised a genetically engineered cell culture-based production system for OP7, which does not require the addition of any infectious STV. Trials in mice suggest that the produced OP7 preparations can be used as a safe and potent antiviral, and further steps towards clinical development seem promising.

Results

Reconstitution of OP7 chimera DIPs without infectious STVs

Previously, OP7 was produced in cell culture in the presence of infectious STVs¹⁹. To obtain an OP7 virus without infectious STVs (STV-free), we modified a plasmid-based reverse genetics system for the reconstitution of Seg 1-derived cDIPs based on the IAV strain A/PR/8/34 (PR8) as described previously⁴⁴. As Seg 1 cDIPs contain a large internal deletion in Seg 1 and are unable to express the viral PB2 protein, the STV-free reconstitution of clonal Seg 1 cDIPs requires PB2-expressing cells (Fig. 1A–C). Here, a co-culture of adherent PB2-expressing human embryonic kidney (HEK-293T-PB2(adh)) and MDCK-PB2(adh) cells (Fig. 1B) were co-transfected with eight plasmids encoding for the deleted Seg 1 and the remaining seven wild-type (WT) segments (Fig. 1A). After reconstitution, such Seg 1 cDIPs (Fig. 1C) could be propagated in cell culture using PB2-expressing cells, as shown previously^{18,43,45}.

To reconstitute OP7 chimera DIPs without infectious STVs, we added a ninth plasmid encoding for the mutated Seg 7 of OP7 (Seg 7-OP7) (Fig. 1D) for transfection. This resulted in the rescue of a population of two types of DIPs: (i) Seg 1 cDIPs (Fig. 1C) and (ii) OP7 chimera DIPs (Fig. 1E). Accordingly, the Seg 1 cDIPs contained a truncated Seg 1 vRNA and seven WT vRNAs (Fig. 1C) and OP7 chimera DIPs contained Seg 7-OP7 vRNA, a truncated Seg 1 vRNA, and the remaining six WT vRNAs (Fig. 1E). Owing to a deletion in Seg 1 (encoding for PB2), both DIPs could be propagated in MDCK-PB2(sus) cells (Fig. 2). Furthermore, it has to be assumed that the OP7 chimera DIPs (Fig. 1E) are defective in virus replication in PB2-expressing cells, as they contain the mutated and defective Seg 7-OP7 vRNA. Accordingly, for propagation, OP7 chimera DIPs require complementation with Seg 1 cDIPs (Fig. 1C) as they provide the functional Seg 7-WT vRNA (Seg 7-WT). Moreover, as both DIPs (Fig. 1C,E) are replication deficient in non-PB2 expressing cells, we eliminate the need for post-production UV inactivation due to the lack of infectious STVs. Note that the deleted Seg 1 sequence used in the present study was previously identified by us (“Seg 1 gain”), where corresponding DIPs showed a superior *in vitro* interfering efficacy compared to the well-known DI244⁴⁵. A seed virus stock was generated from the reconstituted OP7 chimera DIP material by serial passaging in MDCK-PB2(adh) followed by MDCK-PB2(sus) cells. This seed virus was used for subsequent cell culture-based production (Fig. 2). The absence of infectious STVs in the produced OP7 chimera DIP material was evaluated by two serial passages in adherent WT MDCK (MDCK(adh)) cells (innocuity assay). Both passages showed no virus titer, thus confirming no infectious STV replication (data not shown).

In summary, we reconstituted OP7 chimera DIPs in a mixture with Seg 1 cDIPs without the addition of any infectious STVs. Seg 1 cDIPs can complement the defect of the OP7 chimera DIPs in PB2-expressing MDCK cells, allowing for cell culture-based production.

Cell culture-based production of OP7 chimera DIP preparation in shake flasks shows a strong dependence on the multiplicity of infection

As indicated above, OP7 chimera DIPs are defective in virus replication in MDCK-PB2(sus) cells and propagation requires co-infection with Seg 1 cDIPs. Previously, in a similar production system, we produced OP7 in the presence of infectious STVs in WT MDCK(sus) cells. As expected for virus production, total virus yields were multiplicity of infection (MOI) dependent¹⁹. High MOI conditions increased the likelihood of co-infection of STVs and OP7, resulting in preferential production of OP7 that suppressed STV propagation and thus, total virus yields. In contrast, in a low MOI scenario, more single hit infections occurred. Therefore, STV growth

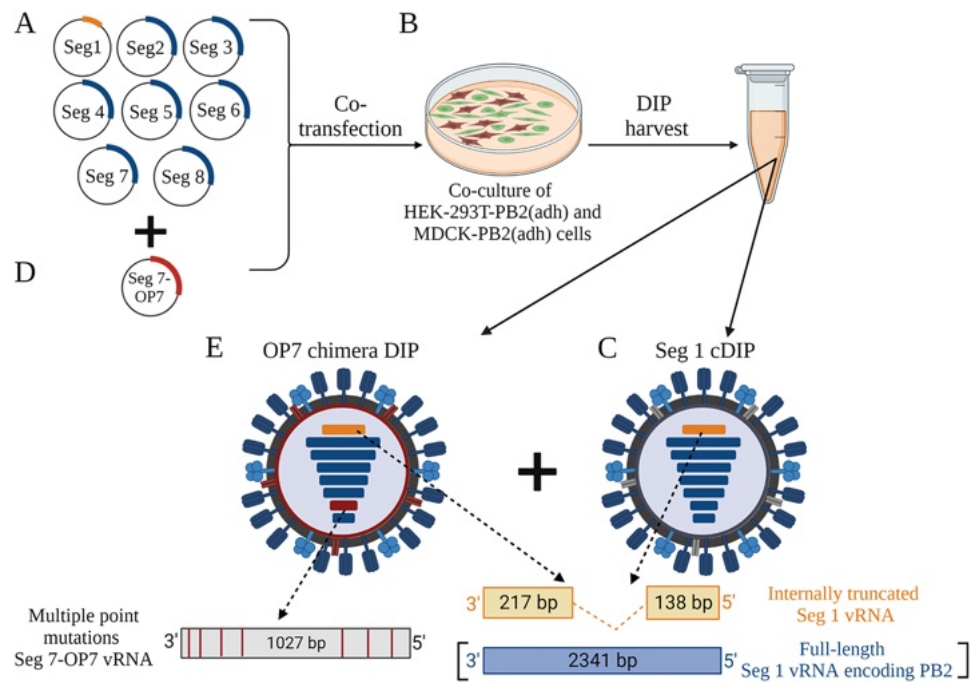


Figure 1. Plasmid-based reconstitution of OP7 chimera DIPs free of infectious STVs. Rescue of Seg 1 conventional DIPs (cDIPs). The reverse genetics system comprises (A) eight plasmids that encode for a deleted Seg 1 vRNA and Seg 2–8 wild type (WT) vRNAs. (B) Co-transfection of a co-culture of PB2-expressing HEK-293T-PB2(adh) (high transfection efficiency) and MDCK-PB2(adh) (high virus titers) cells results in reconstitution of (C) clonal Seg 1 cDIP free of infectious standard viruses (STV). Rescue of OP7 chimera DIPs: addition of a (D) ninth plasmid that encodes for the mutated Seg 7-OP7 vRNA results in the reconstitution of a mixture of DIPs including (E) OP7 chimera DIPs and (C) Seg 1 cDIPs. This mixture of viruses can be propagated in MDCK-PB2(sus) cells (Fig. 2). Image was created with BioRender.com.

occurred predominantly and the propagation-incompetent OP7 was out-diluted, resulting in higher total virus titers with a concomitant lower fraction of OP7¹⁹. We expected that the DIP mixture containing OP7 chimera DIPs and Seg 1 cDIPs would show the same MOI dependency in PB2-expressing cells. Thus, to optimize total virus yields and the fraction of OP7 chimera DIPs within the mixture, we performed infections in shake flasks using MDCK-PB2(sus) cells at different MOIs ranging from 1E-2 to 1E-5 (Fig. 2).

After infection at 2.1×10^6 cells/mL, cells continued to grow (Fig. 2A). The viable cell concentration (VCC) post infection at an MOI of 1E-2 peaked fastest (3.0×10^6 cells/mL, 18 hpi) before there was a decrease in VCC. With decreasing MOIs, the maximum VCC increased and cell death started later. As expected, the hemagglutinin (HA) titer (indicating total virus yield) reached lower values at higher MOIs relative to lower MOIs (Fig. 2B), likely due to the inhibition caused by the increasing accumulation of OP7 chimera DIPs towards higher MOIs. This is in line with greater fractions of OP7 chimera DIPs at higher MOIs (Fig. 2C,D). For instance, we found a fraction of OP7 chimera DIPs of 94.4% (MOI 1E-2) and 24.2% (MOI 1E-5), calculated based on the extracellular vRNA concentration of Seg 7-OP7 and Seg 7 of the WT virus quantified by reverse transcription real time PCR (RT-qPCR) (Fig. 2C). In addition, quantification of IAV proteins by a new mass spectrometry (MS) method developed in our group⁴⁶ showed similar fractions of 90.2% (MOI 1E-2) and 19.0% (MOI 1E-5). Here the fraction was calculated based on the concentration of the extracellular matrix protein 1 (M1, encoded on Seg 7) of OP7 (M1-OP7) and of the WT virus (M1-WT) (Fig. 2D). Further, the total virus concentration (as indicated by the extracellular Seg 5 vRNA concentration (Fig. 2C) and calculated from the nucleoprotein (NP) concentration (Fig. 2D)) showed higher values for lower MOIs in line with HA titers (Fig. 2B). Previously, biological activity of IAV particles decreased over time as seen by a drop in the infectious virus titers towards late process times⁴⁷, which is important for selecting the optimal harvest time point (Fig. 2B). Accordingly, for DIP harvesting, we selected the time point at which the HA titer almost plateaued to ensure maximum virus release and biological activity of the DIPs (MOI 1E-2: 25 hpi, MOI 1E-3: 32 hpi, MOI 1E-4: 40 hpi, MOI 1E-5: 48 hpi). Furthermore, harvesting was performed no later than the onset of cell death (Fig. 2A) to avoid excessive levels of cell debris and host cell DNA in the supernatant that would otherwise interfere with the subsequent downstream purification process. Further, final viral harvests were DIP depleted as we did not observe a strong accumulation of other DI vRNAs in Seg 2–8 as suggested by results from RT-PCR (Fig. 3).

Taken together, our results demonstrate that the MOI has a strong effect on OP7 chimera DIPs production. At high MOI, high fractions of OP7 chimera DIPs were present along with low total virus titers suggesting that OP7 chimera DIPs impeded virus propagation. On the other hand, higher total virus titers, but lower fractions

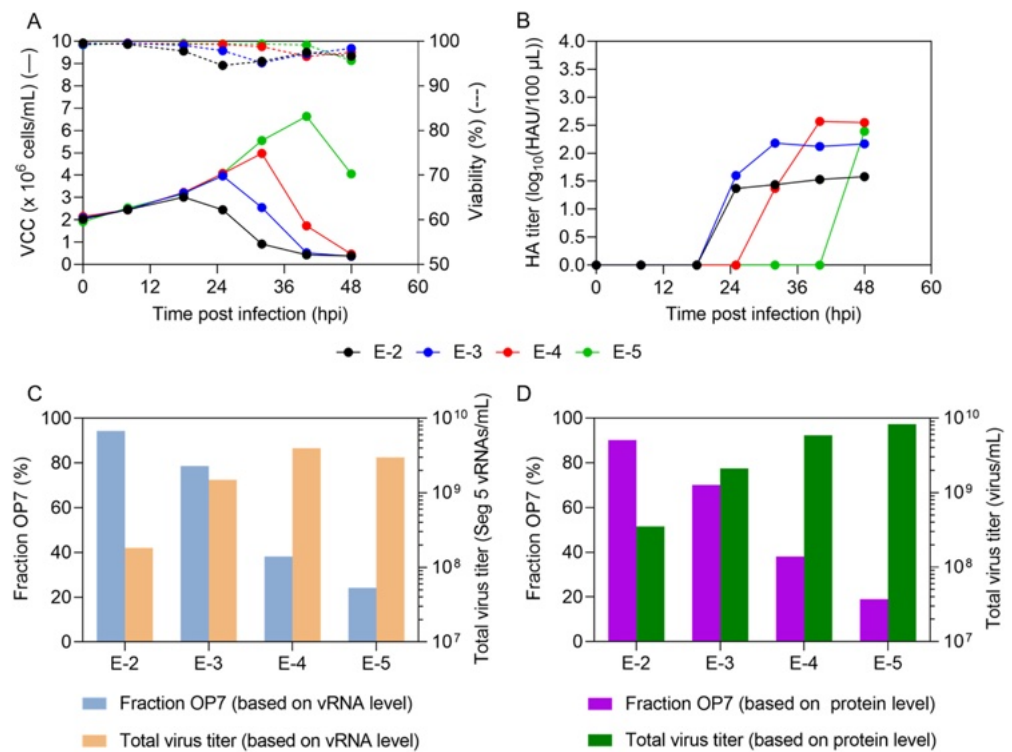


Figure 2. Cell culture-based production of OP7 chimera DIP enriched material in shake flasks. Genetically engineered MDCK-PB2(sus) cells cultivated in 125 mL shake flasks (50 mL working volume), were infected at multiplicity of infections (MOIs) ranging from 1E-2 to 1E-5 after a complete medium exchange. (A) Viable cell concentration (VCC) and viability. (B) Hemagglutinin assay (HA) titer. (C) Fraction of OP7 chimera DIPs (calculated based on extracellular Seg 7-OP7 and Seg 7-WT vRNA concentrations, quantified by reverse transcription real time PCR (RT-qPCR)). Total virus concentration is indicated by the extracellular Seg 5 vRNA concentration. (D) Fraction of OP7 chimera DIPs (calculated based on extracellular M1-OP7 and M1-WT viral protein concentrations, quantified by Mass spectrometry (MS)). Total virus concentration was calculated from the protein concentration of nucleoprotein (NP), encoded by Seg 5. The optimal harvest time points (MOI 1E-2: 25 hpi, 1E-3: 32 hpi, 1E-4: 40 hpi, 1E-5: 48 hpi) were analyzed for C and D. The figure depicts the results of one experiment.

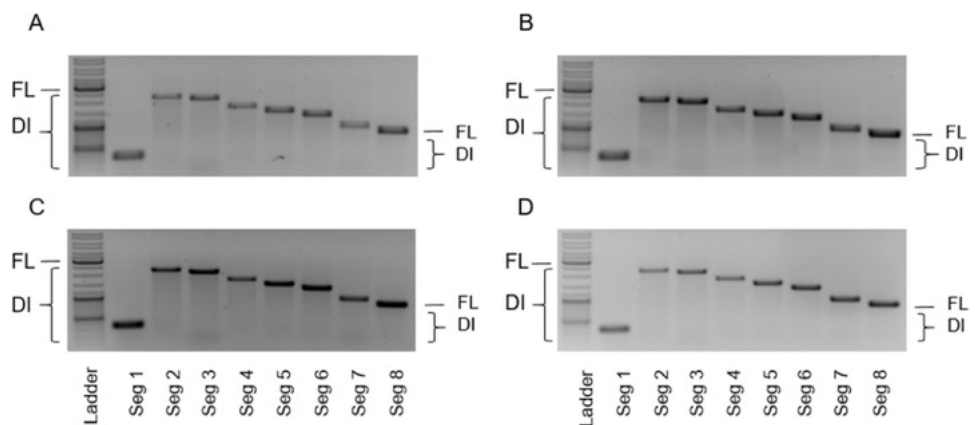


Figure 3. Purity of produced OP7 chimera DIP material with respect to contaminating DIPs. OP7 chimera enriched DIPs were produced at different MOIs in shake flasks (Fig. 2). Samples from 48 hpi were subjected to segment-specific reverse transcription PCR (RT-PCR) and gel electrophoresis. (A) MOI 1E-2, (B) MOI 1E-3, (C) MOI 1E-4, and (D) MOI 1E-5. The indicated signals correspond to FL and DI vRNAs. Upper thicker band of the ladder: 3000 bp, middle thicker band: 1000 bp, lower thicker band: 500 bp. Cropped gels are shown; original gels are presented in Supplementary Fig. S1.

of OP7 chimera DIPs were found at lower MOIs. Infections at intermediate MOIs of 1E-3 and 1E-4 appear to be a good compromise for achieving high OP7 chimera DIP fractions and high virus titers.

The MOI used for production affects the in vitro interfering efficacy

To identify the optimal MOI yielding OP7 chimera DIP material showing the highest in vitro interfering efficacy per product volume an in vitro interference assay (Fig. 4) was carried out. In brief, WT MDCK(adh) cells were either infected with STVs only at a MOI of 10 (negative control, NC) or co-infected with 125 μ L (fixed volume) of DIP material produced at different MOIs (Fig. 2).

Our results indicated the strongest interfering efficacy for the OP7 chimera DIP material produced at a MOI of 1E-3 and 1E-4. This was shown by a suppression of the infectious virus release by more than two orders of magnitude (quantified by the plaque assay), which was significantly more than the decrease of only a factor of two, observed for the material produced at a MOI of 1E-2 ($p < 0.0001$, One-way analysis of variance (ANOVA) followed by Tukey's multiple comparison test), and significantly different to the reduction of one log for the material produced at a MOI of 1E-5 ($p < 0.001$) (Fig. 4A). For the total virus release, as expressed by the HA titer (Fig. 4A) and extracellular Seg 5 vRNA concentration (Fig. 4B), this trend was less pronounced. Further, co-infections with highly interfering DIP material, produced at a MOI of 1E-3 and 1E-4, resulted in a pronounced OP7 phenotype, i.e. an overproportional extracellular Seg 7-OP7 vRNA concentration in comparison to other gene segments^{19,39}, indicating the preferential replication of Seg 7-OP7 vRNA during virus propagation (Fig. 4B). Similarly, an overproportional M1-OP7 concentration relative to M1-WT was found in progeny virions (Fig. 4C).

In summary, the interfering efficacy of OP7 chimera DIP preparations strongly depended on the MOI for production with intermediate MOIs of 1E-3 and 1E-4 representing the optimum.

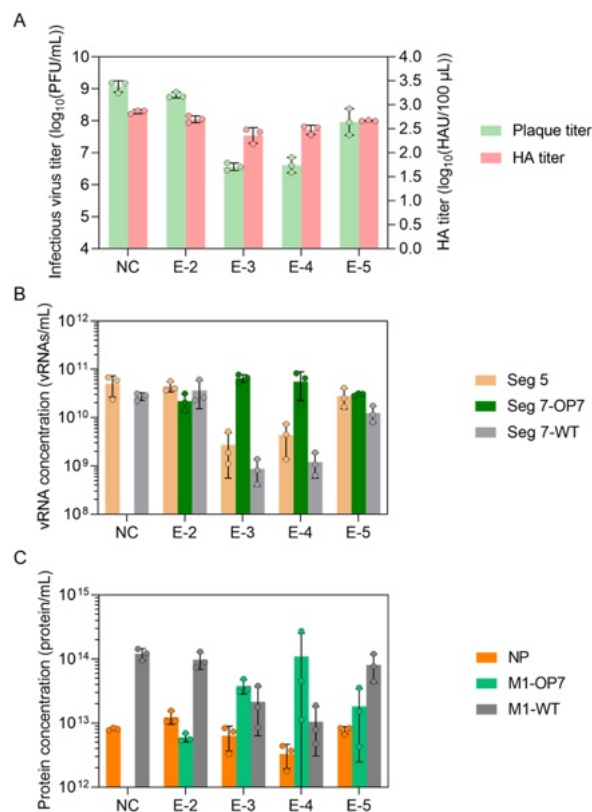


Figure 4. In vitro interference assay with OP7 chimera DIP enriched material produced at different MOIs. MDCK(adh) cells were infected with STVs alone at a MOI of 10 (NC) or co-infected with 125 μ L of indicated DIP material produced at different MOIs in shake flasks (Fig. 2). (A) Infectious virus release, indicated by plaque titer, and total virus release, indicated by HA titer, at 16 hpi. PFU, plaque-forming units; HAU, HA units. (B) Extracellular vRNA concentration, quantified by RT-qPCR. (C) Protein concentration, quantified by MS. NP, nucleoprotein. Interference assay was performed in three independent experiments, corresponding samples were quantified in a single measurement. Error bars indicate the standard deviation (SD). Samples of the optimal harvest time points (Fig. 2) were analyzed.

High in vivo tolerability and antiviral efficacy of OP7 chimera DIP material

To test the tolerability and antiviral efficacy of produced OP7 chimera DIP enriched material in a mouse infection model, DIP material produced in shake flasks and purified by steric exclusion chromatography (SEC)^{18,19,48,49} was used. The material was produced at MOI 1E-4 (8.96×10^9 virions/mL, calculated based on Seg 5 vRNA concentrations; OP7 chimera DIP fraction of 60.07%, calculated based on Seg 7-OP7 and Seg 7-WT vRNA concentrations). As a negative control, an OP7 chimera DIP preparation that was inactivated with UV light for 24 min was utilized, which typically does not show an interfering efficacy in vitro^{18,19}.

First, to test for the tolerability of the OP7 chimera DIP preparations, we administered 20 μ L of active OP7 chimera DIPs (diluted to 1:2 and 1:20, corresponding to 8.96×10^7 and 8.96×10^6 virions per mouse, respectively) intranasally to the animals (Fig. 5A–C). Similar to PBS treatment, OP7 chimera enriched DIP treatment was well-tolerated, as indicated by the absence of weight loss (Fig. 5A) and clinical scores (Fig. 5B). Moreover, serum albumin levels in bronchoalveolar lavage (BAL) samples of PBS and OP7 chimera DIP-treated mice were comparable, indicating that OP7 chimera DIP administration did not compromise lung integrity (Fig. 5C), which is otherwise typically observed in influenza-infected mice^{50–52}. This was further confirmed by histopathological examination of the lungs. For mice treated with PBS (Fig. 6A), only minimal interstitial pneumonia located near the hilus and affecting less than 5% of the lung tissue was observed; a finding that can be typically attributed to intranasal application of liquid to the lungs. Mice treated with OP7 chimera DIPs (1:2 and 1:20 dilution) showed a minimal increase in inflammatory infiltration with rare lymphocytes detectable in the interstitium and few macrophages and neutrophils in the alveoli (Fig. 6A,B middle and right column) affecting only small parts of the lung tissue at the hilus, too. Yet, no histopathological changes that appear to be clinically relevant were observed, which is in line with the presentation of the clinical scores (Fig. 5B). Together, these data demonstrate that intranasal administration of OP7 chimera DIPs alone is well-tolerated.

Next, we treated mice with a lethal dose of 1000 focus-forming units (FFU) of IAV STV (strain PR8) together with either active OP7 chimera DIPs (1:2 and 1:20), inactive OP7 chimera DIPs (1:2) or PBS (1:2) in a total volume of 20 μ L. As expected, severe body weight loss and 100% IAV-induced mortality was observed in PBS co-treated mice (Fig. 5D,F). Further, similar to PBS co-treatment, mice co-treated with inactive OP7 chimera DIPs showed the same high infection-induced morbidity (Fig. 5D,E) and mortality (Fig. 5F), indicating the absence of protective efficacy by UV inactivated DIPs. In strong contrast, no body weight loss was observed when active OP7 chimera DIPs (1:2 diluted) were co-administered, while a higher dilution (1:20) resulted in a modest loss of body weight (approx. 16%). Importantly, all mice co-applied with active OP7 chimera DIPs (1:2 and 1:20) survived the otherwise lethal STV infection (Fig. 5F). Intriguingly, co-administration of active OP7 chimera DIPs (1:2) together with a lethal STV dose completely prevented the development of clinical signs (Fig. 5E) related for influenza infection compared to PBS treatment only (Fig. 5B). Even co-administration of active OP7 chimera DIPs diluted to 1:20 together with a lethal dose of STV was highly effective in preventing a severe course of influenza disease (Fig. 5E). In line with these findings, histopathological analysis revealed only a low-grade pneumonia characterized by mild perivascular and interstitial lymphocytic infiltration, pneumocyte type II hyperplasia and alveolar histiocytosis of mice co-administered with a lethal dose of STVs and OP7 chimera DIPs at a dilution of 1:2 (Fig. 6B middle column). In comparison, a lethal dose of STV of strain PR8 typically resulted in hyper-inflammatory immune responses in infected lungs⁵³. Even the co-application of the low (1:20) dose OP7 chimera DIPs was sufficient to protect the animals from a lethal outcome of pneumonia (Fig. 6B right column). Histopathologically, similar qualitative changes were identified in the animals of this group, but the lesion extent was significantly greater with additional onset of interstitial fibrosis and, in isolated cases, low-grade, florid suppurative inflammation.

Taken together, intranasal application of only the OP7 chimera DIP material is very well-tolerated in mice. Furthermore, the co-administration of OP7 chimera DIPs mediated full protection against an otherwise lethal IAV STV infection. These data demonstrate the safety and remarkable antiviral efficacy of the produced OP7 chimera DIPs in vivo.

Discussion

Previous studies of our group showed that the MOI used for cell culture-based production of DIPs affects total virus yields^{18,19,54,55} and interfering efficacy^{18,19}. Likewise, in the present work, we found the highest interfering efficacy for material produced at intermediate MOIs of 1E-3 and 1E-4 (Fig. 2). Here, a balanced trade-off between the fraction of OP7 chimera DIPs and total virus yields in the produced material appears to be decisive for the optimal interfering efficacy observed in vitro.

In this study, we also evaluated the tolerability and efficacy of OP7 chimera DIP preparations harvested from shake flasks using a mouse model. Most laboratory mouse strains lack the *Mx1* gene, which is an important IFN-induced restriction factor against IAV infections in mice and in humans. Therefore, we used a mouse model expressing a functional *Mx1* gene, called D2(B6).A2G-*Mx1*^{r/r53}. Accordingly, this model better represents the immune response in humans to IAV infections. Intranasal administration of high doses of only OP7 chimera DIP enriched preparations did neither result in disease, nor in clinically relevant histopathological changes in mice lungs, indicating a high tolerability after OP7 chimera DIP treatment (Fig. 5A,B,C and Fig. 6A). These results (and those of other groups^{5,16,20–25,40}) clearly suggest that common concerns regarding adverse effects (e.g., cytokine storm, lung damage) due to DIP administration in animals can be abandoned and that DIPs, as defective, non-replicating viral particles might also be suitable for safe clinical applications in humans. Moreover, co-infection with a lethal dose of STV together with OP7 chimera DIPs resulted in 100% survival of the mice (Fig. 5F), and these animals did not even show signs of clinical disease (Fig. 5E). A similarly high antiviral activity (against lethal STV infection) was found for DIPs derived from IAV and from other viral species in different animal models^{5,16,18–25,40}. Earlier investigations on the use of DIPs as prophylactic antiviral agents have shown promising

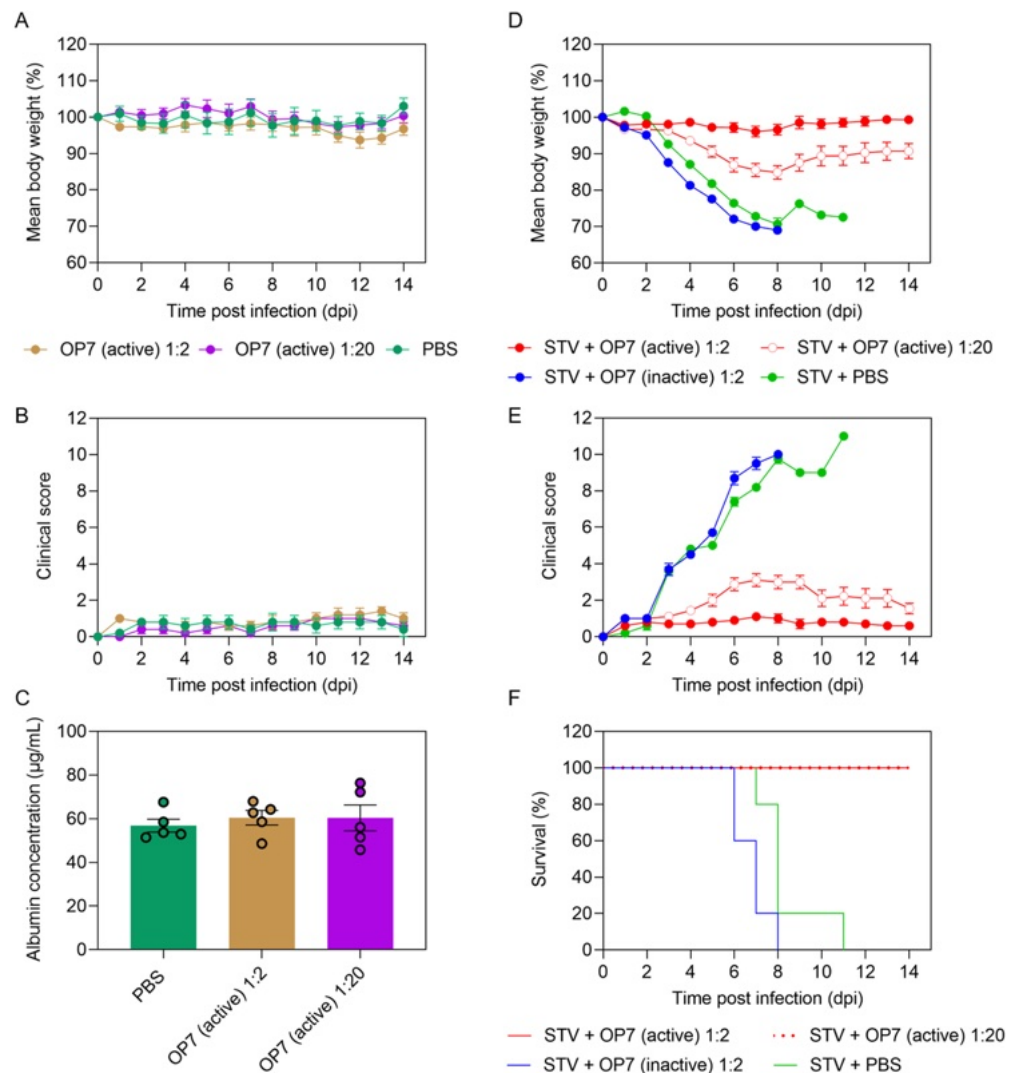


Figure 5. In vivo tolerability and antiviral efficacy of OP7 chimera DIP preparations in a mouse infection model. (A–C) 20 µL of active OP7 chimera DIP material diluted to 1:2 (8.96×10^7 virions/mouse) or 1:20 (8.96×10^6 virions/mouse), or 20 µL PBS was intranasally administered to 12–24 weeks old female D2(B6). A2G-Mx1^{fl/fl} mice (n = 5). (A) Mean body weight loss. Two-way ANOVA and Tukey correction for multiple comparison did not reveal a significant difference between groups ($p > 0.05$). (B) Clinical score. (C) Serum albumin concentrations in bronchoalveolar (BAL) fluid were measured by ELISA at 14 dpi. One-way ANOVA did not reveal a significant difference between means ($p > 0.05$). (D–F) Mice were treated with a lethal dose of 1000 FFU of IAV STV (strain PR8) together with either active OP7 chimera DIPs, diluted to 1:2 (n = 10) or 1:20 (n = 9), inactive OP7 chimera DIPs diluted to 1:2 (n = 10) or PBS (n = 5) in a total volume of 20 µL. (D) Mean body weight loss. The differences between the mean body weight of mice co-treated with 1:2 (mixed-effects model and Tukey correction for multiple comparison, $p < 0.0001$) or 1:20 OP7 chimera DIPs ($p < 0.05$) were significant relative to co-treatment with PBS. (E) Clinical score. (F) Kaplan-Meier curve representing the survival rate. The differences between the survival of mice co-treated with 1:2 (log-rank test for two groups, $p < 0.0001$) or 1:20 OP7 chimera DIPs ($p < 0.0001$) were significant relative to co-treatment with PBS. (A–F) Clinical score. (A–F) Error bars indicate the standard error of the mean (SEM).

results^{26,27}. Here, mice were intranasally pre-treated with DI244 (a well-characterized Seg 1 cDIP) seven days before infection with a lethal dose of IAV, and the DIP pre-administration continued to provide protection²⁵. Also, it was proposed to use DIPs as a therapeutic treatment due to its early onset of antiviral activity. Again, DI244 administered one or two days after lethal IAV challenge rendered full or partial protection, respectively²⁵.

In light of imminent pandemic threats, new broadly-acting antivirals that are readily available at low costs are required. IAV DIPs typically suppress a wide range of IAV strains including contemporary human epidemic, pandemic and even highly pathogenic avian IAV as demonstrated in vitro and in mouse and ferret

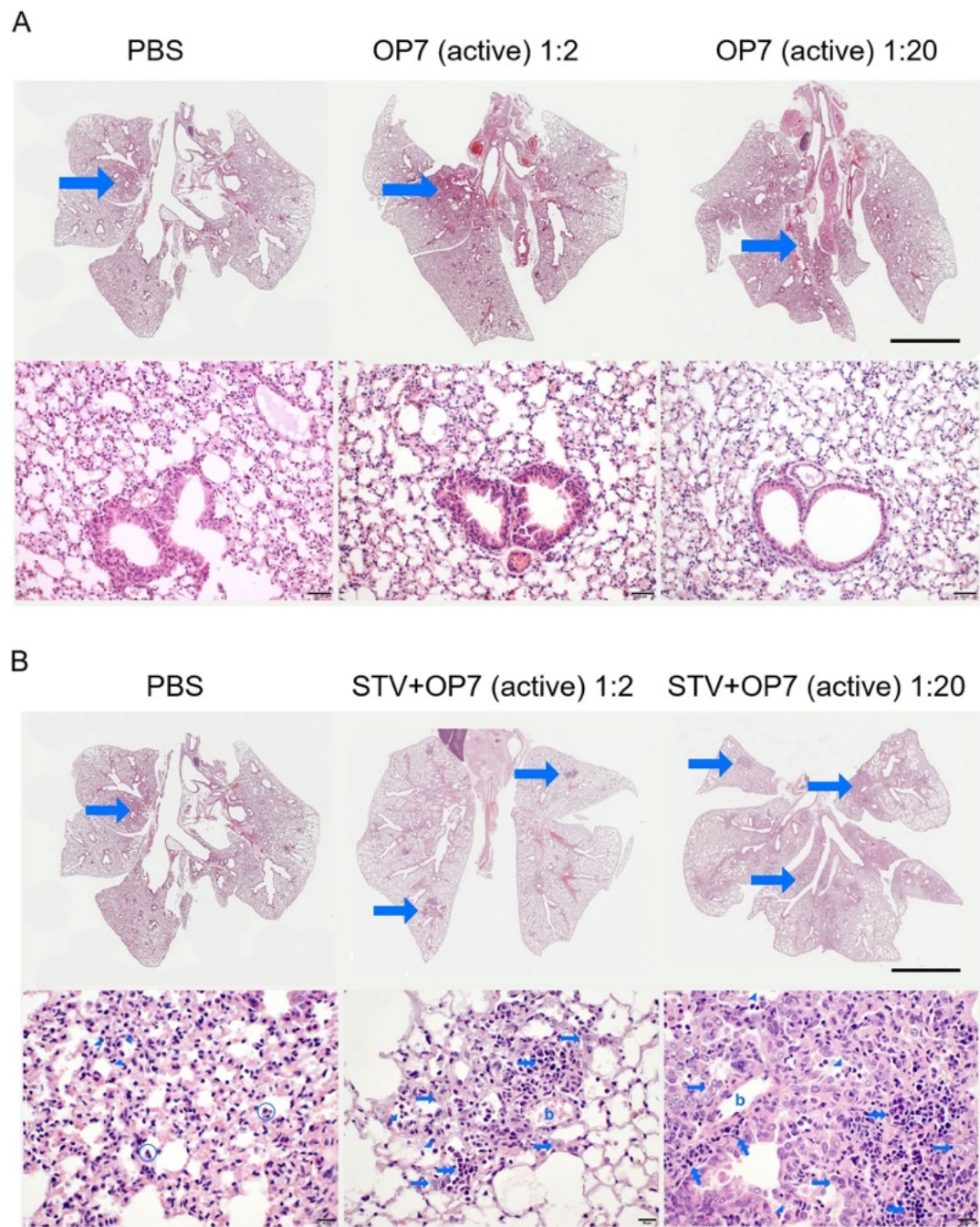


Figure 6. Histopathological changes in mouse lung sections after administration of OP7 chimera DIP enriched preparations and co-administration of STV with OP7 chimera DIP enriched preparations. **(A)** 20 μ L of active OP7 material diluted to 1:2 (8.96×10^7 virions/mouse) or 1:20 (8.96×10^6 virions/mouse), or 20 μ L PBS was intranasally administered to 12–24 weeks old female D2(B6).A2G-Mx1^{fl/y} mice (n = 5). Histopathological pictures of the lungs (14 days post infection) after hematoxylin–eosin (H&E) staining in overview (top row, bar = 1 cm) and peripheral lung in detail (bottom row, bar = 50 μ m). All lungs appear almost unchanged with only minimal interstitial pneumonia located near the hilus (arrows, for detail see image in the bottom row). **(B)** Mice were co-treated by administering 20 μ L volume containing a lethal dose of 1000 FFU of STV (strain PR8) with either active OP7, diluted to 1:2 (6.5×10^8 virions/mouse) or 1:20 (6.5×10^7 virions/mouse). Histopathological pictures of the lungs after H&E staining in overview (top row, bar = 1 cm) and areas of pneumonia in detail (bottom row, bar = 20 μ m) with minimal interstitial pneumonia located near the hilus after treatment with PBS (left image), few multifocal foci of inflammation after treatment with active OP7, diluted to 1:2 (middle image) and multifocal to confluent inflammatory infiltration after treatment with active OP7, diluted to 1:20 (right image). Arrowheads: alveolar histiocytosis; encircled: neutrophils; arrows: pneumocyte type II hyperplasia; double arrows: perivascular and interstitial lymphocytic infiltration; b: blood vessel.

experiments^{16,21,25,39,40}. Surprisingly, IAV DIPs can even suppress unrelated virus replication. This unspecific protection is mediated by the ability of DIPs to stimulate innate immunity and to establish a so-called antiviral state. For instance, mice were rescued from a lethal dose of influenza B virus and pneumonia virus of mice by DIP co-administration^{38,41}. In addition, we demonstrated a pronounced antiviral effect against SARS-CoV-2³⁷ and against respiratory syncytial, yellow fever and Zika virus replication *in vitro*⁴². Such broad protective immunity against many different unrelated viruses was also observed for dengue and poliovirus DIPs^{24,56}. This suggests that DIPs could be used as broadly-acting antiviral agents to treat viral infections as a fast countermeasure to protect people at risk and restrict virus spreading, e.g., in the case of a pandemic.

In future studies, a scalable cell culture-based production and purification process for OP7 chimera enriched DIPs should be established to achieve even higher titers and improve the purity of OP7 chimera DIP preparations. To leverage the antiviral potential of OP7 chimera DIPs, e.g. for use as an intranasal droplet spray^{26,27}, the establishment of a good manufacturing practice (GMP) production process would then be the base for toxicology and safety studies, clinical trials and later on to market approval.

Materials and methods

Cells and viruses

MDCK(adh) cells (obtained from ECACC, #84121903) and MDCK-PB2(adh) cells (expressing IAV PB2, generated by retroviral transduction, as described previously⁴⁴) were maintained in Glasgow Minimum Essential Medium (GMEM, Thermo Fisher Scientific, #221000093) supplemented with 10% fetal bovine serum (FBS, Merck, #F7524) and 1% peptone (Thermo Fisher Scientific, #211709). Puromycin (Thermo Fisher Scientific, #A1113803) was added to a concentration of 1.5 µg/mL for MDCK-PB2(adh) cells. HEK-293T-PB2(adh) cells (expressing IAV PB2, generated previously⁴⁴) were cultured in Dulbecco's Modified Eagle Medium (DMEM) supplemented with 10% FBS, 1% penicillin/streptomycin (10,000 units/mL penicillin and 10,000 µg/mL streptomycin, Thermo Fisher Scientific, #15140122) and puromycin at a concentration of 1 µg/mL. All adherent cells were maintained at 37 °C and 5% CO₂.

MDCK-PB2(sus) cells (expressing IAV PB2, previously generated by retroviral transduction^{18,44}) were grown in chemically defined Xeno[™] medium (Shanghai BioEngine Sci-Tech), supplemented with 8 mM glutamine and 0.5 µg/mL puromycin. Cultivation of the suspension cells was performed in shake flasks (125 mL baffled Erlenmeyer flask with vent cap, Corning, #1356244) in 50 mL working volume in an orbital shaker (Multitron Pro, Infors HT; 50 mm shaking orbit) at 185 rpm, 37 °C and 5% CO₂. To quantify VCC, viability and diameter of cell, Vi-cell[™] XR (Beckman Coulter, #731050) was used. IAV strain PR8 (provided by Robert Koch institute, #3138) was used for the interference assay. MOIs were based on the TCID₅₀ titer for STV⁵⁷ (interference assay) or the plaque assay (OP7 chimera DIP material production).

Rescue of OP7 chimera DIP

The generation of OP7 chimera DIPs was based on a previously established plasmid-based reverse genetics system for the rescue of PR8-derived Seg 1 cDIPs⁴⁴. Here, to complement the missing PB2 protein (deleted in Seg 1 cDIPs), a co-culture of HEK-293T-PB2(adh) cells and MDCK-PB2(adh) cells were used for plasmid transfections. For rescue of OP7 chimera DIPs, a pHW-based plasmid⁵⁸ harboring the sequence of Seg 7-OP7 (GenBank accession number: MH085234) was newly generated and kindly provided by Stefan Pöhlmann and Michael Winkler (German Primate Center, Goettingen, Germany). 50 ng of this plasmid was co-transfected with 500 ng of a pHW-based plasmid harboring the deleted Seg 1 sequence of a previously described cDIP ("Seg 1 gain"⁴⁵) and 1 µg of the remaining plasmids for Seg 2–6 and 8 (pHW192-pHW196 and pHW198⁵⁸, respectively) via the calcium phosphate-mediated transfection method. After reconstitution, OP7 chimera DIP material was amplified in MDCK-PB2(adh) cells and later used to infect MDCK-PB2(sus) cells for seed virus production.

OP7 chimera DIP material production in shake flasks

Production of OP7 chimera DIP preparations in shake flasks using MDCK-PB2(sus) cells was conducted with complete medium exchange prior to infection as described previously^{18,43}. In brief, cells in exponential growth phase were centrifuged (300×g, 5 min, room temperature) and resuspended in fresh medium (without puromycin) containing trypsin (final activity 20 U/mL, Thermo Fisher Scientific, #27250-018) at 2.0 × 10⁶ cells/mL. Cells were infected at different MOIs ranging from 1E-2 to 1E-5 at 37 °C and 5% CO₂. At indicated time points, samples were centrifuged (3000×g, 4 °C, 10 min) and supernatants were stored at -80 °C until further analysis. RNA of progeny virions was extracted from supernatants using the NucleoSpin RNA virus kit (Macherey-Nagel, #740956) according to the manufacturer's instructions and stored at -80 °C until PCR-based analysis.

OP7 chimera DIP material for mouse infection studies was produced in shake flasks at a MOI of 1E-4. Harvested DIP material was clarified (3000×g, 10 min and 4 °C) and sucrose (Merck, #84097) was added at a final concentration of 4%. Next, the material was purified and concentrated by SXC as previously described^{18,19,48}. Part of the purified, concentrated and sterile filtered DIP material was UV inactivated for 24 min. Active (no UV inactivation), inactive (UV inactivated) DIP material and PBS spiked with sucrose (4% final concentration) were stored at -80 °C until further use.

Virus quantification

Infectious virus titers were quantified using the plaque assay as previously described^{18,19,39} using MDCK(adh) cells (interfering assay) or MDCK-PB2(adh) cells (determination of OP7 chimera DIP containing seed virus titer). Infectious virus titers were expressed as plaque-forming units (PFU)/mL. Furthermore, total virus concentrations were quantified using the HA assay as previously described⁵⁹.

Segment-specific RT-PCR

To detect contaminating DI vRNAs in Seg 2–Seg 8 in progeny virions, purified extracellular RNA was subjected to segment-specific PCR as described previously^{39,54}. In brief, RNA was reverse transcribed to cDNA using a universal “Uni12” primer⁶⁰ that binds to all eight genome segments. The resulting cDNA samples were used to amplify each genomic segment individually using segment-specific primers. PCR products were analyzed by agarose gel electrophoresis.

RT-qPCR

In order to quantify the vRNAs purified from progeny virions, we used a previously described RT-qPCR method that enables polarity- and gene-specific quantification of individual vRNAs^{19,39,54}. For this, a methodology involving tagged primers was employed⁶¹. Primers used for quantification of the vRNA of Seg 5 are listed in^{39,54}, for Seg 7-OP7 in¹⁹, and for Seg 7-WT, new primers were designed for the present study (for reverse transcription, Seg 7-WT tagRT for: 5'-ATTTAGGTGACACTATAGAAGCGTCTCGCTATTGCCGAAA-3' and for qPCR, Seg 7-WT realtime rev: 5'-CCTTTCAGTCCGTATTTAAAGC-3'). In order to allow for absolute quantification, RNA reference standards were used. vRNA concentrations were calculated based on calibration curves.

Interference assay

The produced OP7 chimera DIP material was tested for the interfering efficacy *in vitro* according to a previously established protocol^{19,39}. Here, we assessed the inhibition of STV propagation upon co-infection with OP7 chimera DIP preparations. After infection, supernatants were analyzed for infectious and total virus titers using the plaque and HA assay, respectively. RT-qPCR and MS were used for quantification of vRNA and viral protein, respectively, of the progeny virions.

Quantification of IAV proteins

MS analysis was used for absolute quantification of M1-WT, M1-OP7 and NP according to a method described previously⁴⁶. For this, we used isotopically labelled peptides of synthetic origin of corresponding proteins that were added as an internal standard before tryptic digestion of the samples for absolute quantification (AQUA). For M1-OP7, a peptide containing one mutation, which is not present in the M1-WT (EITFYGAK) was used. For quantification of M1-WT, two peptides exclusive for M1-WT (LEDVFAGK, QMVTTTNPLIR) were used. In brief, supernatant samples containing DIPs were heat inactivated (3 min, 80 °C) for further processing. Next, total protein concentration was determined using a Pierce® BCA protein assay (Thermo Fisher Scientific, #23227) according to the manufacturer's protocol. Sample preparation for MS analysis was performed by using filter-aided sample preparation as described previously^{46,62}. After drying of the eluted peptides, 80 µL of mobile phase A (LC-MS-grade water, 0.1% trifluoroacetic acid) and 20 µL (= 2 pmol of each peptide) of peptide standard mix containing isotopically labelled peptides of synthetic origin for M1-WT, M1-OP7 and NP were added to each sample. Subsequently, MS analysis was carried out as described before⁴⁶. Raw files from Bruker timsTOF Pro were analysed by using Skyline (vs. 19.1)⁶³. Absolute protein copy numbers and virus concentrations were calculated as described previously⁴⁶.

Mouse infection experiments

D2(B6).A2G-Mx1^{+/r} mice were generated by backcrossing DBA/2Jr mice for 10 generations onto congenic B6.A2G-Mx1^{r/r} mice as described previously⁵³. Mice were bred and maintained in individually ventilated cages in a specific pathogen-free environment as per relevant guidelines and regulations (animal facility, Helmholtz Centre for Infection Research, Braunschweig Germany); food and water were provided *ad libitum*. Female, age-matched (12–24 weeks) D2(B6).A2G-Mx1^{+/r} mice that harbor a functional MX dynamin-like GTPase 1 (Mx1) resistance gene were randomly allocated into experimental groups. Following intraperitoneal injection of ketamine/xylazine, mice were intranasally administered with 20 µL of active OP7 chimera DIPs or PBS at indicated concentrations to test for the tolerability. Moreover, antiviral efficacy was studied by inoculation with a lethal dose of 1000 FFU of IAV STV strain PR8 and co-treatment with active OP7 chimera DIP enriched preparations at indicated concentrations, inactive OP7 chimera DIP enriched preparations or PBS in a total volume of 20 µL. Determination of the FFU titer was conducted as described elsewhere⁶⁴. Following administration, health status (body weight, appearance of fur, posture, activity) of mice was monitored at least once per day. In case humane endpoint criteria were reached, animals were humanely euthanized (via isoflurane inhalation and subsequent exsanguination) and the infection was recorded as lethal (AVMA guidelines were adhered). BAL samples were harvested as described previously⁶⁵. Serum albumin concentrations in BAL fluids were measured by ELISA (Fortis Life Sciences, #E90-134).

Histopathological analysis

Complete lungs of the mice were routinely fixed in 4% formalin and embedded in paraffin. Sections with 5 µm thickness were cut, dewaxed, and stained with hematoxylin–eosin (H&E). Histopathological evaluation was performed in a blinded manner by a veterinary pathologist certified by the European College of Veterinary Pathologists.

Statistical analysis

All the statistical analysis and graph generation were performed using GraphPad Prism 9 software.

Approval for animal experiments

Animals were maintained and treated as per ARRIVE guidelines. All in vivo experiments were conducted after review and approval of the study protocol by institutional (Helmholtz Centre for Infection Research) and regional ethical bodies (Niedersächsisches Landesamt fuer Verbraucherschutz und Lebensmittelsicherheit, LAVES 33.19-42502-04-18/2922).

Data availability

Data generated during this study can be requested from the corresponding co-author upon request.

Received: 21 August 2023; Accepted: 15 November 2023

Published online: 28 November 2023

References

1. Qiu, Z. & Feng, Z. Transmission dynamics of an influenza model with vaccination and antiviral treatment. *Bull. Math. Biol.* **72**, 1–33 (2010).
2. Taubenberger, J. K., Reid, A. H. & Fanning, T. G. The 1918 influenza virus: A killer comes into view. *Virology* **274**(2), 241–245 (2000).
3. Chen, J. *et al.* Advances in development and application of influenza vaccines. *Front. Immunol.* **12**, 711997 (2021).
4. Alnaji, F. G. & Brooke, C. B. Influenza virus DI particles: Defective interfering or delightfully interesting?. *PLoS Pathog.* **16**(5), e1008436 (2020).
5. Chaturvedi, S. *et al.* Identification of a therapeutic interfering particle-A single-dose SARS-CoV-2 antiviral intervention with a high barrier to resistance. *Cell* **184**(25), 6022–6036 (2021).
6. Girgis, S. *et al.* Evolution of naturally arising SARS-CoV-2 defective interfering particles. *Commun. Biol.* **5**(1), 1140 (2022).
7. Kalamvoki, M. & Norris, V. A defective viral particle approach to COVID-19. *Cells* **11**(2), 1 (2022).
8. Levi, L. I. *et al.* Defective viral genomes from chikungunya virus are broad-spectrum antivirals and prevent virus dissemination in mosquitoes. *PLoS Pathog.* **17**(2), e1009110 (2021).
9. Li, D. *et al.* Dengue virus-free defective interfering particles have potent and broad anti-dengue virus activity. *Commun. Biol.* **4**(1), 557 (2021).
10. Mendes, M. & Russell, A. B. Library-based analysis reveals segment and length dependent characteristics of defective influenza genomes. *PLoS Pathog.* **17**(12), e1010125 (2021).
11. Rezelj, V. V. *et al.* Defective viral genomes as therapeutic interfering particles against flavivirus infection in mammalian and mosquito hosts. *Nat. Commun.* **12**(1), 2290 (2021).
12. Rudiger, D. *et al.* Multiscale modeling of influenza A virus replication in cell cultures predicts infection dynamics for highly different infection conditions. *PLoS Comput. Biol.* **15**(2), e1006819 (2019).
13. Smither, S. J. *et al.* An investigation of the effect of transfected defective, ebola virus genomes on ebola replication. *Front. Cell Infect. Microbiol.* **10**, 159 (2020).
14. Tilston-Lunel, N. L. *et al.* Sustained replication of synthetic canine distemper virus defective genomes in vitro and in vivo. *mSphere* **6**(5), e0053721 (2021).
15. Wang, S. *et al.* Subgenomic RNA from dengue virus type 2 suppresses replication of dengue virus genomes and interacts with virus-encoded NS3 and NS5 proteins. *ACS Infect. Dis.* **6**(3), 436–446 (2020).
16. Zhao, H. *et al.* Dual-functional peptide with defective interfering genes effectively protects mice against avian and seasonal influenza. *Nat. Commun.* **9**(1), 2358 (2018).
17. Yao, S. *et al.* A synthetic defective interfering SARS-CoV-2. *PeerJ* **9**, e11686 (2021).
18. Hein, M. D. *et al.* Cell culture-based production and in vivo characterization of purely clonal defective interfering influenza virus particles. *BMC Biol.* **19**(1), 91 (2021).
19. Hein, M. D. *et al.* OP7, a novel influenza A virus defective interfering particle: Production, purification, and animal experiments demonstrating antiviral potential. *Appl. Microbiol. Biotechnol.* **105**(1), 129–146 (2021).
20. Zhao, H. *et al.* Peptidic defective interfering gene nanoparticles against Omicron, Delta SARS-CoV-2 variants and influenza A virus in vivo. *Signal Transduct. Target Ther.* **7**(1), 266 (2022).
21. Huo, C. *et al.* Defective viral particles produced in mast cells can effectively fight against lethal influenza A virus. *Front. Microbiol.* **11**, 553274 (2020).
22. Huo, C. *et al.* Safety, immunogenicity, and effectiveness of defective viral particles arising in mast cells against influenza in mice. *Front. Immunol.* **11**, 585254 (2020).
23. Welch, S. R. *et al.* Defective interfering viral particle treatment reduces clinical signs and protects hamsters from lethal nipah virus disease. *mBio.* **13**(2), e0329421 (2022).
24. Xiao, Y. *et al.* A defective viral genome strategy elicits broad protective immunity against respiratory viruses. *Cell* **184**(25), 6037–6051 (2021).
25. Dimmock, N. J. *et al.* Influenza virus protecting RNA: An effective prophylactic and therapeutic antiviral. *J. Virol.* **82**(17), 8570–8578 (2008).
26. Dimmock, N. J. & Easton, A. J. Cloned defective interfering influenza RNA and a possible pan-specific treatment of respiratory virus diseases. *Viruses* **7**(7), 3768–3788 (2015).
27. Dimmock, N. J. & Easton, A. J. Defective interfering influenza virus RNAs: Time to reevaluate their clinical potential as broad-spectrum antivirals?. *J. Virol.* **88**(10), 5217–5227 (2014).
28. Bdeir, N. *et al.* Evidence that two instead of one defective interfering RNA in influenza A virus-derived defective interfering particles (DIPs) does not enhance antiviral activity. *Sci. Rep.* **11**(1), 20477 (2021).
29. Wang, C. *et al.* Cell-to-cell variation in defective virus expression and effects on host responses during influenza virus infection. *J. Biol.* **11**(1), 1 (2020).
30. Alnaji, F. G. *et al.* Influenza A virus defective viral genomes are inefficiently packaged into virions relative to wild-type genomic RNAs. *mBio* **12**(6), e0295921 (2021).
31. Boergeling, Y. *et al.* Evidence for a novel mechanism of influenza virus-induced type I interferon expression by a defective rna-encoded protein. *PLoS Pathog.* **11**(5), e1004924 (2015).
32. Nayak, D. P., Chambers, T. M. & Akkina, R. K. Defective-interfering (DI) RNAs of influenza viruses: origin, structure, expression, and interference. *Curr. Top. Microbiol. Immunol.* **114**, 103–151 (1985).
33. Laske, T. *et al.* Modeling the intracellular replication of influenza A virus in the presence of defective interfering RNAs. *Virus Res.* **213**, 90–99 (2016).
34. Duhaut, S. D. & McCauley, J. W. Defective RNAs inhibit the assembly of influenza virus genome segments in a segment-specific manner. *Virology* **216**(2), 326–337 (1996).

35. Ziegler, C. M. & Botten, J. W. Defective interfering particles of negative-strand RNA viruses. *Trends Microbiol.* **28**(7), 554–565 (2020).
36. Yang, Y. C. *et al.* The antiviral and antitumor effects of defective interfering particles/genomes and their mechanisms. *Front. Microbiol.* **10**, 1 (2019).
37. Rand, U. *et al.* Antiviral activity of influenza A virus defective interfering particles against SARS-CoV-2 replication in vitro through stimulation of innate immunity. *Cells* **10**(7), 1 (2021).
38. Scott, P. D. *et al.* Defective interfering influenza A virus protects in vivo against disease caused by a heterologous influenza B virus. *J. Gen. Virol.* **92**(Pt 9), 2122–2132 (2011).
39. Kupke, S. Y. *et al.* A novel type of influenza A virus-derived defective interfering particle with nucleotide substitutions in its genome. *J. Virol.* **93**(4), 1 (2019).
40. Dimmock, N. J. *et al.* Cloned defective interfering influenza virus protects ferrets from pandemic 2009 influenza A virus and allows protective immunity to be established. *PLoS One* **7**(12), e49394 (2012).
41. Easton, A. J. *et al.* A novel broad-spectrum treatment for respiratory virus infections: Influenza-based defective interfering virus provides protection against pneumovirus infection in vivo. *Vaccine* **29**(15), 2777–2784 (2011).
42. Pelz, L. *et al.* Broad-spectrum antiviral activity of Influenza A defective interfering particles against respiratory syncytial, Yellow Fever, and Zika Virus replication in vitro. *Viruses* **15**(9), 1 (2023).
43. Hein, M. D. *et al.* Cell culture-based production of defective interfering influenza A virus particles in perfusion mode using an alternating tangential flow filtration system. *Appl. Microbiol. Biotechnol.* **105**(19), 7251–7264 (2021).
44. Bdeir, N. *et al.* A system for production of defective interfering particles in the absence of infectious influenza A virus. *PLoS One* **14**(3), e0212757 (2019).
45. Pelz, L. *et al.* Semi-continuous propagation of Influenza A virus and its defective interfering particles: Analyzing the dynamic competition to select candidates for antiviral therapy. *J. Virol.* **95**(24), e0117421 (2021).
46. Kuchler, J. *et al.* Absolute quantification of viral proteins during single-round replication of MDCK suspension cells. *J. Proteom.* **259**, 104544 (2022).
47. Genzel, Y. *et al.* MDCK and Vero cells for influenza virus vaccine production: A one-to-one comparison up to lab-scale bioreactor cultivation. *Appl. Microbiol. Biotechnol.* **88**(2), 461–475 (2010).
48. Marichal-Gallardo, P. *et al.* Steric exclusion chromatography for purification of cell culture-derived influenza A virus using regenerated cellulose membranes and polyethylene glycol. *J. Chromatogr. A* **1483**, 110–119 (2017).
49. Marichal-Gallardo, P. *et al.* Single-use capture purification of adeno-associated viral gene transfer vectors by membrane-based steric exclusion chromatography. *Hum. Gene Ther.* **32**(17–18), 959–974 (2021).
50. Wiley, J. A. *et al.* Inducible bronchus-associated lymphoid tissue elicited by a protein cage nanoparticle enhances protection in mice against diverse respiratory viruses. *PLoS One* **4**(9), e7142 (2009).
51. Kim, C. U. *et al.* Influenza viral matrix 1 protein aggravates viral pathogenicity by inducing TLR4-mediated reactive oxygen species production and apoptotic cell death. *Cell Death Dis.* **14**(3), 228 (2023).
52. Schmit, T. *et al.* Interferon-gamma promotes monocyte-mediated lung injury during influenza infection. *Cell Rep.* **38**(9), 110456 (2022).
53. Shin, D. L. *et al.* Protection from severe influenza virus infections in mice carrying the Mx1 influenza virus resistance gene strongly depends on genetic background. *J. Virol.* **89**(19), 9998–10009 (2015).
54. Frensch, T. *et al.* Impact of defective interfering particles on virus replication and antiviral host response in cell culture-based influenza vaccine production. *Appl. Microbiol. Biotechnol.* **98**(21), 8999–9008 (2014).
55. Rudiger, D. *et al.* Multiscale model of defective interfering particle replication for influenza A virus infection in animal cell culture. *PLoS Comput. Biol.* **17**(9), e1009357 (2021).
56. Lin, M. H. *et al.* Defective interfering particles with broad-acting antiviral activity for dengue, Zika, Yellow Fever, respiratory syncytial and SARS-CoV-2 virus infection. *Microbiol. Spectr.* **10**(6), e0394922 (2022).
57. Genzel, Y. & Reichl, U. Vaccine production. In *Animal Cell Biotechnology* (ed. Portner, R.) 457–473 (Humana Press, 2007).
58. Hoffmann, E. *et al.* A DNA transfection system for generation of influenza A virus from eight plasmids. *Proc. Natl. Acad. Sci. USA* **97**(11), 6108–6113 (2000).
59. Kalbfuss, B. *et al.* Monitoring influenza virus content in vaccine production: Precise assays for the quantitation of hemagglutination and neuraminidase activity. *Biologicals* **36**(3), 145–161 (2008).
60. Hoffmann, E. *et al.* Universal primer set for the full-length amplification of all influenza A viruses. *Arch. Virol.* **146**(12), 2275–2289 (2001).
61. Kawakami, E. *et al.* Strand-specific real-time RT-PCR for distinguishing influenza vRNA, cRNA, and mRNA. *J. Virol. Methods* **173**(1), 1–6 (2011).
62. Wiśniewski, J. R. *et al.* Universal sample preparation method for proteome analysis. *Nat. Methods* **6**(5), 359–362 (2009).
63. MacLean, B. *et al.* Skyline: An open source document editor for creating and analyzing targeted proteomics experiments. *Bioinformatics* **26**(7), 966–968 (2010).
64. Lambertz, R. L. O. *et al.* Exchange of amino acids in the H1-haemagglutinin to H3 residues is required for efficient influenza A virus replication and pathology in Tmprss2 knock-out mice. *J. Gen. Virol.* **99**(9), 1187–1198 (2018).
65. Sharma-Chawla, N. *et al.* In vivo neutralization of pro-inflammatory cytokines during secondary streptococcus pneumoniae infection post Influenza A virus infection. *Front. Immunol.* **10**, 1864 (2019).

Acknowledgements

For the excellent technical assistance we thank Claudia Best, Nancy Wynserski, and Karin Lammert. Xeno™ medium used in the study was kindly supplied by Shanghai BioEngine Sci-Tech and Prof. Tan from the East China University of Science and Technology. We would like to thank Prof. Stefan Pöhlmann and Michael Winkler from the German Primate Center, Goettingen, Germany for providing WT IAV segments and Seg 7-OP7 vRNA encoding plasmids.

Author contributions

Conceptualization, T.D., L.P., M.D.H., S.Y.K., and U.R.; formal analysis, L.P., J.B.; funding acquisition, A.G., D.B. (Dunja Bruder), U.R.; investigation, T.D., L.P., J.B., J.K., O.K., P.M., M.B.; project administration, T.D., L.P., S.Y.K.; supervision, D.B. (Dirk Benndorf), A.G., Y.G., D.B. (Dunja Bruder), S.Y.K., U.R.; visualization, T.D., L.P., O.K., S.Y.K.; writing—original draft, T.D.; L.P.; writing—review and editing, T.D., L.P., J.B., J.K., O.K., P.M., M.B., M.D.H., A.G., D.B. (Dirk Benndorf), Y.G., D.B. (Dunja Bruder), S.Y.K., U.R..

Funding

Open Access funding enabled and organized by Projekt DEAL.

Competing interests

A patent to treat IAV infections with OP7 as an antiviral agent is pending. Patent holders are S.Y.K. and U.R. Another patent about treating coronavirus infection using DI244 and OP7 as antiviral agents is pending. Patent holders are S.Y.K., U.R., M.D.H., D.B. (Dunja Bruder). All other authors declare that they do not hold any competing interest.

Additional information

Supplementary Information The online version contains supplementary material available at <https://doi.org/10.1038/s41598-023-47547-1>.

Correspondence and requests for materials should be addressed to S.Y.K.

Reprints and permissions information is available at www.nature.com/reprints.

Publisher's note Springer Nature remains neutral with regard to jurisdictional claims in published maps and institutional affiliations.



Open Access This article is licensed under a Creative Commons Attribution 4.0 International License, which permits use, sharing, adaptation, distribution and reproduction in any medium or format, as long as you give appropriate credit to the original author(s) and the source, provide a link to the Creative Commons licence, and indicate if changes were made. The images or other third party material in this article are included in the article's Creative Commons licence, unless indicated otherwise in a credit line to the material. If material is not included in the article's Creative Commons licence and your intended use is not permitted by statutory regulation or exceeds the permitted use, you will need to obtain permission directly from the copyright holder. To view a copy of this licence, visit <http://creativecommons.org/licenses/by/4.0/>.

© The Author(s) 2023

3.5. Fifth Manuscript

In the study of the fifth manuscript, the development of a scalable, more productive and robust process for production in STR of highly efficacious and almost pure OP7 chimera DIP preparations is presented. Moreover, the possibility of process intensification for production of OP7 chimera DIPs in perfusion mode is evaluated to increase VCC and virus titers.

Pelz, Lars; Dogra, Tanya; Marichal-Gallardo, Pavel; Hein, Marc D.; Hemissi, Ghada; Kupke, Sascha Y.; Genzel, Yvonne; Reichl, Udo

Production of antiviral “OP7 chimera” defective interfering particles free of infectious virus

Applied Microbiology and Biotechnology, 2024

(Pelz et al., 2024)

Reproduced with permission from Springer Nature.

No changes were made

<https://creativecommons.org/licenses/by/4.0/>

Individual contribution:

In the study of the fifth manuscript, I carried out the experiments shown in Figure 2, 3, and 5. In addition, I visualized data, wrote the abstract and results section (except for Figure 4) and major parts of materials & methods and discussion section.



Production of antiviral “OP7 chimera” defective interfering particles free of infectious virus

Lars Pelz¹ · Tanya Dogra¹ · Pavel Marichal-Gallardo¹ · Marc Dominique Hein² · Ghada Hemissi¹ · Sascha Young Kupke¹ · Yvonne Genzel¹ · Udo Reichl^{1,2}

Received: 21 August 2023 / Revised: 26 October 2023 / Accepted: 5 November 2023
© The Author(s) 2024

Abstract

Defective interfering particles (DIPs) of influenza A virus (IAV) are suggested for use as broad-spectrum antivirals. We discovered a new type of IAV DIP named “OP7” that carries point mutations in its genome segment (Seg) 7 instead of a deletion as in conventional DIPs (cDIPs). Recently, using genetic engineering tools, we generated “OP7 chimera DIPs” that carry point mutations in Seg 7 plus a deletion in Seg 1. Together with cDIPs, OP7 chimera DIPs were produced in shake flasks in the absence of infectious standard virus (STV), rendering UV inactivation unnecessary. However, only part of the virions harvested were OP7 chimera DIPs (78.7%) and total virus titers were relatively low. Here, we describe the establishment of an OP7 chimera DIP production process applicable for large-scale production. To increase total virus titers, we reduced temperature from 37 to 32 °C during virus replication. Production of almost pure OP7 chimera DIP preparations (99.7%) was achieved with a high titer of 3.24 log₁₀(HAU/100 μL). This corresponded to an 11-fold increase relative to the initial process. Next, this process was transferred to a stirred tank bioreactor resulting in comparable yields. Moreover, DIP harvests purified and concentrated by steric exclusion chromatography displayed an increased interfering efficacy in vitro. Finally, a perfusion process with perfusion rate control was established, resulting in a 79-fold increase in total virus yields compared to the original batch process in shake flasks. Again, a very high purity of OP7 chimera DIPs was obtained. This process could thus be an excellent starting point for good manufacturing practice production of DIPs for use as antivirals.

Key points

- Scalable cell culture-based process for highly effective antiviral OP7 chimera DIPs
- Production of almost pure OP7 chimera DIPs in the absence of infectious virus
- Perfusion mode production and purification train results in very high titers

Keywords Influenza A virus · Defective interfering particles · Antiviral · Cell culture · Perfusion · Alternating tangential flow filtration

Introduction

Influenza A virus (IAV) is a respiratory pathogen, which contains a negative-sense, single-stranded RNA genome with eight viral RNA (vRNA) segments (Krammer et al. 2018). Each year, IAV infections lead to a high disease burden with up to 290,000–650,000 deaths globally (WHO 2023). Current preventive measures include annual flu vaccination and the use of antivirals. However, the update in the composition of seasonal vaccines for the northern and southern hemisphere is a time-consuming process that involves the risk of poor vaccine effectiveness due to a mismatch of vaccine strains (reviewed by Chen et al. (Chen et al. 2021)). Moreover, the use of presently available antivirals like

✉ Sascha Young Kupke
kupke@mpi-magdeburg.mpg.de

✉ Yvonne Genzel
genzel@mpi-magdeburg.mpg.de

¹ Max Planck Institute for Dynamics of Complex Technical Systems, Bioprocess Engineering, Magdeburg, Germany

² Otto Von Guericke University Magdeburg, Bioprocess Engineering, Magdeburg, Germany

neuraminidase or M2 ion channel inhibitors has resulted in the emergence of resistant IAV strains (Chen et al. 2021). Consequently, further options for flu disease prevention and treatment would be highly appreciated.

Defective interfering particles (DIPs) of IAV are naturally occurring viral mutants that inhibit infectious standard virus (STV) propagation of IAV (Dimmock et al. 2008; Hein et al. 2021a; Huo et al. 2020; Pelz et al. 2021; Zhao et al. 2018). In addition, DIPs with antiviral activity exist for many other virus families (Chaturvedi et al. 2021; Levi et al. 2021; Rezelj et al. 2021; Smither et al. 2020; Welch et al. 2020). Therefore, DIPs were suggested as promising antivirals (Bdeir et al. 2019; Frensing 2015; Genoyer and Lopez 2019; Karki et al. 2022; Vasilijevic et al. 2017). Conventional IAV DIPs (cDIPs) contain a large internal deletion in one of the eight vRNAs (Dimmock and Easton 2015). The short defective interfering (DI) vRNAs are believed to replicate faster than the parental full-length (FL) vRNA in a co-infection with STV, thereby drawing away cellular and viral resources from STV (i.e., “replication inhibition”) (Laske et al. 2016; Marriott and Dimmock 2010; Nayak et al. 1985; Rüdiger et al. 2021). As a result, IAV DIPs can suppress a variety of IAV strains including epidemic and pandemic human, and even highly pathogenic avian IAV as shown in *in vitro* and in animal experiments (Dimmock et al. 2008, Dimmock et al. 2012b; Huo et al. 2020; Kupke et al. 2019; Zhao et al. 2018). Simultaneously, they strongly stimulate the interferon (IFN)-induced antiviral activity against IAV infections (Frensing et al. 2014; Huo et al. 2020; Penn et al. 2022). Furthermore, this unspecific innate immune response stimulation can also suppress replication of unrelated viruses including severe acute respiratory syndrome coronavirus (SARS-CoV-2) (Easton et al. 2011; Pelz et al. 2023; Rand et al. 2021; Scott et al. 2011). Previously, we discovered a new type of IAV DIP named “OP7”. OP7 harbors multiple

nucleotide substitutions in segment (Seg) 7 vRNA instead of the large internal deletion of cDIPs. The 37 point mutations involve promoter regions, genome packaging signals, and encoded proteins (Kupke et al. 2019). Relative to cDIPs, OP7 exhibited an even higher interfering efficacy *in vitro* and *in vivo*, highlighting its potential for use as an antiviral (Hein et al. 2021a, 2021c; Rand et al. 2021).

Recently, we established a cell culture-based production system for “OP7 chimera DIPs” that harbor both, nucleotide substitutions in Seg 7 vRNA plus a large internal deletion in Seg 1. In the presence of cDIPs, the addition of STV is not required for their propagation, and DIP harvests do not contain any infectious material. This renders UV inactivation unnecessary and alleviates safety and regulatory concerns with respect to medical application (Dogra et al. 2023). For this, we modified a reverse genetics workflow (Bdeir et al. 2019; Hein et al. 2021a) and reconstituted a population of two types of DIPs: OP7 chimera DIPs (Fig. 1a) and Seg 1 cDIPs (Fig. 1b). OP7 chimera DIPs harbor Seg 7 of OP7 (Seg 7-OP7) vRNA, a truncated Seg 1 vRNA, and the remaining six FL vRNAs. Seg 1 cDIPs contain a deletion in Seg 1 vRNA and seven FL vRNAs. To complement for the defect in virus replication, suspension Madin-Darby canine kidney (MDCK) cells were genetically engineered that express the viral polymerase basic 2 (PB2) protein (encoded on Seg 1) (Bdeir et al. 2019; Hein et al. 2021a) and are used for cell culture-based production. First results with OP7 chimera DIP material harvested from shake flasks suggest a high tolerability and high antiviral efficacy after intranasal administration in mice. These initial experiments, however, only resulted in relatively low total virus titers with OP7 chimera DIP fractions of 78.7% (Dogra et al. 2023).

In the present work, we developed a scalable laboratory-scale process in a stirred tank bioreactor (STR) for high-yield production of almost pure OP7 chimera

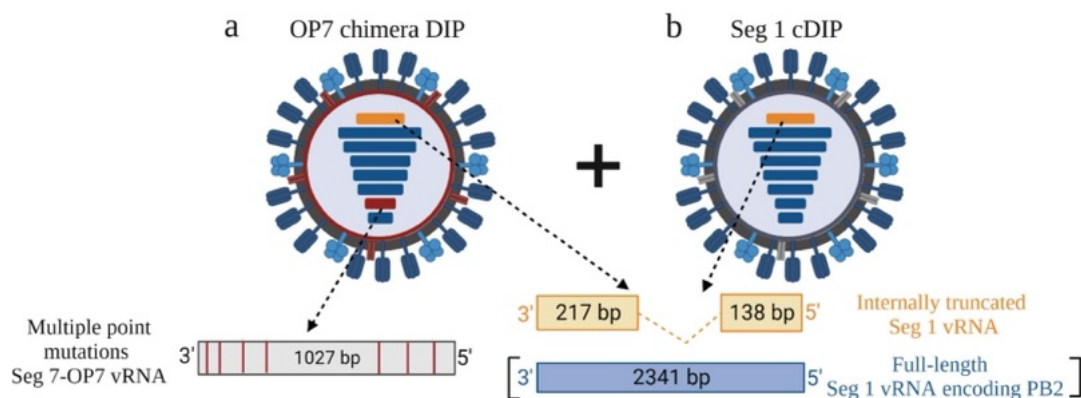


Fig. 1 Scheme of OP7 chimera DIPs and Seg 1 cDIPs. Reverse genetics was used to generate a mixture of **a**) OP7 chimera DIPs and **b**) Seg 1 cDIPs. Both together replicate without addition of infectious

standard virus as the missing PB2 is provided by MDCK-PB2(sus) cells. Figure adapted from (Dogra et al. 2023). Created with BioRender.com

DIPs preparations. In perfusion mode, we even achieved a 79-fold increase in total virus yields compared to the original batch process in shake flasks. Together with a steric exclusion-based chromatographic purification train, this process may be adopted towards good manufacturing practice (GMP) production for safety and toxicology studies and clinical trials.

Materials and methods

Cells and viruses

MDCK cells growing in suspension culture (Lohr et al. 2010) and stably expressing PB2 (encoded by Seg 1) (Bdeir et al. 2019; Hein et al. 2021b), referred to as MDCK-PB2(sus) cells, were used. These cells were cultivated in Xeno™ medium (Shanghai BioEngine Sci-Tech) supplemented with 8 mM glutamine and 0.5 µg/mL puromycin as selection antibiotic and maintained in shake flasks (125 mL baffled Erlenmeyer flask with vent cap, Corning, #1356244) in 50 mL working volume (V_w). Cultivations of cell cultures were performed in an orbital shaker (Multitron Pro, Infors HT; 50 mm shaking orbit) at 185 rpm, 37 °C, and 5% CO₂ environment. MDCK(adh) cells grew in Glasgow Minimum Essential Medium (GMEM) supplemented with 10% fetal bovine serum (FBS, Merck, #F7524) and 1% peptone (Thermo Fisher Scientific, #211709). For adherent MDCK cells (ECACC, #84121903) expressing PB2 (MDCK-PB2(adh), generated by retroviral transduction, as described in (Bdeir et al. 2019)), the medium was supplemented with 1.5 µg/mL puromycin. Human alveolar epithelial Calu-3 cells were provided by Dunja Bruder (Helmholtz Centre for Infection Research, Braunschweig, Germany) and cultivated in Minimum Essential Medium (MEM) with 10% FBS, 1% penicillin/streptomycin, and 1% sodium pyruvate at 37 °C and 5% CO₂. Viable cell concentration (VCC), viability, and cell diameter were quantified by a cell counter (Vi-Cell™ XR, Beckman coulter). Metabolite concentrations (glucose, lactate, glutamine, ammonium) were quantified with a Cedex Bio® Analyzer (Roche).

IAV strain A/PR/8/34 H1N1 (STV PR8) was provided by the Robert Koch Institute (Berlin, Germany, #3138) (seed virus: infectious virus titer 1.1×10^9 50% tissue culture infectious dose ((TCID₅₀)/mL). The OP7 chimera DIP seed virus (4.5×10^6 plaque-forming units ((PFU)/mL) was previously produced in MDCK-PB2(sus) cells in batch mode after a complete medium exchange (CME) in shake flasks at a multiplicity of infection (MOI) of 10^{-4} at 37 °C (Dogra et al. 2023). MOIs reported in the following are based on the TCID₅₀ titer (Genzel and Reichl 2007) (interference assay) or the plaque titer (OP7 chimera DIP production).

Production of OP7 chimera DIPs in shake flasks

For infection experiments in shake flasks, 250-mL shake flasks (baffled Erlenmeyer flask with vent cap, Corning, #1356246) with 100 mL V_w were used. To produce OP7 chimera DIPs in batch mode, cells were infected at 2.0×10^6 cells/mL either by direct inoculation after a CME, or by 1:2 dilution with fresh medium (MD) of a culture grown to 4.0×10^6 cells/mL. Production with CME was performed as described recently (Hein et al. 2021a). In brief, MDCK-PB2(sus) cells in exponential growth phase were centrifuged (300 × g, 5 min, room temperature (RT)). The cell pellet was resuspended in fresh medium (without puromycin) containing trypsin (final activity 20 U/mL, Thermo Fisher Scientific, #27250–018). Subsequently, cells were seeded into shake flasks and infected at a MOI of 10^{-4} at about 2.0×10^6 cells/mL at 37 °C. For production with MD, cells were centrifuged (300 × g, 5 min, RT) and resuspended at 0.6×10^6 cells/mL in fresh medium (without puromycin). Next, cells were cultivated up to about 4.0×10^6 cells/mL and then diluted (1:2) with fresh medium containing trypsin (final activity of 20 U/mL) for subsequent infection at 37 °C or at 32 °C using indicated MOIs. For sampling, aliquots of cell suspensions were centrifuged (3000 × g, 4 °C, 10 min) and supernatants were stored at -80 °C until further analysis. From these supernatants, vRNAs of progeny virions were purified using the NucleoSpin RNA virus kit (Macherey–Nagel, #740956) according to the manufacturers' instructions, and stored at -80 °C until real-time reverse transcription-quantitative PCR (real-time RT-qPCR).

Batch mode production of OP7 chimera DIPs in a STR

Cells grown in shake flasks were centrifuged (300 × g, 5 min, RT), resuspended in fresh puromycin-free medium and used to inoculate a 1 L STR (DASGIP® Parallel Bioreactor System, Eppendorf AG, #76DG04CCBB) at 0.5×10^6 cells/mL (400 mL V_w). The STR was equipped with an inclined blade impeller (three blades, 30° angle, 50 mm diameter, 150 rpm) and a L-macrosparger. A mixture of air and oxygen was provided to control the dissolved oxygen above 40% air saturation. pH control (pH 7.6, reduced to 7.4 as soon set point pH 7.6 could no longer be maintained) was achieved by CO₂ sparging and addition of 7.5% NaHCO₃. During the cell growth phase, temperature was set to 37 °C and cells were grown to about 4.0×10^6 cells/mL. Prior to infection, temperature was reduced to 32 °C, MD (1:2 dilution with fresh medium) was performed (final V_w about 700 mL) and cells were infected at a MOI of 10^{-4} and pH of 7.4.

Production of OP7 chimera DIPs in a STR in perfusion mode

An alternating tangential flow filtration (ATF2) system with C24U-v2 controller (Repligen), equipped with a hollow fiber membrane (polyethersulfone (PES), 0.2 μm pore size, Spectrum Labs) was coupled to the 1 L STR described above (final V_W about 700 mL) for perfusion cultivation. Cells were inoculated at 1.2×10^6 cells/mL and cultivated for 1 day in batch mode. Subsequently, perfusion was started and the recirculation rate was set to 0.9 L/min. For perfusion rate control, a capacitance probe connected to an ArcView Controller 265 (Hamilton) was utilized (Göbel et al. 2023; Gränicher et al. 2021; Hein et al. 2021b, 2023; Nikolay et al. 2018; Wu et al. 2021). Using linear regression, the permittivity signal was converted to the VCC and used to control the permeate flow rate of a connected peristaltic pump (120 U, Watson-Marlow). The cell factor in the ArcView controller was re-adjusted after every sample taking to keep a cell-specific perfusion rate (CSPR) of 200 $\mu\text{L}/\text{cell}/\text{day}$ as described previously (Hein et al. 2021b). The feed flow rate was controlled based on the weight of the bioreactor. Prior to infection, one reactor volume (RV) was exchanged with fresh medium and temperature was lowered to 32 $^\circ\text{C}$. After infection at a MOI of 10^{-4} , the permeate flow rate was set to 0 RV/day for 1 h, kept constant at 2.4 RV/day until 30 h post infection (hpi) and finally increased to 2.6 RV/day. In order to prevent oxygen limitation during cell growth phase (Hein et al. 2021b), 0.5 L/h of air was provided 77.2 h after inoculation using an additional microsparger.

Membrane-based steric exclusion chromatography

Harvested OP7 chimera DIP material was clarified (3000 \times g, 10 min, 4 $^\circ\text{C}$) and spiked with sucrose (5%, 84097, Merck). Next, consecutive filtration steps with regenerated cellulose membranes (1.0 μm , #10410014; 0.45 μm , #10410214; 0.2 μm , #10410314, Cytiva) were performed for clarification using a bottle top system coupled to a vacuum pump. To remove host cell DNA, the clarified OP7 chimera DIP material was supplemented with MgCl_2 (2 mM final concentration, #M8266, Merck) and treated with an unspecific nuclease (40 U/mL final activity, Denarase®, #2DN100KU99, Sartorius Stedim Biotech) for 4 h under mixing. Purification was done by membrane-based steric exclusion chromatography (SXC) (Marichal-Gallardo et al. 2017, Marichal-Gallardo et al. 2021) as described recently (Hein et al. 2021a, 2021c). An ÄKTA Pure 25 system (Cytiva) was used for chromatography at RT. UV monitoring was performed at 280 nm and virus particles were monitored using a NICOMPTM 380 (Particle Sizing Systems) at 632.8 nm. The filter unit (in the following referred to as “column”) was packed with regenerated cellulose membranes (1.0 μm pore size, 20 layers, 100 cm^2

total surface) and installed in a 25 mm stainless steel filter housing. The flow rate was 10 mL/min. For equilibration, the column was washed with water and then with binding buffer (8% PEG-6000 in PBS, #81260, Merck). Next, the sample was injected (in-line mixing with 16% PEG-6000 in PBS to achieve 8% PEG-6000). Subsequently, the column was washed with binding buffer until baseline UV absorbance was reached. Elution was conducted with 20 column volumes of elution buffer (PBS). The eluate was dialyzed overnight at 4 $^\circ\text{C}$ against PBS (sample to buffer ratio of 1:1000) using cellulose ester dialysis tubing (300 kDa cut-off, #GZ-02890–77). Subsequently, the material was spiked with sucrose (5%). Finally, the material was sterile filtered (0.2 μm , cellulose acetate syringe filter, #16534-K, Sartorius Stedim Biotech).

Virus quantification

Real-time RT-qPCR was used to quantify purified vRNAs of progeny virions as described previously (Kupke et al. 2019). Primers used for quantification of the vRNA of Seg 7-OP7 are listed in (Hein et al. 2021c) and, for Seg 7 of the wild-type (WT) virus (Seg 7-WT), in (Dogra et al. 2023). The plaque assay was carried out to quantify infectious virus titers with MDCK(adh) cells (interference assay) and MDCK-PB2(adh) cells (seed virus titer of OP7 chimera DIP preparation) as described previously (Hein et al. 2021a, 2021c; Kupke et al. 2020) with a measurement error of $\pm 0.2 \log_{10}$. A hemagglutination assay (HA assay) was used to determine total virus titers ($\log_{10}(\text{HAU}/100 \mu\text{L})$) with a measurement error of $\pm 0.15 \log_{10}(\text{HAU}/100 \mu\text{L})$ (Kalbfuss et al. 2008).

The accumulated HA titer ($\log_{10}(\text{HAU}/100 \mu\text{L})$) was estimated from the HA titer of the harvest in the bioreactor vessel plus the virus particles collected after the hollow fiber membrane (detected in the permeate line) and quantified according to Eq. 1. HA_B denotes the HA titer of the sample taken at the optimal harvest time point in the bioreactor vessel, V_W (mL) of the bioreactor vessel, HA_P the average HA titer of material collected in the permeate line between the sample time point t_n and the previous sample time point t_{n-1} with the harvested volume (V_p).

$$\text{HA}_{acc} = \log_{10} \frac{10^{\text{HA}_B} \times V_W + \sum (10^{\text{HA}_P} \times V_p)}{V_W} \quad (1)$$

The concentration of DIPs (c_{DIP} , virions/mL) was calculated using Eq. 2, where c_{RBC} denotes the concentration of red blood chicken cells used in the HA assay (2.0×10^7 cells/mL).

$$c_{\text{DIP}} = 10^{\log_{10} \left(\frac{\text{HAU}}{100 \mu\text{L}} \right)} \times c_{\text{RBC}} \quad (2)$$

The total number of produced virus particles vir_{tot} (virions) was determined according to Eq. 3. c_B denotes the c_{DIP}

in the bioreactor vessel at the optimal harvest time point, and c_p the average c_{DIP} in the permeate line between t_n and t_{n-1} .

$$vir_{tot} = c_B \times V_W + \sum c_P \times V_P \quad (3)$$

The cell-specific virus yield (CSVY, virions/cell) was calculated using Eq. 4, where VCC_{max} (cells/mL) denotes the maximum VCC after time of infection (TOI).

$$CSVY = \frac{vir_{tot}}{VCC_{max} \times V_W} \quad (4)$$

The space–time yield (STY, virions/L/day) was determined using Eq. 5. t_{tot} (day) denotes the total time from inoculation until the optimal harvest time point.

$$STY = \frac{vir_{tot}}{V_W \times t_{tot}} \quad (5)$$

The volumetric virus productivity (VVP, virions/L/day) was estimated according to Eq. 6, where V_{tot} denotes the total volume of the spent medium during cell growth and virus production phase.

$$VVP = \frac{vir_{tot}}{V_{tot} \times t_{tot}} \quad (6)$$

The percentage of virus particles that passed the pores of the hollow fibers (P_{perm} , %) was determined according to Eq. 7. n denotes the total number of sample time points, HA_p the HA titer in the permeate line at t_n , and HA_B the HA titer in the bioreactor vessel at t_n .

$$P_{perm} = \frac{1}{n} \sum \left(\frac{10^{HA_p}}{10^{HA_B}} \right) \times 100\% \quad (7)$$

Interference assay

To determine the in vitro interfering efficacy of the produced OP7 chimera DIP material, an interference assay was used. Specifically, we evaluated the inhibition of STV propagation after co-infection with OP7 chimera DIPs. Co-infections were performed in MDCK(adh) cells (Hein et al. 2021a, 2021c) or in Calu-3 cells. Calu-3 cells were seeded at a concentration of 3.0×10^6 cells/well in a 12-well plate and incubated for 24 h prior to infection. For infection, cells were washed with PBS and infected with STV PR8 at a MOI of 0.05 or co-infected with 125 μ L of the produced OP7 chimera DIP material in a total volume of 250 μ L of media. After 1 h, we filled up to 2 mL with medium. Supernatants were harvested at indicated time points, centrifuged at $3000 \times g$ for 10 min at 4 °C and cell-free supernatants stored at -80°C until virus quantification. To extract intracellular RNAs, 350 μ L of RA1 buffer (Macherey Nagel, #740961),

1% β -mercaptoethanol was added to cells remaining in wells for lysis. RNA purification from these lysates was carried out according to the manufacturer's instructions and samples were stored at -80°C until real-time RT-qPCR to monitor IFN- β gene expression as described previously (Kupke et al. 2019; Rand et al. 2021). Fold changes were calculated using the $\Delta\Delta c_T$ method.

Statistical analysis and data visualization

GraphPad Prism 9 (GraphPad Software) was used for statistical analysis and data visualization. Either one-way analysis of variance (ANOVA) followed by Tukey's multiple comparison test, two-way ANOVA followed by Dunnett's multiple comparison test, or unpaired t test were used to determine significance.

Results

Medium dilution impairs yields, whereas infection at 32 °C increases OP7 chimera DIP titers and fractions in shake flasks

Previously, a CME prior to infection has been performed for cell culture-based production of OP7 chimera DIPs (Dogra et al. 2023). However, this is difficult to implement at larger scales without cell retention devices. Therefore, following a cell growth phase until about 4.0×10^6 cells/mL, we added fresh medium (MD, 1:2 dilution) to supply substrates and reduce the level of inhibitors accumulated as by-products. To investigate whether a reduction in temperature has a positive effect on virus replication and yields (Hein et al. 2021b; Wu et al. 2021), two cultivations were performed at 37 °C and 32 °C with MD; in addition, one cultivation at 37 °C with CME was performed as a control.

The infection with MD at 37 °C resulted in a similar VCC dynamics relative to the production with CME (Fig. 2a). However, a slightly lower maximum HA titer of $2.05 \log_{10}(\text{HAU}/100 \mu\text{L})$ compared to $2.20 \log_{10}(\text{HAU}/100 \mu\text{L})$ was found (Fig. 2b). The lower total virus titer is likely associated with an increased ammonium (inhibitor) concentration and a depletion of glutamine during the infection phase (Fig. S1). A low OP7 chimera DIP fraction of 31.6% (MD) relative to 71.2% (CME) was reached (Fig. 2c, based on the extracellular vRNA concentration of Seg 7-OP7 and Seg 7-WT quantified by real-time RT-qPCR). Lowering the temperature to 32 °C before infection counterbalanced this negative effect of MD and resulted in higher HA titers (Fig. 2b). Here, a maximum of $3.24 \log_{10}(\text{HAU}/100 \mu\text{L})$ was observed at 44 hpi corresponding to an 11-fold increase relative to the production at 37 °C with CME. In addition, virus production at 32 °C resulted in

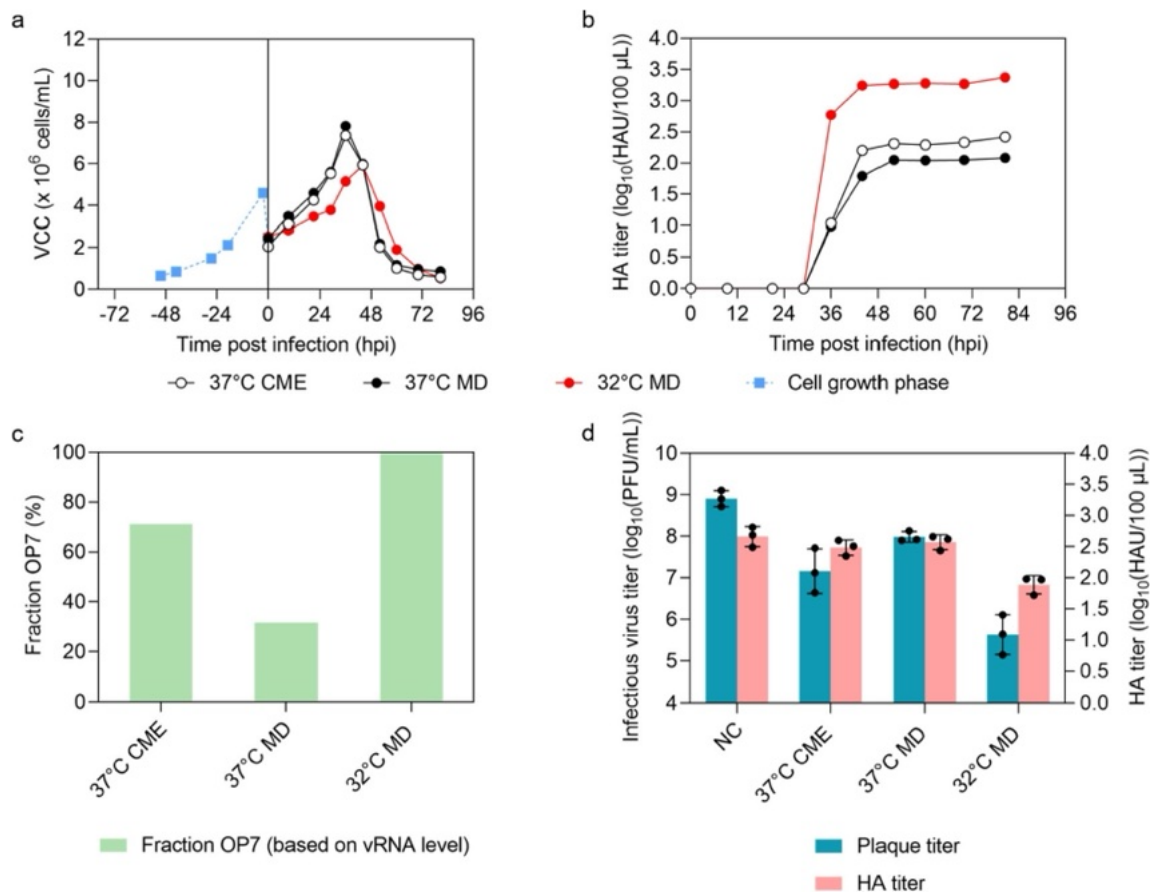


Fig. 2 Batch mode production of OP7 chimera DIPs in shake flasks with MD and temperature decrease to 32 °C. MDCK-PB2(sus) cells, cultivated in 250 mL shake flasks (100 mL V_w) at 37 °C, were grown to about 4.0×10^6 cells/mL. Subsequently, the suspension culture was diluted (MD, 1:2) with fresh medium (100 mL V_w), cells were infected at a MOI of 10^{-4} and temperature was reduced to 32 °C. For comparison, two cultivations were performed at 37 °C, one with MD at an optimal MOI of 10^{-3} , one with CME at an optimal MOI of 10^{-4} . **a**) VCC. **b**) HA titer. **c**) Fraction of OP7 chimera DIPs, calculated using the extracellular Seg 7-OP7 and

Seg 7-WT vRNA concentrations, quantified by real-time RT-qPCR. **a-c** depict the results of one experiment. **d**) Interference assay. WT MDCK(adh) cells were infected with STV PR8 at a MOI of 10 (negative control, NC) or co-infected with 125 µL of indicated OP7 chimera DIP material. Infectious virus particle release is indicated by the plaque titer and total virus particle release by HA titer (16 hpi). Interference assay was performed in three independent experiments. Error bars indicate standard deviation (SD). The optimal harvest time point (37 °C CME: 44 hpi, 37 °C MD: 52 hpi, 32 °C MD: 44 hpi) was analyzed for **c** and **d**

reduced concentrations of ammonium (< 3.6 mM, Fig. S1), which should also favor IAV propagation. Finally, the OP7 chimera DIP fraction was greatly increased to 99.7% (Fig. 2c), an almost pure OP7 chimera DIP preparation. To demonstrate reproducibility of this optimized production, a second production run was carried out subsequently (Fig. S2) that confirmed these findings.

Next, we tested the interfering efficacy of the produced material in vitro, in which we assessed the inhibition of STV PR8 replication during co-infection with different produced OP7 chimera DIP materials. For this, we used samples at the respective optimal harvest time points (37 °C CME: 44 hpi, 37 °C MD: 52 hpi, 32 °C MD: 44 hpi) (Fig. 2d). Here, the HA titer almost plateaued and biological activity of the

virus particles sampled is assumed highest before onset of unspecific degradation over time (Genzel et al. 2010). For material produced at 32 °C and MD, we observed a strong reduction of the infectious STV PR8 titer (more than three orders of magnitude), which was significantly different to the small reduction observed for material produced at 37 °C and MD ($p < 0.001$, one-way ANOVA followed by Tukey's multiple comparison test). In addition, the reduction of the infectious virus titer was significantly higher than for material produced at 37 °C and CME ($p < 0.01$). Overall, this confirms a high interfering efficacy of OP7 chimera DIP preparations produced at 32 °C and MD. Regarding the total virus particle release, as expressed by the HA titer, this trend was less pronounced.

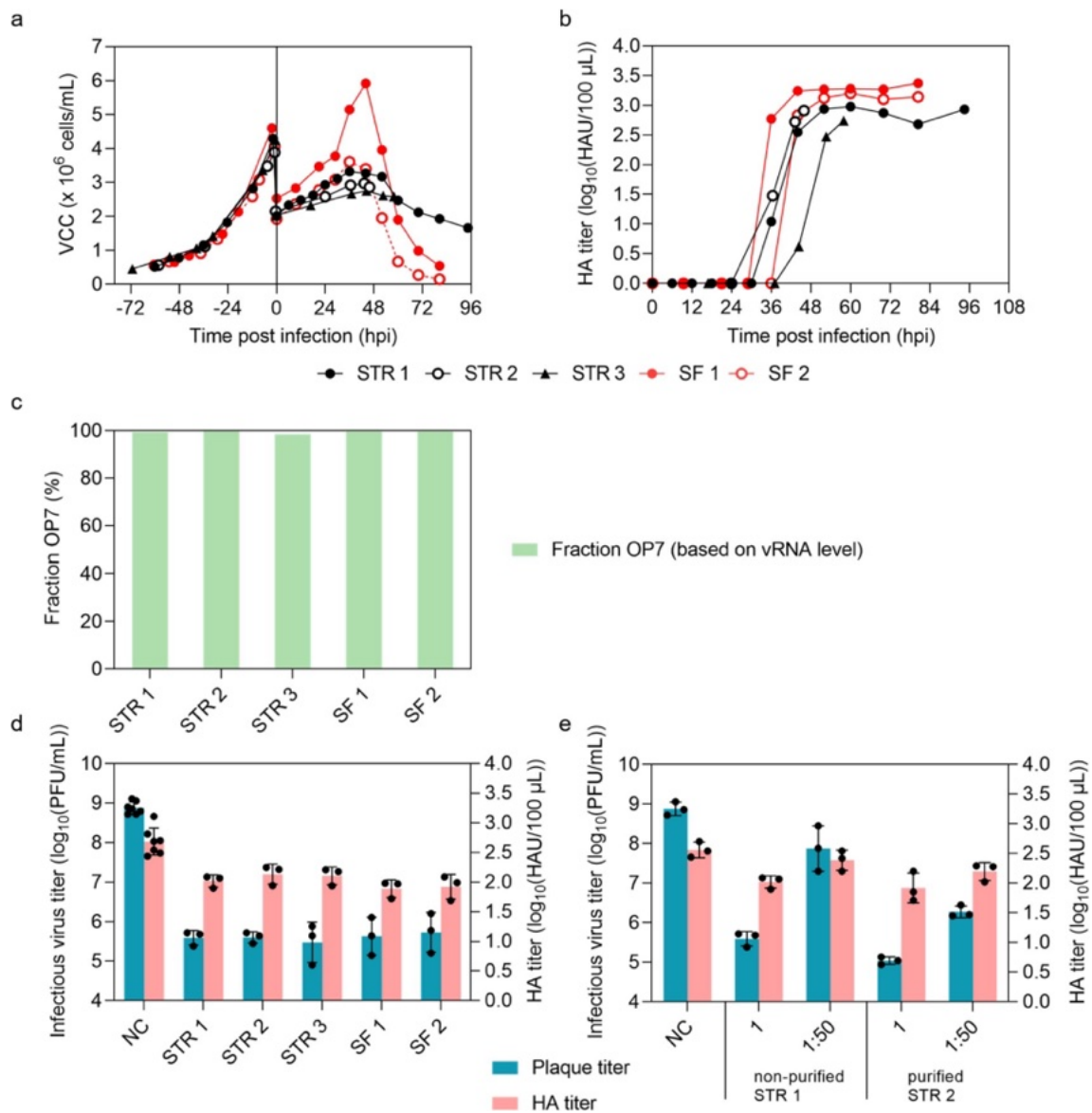


Fig. 3 OP7 chimera DIP production in batch mode in a 1 L STR versus shake flask production and interfering efficacy of produced material after purification by SXC. MDCK-PB2(sus) cells were grown in a 1 L STR (400 mL V_w , 37 °C). After growth to about 4.0×10^6 cells/mL, cells were diluted (1:2) with fresh medium (approx. 700 mL final V_w), temperature was set to 32 °C, pH was set to 7.4, and cells were infected at a MOI of 10^{-4} . In total, three independent productions were carried out in STR (STR 1–3) and compared to two independent productions in shake flasks (SF 1–2, 100 mL V_w) for comparison (also shown in Fig. 2 and Fig. S2). **a**) VCC. **b**) HA titer. **c**)

Fraction of OP7 chimera DIPs (see Fig. 1). **d**) Interference assay with MDCK(adh) cells was performed in seven independent experiments for NC, and three experiments for STRs and SFs. **e**) Interference assay with MDCK(adh) cells of purified (SXC) vs non-purified material. Dilutions of the tested materials are indicated. Interference assay was performed in three independent experiments. Error bars indicate the SD. The optimal harvest time point (STR 1: 52 hpi, STR 2: 46 hpi, STR 3: 58 hpi, SF 1: 44 hpi, SF 2: 44 hpi) was analyzed for **c**, **d** and **e**

Previous studies suggested clearly that OP7 chimera DIP production and interfering efficacy strongly depend on the MOI (Dogra et al. 2023). Therefore, only productions performed at the optimal MOIs were shown in Fig. 2. Interestingly, however, MOI dependency on total virus titers, OP7

chimera DIP fraction and interfering efficacy was negligible for MD and 32 °C (Fig. S3).

In summary, the optimized production at 32 °C with MD (1:2) resulted in an increase of total virus yields by 11-fold compared to the previous processes operated at 37 °C and

CME. In addition, a production of almost pure OP7 chimera DIP preparation was achieved.

Batch mode production of OP7 chimera DIPs in a bioreactor and purification by SXC

In order to show that production of OP7 chimera DIPs at larger scale is possible, the process was transferred to a STR with 700 mL V_w . Three independent productions were performed (STR 1, STR 2, and STR 3) and compared to two productions in shake flasks (SF 1 (Fig. 2), and SF 2 (Fig. S2)).

MDCK-PB2(sus) cells were seeded into the STR at approx. 0.5×10^6 cells/mL and cultivated (400 mL, 37 °C) until a VCC of about 4.0×10^6 cells/mL (Fig. 3a) was obtained. As in SF, cultivations were performed at 32 °C and MD (1:2) (final V_w about 700 mL). Cells were infected at a MOI of 10^{-4} . After infection, cells continued to grow (Fig. 3a), with STR 1–3 and SF 2 showing very similar growth curves before onset of virus-induced cell lysis (max. VCC 2.8 – 3.6×10^6 cells/mL). SF 1 revealed a peak VCC of 5.9×10^6 cells/mL likely due to a more rapid growth and higher VCC at TOI. HA titers were similar ($p > 0.05$, unpaired t test) (Fig. 3b) for all STR runs compared to SF productions. (Note that STR 2 and 3 were terminated at 46 hpi and 58 hpi, respectively, for virus harvest.) In addition, all cultivations showed very high OP7 chimera DIP fractions (98.5–99.7%) at the optimal harvest time point (Fig. 3c). Finally, results from the in vitro interference assay (Fig. 3d) showed no significant difference in the reduction of infectious virus particle release ($p > 0.05$, one-way ANOVA followed by Tukey's multiple comparison test) and total virus particle release (HA titer) ($p > 0.05$).

For virus purification, material harvested from STR 2 was subjected to SXC. The purified material was tested for antiviral efficacy in comparison to the non-purified material using the in vitro interfering assay (Fig. 3e). There was no significant reduction in infectious virus particle release for purified material (STR 2, 1.1×10^5 PFU/mL) compared to non-purified material (STR 1, 4.1×10^5 PFU/mL) ($p > 0.05$) (Fig. 3d and e). Yet, a higher interfering efficacy of the purified material was found for diluted samples (1:50) that showed a significantly higher decrease in the release of infectious virus particles (STR 2, 2.0×10^6 PFU/mL) compared to the diluted non-purified material (STR 1, 1.3×10^8 PFU/mL) ($p < 0.001$) (Fig. 3e).

Next, we investigated the antiviral activity of the purified OP7 chimera DIP material in vitro in human alveolar epithelial (Calu-3) cells (Fig. 4). In contrast to MDCK(adh) cells used for this assay before (Figs. 2d, 3d and e), Calu-3 cells have a functional innate immune response against human IAV (Hsu et al. 2011; Seitz et al. 2010) including an IFN response that induces a cellular

antiviral state. Accordingly, MDCK cells were used to only monitor replication inhibition caused by DIP co-infections, whereas the use of Calu-3 cells allowed additional contribution of innate immunity. With the Calu-3 cell assay, we observed a strong suppression of infectious virus particle release (by roughly two orders of magnitude) upon co-infection with non-purified OP7 chimera DIP preparations produced in SF at 37 °C and CME (original process) (Fig. 4a). After process optimization (32 °C MD DSP), including STR production at 32 °C and SXC purification, the preparations appeared to interfere slightly stronger (three instead of two orders of magnitude, Fig. 4a), but this difference was statistically not significant ($p = 0.07$, one-way ANOVA followed by Tukey's multiple comparison test). In addition, we observed an early and enhanced upregulation of IFN- β gene expression for both materials compared to STV PR8 infection alone at 6 hpi ($p < 0.0001$, two-way ANOVA followed by Dunnett's multiple comparison test) (Fig. 4b). This early stimulation may explain part of the inhibitory effect during OP7 chimera DIP co-infection in Calu-3 cells. (Note: There was not enough purified DIP material available that was produced at 32 °C and MD at 48 hpi to perform an analysis.)

In summary, the transfer of production from a SF to a STR resulted in similar HA titers, purity and very comparable interfering efficacies of OP7 chimera DIP harvests. SXC purification of the material obtained from STR resulted in a higher in vitro interfering efficacy in MDCK(adh) but not in Calu-3 cells. These results indicate that further scale-up to higher reactor volumes (e.g., industrial scale) should be easily accomplished.

Perfusion mode production in a bioreactor leads to high cell concentrations, superior yields, and high OP7 chimera DIP purity

Next, we evaluated the possibility of process intensification by cultivation in perfusion mode for OP7 chimera DIP production to achieve higher cell concentrations and thus, higher total virus yields (Bissinger et al. 2019; Wu et al. 2021). Therefore, we implemented a perfusion system using an ATF2 system (Hein et al. 2021b).

Cells were seeded at 1.2×10^6 cells/mL into the STR (700 mL V_w) (Fig. 5a) and perfusion mode was initiated 24 h after inoculation. During the cell growth phase (-97 to -2 hpi), a cell-specific growth rate of 0.031 h^{-1} was achieved, which is comparable to batch production with MD in STR (0.032 – 0.036 h^{-1}) (Fig. 3a). In addition, viability remained above 97% (Fig. 5a). This indicates that the use of an ATF2 system has no negative impact on cell growth and survival. During the cell growth phase, the perfusion rate was controlled at a predefined CSPR of 200 pL/cell/day. The linear regression of the offline

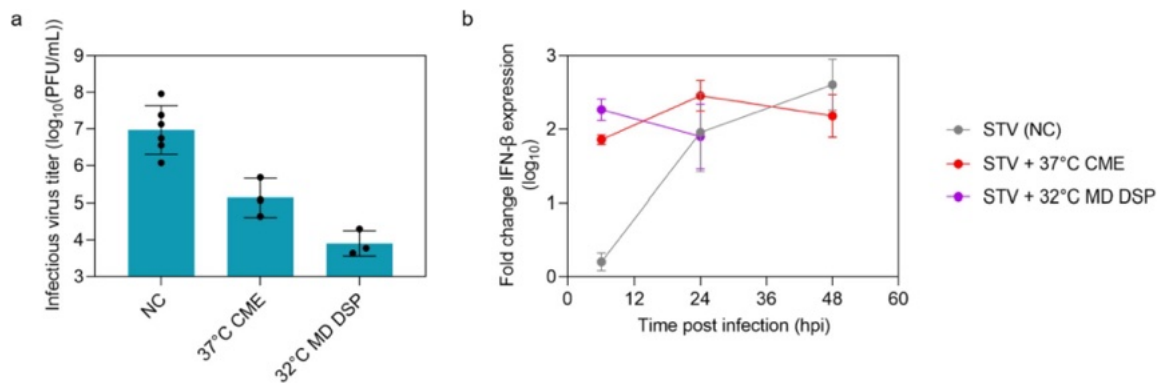


Fig. 4 Interfering efficacy in human alveolar epithelial Calu-3 cells of OP7 chimera DIP material purified by SXC. Calu-3 cells were infected with STV PR8 alone at a MOI of 0.05 (NC) or co-infected with 125 μ L of indicated OP7 chimera DIP material. **a)** Infectious virus particle release, shown by the plaque titer (24 hpi). **b)** Fold change in IFN- β gene expression, quantified by real-time RT-qPCR.

Results of six independent experiments for NC, or three experiments for the co-infection are shown. Material produced in shake flasks at 37 °C with CME (37 °C CME, Fig. 2) was compared to material produced in a STR at 32 °C with MD and further SXC purification (32 °C MD Downstream Processing (DSP), Fig. 3e). Error bars indicate the SD

measured VCC and the online permittivity signal during the cell growth phase showed a R^2 of 0.997 (Fig. S4).

After 97 h, cells were infected at 24.9×10^6 cells/mL (as suggested by Hein et al. (Hein et al. 2021b) at a MOI of 10^{-4} . Before infection, one RV was exchanged with fresh medium (Fig. 5b and c) by employing an average perfusion rate of 17.6 RV/day for 1 h; in addition, the temperature was lowered to 32 °C. Following infection, the perfusion rate was set at 0 RV/day for 1 h to avoid virus particle wash-out. Subsequently, medium was fed constantly (2.4 RV/day, increased to 2.6 RV/day at 30 hpi) (Fig. 5b). Over process time, neither a glucose nor a glutamine limitation was detected (Fig. 5c). Maximum lactate and ammonium concentrations were 34.7 mmol/L and 2.5 mmol/L, respectively (Fig. 5c). After infection, VCC remained constant until 37 hpi, after which cell lysis started (Fig. 5a). At 45 hpi, the HA titer peaked with $4.04 \log_{10}$ (HAU/100 μ L) in the bioreactor vessel (Fig. 5d). Also note that until time of optimal harvest part of the virus particles passed the pores of the hollow fiber membrane (0.2 μ m) ($P_{\text{perm}} = 26\%$) (Fig. 5d) resulting in an accumulated HA titer (HA_{acc}) of $4.10 \log_{10}$ (HAU/100 μ L). This corresponded to more than 14-fold higher total virus yields compared to the STRs operated in batch mode with MD (all below $3 \log_{10}$ (HAU/100 μ L)) (Fig. 3b). After time of optimal harvest, decreasing total virus titers were observed in the permeate line (Fig. 5d), likely due to membrane fouling. Importantly, no cells passed the hollow fiber membrane (data not shown).

Table 1 summarizes HA_{acc} , the total number of produced virus particles (vir_{tot}), CSVY, space-time yield (STY) and volumetric virus productivity (VVP), which were all increased compared to the STR batch process performed at 32 °C and MD, except for the VVP. Further, these

coefficients were slightly increased for the perfusion process when virus particles in the permeate line were taken into account as well, relative to harvesting the bioreactor vessel alone. In addition, very high OP7 chimera DIP fractions (99.8%) were present in both the bioreactor vessel and permeate line (Fig. 5e). Ultimately, the in vitro interfering efficacy was evaluated in MDCK(adh) cells (Fig. 5f). At a dilution of 1:50, the material produced in the perfusion culture showed a significantly higher reduction of the infectious virus particle release compared to the batch process with MD (STR 1, Fig. 3) ($p < 0.001$, one-way ANOVA followed by Tukey's multiple comparison test).

Overall, we demonstrate the successful establishment of a perfusion process for cell culture-based production of OP7 chimera DIPs free of contaminating infectious STV. Besides, an increase in total virus yields and a CSVY exceeding those of conventional batch processes and very high purity of OP7 chimera DIPs (99.8%) was obtained.

Discussion

IAV DIPs are regarded as a highly interesting option for future broad-spectrum antiviral therapy (Dimmock et al. 2008, 2012b; Easton et al. 2011; Huo et al. 2020; Kupke et al. 2019; Rand et al. 2021; Scott et al. 2011; Zhao et al. 2018). We recently established a cell-culture-based production of OP7 chimera DIPs together with cDIPs in the absence of infectious STVs. Yet, only relatively low total virus yields and OP7 chimera DIP fractions were achieved for production in shake flasks (Dogra et al. 2023). Here, we present results for scalable processes in laboratory-scale STRs including batch- and perfusion mode strategies that

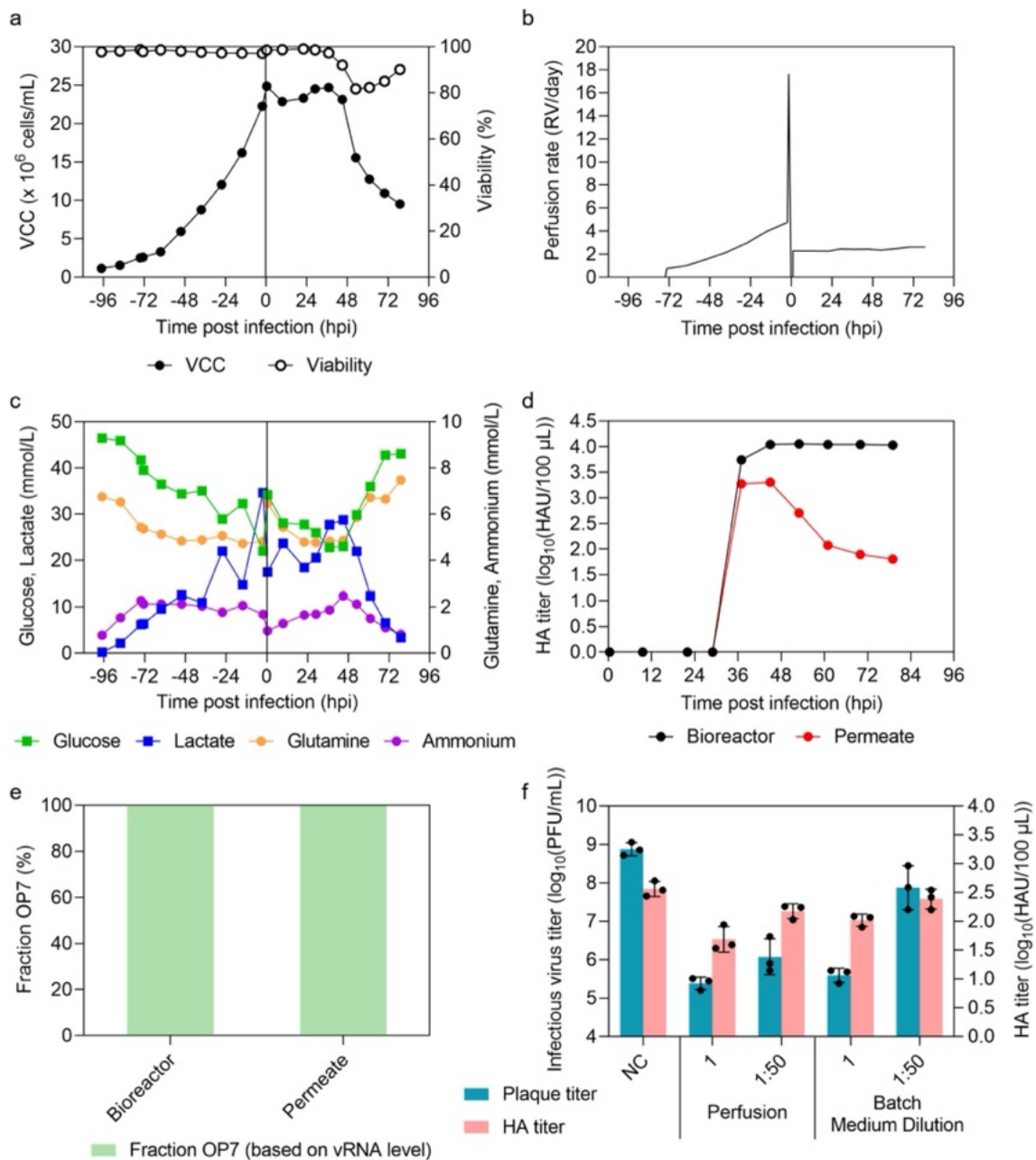


Fig. 5 Production of OP7 chimera DIPs in a 1 L STR (700 mL V_w) in perfusion mode. Inoculation of MDCK-PB2(sus) cells at 1.2×10^6 cells/mL, perfusion start after 24 h of batch mode by using an alternating tangential flow filtration system (ATF2) with a hollow fiber membrane (0.2 μ m pore size). Perfusion rate during cell growth controlled by capacitance probe measuring of VCC. Before infection at a MOI of 10^{-4} , one RV was exchanged with fresh medium and temperature was reduced to 32 °C. **a**) VCC. **b**) Perfusion rate. **c**) Glucose,

lactate, glutamine and ammonium concentration. **d**) HA titer. **e**) Fraction of OP7 chimera DIPs. **a-e** depict the results of one experiment. The optimal harvest time point (45 hpi) was analyzed for **e** and **f**. **f**) Interference assay with MDCK(adh) cells. For comparison, material produced in batch mode using medium dilution (MD) (STR 1) is shown (Fig. 3). Interference assay was performed in three independent experiments. Error bars indicate the SD

yielded up to a 79-fold increase (perfusion) in total virus yields compared to an original batch process in shake flasks. In addition, we demonstrate the production of almost pure

OP7 chimera DIP preparations (up to 99.8%), which is advantageous with respect to regulatory requirements for GMP production towards clinical development.

Table 1 Summary of OP7 chimera DIP production in a 1 L STR in batch mode (with medium dilution) and perfusion mode

	Spent medium ^a	VCC _{max} ^b	HA _{acc} ^c	vir _{tot} ^d	CSVY ^e	STY ^f	VVP ^g
	mL	× 10 ⁶ cells/mL	log ₁₀ (HAU/100 μL)	virions	virions/cell	log ₁₀ (virions/L/day)	log ₁₀ (virions/L/day)
Batch STR 1	692	3.3	2.94	1.2 × 10 ¹³	5289	12.6	12.6
Batch STR 2	691	3.0	2.91	1.1 × 10 ¹³	5423	12.6	12.6
Batch STR 3	707	2.8	2.74	7.9 × 10 ¹²	4039	12.3	12.3
Perfusion STR4 B ^h	8804	24.9	4.04	1.5 × 10 ¹⁴	8789	13.6	12.5
Perfusion STR4 B + P ⁱ	8804	24.9	4.10	1.9 × 10 ¹⁴	10,648	13.7	12.6

^aBatch: V_w at TOI. Perfusion: V_w plus spent medium volume until time of optimal harvest (45 hpi)

^bMaximum VCC (VCC_{max}) after TOI

^cAccumulated HA titer (HA_{acc}) according to Eq. 1

^dTotal number of produced virus particles (vir_{tot}) was derived from the HA titer according to Eq. 3

^eCell-specific virus yield (CSVY) was derived from the HA titer according to Eq. 4

^fSpace-time yield (STY) was derived from the HA titer according to Eq. 5

^gVolumetric virus productivity (VVP) was derived from the HA titer according to Eq. 6

^hCalculations based only on virus particles in the bioreactor vessel

ⁱCalculations based on virus particles in the bioreactor vessel plus in the permeate

Effect of temperature reduction on DIP titers, purity and interfering efficacy

Our data confirms other studies reporting that a temperature reduction during the virus production phase can increase IAV yields (Fig. 2b) (Hein et al. 2021b; Wu et al. 2021). Similar findings were obtained for vesicular stomatitis virus (VSV) (Elahi et al. 2019), Newcastle disease virus (NDV) (Jug et al. 2023) and recombinant adenovirus (Jardon and Garnier 2003). In contrast, other studies did not see a positive effect of temperature reduction on the replication of viruses, e.g., for recombinant VSV-NDV (Göbel et al. 2023) and yellow fever virus (YFV) production (Nikolay et al. 2018). Furthermore, a reduction of temperature during virus production might also be beneficial regarding virus degradation as shown for YFV, Zika virus and IAV (Nikolay et al. 2018; Petiot et al. 2011). At lower temperatures, enzyme activities are reduced and the degradation of infectious virus particles by, e.g., proteases released by lysed cells, can be partly prevented. Eventually, a reduction in temperature to 32 °C can support a shift in cellular metabolism, resulting in a reduced accumulation of ammonium, lactate and other inhibitory metabolites released in the supernatant. In our study, increased concentrations of ammonium (> 4 mM) were likely associated with lower total virus yields for OP7 chimera DIP production at 37 °C (Fig. S1d). This is in line with a review reporting that ammonium and lactate concentrations at 2–3 mM and above 20–30 mM, respectively, can affect cell growth and virus yield, depending on the cell line (Schneider et al. 1996). The higher purity of OP7 chimera DIPs (up to 99.8%) for all performed runs at 32 °C might be explained by increased virus replication. As a result, OP7

chimera DIPs likely overgrew Seg 1 cDIPs due to the replication advantage of Seg 7-OP7 vRNA. The higher interfering efficacy of material produced with MD at 32 °C relative to 37 °C can be attributed to the higher total virus yield and fraction of OP7 chimera DIPs.

Previously, we showed for cultivations with CME performed at 37 °C that production and interfering efficacy of OP7 chimera DIPs was highly dependent on MOI (Dogra et al. 2023). For MD and 32 °C, however, total virus titers, OP7 chimera DIP fraction and interfering efficacy were almost not affected by MOI. This suggests that the selection of the optimal MOI is less important under this production condition, and process robustness could be improved. Using lower MOIs for production could reduce costs required for seed virus generation.

Process intensification using perfusion mode cultivation

Through process intensification, we achieved a high total virus yield of the OP7 chimera DIPs in perfusion culture (24.9 × 10⁶ cells/mL) with strongly increased total number of virus particles and STY (up to 23-fold) relative to the batch process (2.8–3.3 × 10⁶ cells/mL), while VVP was comparable (Table 1). Moreover, we produced similar yields of virus particles (4.10 log₁₀(HAU/100 μL), a CSVY of 10648 virions/cell, 24.9 × 10⁶ cells/mL, 32 °C) compared to a production of STV IAV in perfusion mode with a different suspension MDCK cell line derived from an adherent MDCK cell line originating from the American-Type Culture Collection (ATCC, MDCK ATCC CCL-34) (≥ 4.37 log₁₀(HAU/100 μL), ≥ 9299 virions/

cell, $\geq 43 \times 10^6$ cells/mL, 33 °C) (Wu et al. 2021). An often described phenomenon in virus production is the so-called “cell density effect”—a reduction of CSVY with an increase in VCC (Nadeau and Kamen 2003). This effect is often attributed to the exhaustion of nutrients and the accumulation of inhibitory by-products of metabolism including ammonium or lactate, but can be prevented by cultivation in perfusion mode (Bock et al. 2011; Genzel et al. 2014; Henry et al. 2004). The about 2-fold higher CSVY compared to the batch process (Table 1) confirmed that the “cell density effect” is not relevant for perfusion mode cultivations. Clearly, the relatively high CSPR (200 pL/cell/day) and the exchange of one RV with fresh medium prior to infection was sufficient to prevent the depletion of substrates and avoid the accumulation of ammonium and lactate as inhibiting metabolic by-products. Similar results were already reported for the production of DI244, a well-known cDIP of IAV (Dimmock et al. 2008, 2012a; Hein et al. 2021a) using the same cell line (Hein et al. 2021b). Furthermore, for other suspension MDCK cells (ATCC) cultivated in the same medium in perfusion culture, a CSPR of only 40–60 pL/cell/day was sufficient to achieve good process performance (Wu et al. 2021). Although, the applied high perfusion rate resulted in higher costs, the increased STY achieved relative to the batch process possibly should help to overcome this disadvantage (Göbel et al. 2022). Nevertheless, additional studies should be performed regarding optimal setting of the CSPR for manufacturing at final process scale.

During the cell growth phase, the perfusion rate was controlled using a capacitance probe to improve process robustness and reduce medium use as already demonstrated for other cell lines (Gränicher et al. 2021; Hein et al. 2021b; Nikolay et al. 2018; Wu et al. 2021). Recent studies reported that the presence of trypsin in the virus production phase influences the permittivity signal (Petiot et al. 2017; Wu et al. 2021). To avoid an interference of trypsin on the perfusion rate control, which is based on the permittivity signal, we decided to set a constant perfusion rate after virus infection as also done by others (Hein et al. 2021b; Vázquez-Ramírez et al. 2018).

Filter fouling is a typical phenomenon to be considered for use of retention devices including hollow fiber membranes (Genzel et al. 2014; Hein et al. 2021b; Nikolay et al. 2020). For virus retention, not only the nominal pore size, but also the membrane material itself plays a crucial role (Nikolay et al. 2020). Furthermore, the temperature during production can affect virus retention. For IAV production at 37 °C, only a very low fraction of virus particles passed a PES hollow fiber membrane (0.2 µm pore size) (Wu et al. 2021) as expected (Genzel et al. 2014). However, reducing the temperature to 33 °C at TOI allowed harvesting of a considerable percentage of virus particles via the permeate (Wu et al. 2021), as also shown in our study ($P_{\text{Perm}} = 26\%$)

at a production temperature of 32 °C. In contrast, for the production of DI244, virus particles did not seem to pass the hollow fiber membrane at 32 °C. However, virus quantification in the referred study was only carried out at very late time points of production in the permeate line, so that number of virus particles passing the membrane most likely was underestimated largely (Hein et al. 2021b). Nevertheless, filter fouling could not be prevented at later time points in our study (Fig. 5d). Recently, a novel tubular membrane (about 10 µm pore size, Artemis Biosystems) with an ATF-2 system was successfully tested for continuous virus harvesting of DI244 with a very high cell retention efficiency (Hein et al. 2021b). Continuous virus harvesting was also demonstrated by using the Tangential Flow Depth Filtration system (TFDF, Repligen) for lentiviral vector (Tona et al. 2023; Tran and Kamen 2022) and adeno-associated virus (Mendes et al. 2022) production in perfusion mode. In general, continuous virus harvesting through a membrane that allows for direct cooling of produced virus material with a first clarification improves virus stability and, therefore, yields. The use of an acoustic settler (Gränicher et al. 2020; Henry et al. 2004) or an inclined settler (Coronel et al. 2020) would be alternative options. Regarding the former, a more than 1.5-fold higher CSVY and VVP compared to an ATF system with a PES hollow fiber membrane (0.2 µm pore size) was obtained for harvesting IAV (Gränicher et al. 2020). For the production of OP7 chimera DIPs in perfusion mode, the use of a membrane or the implementation of another perfusion system that allows for continuous virus harvest over the complete production time would likely be beneficial and should be envisaged in the design and optimization of a GMP-ready manufacturing process.

Overall, a scalable and high-yield cell culture-based production process in perfusion mode for OP7 chimera DIPs not contaminated with infectious STV and almost free of Seg 1 cDIPs is now available. Together with the encouraging data obtained from recent animal studies of OP7 chimera DIPs, this paves the way towards GMP-process development and clinical studies.

Supplementary Information The online version contains supplementary material available at <https://doi.org/10.1007/s00253-023-12959-6>.

Acknowledgements The authors thank Claudia Best and Nancy Wynserski for their excellent technical assistance. We appreciate the supply of the XenoTM medium from Shanghai BioEngine Sci-Tech and Prof. Tan from the East China University of Science and Technology. Moreover, we thank Dunja Bruder from the Helmholtz Centre for Infection Research, Braunschweig, Germany for providing Calu-3 cells.

Author contribution Conceptualization, L.P., T.D., M.D.H., S.Y.K., Y.G., U.R.; Formal analysis, L.P.; Funding acquisition, U.R.; Investigation, L.P., T.D., P.M., G.H.; Project administration, L.P., S.Y.K.; Supervision, S.Y.K., Y.G., U.R.; Visualization, L.P.; Writing – original draft, L.P., T.D.; Writing – review & editing, L.P., T.D., P.M., M.D.H., G.H., S.Y.K., Y.G., U.R.

Funding Open Access funding enabled and organized by Projekt DEAL.

Data availability The datasets generated during and/or analyzed during the current study are available from the corresponding author upon request.

Declarations

Ethical approval This article does not contain any studies with human participants or animals performed by any of the author.

Conflict of interest A patent for the use of OP7 as an antiviral agent for treatment of IAV infection is pending. Patent holders are S.Y.K. and U.R. In addition a patent for the use of DI244 and OP7 as an antiviral agent for treatment of coronavirus infection is pending. Patent holders are S.Y.K., U.R., and M.D.H.

Open Access This article is licensed under a Creative Commons Attribution 4.0 International License, which permits use, sharing, adaptation, distribution and reproduction in any medium or format, as long as you give appropriate credit to the original author(s) and the source, provide a link to the Creative Commons licence, and indicate if changes were made. The images or other third party material in this article are included in the article's Creative Commons licence, unless indicated otherwise in a credit line to the material. If material is not included in the article's Creative Commons licence and your intended use is not permitted by statutory regulation or exceeds the permitted use, you will need to obtain permission directly from the copyright holder. To view a copy of this licence, visit <http://creativecommons.org/licenses/by/4.0/>.

References

- Bdeir N, Arora P, Gärtner S, Hoffmann M, Reichl U, Pöhlmann S, Winkler M (2019) A system for production of defective interfering particles in the absence of infectious influenza A virus. *PLoS One* 14(3):e0212757. <https://doi.org/10.1371/journal.pone.0212757>
- Bissinger T, Fritsch J, Mihut A, Wu Y, Liu X, Genzel Y, Tan WS, Reichl U (2019) Semi-perfusion cultures of suspension MDCK cells enable high cell concentrations and efficient influenza A virus production. *Vaccine* 37(47):7003–7010. <https://doi.org/10.1016/j.vaccine.2019.04.054>
- Bock A, Schulze-Horsel J, Schwarzer J, Rapp E, Genzel Y, Reichl U (2011) High-density microcarrier cell cultures for influenza virus production. *Biotechnol Prog* 27(1):241–250. <https://doi.org/10.1002/btpr.539>
- Chaturvedi S, Vasen G, Pablo M, Chen X, Beutler N, Kumar A, Tanner E, Illouz S, Rahgoshay D, Burnett J, Holguin L, Chen PY, Ndjamen B, Ott M, Rodick R, Rogers T, Smith DM, Weinberger LS (2021) Identification of a therapeutic interfering particle-A single-dose SARS-CoV-2 antiviral intervention with a high barrier to resistance. *Cell* 184(25):6022–6036.e18. <https://doi.org/10.1016/j.cell.2021.11.004>
- Chen J, Wang J, Zhang J, Ly H (2021) Advances in development and application of influenza vaccines. *Front Immunol* 12:711997. <https://doi.org/10.3389/fimmu.2021.711997>
- Coronel J, Gränicher G, Sandig V, Noll T, Genzel Y, Reichl U (2020) Application of an Inclined Settler for Cell Culture-Based Influenza A Virus Production in Perfusion Mode. *Front Bioeng Biotechnol* 8:672. <https://doi.org/10.3389/fbioe.2020.00672>
- Dimmock NJ, Easton AJ (2015) Cloned defective interfering influenza RNA and a possible pan-specific treatment of respiratory virus diseases. *Viruses* 7(7):3768–3788. <https://doi.org/10.3390/v7072796>
- Dimmock NJ, Rainsford EW, Scott PD, Marriott AC (2008) Influenza virus protecting RNA: an effective prophylactic and therapeutic antiviral. *J Virol* 82(17):8570–8578. <https://doi.org/10.1128/JVI.00743-08>
- Dimmock NJ, Dove BK, Meng B, Scott PD, Taylor I, Cheung L, Hallis B, Marriott AC, Carroll MW, Easton AJ (2012a) Comparison of the protection of ferrets against pandemic 2009 influenza A virus (H1N1) by 244 DI influenza virus and oseltamivir. *Antiviral Res* 96(3):376–385. <https://doi.org/10.1016/j.antiviral.2012.09.017>
- Dimmock NJ, Dove BK, Scott PD, Meng B, Taylor I, Cheung L, Hallis B, Marriott AC, Carroll MW, Easton AJ (2012b) Cloned defective interfering influenza virus protects ferrets from pandemic 2009 influenza A virus and allows protective immunity to be established. *PLoS One* 7(12):e49394. <https://doi.org/10.1371/journal.pone.0049394>
- Dogra T, Pelz L, Boehme JD, Kuechler J, Kershaw O, Marichal-Gallardo P, Baelkner M, Hein MD, Gruber AD, Benndorf D, Genzel Y, Bruder D, Kupke SY, Reichl U (2023) Generation of “OP7 chimera” defective interfering influenza A particle preparations free of infectious virus that show antiviral efficacy in mice. *Sci Rep* 13(1):20936. <https://doi.org/10.1038/s41598-023-47547-1>
- Easton AJ, Scott PD, Edworthy NL, Meng B, Marriott AC, Dimmock NJ (2011) A novel broad-spectrum treatment for respiratory virus infections: influenza-based defective interfering virus provides protection against pneumovirus infection in vivo. *Vaccine* 29(15):2777–2784. <https://doi.org/10.1016/j.vaccine.2011.01.102>
- Elahi SM, Shen CF, Gilbert R (2019) Optimization of production of vesicular stomatitis virus (VSV) in suspension serum-free culture medium at high cell density. *J Biotechnol* 289:144–149. <https://doi.org/10.1016/j.jbiotec.2018.11.023>
- Frensing T (2015) Defective interfering viruses and their impact on vaccines and viral vectors. *Biotechnol J* 10(5):681–689. <https://doi.org/10.1002/biot.201400429>
- Frensing T, Pflugmacher A, Bachmann M, Peschel B, Reichl U (2014) Impact of defective interfering particles on virus replication and antiviral host response in cell culture-based influenza vaccine production. *Appl Microbiol Biotechnol* 98(21):8999–9008. <https://doi.org/10.1007/s00253-014-5933-y>
- Genoyer E, Lopez CB (2019) The impact of defective viruses on infection and immunity. *Annu Rev Virol* 6(1):547–566. <https://doi.org/10.1146/annurev-virology-092818-015652>
- Genzel Y, Reichl U (2007) Vaccine Production. In: Portner R (ed) *Animal Cell Biotechnology*. Humana Press, Totowa, NJ, *Methods in Biotechnology*, pp 457–473
- Genzel Y, Dietzsch C, Rapp E, Schwarzer J, Reichl U (2010) MDCK and Vero cells for influenza virus vaccine production: a one-to-one comparison up to lab-scale bioreactor cultivation. *Appl Microbiol Biotechnol* 88(2):461–475. <https://doi.org/10.1007/s00253-010-2742-9>
- Genzel Y, Vogel T, Buck J, Behrendt I, Ramirez DV, Schiedner G, Jordan I, Reichl U (2014) High cell density cultivations by alternating tangential flow (ATF) perfusion for influenza A virus production using suspension cells. *Vaccine* 32(24):2770–2781. <https://doi.org/10.1016/j.vaccine.2014.02.016>
- Göbel S, Pelz L, Reichl U, Genzel Y (2022) Upstream processing for viral vaccines-Process intensification. In: Kamen A, Cervera L (eds) *Bioprocessing of Viral Vaccines*. CRC Press, Boca Raton
- Göbel S, Jaén KE, Dorn M, Neumeyer V, Jordan I, Sandig V, Reichl U, Altomonte J, Genzel Y (2023) Process intensification strategies toward cell culture-based high-yield production of a fusogenic oncolytic virus. *Biotechnol Bioeng* 120:2639–2657. <https://doi.org/10.1002/bit.28353>
- Gränicher G, Coronel J, Trampler F, Jordan I, Genzel Y, Reichl U (2020) Performance of an acoustic settler versus a hollow fiber-based ATF technology for influenza virus production in perfusion.

- Appl Microbiol Biotechnol 104(11):4877–4888. <https://doi.org/10.1007/s00253-020-10596-x>
- Gränicher G, Babakhani M, Göbel S, Jordan I, Marichal-Gallardo P, Genzel Y, Reichl U (2021) A high cell density perfusion process for Modified Vaccinia virus Ankara production: Process integration with inline DNA digestion and cost analysis. *Biotechnol Bioeng* 118(12):4720–4734. <https://doi.org/10.1002/bit.27937>
- Hein MD, Arora P, Marichal-Gallardo P, Winkler M, Genzel Y, Pöhlmann S, Schughart K, Kupke SY, Reichl U (2021a) Cell culture-based production and in vivo characterization of purely clonal defective interfering influenza virus particles. *BMC Biol* 19(1):91. <https://doi.org/10.1186/s12915-021-01020-5>
- Hein MD, Chawla A, Cattaneo M, Kupke SY, Genzel Y, Reichl U (2021b) Cell culture-based production of defective interfering influenza A virus particles in perfusion mode using an alternating tangential flow filtration system. *Appl Microbiol Biotechnol* 105(19):7251–7264. <https://doi.org/10.1007/s00253-021-11561-y>
- Hein MD, Kollmus H, Marichal-Gallardo P, Püttker S, Benndorf D, Genzel Y, Schughart K, Kupke SY, Reichl U (2021c) OP7, a novel influenza A virus defective interfering particle: production, purification, and animal experiments demonstrating antiviral potential. *Appl Microbiol Biotechnol* 105(1):129–146. <https://doi.org/10.1007/s00253-020-11029-5>
- Hein MD, Kazenmaier D, van Heuvel Y, Dogra T, Cattaneo M, Kupke SY, Stitz J, Genzel Y, Reichl U (2023) Production of retroviral vectors in continuous high cell density culture. *Appl Microbiol Biotechnol*. <https://doi.org/10.1007/s00253-023-12689-9>
- Henry O, Dormond E, Perrier M, Kamen A (2004) Insights into adenoviral vector production kinetics in acoustic filter-based perfusion cultures. *Biotechnol Bioeng* 86(7):765–774. <https://doi.org/10.1002/bit.20074>
- Hsu AC, Barr I, Hansbro PM, Wark PA (2011) Human influenza is more effective than avian influenza at antiviral suppression in airway cells. *Am J Respir Cell Mol Biol* 44(6):906–913. <https://doi.org/10.1165/rcmb.2010-01570C>
- Huo C, Cheng J, Xiao J, Chen M, Zou S, Tian H, Wang M, Sun L, Hao Z, Hu Y (2020) Defective viral particles produced in mast cells can effectively fight against lethal influenza A virus. *Front Microbiol* 11:553274. <https://doi.org/10.3389/fmicb.2020.553274>
- Jardon M, Garnier A (2003) pH, pCO₂, and Temperature Effect on R-Adenovirus Production. *Biotechnol Prog* 19(1):202–208. <https://doi.org/10.1021/bp025585a>
- Jug H, Hosta N, Tajnik M, Strancar A, Brodesser D, Tisch B, Heger T, Wolschek M, Seipelt J, Reiter M (2023) Production and purification of newcastle disease virus. *BioProcess Int* 21:18
- Kalbfuss B, Knöchlein A, Kröber T, Reichl U (2008) Monitoring influenza virus content in vaccine production: precise assays for the quantitation of hemagglutination and neuraminidase activity. *Biologicals* 36(3):145–161. <https://doi.org/10.1016/j.biologicals.2007.10.002>
- Karki B, Bull JJ, Krone SM (2022) Modeling the therapeutic potential of defective interfering particles in the presence of immunity. *Virus Evol* 8(2):1–11. <https://doi.org/10.1093/ve/veac047>
- Krammer F, Smith GJD, Fouchier RAM, Peiris M, Kedzierska K, Doherty PC, Palese P, Shaw ML, Treanor J, Webster RG, Garcia-Sastre A (2018) Influenza. *Nat Rev Dis Primers* 4(1):3. <https://doi.org/10.1038/s41572-018-0002-y>
- Kupke SY, Riedel D, Frensing T, Zmora P, Reichl U (2019) A novel type of influenza A virus-derived defective interfering particle with nucleotide substitutions in its genome. *J Virol* 93(4):e01786–e1818. <https://doi.org/10.1128/JVI.01786-18>
- Kupke SY, Ly LH, Borno ST, Ruff A, Timmermann B, Vingron M, Haas S, Reichl U (2020) Single-cell analysis uncovers a vast diversity in intracellular viral defective interfering RNA content affecting the large cell-to-cell heterogeneity in influenza A virus replication. *Viruses* 12(1):71. <https://doi.org/10.3390/v12010071>
- Laske T, Heldt FS, Hoffmann H, Frensing T, Reichl U (2016) Modeling the intracellular replication of influenza A virus in the presence of defective interfering RNAs. *Virus Res* 213:90–99. <https://doi.org/10.1016/j.virusres.2015.11.016>
- Levi LI, Rezelj VV, Henrion-Lacritick A, Erazo D, Boussier J, Vallet T, Bernhauerova V, Suzuki Y, Carrau L, Weger-Lucarelli J, Saleh MC, Vignuzzi M (2021) Defective viral genomes from chikungunya virus are broad-spectrum antivirals and prevent virus dissemination in mosquitoes. *PLoS Pathog* 17(2):e1009110. <https://doi.org/10.1371/journal.ppat.1009110>
- Lohr V, Genzel Y, Behrendt I, Scharfenberg K, Reichl U (2010) A new MDCK suspension line cultivated in a fully defined medium in stirred-tank and wave bioreactor. *Vaccine* 28(38):6256–6264. <https://doi.org/10.1016/j.vaccine.2010.07.004>
- Marichal-Gallardo P, Pieler MM, Wolff MW, Reichl U (2017) Steric exclusion chromatography for purification of cell culture-derived influenza A virus using regenerated cellulose membranes and polyethylene glycol. *J Chromatogr A* 1483:110–119. <https://doi.org/10.1016/j.chroma.2016.12.076>
- Marichal-Gallardo P, Börner K, Pieler MM, Sonntag-Buck V, Obr M, Bejarano D, Wolff MW, Krausslich HG, Reichl U, Grimm D (2021) Single-use capture purification of adeno-associated viral gene transfer vectors by membrane-based steric exclusion chromatography. *Hum Gene Ther*. <https://doi.org/10.1089/hum.2019.284>
- Marriott AC, Dimmock NJ (2010) Defective interfering viruses and their potential as antiviral agents. *Rev Med Virol* 20(1):51–62. <https://doi.org/10.1002/rmv.641>
- Mendes JP, Fernandes B, Pineda E, Kudugunti S, Bransby M, Gantier R, Peixoto C, Alves PM, Roldao A, Silva RJS (2022) AAV process intensification by perfusion bioreaction and integrated clarification. *Front Bioeng Biotechnol* 10:1020174. <https://doi.org/10.3389/fbioe.2022.1020174>
- Nadeau I, Kamen A (2003) Production of adenovirus vector for gene therapy. *Biotechnol Adv* 20(7–8):475–489. [https://doi.org/10.1016/s0734-9750\(02\)00030-7](https://doi.org/10.1016/s0734-9750(02)00030-7)
- Nayak DP, Chambers TM, Akkina RK (1985) Defective-Interfering (DI) RNAs of influenza viruses: origin, structure, expression, and interference. In: Cooper M, Eisen H, Goebel W, Hofschneider PH, Koprowski H, Melchers F, Oldstone M, Rott R, Schweiger HG, Vogt PK, Wilson I (eds) *Current Topics in Microbiology and Immunology*. Springer, Berlin Heidelberg, Berlin, Heidelberg, pp 103–151
- Nikolay A, Leon A, Schwamborn K, Genzel Y, Reichl U (2018) Process intensification of EB66(R) cell cultivations leads to high-yield yellow fever and Zika virus production. *Appl Microbiol Biotechnol* 102(20):8725–8737. <https://doi.org/10.1007/s00253-018-9275-z>
- Nikolay A, de Groot J, Genzel Y, Wood JA, Reichl U (2020) Virus harvesting in perfusion culture: choosing the right type of hollow fiber membrane. *Biotechnol Bioeng* 117(10):3040–3052. <https://doi.org/10.1002/bit.27470>
- Pelz L, Rüdiger D, Dogra T, Alnaji FG, Genzel Y, Brooke CB, Kupke SY, Reichl U (2021) Semi-continuous propagation of influenza A virus and its defective interfering particles: analyzing the dynamic competition to select candidates for antiviral therapy. *J Virol* 95(24):e01174–e1221. <https://doi.org/10.1128/JVI.01174-21>
- Pelz L, Piagnani E, Marsall P, Wynserski N, Hein MD, Marichal-Gallardo P, Kupke SY, Reichl U (2023) Broad-spectrum antiviral activity of influenza A defective interfering particles against respiratory syncytial, yellow fever, and Zika virus replication in vitro. *Viruses* 15(9):1872
- Penn R, Tregoning JS, Flight KE, Baillon L, Frise R, Goldhill DH, Johansson C, Barclay W (2022) Levels of influenza A virus

- defective viral genomes determine pathogenesis in the BALB/c mouse model. *J Virol* 96(21):e01178–e1222. <https://doi.org/10.1128/jvi.01178-22>
- Petiot E, Jacob D, Lanthier S, Lohr V, Ansoerge S, Kamen AA (2011) Metabolic and kinetic analyses of influenza production in perfusion HEK293 cell culture. *BMC Biotechnol* 11(1):84. <https://doi.org/10.1186/1472-6750-11-84>
- Petiot E, Ansoerge S, Rosa-Calatrava M, Kamen A (2017) Critical phases of viral production processes monitored by capacitance. *J Biotechnol* 242:19–29. <https://doi.org/10.1016/j.jbiotec.2016.11.010>
- Rand U, Kupke SY, Shkarlet H, Hein MD, Hirsch T, Marichal-Gallardo P, Cicin-Sain L, Reichl U, Bruder D (2021) Antiviral activity of influenza a virus defective interfering particles against SARS-CoV-2 replication in vitro through stimulation of innate immunity. *Cells* 10(7):1756. <https://doi.org/10.3390/cells10071756>
- Rezeli VV, Carrau L, Merwaiss F, Levi LL, Erazo D, Tran QD, Henrion-Lacritick A, Gausson V, Suzuki Y, Shengjuler D, Meyer B, Vallet T, Weger-Lucarelli J, Bernhauerova V, Titievsky A, Sharov V, Pietropaoli S, Diaz-Salinas MA, Legros V, Pardigon N, Barba-Spaeth G, Brodsky L, Saleh MC, Vignuzzi M (2021) Defective viral genomes as therapeutic interfering particles against flavivirus infection in mammalian and mosquito hosts. *Nat Commun* 12(1):2290. <https://doi.org/10.1038/s41467-021-22341-7>
- Rüdiger D, Pelz L, Hein MD, Kupke SY, Reichl U (2021) Multiscale model of defective interfering particle replication for influenza a virus infection in animal cell culture. *PLoS Comput Biol* 17(9):e1009357. <https://doi.org/10.1371/journal.pcbi.1009357>
- Schneider M, Marison IW, von Stockar U (1996) The importance of ammonia in mammalian cell culture. *J Biotechnol* 46(3):161–185. [https://doi.org/10.1016/0168-1656\(95\)00196-4](https://doi.org/10.1016/0168-1656(95)00196-4)
- Scott PD, Meng B, Marriott AC, Easton AJ, Dimmock NJ (2011) Defective interfering influenza a virus protects in vivo against disease caused by a heterologous influenza B virus. *J Gen Virol* 92(Pt 9):2122–2132. <https://doi.org/10.1099/vir.0.034132-0>
- Seitz C, Frensing T, Hoper D, Kochs G, Reichl U (2010) High yields of influenza a virus in Madin-Darby canine kidney cells are promoted by an insufficient interferon-induced antiviral state. *J Gen Virol* 91(Pt 7):1754–1763. <https://doi.org/10.1099/vir.0.020370-0>
- Smither SJ, Garcia-Dorival I, Eastaugh L, Findlay JS, O'Brien LM, Carruthers J, Williamson ED, Molina-París C, Hiscox JA, Laws TR (2020) An investigation of the effect of transfected defective, ebola virus genomes on ebola replication. *Front Cell Infect Microbiol* 10:159. <https://doi.org/10.3389/fcimb.2020.00159>
- Tona RM, Shah R, Middaugh K, Steve J, Marques J, Roszell BR, Jung C (2023) Process intensification for lentiviral vector manufacturing using tangential flow depth filtration. *Mol Ther Methods Clin Dev* 29:93–107. <https://doi.org/10.1016/j.omtm.2023.02.017>
- Tran MY, Kamen AA (2022) Production of lentiviral vectors using a HEK-293 producer cell line and advanced perfusion processing. *Front Bioeng Biotechnol* 10:887716. <https://doi.org/10.3389/fbioe.2022.887716>
- Vasilijevic J, Zamarreño N, Oliveros JC, Rodriguez-Frandsen A, Gómez G, Rodríguez G, Pérez-Ruiz M, Rey S, Barba I, Pozo F, Casas I, Nieto A, Falcón A (2017) Reduced accumulation of defective viral genomes contributes to severe outcome in influenza virus infected patients. *PLoS Pathog* 13(10):e1006650. <https://doi.org/10.1371/journal.ppat.1006650>
- Vázquez-Ramírez D, Genzel Y, Jordan I, Sandig V, Reichl U (2018) High-cell-density cultivations to increase MVA virus production. *Vaccine* 36(22):3124–3133. <https://doi.org/10.1016/j.vaccine.2017.10.112>
- Welch SR, Tilston NL, Lo MK, Whitmer SLM, Harmon JR, Scholte FEM, Spengler JR, Duprex WP, Nichol ST, Spiropoulou CF (2020) Inhibition of Nipah virus by defective interfering particles. *J Infect Dis* 221(Suppl 4):S460–S470. <https://doi.org/10.1093/infdis/jiz564>
- WHO (2023) Influenza (Seasonal). [https://www.who.int/news-room/fact-sheets/detail/influenza-\(seasonal\)#:~:text=There%20are%20around%20a%20billion,650%20000%20respiratory%20deaths%20annually](https://www.who.int/news-room/fact-sheets/detail/influenza-(seasonal)#:~:text=There%20are%20around%20a%20billion,650%20000%20respiratory%20deaths%20annually). Accessed 18 Oct 2023
- Wu Y, Bissinger T, Genzel Y, Liu X, Reichl U, Tan WS (2021) High cell density perfusion process for high yield of influenza a virus production using MDCK suspension cells. *Appl Microbiol Biotechnol* 105(4):1421–1434. <https://doi.org/10.1007/s00253-020-11050-8>
- Zhao H, To KKW, Chu H, Ding Q, Zhao X, Li C, Shuai H, Yuan S, Zhou J, Kok KH, Jiang S, Yuen KY (2018) Dual-functional peptide with defective interfering genes effectively protects mice against avian and seasonal influenza. *Nat Commun* 9(1):2358. <https://doi.org/10.1038/s41467-018-04792-7>

Publisher's Note Springer Nature remains neutral with regard to jurisdictional claims in published maps and institutional affiliations.

3.6. Sixth Manuscript

In the study of the sixth manuscript, a proof-of principle study to apply the TFD module as perfusion system for the high-titer production of viruses with continuous virus harvesting and clarification is highlighted.

Göbel, Sven*; **Pelz, Lars***; Silva, Cristina A. T.; Brühlmann, Béla; Hill, Charles; Altomonte, Jennifer; Kamen, Amine; Reichl, Udo; Genzel, Yvonne

*Shared first authorship

Production of recombinant vesicular stomatitis virus-based vectors by tangential flow depth filtration

Applied Microbiology and Biotechnology, 2024

(Göbel et al., 2024)

Reproduced with permission from Springer Nature.

No changes were made

<https://creativecommons.org/licenses/by/4.0/>

Individual contribution:

In the study of the sixth manuscript, for Figure 6 and 7, I carried out the experiments, visualized data, wrote the results, discussion, and materials & methods section.



Production of recombinant vesicular stomatitis virus-based vectors by tangential flow depth filtration

Sven Göbel¹ · Lars Pelz¹ · Cristina A. T. Silva² · Béla Brühlmann³ · Charles Hill³ · Jennifer Altomonte⁴ · Amine Kamen⁵ · Udo Reichl^{1,6} · Yvonne Genzel¹

Received: 17 October 2023 / Revised: 14 February 2024 / Accepted: 16 February 2024
© The Author(s) 2024

Abstract

Cell culture-based production of vector-based vaccines and virotherapeutics is of increasing interest. The vectors used not only retain their ability to infect cells but also induce robust immune responses. Using two recombinant vesicular stomatitis virus (rVSV)-based constructs, we performed a proof-of-concept study regarding an integrated closed single-use perfusion system that allows continuous virus harvesting and clarification.

Using suspension BHK-21 cells and a fusogenic oncolytic hybrid of vesicular stomatitis virus and Newcastle disease virus (rVSV-NDV), a modified alternating tangential flow device (mATF) or tangential flow depth filtration (TFDF) systems were used for cell retention. As the hollow fibers of the former are characterized by a large internal lumen (0.75 mm; pore size 0.65 μm), membrane blocking by the multi-nucleated syncytia formed during infection could be prevented. However, virus particles were completely retained. In contrast, the TFDF filter unit (lumen 3.15 mm, pore size 2–5 μm) allowed not only to achieve high viable cell concentrations (VCC, 16.4–20.6 $\times 10^6$ cells/mL) but also continuous vector harvesting and clarification. Compared to an optimized batch process, 11-fold higher infectious virus titers were obtained in the clarified permeate (maximum 7.5 $\times 10^9$ TCID₅₀/mL).

Using HEK293-SF cells and a rVSV vector expressing a green fluorescent protein, perfusion cultivations resulted in a maximum VCC of 11.3 $\times 10^6$ cells/mL and infectious virus titers up to 7.1 $\times 10^{10}$ TCID₅₀/mL in the permeate. Not only continuous harvesting but also clarification was possible. Although the cell-specific virus yield decreased relative to a batch process established as a control, an increased space-time yield was obtained.

Key points

- Viral vector production using a TFDF perfusion system resulted in a 460% increase in space-time yield
- Use of a TFDF system allowed continuous virus harvesting and clarification
- TFDF perfusion system has great potential towards the establishment of an intensified vector production

Keywords Tangential flow depth filtration · Alternating tangential flow filtration · Bioreactor · Perfusion · Recombinant VSV-based vectors · Oncolytics · Vaccines

Sven Göbel and Lars Pelz contributed equally to this work.

✉ Yvonne Genzel
genzel@mpi-magdeburg.mpg.de

¹ Bioprocess Engineering, Max Planck Institute for Dynamics of Complex Technical Systems, Sandtorstr. 1, 39106 Magdeburg, Germany

² Department of Chemical Engineering, Polytechnique Montréal, Montréal, Québec, Canada

³ Repligen, Waltham, MA, USA

⁴ Department of Internal Medicine II, Klinikum rechts der Isar, Technische Universität München, Munich, Germany

⁵ Department of Bioengineering, McGill University, Montréal, Québec, Canada

⁶ Chair for Bioprocess Engineering, Otto von Guericke University Magdeburg, Universitätsplatz 2, 39106 Magdeburg, Germany

Introduction

In the relentless pursuit to combat infectious diseases, recombinant vector-based vaccines produced in cell culture have gained popularity during the last decade. Compared to other vaccine platforms, viral vector-based vaccines retain their ability to infect cells, thereby inducing robust immune responses by increasing both humoral and cellular immunity (Ura et al. 2014). Successful large-scale applications of adenoviral-based vectors against SARS-CoV-2 (Mendonça et al. 2021) combined with their potential application against a wide array of infectious diseases, resulted in tremendous research efforts to develop new recombinant vector-based vaccines (accounting for 14% of global R&D vaccine landscape in 2023 (Yue et al. 2023)) and to improve current manufacturing processes. One such vector is based on the recombinant vesicular stomatitis virus (rVSV). Due to its broad tropism, fast replication kinetics to high titers, low viral pathogenicity, rare pre-existing anti-vector immunity in humans, and ease of genetic manipulation, rVSV has gained popularity for both vaccine and oncolytic applications (Ura et al. 2021). Replacing the native glycoprotein of rVSV to any glycoprotein of interest allows delivery of foreign antigens to elicit robust humoral and cellular immunity for vaccine applications, while simultaneously reducing the manufacturing-associated biosafety standards (e.g., for highly pathogenic viruses) (Zhang and Nagalo 2022). Various vaccine candidates manufactured using a rVSV production platform have shown prophylactic effects against Ebola (Suder et al. 2018), SARS-CoV-2 (Ura et al. 2021), Marburg virus (Jones et al. 2005), Lassa virus (Geisbert et al. 2005), Andes virus (Brown et al. 2011), hepatitis B virus (Cobleigh et al. 2010), *Yersinia pestis* (Palin et al. 2007), respiratory syncytial virus (Kahn et al. 2001), dengue virus (Lauretti et al. 2016), chikungunya virus (van den Pol et al. 2017), Nipah virus (DeBuysscher et al. 2016), Zika virus (Emanuel et al. 2018), human papillomavirus (Liao et al. 2008), and influenza virus (Roberts et al. 1998) in animal models; and some are being tested in clinical trials. Despite the well-demonstrated prophylactic efficacy, currently only one VSV-based vaccine against Zaire ebolavirus (rVSV-ZEBOV) gained FDA and EMA approval in 2019 (EMA 2019; FDA 2019). Usage of rVSV as oncolytic agents is particularly interesting, as its high cytopathogenicity, fast replication cycle, non-integration into the host genome, IFN-sensitivity, selective infection, and potent induction of apoptosis in cancer cells fulfill all critical features for virotherapy (Zhang and Nagalo 2022). Further genetic modification approaches such as pseudotyping innate glycoproteins with heterologous fusion glycoproteins, generating chimeric constructs that can convey fusogenic-based viral propagation, further enhance the

oncolytic abilities of rVSV-based constructs (Abdullahi et al. 2018). One such novel rVSV-based construct contains the fusogenic mutant proteins of Newcastle disease virus (NDV) and has shown promising pre-clinical efficacy in various cancer models (Abdullahi et al. 2018; Krabbe et al. 2021).

To address the unprecedented demand, as well as the high input doses required for many rVSV-based therapies, current batch-based manufacturing strategies need to be intensified. Usage of suspension cell lines in chemically defined media allows for the design of processes that are easier to scale-up, for higher cell concentrations and for smaller footprints compared to traditional adherent-based manufacturing (Pelz et al. 2022). By the establishment of perfusion cultures, where depleted medium is continuously exchanged with fresh medium, while the cells are retained in the bioreactor by the use of a cell retention device, even higher cell concentrations can be achieved. Process intensification in perfusion mode to increase virus titers, cell-specific virus yields (CSVYs), space-time yield (STY), and volumetric virus productivity (VVP) have already been elaborated for different viruses and vectors such as for Zika virus (Nikolay et al. 2018), influenza A virus (IAV) (Wu et al. 2021), lentiviral vectors (LV) (Tran and Kamen 2022; Tona et al. 2023), adeno-associated virus (AAV) (Mendes et al. 2022), rVSV-COV-2 (Yang et al. 2023), rVSV-NDV (Göbel et al. 2023a), and modified vaccinia virus Ankara (Gränicher et al. 2021a; Gränicher et al. 2021b). However, by targeting higher cell concentrations, the CSVY might be decreased (high-cell density effect) thus lowering the STY and VVP (Bock et al. 2011; Nadeau and Kamen 2003).

For high-cell concentration cultivations, membrane-based systems, i.e., alternating tangential flow (ATF) and tangential flow filtration (TFF) modules are widely employed. One major drawback of these systems is the risk of filter fouling (despite the self-cleaning backflush of the ATF) and retention of virus particles, which leads to unwanted accumulation of virus inside the bioreactor within the cell environment until full harvest of the bioreactor broth is possible (Genzel et al. 2014; Hadpe et al. 2017; Nikolay et al. 2020; Nikolay et al. 2018; Tona et al. 2023; Vázquez-Ramírez et al. 2019). As virus release typically leads to cell lysis, cell debris and DNA increase over time, equally increasing viscosity of the culture broth and further increasing the risk of membrane clogging. Prolonged retention inside the bioreactor can have a negative impact on virus infectivity due to a release of cellular proteases, adsorption of virions to cellular debris, and viral temperature sensitivity (Aunins 2003; Eccles 2021; Genzel et al. 2010; Göbel et al. 2023a; Gränicher et al. 2020; Wu et al. 2021). Additionally, fusogenic oncolytic constructs such as rVSV-NDV that lead to the formation of large multi-nucleated syncytia (>100 µm)

in perfusion cultures are likely to block the small lumen sizes of commonly used hollow-fiber membranes (Göbel et al. 2023a). One approach to overcome this issue is the use of non-membrane-based systems such as an acoustic filter (Göbel et al. 2023a; Gränicher et al. 2020; Manceur et al. 2017) or an inclined settler (Coronel et al. 2020); however, these systems are often complex or not compatible with industrial size bioreactors and have a lower cell retention efficiency. Alternatively, membranes that allow virus particles to pass through could be used. This has been recently demonstrated for the production of IAV defective interfering particles utilizing a tubular membrane (VHU, pore size ~10 µm) coupled to an ATF system (Hein et al. 2021). Using tangential flow depth filtration (TFDF) perfusion modules (pore size 2–5 µm), continuous harvest of LV as well as AAV has been already shown (Mendes et al. 2022; Tona et al. 2023; Tran and Kamen 2022). This allows for shorter residence times of infectious virus particles and the possibility to immediately store harvested material in cooled tanks to increase virus stability and, thus, virus yields and productivity. For instance, continuous virus harvest using an acoustic settler for IAV production enhanced CSVY and VVP by a factor of 1.5 relative to a perfusion run with a hollow fiber membrane with PES (0.2 µm cut-off) (Gränicher et al. 2020). Moreover, the TFDF module can combine continuous virus harvest and clarification in a single step, reducing the number of unit operations and therefore saving time and money (Mendes et al. 2022). All in all, this could allow for a direct integration of upstream (virus production) and downstream processing (virus purification), further reducing costs while increasing flexibility and productivity (Gränicher et al. 2021a; Moleirinho et al. 2020).

In this study, we evaluated the applicability of the TFDF perfusion system as a novel cell retention device and virus transmission away for the host cell environment for both perfusion cultivation and continuous harvest filtration with clarification (turbidity reduction) in a single operation. The process intensification of the production of two different rVSV-based vectors, one which induces classical cytopathic effects and one that mediates cell fusion reactions, was compared to optimized batch processes.

Materials and methods

Cell lines, media, and viral seed stock

Baby hamster kidney (BHK-21) cells (CEVA Animal Health) were cultivated in protein expression medium (PEM) (Gibco, USA) supplemented with 4-mM pyruvate and 8 mM L-glutamine (Sigma-Aldrich, USA). Cells were sub-cultured to 0.5×10^6 cells/mL twice a week using vented, baffled 125-mL shake flasks (50 mL working volume (WV)) at 37

°C and 5% CO₂ with controlled agitation (185 rpm, shaken diameter of 50 mm, Infors HT, Switzerland). Human embryonic kidney (HEK293-SF) cells were kindly provided by National Research Council of Canada (NRC, Montreal, Canada) and grown in vented, non-baffled 125-mL shake flasks (TriForest Enterprises, USA) in HyClone HyCell TransF_x-H medium (Cytiva, USA) supplemented with 6 mM glutamine and 0.1% Koliphor P188 (Merck, USA). HEK293-SF cells were passaged three times a week at 0.2×10^6 or 0.5×10^6 cells/mL and grew in a humidified Multitron orbital shaker (shaking diameter of 25 mm, Infors HT, Switzerland) at 135 rpm, 37 °C, and 5% CO₂. Adherent Huh7 cells were cultivated at 37 °C and 5% CO₂ in T75 flasks in high glucose Dulbecco's Modified Eagle Medium (DMEM, Gibco, USA), supplemented with 1 mM sodium pyruvate (Gibco, USA), 1× non-essential amino acids (Gibco, USA), and 10% FCS. Adherent HEK293 cells were maintained in T75 or T175 flasks in DMEM (Wisent Bioproducts, Canada) supplemented with 10% FCS (Wisent Bioproducts, Canada) at 37 °C and 5% CO₂ in a humidified incubator and sub-cultured twice a week by using TrypLE Express (Thermo Fisher Scientific, USA). Adherent AGE1.CR.pIX cells were maintained at 37 °C, 5% CO₂ in T75 flasks in DMEM-F12 medium (Gibco, USA).

For infections, the previously described BHK-21-derived virus seed (rVSV-NDV) with a titer of 1.33×10^9 50% tissue culture infectious dose (TCID₅₀)/mL was used (Göbel et al. 2023a). Moreover, we used rVSV-green fluorescent protein (GFP) virus seed with a titer of 2.12×10^9 TCID₅₀/mL, which was derived from suspension HEK293 cells and kindly provided by NRC. Aliquots of the stocks and clarified samples were stored at –80 °C and were used once for each experiment or assay to prevent loss of infectivity due to repeated freeze-thaw cycles.

Perfusion mode production of rVSV-NDV in an orbitally shaken bioreactor

To evaluate applicability of membrane-based cell retention for production of fusogenic oncolytic viruses, a perfusion run employing a modified alternating tangential flow filtration device (mATF) as a cell retention device was carried out. Here, a SB10-X orbital shaken bioreactor (OSB) (Adolf Kühner AG) was used with the novel 3 L modular adapter and standard 3-L single-use bags. BHK-21 cells were inoculated at 0.9×10^6 cells/mL with 2.4 L WV at 37 °C and shaken at 100 rpm (50-mm shaking diameter). Aeration was solely carried out through headspace gassing using 300 mL/min air/O₂. By automatic adjustments of the gas composition in the output flow, dissolved oxygen (DO) and pH were controlled at 80% and 7.20, respectively. Perfusion was initiated once viable cell concentration (VCC) reached 4–10⁶ cells/mL. The perfusion rate was manually increased over time

to maintain a cell-specific perfusion rate (CSPR) of 115 pL/cell/day. For virus production, temperature was decreased to 34 °C, and the perfusion rate was set to 1.8 RV/day. Coupling of the 3-L single-use bag to a hollow fiber membrane (0.65- μm modified polyethersulfone (mPES), 1075 cm^2 , Repligen, USA) connected to the mATF (Repligen, USA) was carried out as described previously (Coronel et al. 2019). Exchange flow rates of the diaphragm pump were set to 1.5 L/min. As the ATF2 module was placed below the SB10-X, a height differential of 40 cm was set, while other parameters were kept as given by the supplier.

Perfusion mode production of rVSV-NDV in a STR

Bioreactor perfusion cultivations were performed using a 3-L stirred tank bioreactor (STR) (DASGIP, Eppendorf AG, Germany) equipped with two pitched blade impellers (50-mm diameter; 180 rpm) and a L-drilled hole sparger, as well as a microsparger for gas supply. The DO setpoint of 50% was maintained by varying the gas flow rates (3–9 L/h) and the percentage of O_2 in the gas mixture (21–100%). pH was controlled at 7.20 by sparging CO_2 . Temperature was set to 37 °C for the growth phase and 34 °C for the infection phase. BHK-21 cells were inoculated at 0.8×10^6 cells/mL at 1.3 L WV, and the cells were grown in batch mode until a VCC of 4.0×10^6 cells/mL was reached. Then, perfusion was started, and medium was exchanged with a CSPR of 130 pL/cell/day for BHK-21 cells. For cell retention, a 30- cm^2 TFDF cartridge (polypropylene and polyethylene terephthalate, pore size 2–5 μm , Repligen) connected to a Krosflo TFDF system (Repligen) was used. Using the KrosFlo's integrated flow sensor and weight control system, the recirculation rate and WV were maintained at 0.9 L/min and 1.3 L, respectively. Permeate flow rates were either updated daily based on VCC and the CSPR or controlled automatically through a capacitance probe and pre-amplifier connected to the ArcView controller 265 (Incyte Hamilton, USA), as described previously (Göbel et al. 2023a). A “cell factor” of 0.25 was used to set the cell volume-specific perfusion rate (CVSPR) of 0.06 pL/ μm^3 /day. At time of infection (TOI), an RV was exchanged by temporarily increasing the permeate flow rate to 8–10 mL/min, and cells were subsequently infected with a multiplicity of infection (MOI) of 1E-4. After infection, permeate flow was paused for up to 2 h and then fixed to 1.8 RV/day (1.7 mL/min). The clarified permeate was collected continuously into sterile polyethylene terephthalate bottles, previously filled with sucrose equal to 5% final concentration, at room temperature. The final one-step bioreactor harvest was carried out using a modified concentration-diafiltration-concentration (C1/DF/C2) process (Table S1), where the permeate flow was paused during the diafiltration step. Furthermore, either sterile PBS (TFDF1) or supplemented medium (TFDF2) was used for

diafiltration. The overall setup including devices for control of perfusion is shown in Fig. 1.

Other analytics for rVSV-NDV experiments

VCC and viability were quantified using the automated cell counter ViCell (Coulter Beckman, USA). A pH7110 potentiometer (Inolab, USA) was used to measure off-line pH, and metabolite concentrations (glucose, lactate, glutamine, glutamate, ammonium) were determined by a Cedex Bio Analyzer (Roche, Switzerland). Titration of rVSV-NDV was carried out using adherent AGE1.CR.pIX cells and the previously described TCID₅₀ assay (Göbel et al. 2022a, 2022b). Oncolytic viral potency was confirmed using the previously described half maximal inhibitory concentration (IC₅₀) potency assay in Huh7 cells (Göbel et al. 2023a; Göbel et al. 2022a). Taking into account only the error of the TCID₅₀ assay (–50%/+100% on a linear scale), the CSVY was calculated as previously described by Gränicher et al. 2020. Total DNA and protein were quantified using the Quant-iT™ PicoGreen dsDNA assay kit (Thermo Fisher Scientific, USA) and with Pierce™ BCA assay kit (Thermo Fisher Scientific, USA), respectively, according to the manufacturer's instructions. The solution turbidity of bioreactor and permeate samples was measured using a turbidimeter (2100 Qis Portable, HACH).

Production of rVSV-GFP in shake flasks

For production of rVSV-GFP in batch mode using shake flasks, HEK293-SF cells growing in exponential growth phase were centrifuged (300 \times g, 5 min, room temperature (RT)), supernatant was discarded, and cells were resuspended in penicillin/streptomycin (Pen/Strep)-containing fresh medium. Subsequently, cells were seeded at 0.4×10^6 cells/mL into a shake flask and grown to 1.1×10^6 cells/mL. Cells were infected at an MOI of 1E-3, and temperature was reduced from 37 to 34 °C. Supernatant samples were centrifuged (1200 \times g, 5 min, 4 °C) and stored at –80 °C for analytics.

Batch mode production of rVSV-GFP in a STR

Production of rVSV-GFP in batch mode was conducted in a 3 L (2100 mL WV) or 1 L (700 mL WV) STR (Applikon Biotechnology, Netherlands), which was equipped with two (3 L STR) or one (1 L STR) marine impeller(s) (100 rpm). Continuous surface aeration (12.5 mL/min), with sparging of O_2 (microsparger) when necessary, was used to control dissolved oxygen above 40% DO. The pH set point of 7.15 was controlled by CO_2 injection into the headspace of the bioreactor or addition of 9% NaHCO_3 . HEK293-SF cells cultured in shake flasks were centrifuged (300 \times g, 5 min, RT), resuspended in fresh Pen/Strep-containing medium

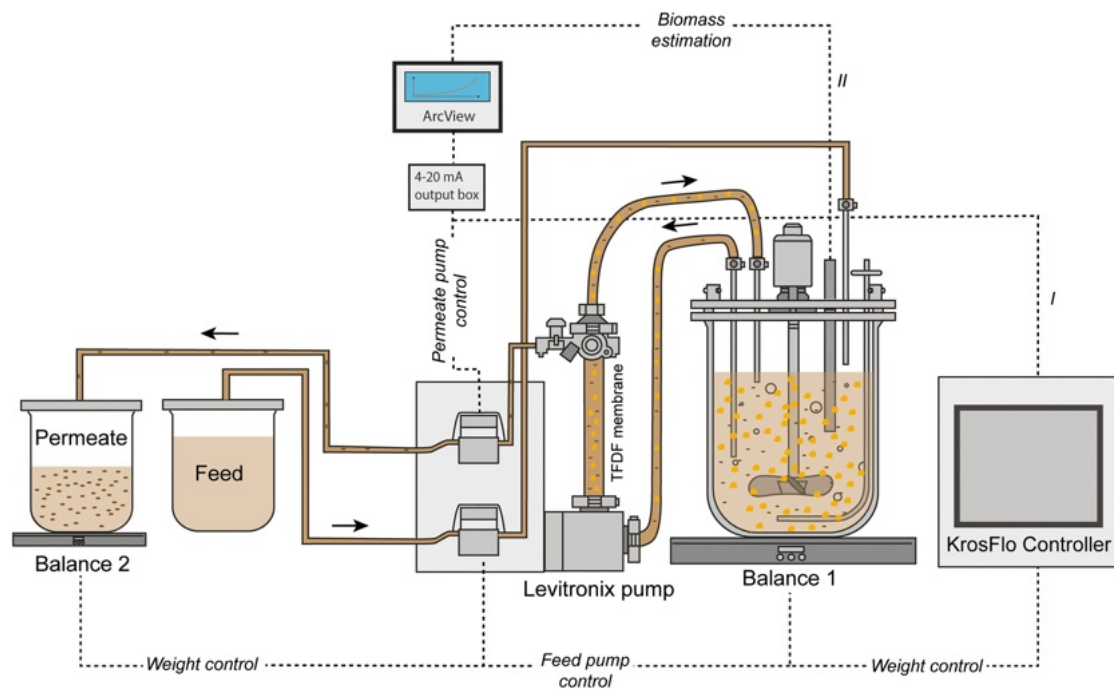


Fig. 1 Scheme of the TFDF setup for perfusion cultivations with manual adjustment (I) or automated (II) perfusion control (adapted from (Göbel et al. 2022b)). BHK-21 cells were continuously pumped through a 30-cm² TFDF cartridge (pore size 2–5.0 μm) by a levitronix impeller pump in unidirectional flow. Flow rates for feed and inlet were controlled using balances and KrosFlo's integrated flow sensor,

respectively. For the cell growth phase, the permeate flow was either manually adjusted (I, using the KrosFlo controller) or controlled (II, using a capacitance probe). Larger orange circles indicate cells, black ellipses indicate virus particles, and dashed lines indicate different types of signal transmission

and inoculated at about 0.3×10^6 cells/mL into the STR. HEK293-SF cells were grown at 37 °C up to $1.2\text{--}1.3 \times 10^6$ cells/mL. Prior to infection, the temperature was reduced to 34 °C, and cells were infected at an MOI of 1E-3.

Perfusion mode production of rVSV-GFP in a STR

For perfusion mode production of rVSV-GFP, a 3 L STR was used at 2100 mL WV. Standard bioreactor setup and process parameters are similar to those described in the previous chapter. Before inoculation, recirculation was started with a recirculation rate of 1.0 L/min. HEK293-SF cells growing in shake flasks in the exponential growth phase were centrifuged ($300 \times g$, 5 min, RT), resuspended in fresh Pen/Strep-containing medium, and seeded at 0.8×10^6 cells/mL. After a cell growth phase in batch mode for 24 h, perfusion was initiated with a permeate flow rate of 0.9 mL/min (0.6 RV/d). In the following, the permeate flow rate was adjusted manually based on a CSPR of 115 pL/cell/day. The bioreactor weight was used to control the feed flow rate. Prior to infection, one RV with medium was exchanged by temporarily increasing the permeate flow rate to 20–33 mL/min. Temperature was reduced to 34 °C, and HEK293-SF cells (10×10^6 cells/mL) were infected

at an MOI of 1E-3. Following infection, the permeate flow was stopped for 1 h, and then set at a constant rate of 2.2 mL/min (1.5 RV/day). Supernatant samples were taken from the bioreactor and permeate line. After infection, the accumulated clarified permeate in the permeate bottle was stored on ice and transferred to a storage bottle (stored at 4 °C) at each sample taking. Lastly, a final “pool sample” was taken from the storage bottle containing the entire volume of collected permeate, without the final harvest step. For final one-step harvest at 31-h post infection (hpi), the recirculation rate was increased to 2.1 L/min to prevent filter fouling and promote self-cleaning. In more detail, a C1/DF/C2 process was conducted (Table S2). In the first step, 980 mL cell broth was pumped (31.3 mL/min) from the bioreactor through the TFDF filter into the harvest bottle. Next, 1049 mL medium was pumped (31.3 mL/min) into the bioreactor for washing, while harvest continued. In the last step, feeding of medium was stopped, while another 491 mL of suspension was pumped from the bioreactor through the TFDF filter into the harvest bottle. Supernatant samples were centrifuged ($1200 \times g$, 5 min, 4 °C) and stored at –80 °C until further analysis. For metabolite measurements, virus was removed using a Vivaspin 500 (Cytiva, USA, molecular weight cut-off of 100 kDa, 10,000×rpm, 5 min).

Other analytics for rVSV-GFP experiments

Quantification of VCC, viability, and cell diameter was performed using a cell counter (Vi-Cell™ XR, Beckman Coulter, USA). Metabolite concentrations were quantified by Bioprofile® FLEX 2 (Nova Biomedical, USA). A TCID₅₀ assay was used to quantify infectious virus titer of rVSV-GFP samples. In brief, adherent HEK293 cells were seeded at a concentration of 0.2×10^5 cells/well (100 μ L per well) in 96-well plates using DMEM (10% FCS, 1% Pen/Strep), followed by incubation for 24 h at 37 °C. Prior to infection, medium was gently removed from wells by a vacuum aspirator (8-channel adaptor). Cells were infected (infection medium: 2% FCS, 1% Pen/Strep) with eight replicates (100 μ L/well) per dilution (serial dilution of 1:10) and incubated for 7 days at 34 °C. Wells containing cytopathic effect under standard light microscope were considered as positive. Spearman/Kärber method was used to calculate TCID₅₀ titer. Each sample was quantified twice in independent TCID₅₀ assays.

Calculations

Metabolite consumption/production rates (q_s), CSVY (TCID₅₀/cell), volumetric virus productivity (VVP; TCID₅₀/L/day), space-time yield (STY, TCID₅₀/L/day), and cell retention efficiency (CRE) were calculated as follows:

$$q_s = \frac{\mu}{Y_{x/s}} \quad (1)$$

$$Y_{x/s} = \frac{x(t_n) - x(t_{n-1})}{c_s(t_{n-1}) - c_s(t_n)} \quad (2)$$

where μ is the cell-specific growth rate (1/h), $Y_{x/s}$ is the biomass yield, x is the VCC (cells/mL) at the cultivation time n (t_n), and c_s the metabolite concentration (mM).

vir_{acc} is the accumulated number of infectious virus particles (TCID₅₀) and was calculated for different production modes as follows:

$$\text{Batch} : vir_{acc} = C_{vir, BR} \times V_{BR} \quad (3)$$

$C_{vir, BR}$ is the infectious virus concentration (TCID₅₀/mL) in the bioreactor. V_{BR} (mL) is the working volume of the cultivation vessel.

$$\text{ATF, AS} : vir_{acc} = C_{vir, BR} \times V_{BR} + \sum \frac{(C_{vir, P, n} + C_{vir, P, n-1})}{2} \times V_H \quad (4)$$

$C_{vir, P, n}$ and $C_{vir, P, n-1}$ are the infectious virus concentrations in the permeate between t_n and t_{n-1} , respectively. V_H represents the harvest volume collected between t_n and t_{n-1} .

$$\text{TFDF} : vir_{acc} = C_{vir, FH} \times V_{FH} + \sum C_{vir, B, n} \times V_{B, n} \quad (5)$$

$C_{vir, FH}$ is the infectious virus concentrations of the final harvest step. V_{FH} represents the volume of the final harvest step. $C_{vir, B, n}$ and $C_{vir, B, n-1}$ are the infectious virus concentrations in the harvest bottles, which were exchanged every sample time point for rVSV-NDV. $V_{B, n}$ represents the volume in the harvest bottle. For the TFDF run with rVSV-GFP, the collected permeate (stored at 4 °C) was sampled combined, and final harvest step was sampled individually. For the TFDF run with rVSV-NDV, all harvest bottles were sampled individually and not combined.

$$\text{CSVY} = \frac{vir_{acc}}{x_{max} \times V_{BR}} \quad (6)$$

$$\text{VVP} = \frac{vir_{acc}}{V_{acc} \times t_{tot}} \quad (7)$$

$$\text{STY} = \frac{vir_{acc}}{V_{BR} \times t_{tot}} \quad (8)$$

x_{max} (cells/mL) is the maximum viable cell concentration reached post-infection in the cultivation vessel. V_{acc} (mL) is the accumulated medium spent during the entire process, and t_{tot} (h) is the total process time until maximum vir_{tot} is reached.

Percentage of infectious virus (P_{Perm}) passing through the membrane was calculated as follows:

$$P_{Perm} = \frac{1}{n} \sum \left(\frac{C_{vir, P, n}}{C_{vir, BR, n}} \right) \times 100\% \quad (9)$$

Cell retention efficiency (CRE), shear rate (γ), and permeate flux (J) were calculated as follows:

$$\text{CRE} = \left(1 - \frac{x_H}{x_{BR}} \right) \times 100 \quad (10)$$

$$\gamma = \frac{4 \times Q}{z \times \pi \times R^3} \quad (11)$$

$$J = \frac{\dot{V}_p}{A} \quad (12)$$

where x_H and x_{BR} are the measured VCC in the permeate line and in the bioreactor, respectively. Q represents the volumetric recirculation rate (m³/s, based on the exchange flow rate of the ATF system or recirculation rates of the TFDF system), R the internal radius of the fiber (m), and z the number of hollow-fibers of the ATF/TFDF membrane. The permeate flux is calculated as the ratio of the permeate flow rate \dot{V}_p (L/h) to the total filtration area of the hollow-fiber membrane A (m²).

Results

rVSV-NDV production using mATF

To evaluate the virus retention of commonly used hollow-fiber membranes and the applicability for fusogenic oncolytic viruses forming large multi-nucleated syncytia, an initial perfusion run using the novel 3-L modular adapter on a SBX-10 OSB with a 0.65- μm mPES membrane connected to a mATF was carried out. Previously, it has been shown that OSB and STR bioreactors perform similarly for cell growth and, therefore, to demonstrate all possible applications, an OSB was chosen (Coronel et al. 2019; Göbel et al. 2023b) for this study. To prevent potential syncytia from blocking the hollow fibers, a membrane with fiber lumen larger than previously observed syncytia (120–140 μm) was chosen (0.75-mm internal fiber lumen). Following inoculation at 0.8×10^6 cells/mL at 2.4 L WV, perfusion was initiated once

VCC reached 4×10^6 cells/mL. Manual adjustment of the perfusion rate allowed growth to 44.5×10^6 cells/mL with viabilities above 98% (Fig. 2A) without any limitations in glucose and glutamine (data not shown); however, the CSPR could not be controlled stably (Figure 2B). In order to conserve medium, no medium exchange prior to infection was carried out for this run. Cells were directly infected at an MOI of $1 \text{E}-4$ once cells reached a VCC of 44.5×10^6 cells/mL, temperature was reduced to 34°C , and perfusion was paused for 4 h. Following re-initiation of perfusion, VCC stagnated until 36 hpi, after which viability and VCC slowly declined (Fig. 2A). Maximum infectious virus titers of 3.2×10^9 TCID₅₀/mL were reached at 42 hpi in the bioreactor, corresponding to a CSVY of 67 TCID₅₀/cell and a VVP of 4.0×10^{10} TCID₅₀/L/day (Table 1).

To assess the virus retention by the 0.65- μm hollow fiber membrane, samples were taken from the bioreactor and the permeate line, respectively. Already at 18 hpi, infectious

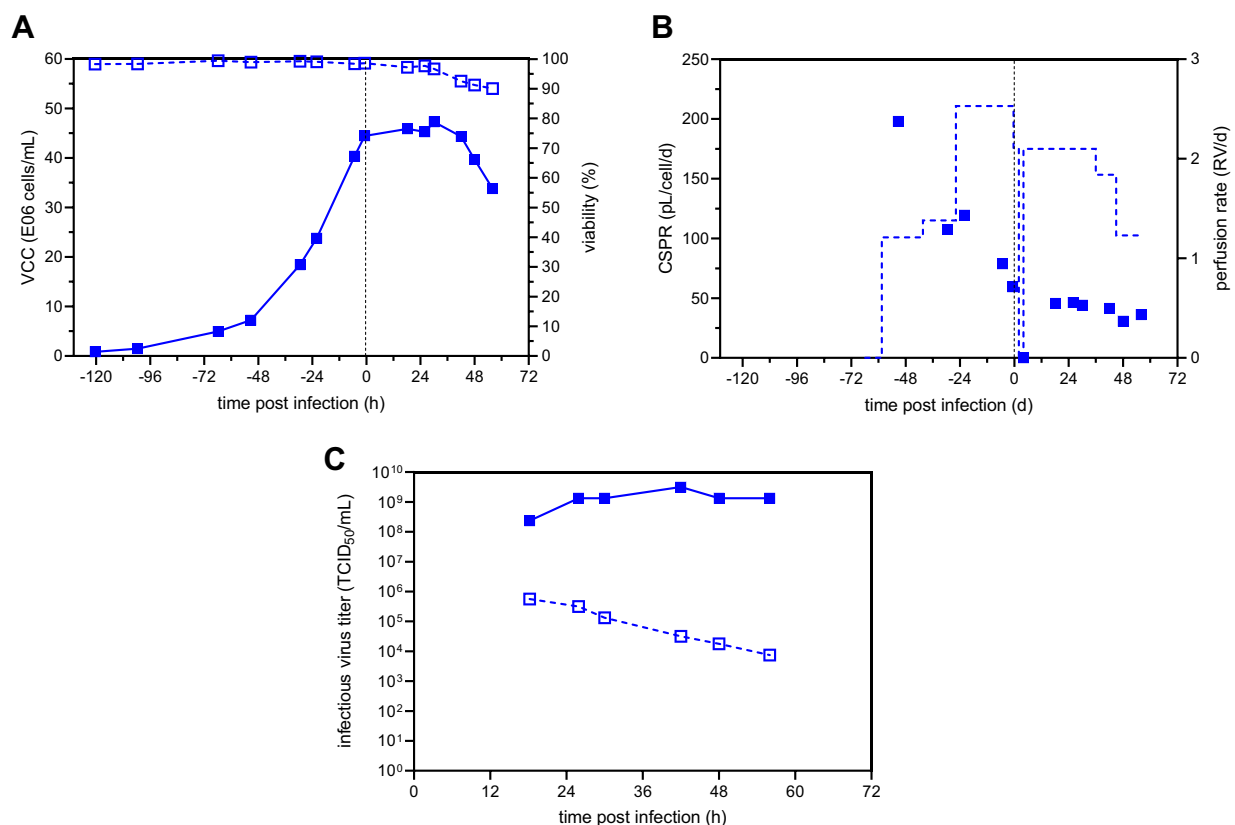


Fig. 2 rVSV-NDV production in BHK-21 cells in perfusion mode using a SB10-X equipped with a 3-L modular adapter and connected to a mATF. BHK-21 cells were inoculated at 0.9×10^6 cells/mL, and perfusion was started 56 h after batch growth phase. The perfusion rate was adjusted manually over time. For cell retention, a 0.65- μm mPES hollow fiber membrane was used. Infection was carried out once a VCC of 44.5×10^6 cells/mL was reached (MOI of $1 \text{E}-4$), tem-

perature was reduced to 34°C , and perfusion was paused for 4 h. **A** VCC (full symbols) and viability (hollow symbols). **B** Cell-specific perfusion rate (full symbols) and perfusion rate (dashed lined, weight of collected permeate divided by WV). **C** Infectious virus titer measured inside the bioreactor (full symbols) and the permeate line (hollow symbols)

virus titers in the permeate were significantly reduced compared to the bioreactor (>2 log), corresponding to 97.0% retention. With increasing process time, virus retention further increased to up to 5 log or nearly 100% (Fig. 2C). Surprisingly, the high flow rate through the hollow fiber membrane of 1.5 L/min and the resulting high shear stress of 5490 1/s neither impacted cell growth (Fig. 2A) nor virus replication (Fig. 2C) and did not prevent the formation of large multi-nucleated syncytia (50–75 μm , Figure S4).

rVSV-NDV production using TFDF

In a next step, we carried out two rVSV-NDV production runs in a 3 L STR using TFDF as the cell retention device for perfusion as a proof of concept for continuous virus harvesting with clarification, targeting a VCC at TOI of 14×10^6 cells/mL. For both TFDF runs, BHK-21 cells were inoculated at 0.8×10^6 cells/mL in 1.3 L WV and grown in batch mode until a VCC of 4×10^6 cells/mL was reached. In a next step, after initiation of perfusion, cell broth was recirculated with a constant recirculation rate of 0.9 L/min, corresponding to a shear rate of 1650 1/s. The perfusion rate was either manually adjusted (TFDF1) or controlled based on capacitance (TFDF2), where the signal was correlated to the biovolume. Both control strategies, enabled cells to grow up to 14×10^6 cells/mL with viabilities above 97%, but with a slightly reduced cell-specific growth rate compared to the initial batch phase ($\mu=0.026$ 1/h to $\mu=0.035 \pm 0.005$

1/h). A linear correlation of the permittivity signal with the VCC was obtained during the growth phase for both runs, enabling the monitoring of cell growth throughout the cultivation and the accurate control of the perfusion rate at the pre-defined CSPR of 130 ± 5 pL/cell/day for TFDF2 (Figure S1, Fig. 3B). As the perfusion rate for TFDF1 was adjusted manually in a step-wise manner (Fig. 3B), the CSPR did not stay stable and varied around 168 ± 36 pL/cell/day during cell growth (Fig. 3B). This resulted in a 15% lower total medium consumption for the growth phase for the capacitance-based control compared to the manual adjustment (Table 1). Interestingly, the glucose uptake rate of TFDF2 was 1.9-fold higher compared to TFDF1 (Table 1) resulting in an increase in lactate concentration up to 20 mM compared to 10 mM for TFDF1 (Figure S2B). However, all measured metabolite concentrations were still in the expected range with no notable limitations (Figure S2), and substrate uptake rates of TFDF 1 were comparable to both acoustic settler and ATF cultivations (Table 1, Göbel et al. 2023a, 2023b). For both runs, high cell retention rates of >99.9% and turbidity reductions >95% were achieved over the entire cultivation period (Fig. 3C). Transmembrane pressure (TMP) remained low (<0.1 psi) throughout the entire run, only showing a slight increase to 0.3 psi at 60 hpi for TFDF1 (Fig. 3D).

Prior to infection of cells with rVSV-NDV at an MOI of 1×10^{-4} , the medium was completely exchanged using a flow rate of 10 mL/min, and the temperature was reduced to 34 °C. Compared to the mATF perfusion, the permeate flow was

Table 1 Comparison of rVSV-NDV production in BHK-21 cells for different production modes. Cell growth parameters were determined before infection.

	Batch _a	Perfusion AS _a	ATF	Perfusion TFDF	
				TFDF1	TFDF2
Bioreactor vessel	STR (1 L)	STR (1 L)	OSB (3 L)	STR (3 L)	STR (3 L)
Cell-specific growth rate (1/h)	0.033	0.019±0.003	0.031	0.027	0.030
Doubling time (h)	21.0	36.1±6.5	22.1	25.9	23.0
qGlc (10^{-11} ×mmol/(cell/h))	5.1±0.9	6.5±2.1	8.25	8.06	15.2
qGln (10^{-11} ×mmol/(cell/h))	3.0±0.7	3.1±2.0	2.42	2.21	3.21
Max. VCC p.i. (10^6 cells/mL)	3.2±0.3	29.7±2.4	44.5	20.6	16.4
Max. infectious virus titer (10^8 TCID ₅₀ /mL)	5.0±0.9	15.8±11.7	31.6	75.0	56.2
CSVY (TCID ₅₀ /cell)	161±40	118±11	67	365	342
VVP (10^{10} TCID ₅₀ /L/d)	9.4±2.6	3.9±0.6	4.0	8.8	11.5
STY (10^{10} TCID ₅₀ /d)	13.4±3.7	29.0±5.2	43.0	75.5	95.4
Used medium (L)	0.7	6.9±1.9	25.1	11.0	9.3
dsDNA level at optimal harvest time point (μg/mL)	n.d.	14.0±0.5	n.d.	7.5	13.9
Protein level at optimal harvest time point (mg/ml)	n.d.	0.5	n.d.	2.0	2.5

qGlc, cell-specific glucose consumption rate; qGln, cell-specific glutamine consumption rate; max., maximum; VCC, viable cell concentration; p.i., post infection; n.d., not determined. Optimal harvest time point was defined as time point when the maximum infectious virus titer was reached in the supernatant. a: Values taken from Göbel et al. 2023a, 2023b carried out as biological replicates with $n=2$

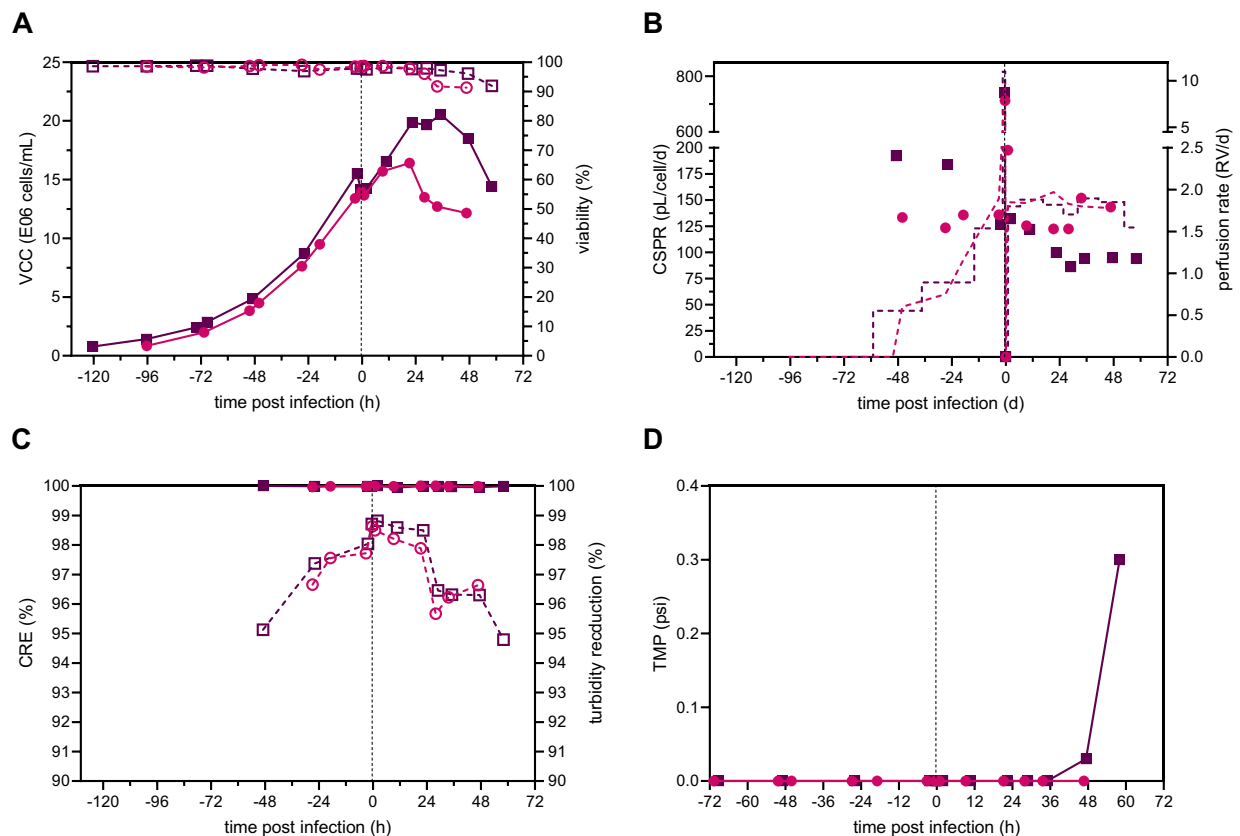


Fig. 3 Critical process parameters of rVSV-NDV production in BHK-21 cells in perfusion mode using a 3-L STR coupled to a TFDF system. BHK-21 cells were inoculated at 0.8×10^6 cells/mL, and perfusion was started 46–51 h after batch growth phase by utilizing a TFDF cartridge (pore size 2–5 μm). The first TFDF run (TFDF1, purple squares) was adjusted manually, while the second TFDF run (TFDF2, pink circles) was controlled based on the biovolume measured by a capacitance probe. Infection was carried out once a VCC

of 14×10^6 cells/mL was reached (MOI of $1E-4$), temperature was reduced to 34°C , and perfusion was paused for 1–2 h. **A** Viable cell concentration (full) and viability (empty). **B** Cell-specific perfusion rate (full) and perfusion rate (dashed lined, weight of collected permeate divided by WV). **C** Cell retention efficiency (full) and turbidity reduction (empty) of TFDF membrane during growth and infection. **D** Transmembrane pressure (TMP) during cell growth and infection phase. The dashed line indicates the time of infection

only paused for 1–2 h (compared to 4 h) before setting the perfusion rate to a constant rate of 1.8 RV/day, as no loss of infectious virus particles into the permeate was observed. For both runs, cells continued to grow for 24–36 hpi up to a VCC of 20.5×10^6 cells/mL and 16.4×10^6 cells/mL displaying high viabilities above 96%. By sampling the bioreactor and permeate line, virus retention by the TFDF membrane can be assessed. For both runs, maximum titers of 7.5×10^9 TCID₅₀/mL and 5.6×10^9 TCID₅₀/mL were reached in the permeate at 29–34 hpi, respectively (Fig. 4A). Overall, infectious titers were very similar between the bioreactor and permeate line, indicating that rVSV-NDV was not retained by the TFDF membrane. On average, the percentage of infectious virus passing through the membrane was calculated as 124% and 118% for TFDF1 and TFDF2, respectively. Determination of the actual recovery was made by integration of the permeate line samples over the collected volume, considering the

changing concentrations within the permeate line and collected volume (Figure S3). Here, the area under the curve represents the maximum available amount of infectious virus particles that can be recovered. Maximum theoretical values were compared to the sum of the actual empirical values for the collected fractions (“Accumulated” Fig. 4B). For both runs, recoveries of 78% were obtained, most likely due to the partial loss of functionality while storing at RT. As expected due to the large pore sizes, impurity concentrations were very similar between the bioreactor and permeate line (Fig. 4C and E) and gradually increased during the infection, reaching maximum values at the time of final harvest, when viabilities were reaching 90% (Fig. 4D and F).

Interestingly, monitoring the bioreactor samples by bright field microscopy showed limited syncytia formation, reaching sizes of 25–38 μm in diameter, for 29 hpi onwards for TFDF1. In contrast, more pronounced syncytia formation

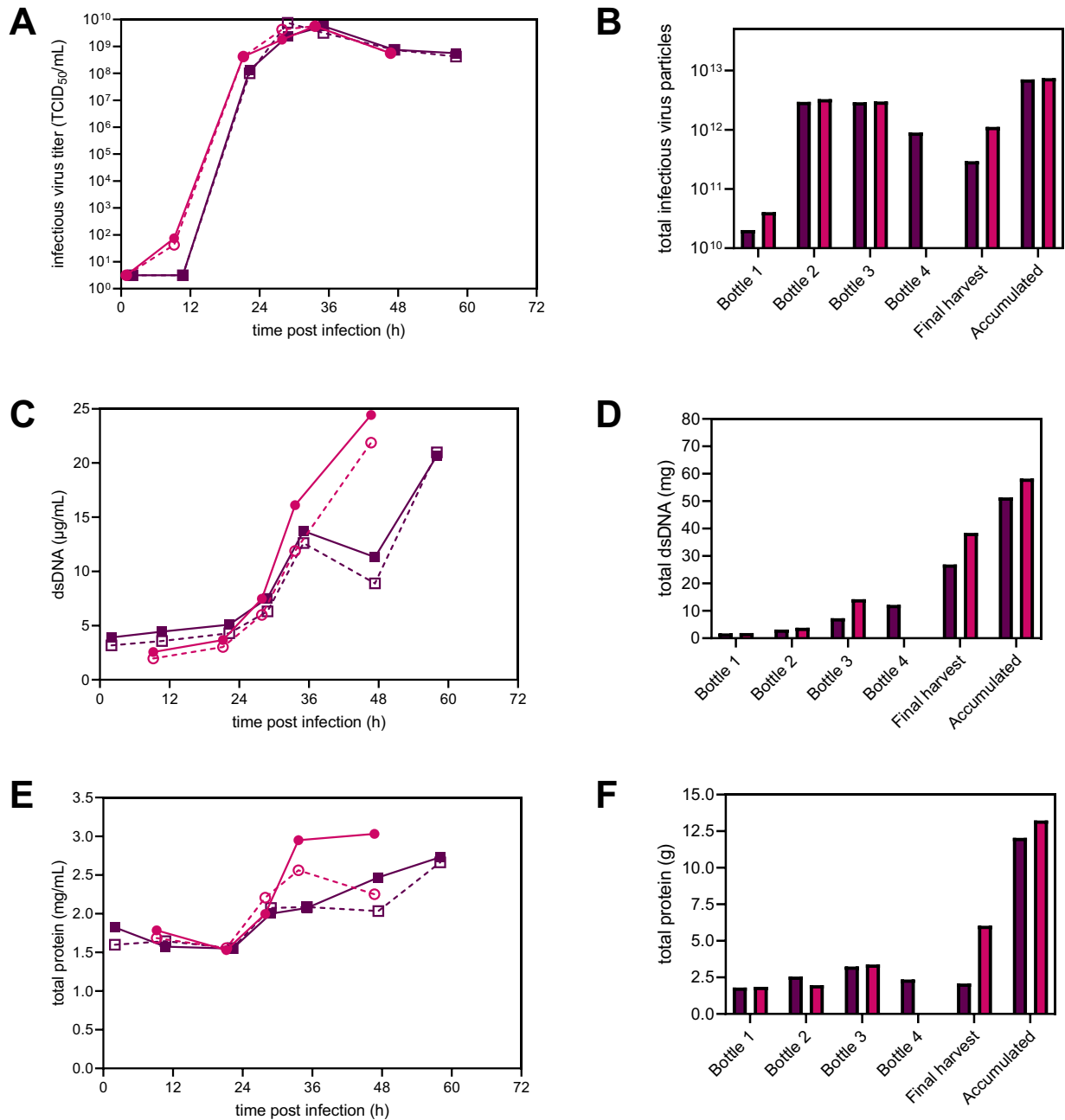


Fig. 4 rVSV-NDV production in BHK-21 cells in perfusion mode for TFDF1 (purple squares) and TFDF2 (pink circles). Time course of **A** infectious virus titer (TCID₅₀/mL), **C** double-stranded DNA (µg/mL), and **E** total protein (mg/mL) measured both in the reactor (full symbols) and permeate line (empty symbols). The TFDF membrane allowed a continuous harvesting of rVSV-NDV via the permeate. **B**, **D**, **F** The permeate was collected in multiple fractions (“Harvest

bottle 1–4”), which were exchanged every 12–24 h to prevent loss of virus infectivity. Bottle 1 refers to permeate collected from 0 to 24 hpi, Bottle 2 24–36 hpi, Bottle 3 36–48 hpi, and bottle 4 48–60 hpi. “Final harvest” refers to material recovered in the final harvest step (concentration 1, diafiltration; final concentration, 2). “Accumulated” refers to the accumulated yields from all bottles and the final harvest

was found for TFDF2, where scattered clusters of fused cells appeared between 18 and 33 hpi, reaching sizes of 50–100 µm in diameter (Figure S4). For the final one-step

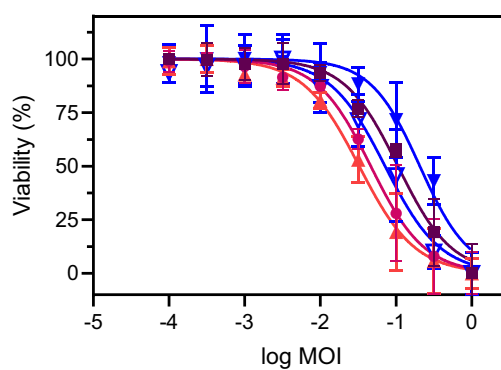
harvest, a modified C1-DF-C2 process was utilized using the same TFDF membrane as for cell growth and infection. For TFDF1, filter fouling was observed for the harvest at 60

hpi, using sterile PBS for diafiltration, and the membrane was completely blocked during the second concentration step after removal of 1100 mL (Figure S5). By carrying out the harvest 12 h earlier at 48 hpi, further increasing the recirculation rate to promote self-cleaning of the membrane while simultaneously reducing the permeate flow, and using medium for diafiltration, filter fouling was prevented, and the TMP was kept below 2 psi for the majority of the harvest for TFDF2 (Figure S5).

Finally, the TFDF production was compared with the ATF perfusion run using the mATF and a previously described optimized batch process and perfusion process using an acoustic settler (AS) as the cell retention device (Table 1). All perfusion systems achieved a higher infectious virus concentration compared to an optimized batch process infected at 2×10^6 cells/mL, with both TFDF runs being more than ten times higher compared to batch and more than 3.5 times higher compared to AS (Table 1). CSVY's of 342–365 TCID₅₀/cell were obtained in TFDF cultures, corresponding to a >twofold improvement compared to ATF and previous batch and AS cultivations. As both ATF and AS perfusion systems were infected at higher VCC's, this might indicate the presence of a cell density effect. In terms of VVP, TFDF cultures were comparable to batch cultivations; however, all perfusion systems had an increased STYs, with TFDF cultures showing an increase of >460% compared to batch cultivations.

In a final step, we evaluated whether sporadic formation of syncytia in TFDF mode (Figure S4) had an impact on the oncolytic properties in target Huh7 cells. Crude samples for both TFDF runs were compared to previously produced STR samples using optimized batch processes and AS perfusions. As expected, all samples displayed a similar oncolytic potential in Huh7 cells (Fig. 5). Regardless of the production mode or production system, the produced virus still maintained the ability to induce adequate oncolysis.

Fig. 5 Comparison of oncolytic viral potency values for rVSV-NDV using different production modes and processes. Viabilities of Huh7 cancer cells were determined 48 hpi for crude rVSV-NDV samples generated in batch mode (red triangle), acoustic settler perfusions (AS1, blue full triangle; AS2, hollow blue triangle), and TFDF perfusions (TFDF1, purple square; TFDF2, pink circle). Following non-linear regression analysis, IC₅₀ and log IC₅₀ values were determined from dose-response curves. All values are reported as the mean of technical triplicates with $n=3$



	Batch	AS1	AS2	TFDF1	TFDF2
Log IC ₅₀	-1.49	-0.69	-1.15	-0.98	-1.33
IC ₅₀	0.03	0.21	0.07	0.11	0.05

Production of rVSV-GFP in batch mode

Initially, a high-yield production process for rVSV-GFP in batch mode in shake flasks (SF) was developed (Fig. 6). Next, the process was transferred to two STRs of different sizes (STR 1, 700 mL WV; STR 2, 2100 mL WV). For this, HEK293-SF cells were inoculated at about 0.3×10^6 cells/mL and grown to 1.3×10^6 cells/mL (STR 1 and 2) or 1.1×10^6 cells/mL (SF) with viabilities above 95% (Fig. 6A). For the three cultivations, very similar cell growth and viability patterns were observed. Cell-specific growth rates ranged between 0.026 and 0.034 1/h (Table 2). As optimized in two recent studies for rVSV-based constructs, cells were infected at an MOI of 1E-3 after a temperature reduction to 34 °C. (Elahi et al. 2019; Gélinas et al. 2019). Maximum VCCs of 1.9×10^6 cells/mL were reached at 11 hpi for SF and STR 1 cultures, before virus-induced cell death occurred (Fig. 6A, for STR 2 data are not available). Virus production dynamics were very comparable between the three productions (Fig. 6B). Slightly higher maximum infectious virus titers were achieved for production in SF (8.8×10^{10} TCID₅₀/mL, 24 hpi) relative to STR 1 (3.2×10^{10} TCID₅₀/mL, 33 hpi) and STR 2 (5.3×10^{10} TCID₅₀/mL, 31 hpi). Thus, higher CSVY and STY/VVP were obtained for SF production (Table 2). Both STR runs showed high infectious virus titers for more than 36 h indicating a high stability of the virus.

Production of rVSV-GFP in perfusion mode using a TFDF system

To further support our proof-of-concept study of a TFDF system, we evaluated the production process for rVSV-GFP cultivating HEK293-SF cells in perfusion mode to reach higher VCC and infectious virus titers (Fig. 7). For this, as for the TFDF runs for rVSV-NDV, a 30-cm² TFDF cartridge

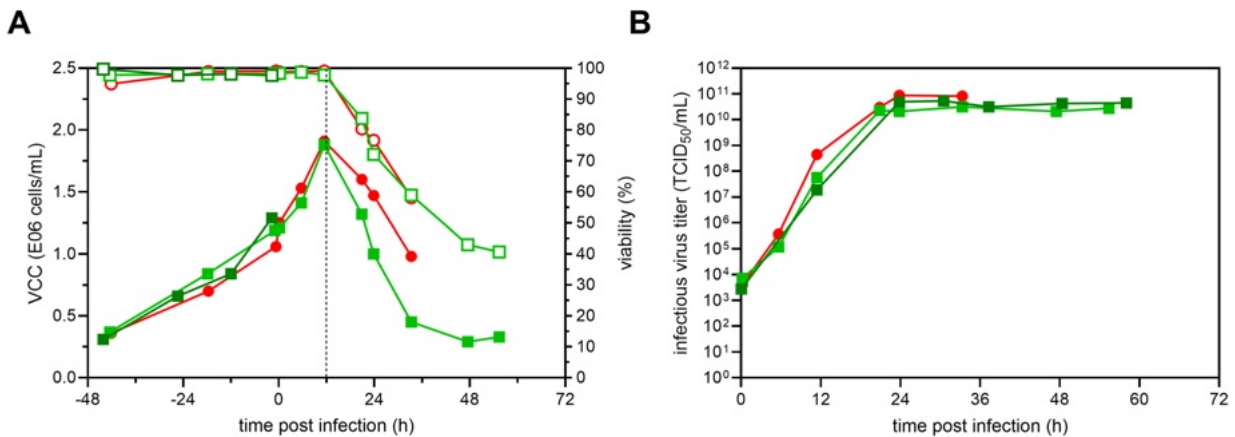


Fig. 6 rVSV-GFP production in HEK293-SF cells in batch mode. Three batch production runs were conducted using one shake flask (SF 1, 50 mL WV, red circles), one 1 L STR (STR 1, 700 mL WV, light green squares), and one 3 L STR (STR 2, 2100 mL, dark green squares). Cells were inoculated at $0.3\text{--}0.4 \times 10^6$ cells/mL and culti-

ated to $1.1\text{--}1.3 \times 10^6$ cells/mL. Prior to infection, temperature was lowered from 37 to 34 °C. Cells were infected at an MOI of 1E-3. **A** VCC (full symbols) and viability (hollow symbols). **B** Infectious virus titer (TCID₅₀/mL)

Table 2 Comparison of rVSV-GFP production in HEK293-SF cells for different production modes. Cell growth parameters were determined before infection.

	Batch			Perfusion
	STR 1 (1 L)	STR 2 (3 L)	SF	TFDF STR (3 L)
Cell-specific growth rate (1/h)	0.028	0.034	0.026	0.022
Doubling time (h)	24.6	20.7	26.6	31.0
Max. VCC p.i. (10^6 cells/mL)	1.9	n.d.	1.9	11.3
Max. infectious virus titer (10^{10} TCID ₅₀ /mL)	3.2	5.3	8.8	7.1
CSVY (TCID ₅₀ /cell)	16,865	n.d.	45,948	10,338
STY (10^{13} TCID ₅₀ /L/d)	1.0	1.7	2.8	1.9
VVP (10^{13} TCID ₅₀ /L/d)	1.0	1.7	2.8	0.2
Used medium (L)	0.67	2.10	4.60	13.93

max., maximum; VCC, viable cell concentration; *p.i.*, post infection; *n.d.*, not determined. Optimal harvest time point was defined as time point when the maximum infectious virus titer was reached in the supernatant. For the perfusion run, the calculations were based on infectious virus particles of the collected permeate in the harvest (stored at 4 °C) and final harvest

(pore size 2–5 μm), connected to a Krosflo TFDF system (Repligen), was coupled to the 3 L STR. Recirculation was already started before cell inoculation with a recirculation rate of 1.0 L/min corresponding to a shear rate of 1830 1/s. HEK293-SF cells were inoculated at 0.8×10^6 cells/mL into the 3 L STR (2100 mL WV) (Fig. 7A). After a batch growth phase for 24 h, perfusion mode was started (Fig. 7B). Cells grew at a slightly lower cell-specific growth rate of 0.022 1/h relative to the batch cultivation in STR 2 (0.028 to 0.034 1/h) (Table 2) during the total cell growth phase, while viabilities remained above 95% (Fig. 7A). The perfusion rate was manually adjusted based on a CSPR of 115 pL/cell/day (Fig. 7B). Due to an initial permeate flow rate of 0.9 mL/min (0.6 RV/day) (Fig. 7B), the actual CSPR was higher at the beginning of the cultivation. Before infection, one RV with

fresh medium was exchanged (10–33 mL/min) (Fig. 7B), and temperature was lowered from 37 to 34 °C. Cells were infected at 10.3×10^6 cells/mL at an MOI of 1E-3. After infection, perfusion was stopped for 1 h and, subsequently, the perfusion rate was kept constant at 1.4 RV/day (Fig. 7B). During the perfusion cultivation, no glucose or glutamine limitation was observed (Figure S6). Moreover, no toxic maximum levels of lactate (22.4 mM) or ammonium (1.4 mM) were found. After infection, cells continued to grow slightly until 11.3×10^6 cells/mL (12 hpi) with viabilities above 94% (Fig. 7A). Throughout the whole cultivation, the cell retention efficiency of the membrane was maintained above 99.6% (Fig. 7C). A maximum infectious virus titer of 7.1×10^{10} TCID₅₀/mL at 18 hpi was detected in the permeate line relative to 10.4×10^{10} TCID₅₀/mL at 24 hpi in the

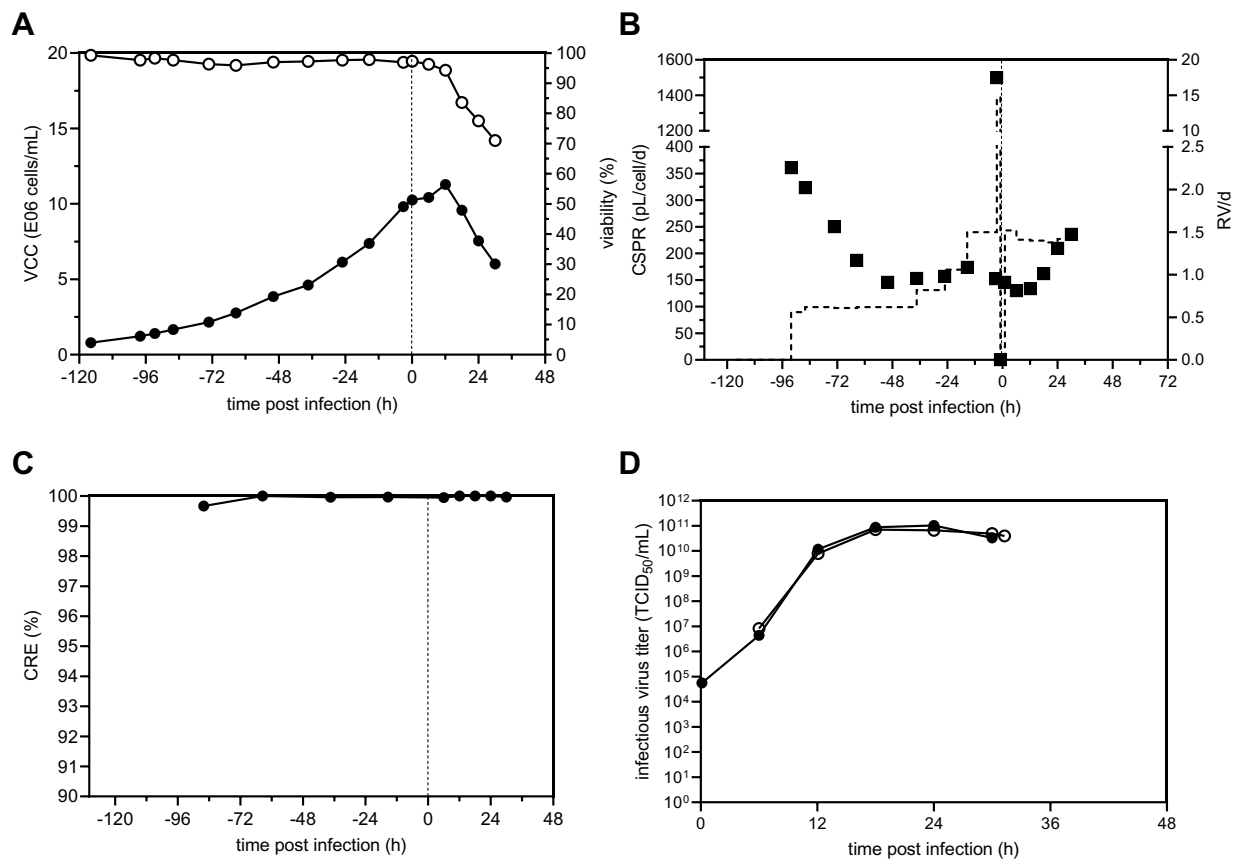


Fig. 7 rVSV-GFP production in HEK293-SF cells in perfusion mode using a 3-L STR coupled to a TFDF system. Recirculation was started prior to inoculation. HEK293-SF cells were inoculated at 0.8×10^6 cells/mL, and perfusion was started after 24 h of batch growth by utilizing a TFDF cartridge (pore size 2–5 μm). The perfusion rate was adjusted manually over time. Prior to infection, temperature was reduced to 34 °C. Cells (10×10^6 cells/mL) were infected at an MOI of 1E-3, and perfusion was paused for 1 h. **A** Viable cell con-

centration (full) and viability (empty). **B** Cell-specific perfusion rate (full) and perfusion rate (dashed line, weight of collected permeate divided by WV). **C** Cell retention efficiency (full) of TFDF membrane during growth and infection. **D** Infectious virus titer (TCID₅₀/mL) in the reactor (full symbols) and permeate line (empty symbols) are plotted against the time post infection (h). Last time point shown for the permeate line (31 hpi) refers to the final harvest step

bioreactor vessel. Very similar infectious virus titers were observed by comparing the bioreactor vessel and permeate line during the virus production phase (Fig. 7D). On average, the percentage of infectious virus passing through the TFDF membrane was calculated to be 112%. In addition, the infectious virus titer of the final harvest step (4.0×10^{10} TCID₅₀/mL) starting at 31 hpi using the same TFDF membrane was similar to the last permeate sample time point of the production phase (4.9×10^{10} TCID₅₀/mL, 30 hpi), confirming that all infectious virus particles passed through the membrane even in the final harvest step with a significantly higher permeate flow rate that could cause membrane clogging. Comparing the theoretical maximum values of the amount of infectious virus particles in the permeate line (Figure S7) with the empirical values of the virus in the harvest bulk (collected permeate stored at 4 °C and final harvest, sampled

individually) resulted in a recovery of 103.5%, indicating no loss of virus infectivity during storage in the virus production phase. Next, we compared important production coefficients of the batch and perfusion run (Table 2). The perfusion process showed increased STY (1.9-fold (STR 1) and 1.1-fold (STR 2)); however, VVP and CSVY were lower.

Discussion

The first vaccine based on rVSV, the Ebola virus vaccine Ervebo[®], has been approved in 2019 (EMA 2019; FDA 2019). Moreover, multiple rVSV-based constructs for vaccine and oncolytic applications are currently undergoing clinical trials. Therefore, the development of a high-yield production platform is essential to meet clinical trial and

market demand regardless of the intended use. Compared to traditional vector platforms, induction of syncytia by rVSV-NDV introduces additional challenges to manufacturing processes. In this proof-of-concept study, we evaluated the versatility of the TFDF system for intensified high-cell density production for two different rVSV-based constructs (rVSV-NDV and rVSV-GFP) to allow continuous virus harvest and clarification.

rVSV-NDV production using mATF

Product retention of hollow-fiber membranes is a well-known challenge of ATF-based cell culture productions, preventing continuous harvest of, e.g., viral particles (Genzel et al. 2014; Hadpe et al. 2017; Nikolay et al. 2020; Nikolay et al. 2018; Tona et al. 2023; Vázquez-Ramírez et al. 2019). To evaluate the applicability of hollow-fiber membranes for the production of fusogenic oncolytic viruses forming large multi-nucleated syncytia, a commercially available 0.65- μm mPES membrane with a lumen size bigger than previously observed syncytia (120–140 μm) was selected, connected to a mATF, and characterized for virus retention. Impact of the membrane material on product retention is still not fully elaborated. While some studies found a more pronounced retention rate of antibodies using polysulfone (PS) membranes compared to polyethersulfone (PES) and mPES due to the higher negative charge densities (Su et al. 2021), others reported more favorable physiochemical and structural properties (open pore structure, high porosity) of PS membranes enabling virus harvest of yellow fever virus particles (~50 nm) even at low cut-offs of 0.34 μm (Nikolay et al. 2020). Beside membrane material, pore size plays a critical role regarding product retention. Surprisingly, membranes with higher cut-offs, e.g., 0.65 μm often display higher product retention rates compared to lower cut-offs, e.g., 0.2 μm (Nikolay et al. 2020; Su et al. 2021; Vázquez-Ramírez et al. 2019). More pronounced heterogeneous pore distributions for larger cut-offs can increase the susceptibility of fouling as variation in filtrate flux along the membrane makes larger pores prone to deposition of particles and concentration polarization (Nikolay et al. 2020). Moreover small-size cell debris (0.2–0.5 μm), caused by virus induced cell lysis, can enter larger pores causing membrane clogging and product retention, but can be rejected by smaller pores (Su et al. 2021). Usage of a 0.2- μm PES hollow fiber membrane for a rVSV-NDV ATF production using HEK293 cells resulted in a complete membrane blocking at 18 hpi, after first syncytia formation was observed (data not shown). Therefore, the choice of membrane was primarily based on internal fiber lumen rather than pore size or material. A higher flow rate inside the hollow fibers (1.5 L/min) was chosen compared to the initial ATF run using a 0.2- μm PES membrane (0.8 L/min) to increase the backflush over the membrane

and prevent or hamper the formation of syncytia due to increased shear stress. Surprisingly, the resulting shear rate of 5490 1/s neither impacted cell growth, as high VCCs of 44.5×10^6 cells/mL with high cell-specific growth rates of 0.031 1/h (Table 1) were reached, nor did it prevent the formation of syncytia (Figure S4). However, formed syncytia were smaller (up to 75- μm diameter) as previously observed with an acoustic settler (up to 140 μm (Göbel et al. 2023a)), allowing entrance into the larger fibers, which likely prevented complete blockage. Nevertheless, combination of high hollow fiber flow rates with low permeate flux rates of 1.91 L/h/m² did not prevent rVSV-NDV retention by the membrane. Already at 18 hpi, 97% of all infectious virus was retained, further underlining the challenge of using hollow fiber membranes for continuous harvest of viral particles.

rVSV-NDV production using TFDF

As a proof-of-concept, we set out to utilize the TFDF system as a cell retention device for perfusion and subsequent continuous harvest filtration. Performance was characterized by cell growth, TMP, and quantification of bioreactor and permeate turbidities, as well as virus permeability. The use of the TFDF system allowed BHK-21 cells to achieve high VCCs, with similar growth behavior compared to the mATF system despite the drastically lower shear stress there. Due to the lower CSVY obtained at very high VCCs in the previous experiment, the targeted cell concentration for infection was lowered drastically. The metabolic uptake rates for all perfusion cultures were slightly increased compared to those previously reported for batch cultivations ((Göbel et al. 2023a), Table 1). Increased shear stress, particularly in ATF and TFF systems, has been identified as one cause of increased substrate uptake rates (Zhan et al. 2020). Control of the perfusion rate via a capacitance probe did not improve overall process performance, but robustly maintained stable CSPR values over the entire growth phase (Fig. 3), reducing medium consumption by 15%. Compared to the manual perfusion control for TFDF1, where CSPR values were higher due to partial overfeeding, glucose levels were not stably maintained and fell below 5 mM prior to infection (Figure S2). The slightly increased growth rate of TFDF2 most likely resulted in an increased uptake of glucose and thus increased lactate formation. To support even higher VCCs, the set point of the CSPR should be increased for future capacitance-controlled runs.

The combination of DF with tangential cross filtration provides several benefits such as shearing of the membrane surface, minimizing deposition of particles within the filter, while simultaneously allowing some particles to be captured within channels of the DF without blocking the liquid flow through that same channel (Williams et al. 2020). Low TMP values (below 0.3 psi) for both TFDF runs, even after virus

infection, high cell retention efficiencies (>99%), and a low turbidity in the permeate (>95% reduction) indicated minimal particle breakthrough. Previous studies already demonstrated the applicability of the TFDF system for continuous harvest of AAV and LV (Mendes et al. 2022; Tona et al. 2023; Tran and Kamen 2022). As expected, we also achieved equal concentrations of infectious virus in both the bioreactor and permeate sample, taken at the same time. Calculated percentages of infectious virus passing through the membrane above 100% for both runs are not possible and were only achieved as the measured titer in the permeate sample was higher than the bioreactor sample. While comparison to theoretical yields only resulted in a total recovery of 78%, this is most likely due to partial losses of functionality while storing the harvest bulks at RT, as well as the quite large error of the TCID₅₀ assay itself (± 0.3 log (Göbel et al. 2022b)). Stabilizing effects of sucrose on proteins and enveloped viral vectors are well known (Croyle et al. 2001; Cruz et al. 2006; Evans et al. 2004); however, it acts mainly as a cryoprotectant or is only a small part of a complex storage formulation. Therefore, premature addition of sucrose was probably not sufficient to prevent degradation, and direct cooling of the harvest bulk at 4 °C should be preferred.

In terms of virus production, our intensified TFDF processes achieved the highest reported infectious virus titers of $5.6\text{--}7.5 \times 10^9$ TCID₅₀/mL in the permeate so far. Compared to optimized batch processes, VCCs were increased by five- to six-fold, but infectious virus titers were even more than 11-fold higher. Moreover, CSVYs were improved by twofold, STY by 460% (5.6-fold), and similar VVPs were reached. Lastly, the TFDF runs were compared to other perfusion cultivations using the same cell line but different cell retention devices. Compared to AS and ATF perfusions, maximum titers reached in TFDF systems were >threefold and >1.5-fold higher. This was also reflected in terms of VVP and STY, which were always more than twofold higher for TFDF runs. Surprisingly, CSVYs strongly decreased with increasing VCCs for the respective systems. For the ATF cultivation, where the highest VCC of 44.5×10^6 cells/mL was reached, the lowest CSVY was obtained, clearly indicating the presence of a “high cell density effect” (Bock et al. 2011; Nadeau and Kamen 2003). One major reason for this effect is typically the scarcity in nutrients or the accumulation of inhibitory ammonium and glucose. One study showed that ammonium and lactate concentrations at 2–3 mM and above 20–30 mM, respectively, can have negative effects on virus productivity and cell growth (Schneider et al. 1996). However, neither a nutrient limitation nor an accumulation of lactate and ammonium to excessively high concentrations was observed for any run ((Göbel et al. 2023a), Figure S2, data not shown for ATF). This suggests that other reasons, including the limitation or accumulation

of non-monitored metabolites or unknown cellular factors may play a role and are subject to further investigation. Another reason could be the formation of syncytia, which was observed to occur to differential extents, depending on the system used (Figure S4). Virus replication is possibly more efficient if the cells do not fuse, as we have observed the production of higher titers in oncolytic applications when a non-fusogenic VSV is used, despite similar levels of oncolysis (Abdullahi et al. 2018); however, whether or not this is also true in suspension culture systems which is not entirely clear and would warrant further investigation. Regardless, the direct comparison of the three perfusion systems should be considered very carefully, as various production parameters were different. For a fair comparison, re-evaluation should include the same bioreactor set-up and similar infection cell concentrations. For our proof-of-concept study this was, however, out of scope.

Fusogenic oncolytic viruses and the formation of syncytia introduce novel challenges for process controls and scale-up of manufacturing processes. We hypothesize that fusion of cells is dependent on three factors: high VCC, low shear stress, and long cell-to-cell contact time. Combination of all three factors most likely facilitates the formation of large multi-nucleated syncytia. Production in batch mode is associated with low VCC (up to 3.2×10^6 cells/mL), low shear stress, and short cell-to-cell contact times and does not lead to the formation of syncytia. Productions using ATF or TFDF systems allow for high VCCs (up to 44.5×10^6 cells/mL); however, shear rates are drastically increased (up to 5490 1/s), and cell-to-cell contact times are short, leading to the formation of small sized syncytia. Retention systems such as AS, combine high VCCs (up to 29.7×10^6 cells/mL), low shear rates (~340 1/s (Gränicher et al. 2020)), and long cell-to-cell contact times within the acoustic field and recirculation loop (3–12 min (Gränicher et al. 2020)), facilitating the formation of large multi-nucleated syncytia. Increased cell-to-cell contact by induction of aggregation by CaCl₂ supplementation at low VCC in batch mode did not result in the formation of syncytia, highlighting the complex interplay of all three factors (Göbel et al. 2022a). Future studies investigating the actual cause of syncytia formation in suspension cultures could be considered to better control their formation. However, whether or not syncytia are formed in suspension cultures during production is independent of the inherent fusogenicity of the virus, as the fusion proteins are encoded within its genome and need to be expressed in order to carry out an infection (Abdullahi et al. 2018). Nonetheless, a potency assay was carried out to assess potential effects of mode of production, as well as formation or non-formation of syncytia during production, on the ability of the virus to induce oncolysis. As expected, oncolytic potency was not affected by production mode or occurrence of syncytia (Fig. 5).

rVSV-GFP production in batch and perfusion mode

To take our proof-of-concept study one step further, we also wanted to evaluate the TFDF performance for a high-yield virus production process for rVSV-based vectors for a possible application as vaccine using the model vector rVSV-GFP. Process intensification using perfusion mode and the TFDF module led to a sixfold higher VCC of 11.3×10^6 cells/mL with an up to 1.9-fold higher STY compared to the STR 1 process in batch mode, allowing for a smaller footprint of the bioreactor. However, a more than 3.3-fold lower VVP and 1.6-fold reduced CSVY were observed compared to the STR batch process. As described before, this decline is most likely due to the “high cell density effect.” As neither limitation of monitored nutrients, nor accumulation of inhibitory byproducts was observed, it is clear that there is certainly room for optimization for this perfusion process, hopefully targeting even higher VCCs. For now, this perfusion run was a proof-of-concept run only to evaluate the TFDF system. Testing different feeding schemes (Vázquez-Ramírez et al. 2019), media compositions (Göbel et al. 2023a), or additives could be envisaged as next steps.

Using the TFDF module, we were able to directly harvest rVSV-GFP particles with a simultaneous clarification by depth filtration with a full recovery. Our proof-of-concept study together with the data on LV (Tona et al. 2023; Tran and Kamen 2022) and AAV (Mendes et al. 2022) seems to indicate that TFDF for continuous virus harvest in perfusion will play a big role in next generation processes and might be applicable for other viruses as well. Moreover, all HEK293-SF cells were retained inside the bioreactor enabling full production capacity. Perfusion cultivation with the TFDF module showed a slightly lower cell-specific growth rate (0.022 1/h) relative to the batch production (0.034 to 0.028 1/h), indicating that there is also room for improvement here and a need for further optimization. As previously discussed, cooling the harvest bulk to 4 °C increases virus stability. Indeed, we found a recovery of 103.5% in the final harvest bulk.

Overall, the TFDF module showed very good performance as a perfusion system for our tested rVSV-based vectors and cell lines. In addition, the continuous virus harvest, together with the clarification through the TFDF module in one step can simplify process operations and help to develop an integrated, scalable (up to 2000 L), and economical process for the future.

Supplementary Information The online version contains supplementary material available at <https://doi.org/10.1007/s00253-024-13078-6>.

Acknowledgements The authors would like to thank Gene Therapy Repligen for providing a KrosFlo TFDF lab unit as well as the custom TFDF membranes as part of the collaborative effort. Special thanks to Rachel Legmann (Gene Therapy Repligen) and Barbara Paes (Kamen

lab) for their active technical support and participation in fruitful discussions. We also want to thank Kühner AG, in particular, Tibor Anderlei and Tim Bürgin, for providing the 3-L modular adapter as well as the 3-L single-use bags. The excellent technical support of Ilona Behrendt is equally acknowledged.

Author contribution Conceptualization: S.G., L.P., U.R., and Y.G. Methodology: S.G., L.P., C.A.S.T., and Y.G. Investigation: S.G., L.P., C.A.S.T., and J.A. Writing—original draft: S.G. and L.P. Writing—review and editing: S.G., L.P., C.A.S.T., J.A., A.K., U.R., and Y.G. Supervision: A.K., U.R., and Y.G. Project administration: S.G., L.P., and Y.G.

Funding Open Access funding enabled and organized by Projekt DEAL.

Data availability Data available in article supplementary material. Additional data is available on request from the authors. The data that support the findings of this study are available from the corresponding author, Yvonne Genzel, upon reasonable request.

Declarations

Ethics approval This article does not contain any studies with human participants or animals performed by any of the authors.

Consent to participate Not applicable.

Consent for publication Not applicable.

Conflict of interest J. Altomonte (WO 2017/198779) holds a patent for the development and use of rVSV-NDV as an oncolytic therapy of cancer and is co-founder of Fusix Biotech GmbH, which is developing the rVSV-NDV technology for clinical use. B. Brühlmann and C.Hill are employees of Repligen where the Krosflo TFDF system has been developed.

Open Access This article is licensed under a Creative Commons Attribution 4.0 International License, which permits use, sharing, adaptation, distribution and reproduction in any medium or format, as long as you give appropriate credit to the original author(s) and the source, provide a link to the Creative Commons licence, and indicate if changes were made. The images or other third party material in this article are included in the article's Creative Commons licence, unless indicated otherwise in a credit line to the material. If material is not included in the article's Creative Commons licence and your intended use is not permitted by statutory regulation or exceeds the permitted use, you will need to obtain permission directly from the copyright holder. To view a copy of this licence, visit <http://creativecommons.org/licenses/by/4.0/>.

References

- Abdullahi S, Jäkel M, Behrend SJ, Steiger K, Topping G, Krabbe T, Colombo A, Sandig V, Schiergens TS, Thasler WE, Werner J, Lichtenthaler SF, Schmid RM, Ebert O, Altomonte J (2018) A novel chimeric oncolytic virus vector for improved safety and efficacy as a platform for the treatment of hepatocellular carcinoma. *J Virol* 92(23). <https://doi.org/10.1128/jvi.01386-18>
- Aunins JG (2003) Viral vaccine production in cell culture. In: Spier RE (ed) Encyclopedia of cell technology. <https://doi.org/10.1002/0471250570.sp1105>

- Bock A, Schulze-Horsel J, Schwarzer J, Rapp E, Genzel Y, Reichl U (2011) High-density microcarrier cell cultures for influenza virus production. *Biotechnol Progr* 27(1):241–250. <https://doi.org/10.1002/btpr.539>
- Brown KS, Safronetz D, Marzi A, Ebihara H, Feldmann H (2011) Vesicular stomatitis virus-based vaccine protects hamsters against lethal challenge with Andes virus. *J Virol* 85(23):12781–12791. <https://doi.org/10.1128/jvi.00794-11>
- Cobleigh MA, Buonocore L, Uprichard SL, Rose JK, Robek MD (2010) A vesicular stomatitis virus-based hepatitis B virus vaccine vector provides protection against challenge in a single dose. *J Virol* 84(15):7513–7522. <https://doi.org/10.1128/jvi.00200-10>
- Coronel J, Behrendt I, Bürgin T, Anderlei T, Sandig V, Reichl U, Genzel Y (2019) Influenza A virus production in a single-use orbital shaken bioreactor with ATF or TFF perfusion systems. *Vaccine* 37(47):7011–7018. <https://doi.org/10.1016/j.vaccine.2019.06.005>
- Coronel J, Gränicher G, Sandig V, Noll T, Genzel Y, Reichl U (2020) Application of an inclined settler for cell culture-based influenza A virus production in perfusion mode. *Front Bioeng Biotechnol* 8:672–672. <https://doi.org/10.3389/fbioe.2020.00672>
- Croyle MA, Cheng X, Wilson JM (2001) Development of formulations that enhance physical stability of viral vectors for gene therapy. *Gene Ther* 8(17):1281–1290. <https://doi.org/10.1038/sj.gt.3301527>
- Cruz PE, Silva AC, Roldão A, Carmo M, Carrondo MJ, Alves PM (2006) Screening of novel excipients for improving the stability of retroviral and adenoviral vectors. *Biotechnol Progr* 22(2):568–576. <https://doi.org/10.1021/bp050294y>
- DeBuyscher BL, Scott D, Thomas T, Feldmann H, Prescott J (2016) Peri-exposure protection against Nipah virus disease using a single-dose recombinant vesicular stomatitis virus-based vaccine. *NPJ Vaccines* 1:16002. <https://doi.org/10.1038/npjvaccines.2016.2>
- Eccles R (2021) Why is temperature sensitivity important for the success of common respiratory viruses? *Rev Med Virol* 31(1):1–8. <https://doi.org/10.1002/rmv.2153>
- Elahi SM, Shen CF, Gilbert R (2019) Optimization of production of vesicular stomatitis virus (VSV) in suspension serum-free culture medium at high cell density. *J Biotechnol* 289:144–149
- EMA (2019) Ervebo: Ebola vaccine (rVSVΔG-ZEBOV-GP, live). European Medicines Agency. <https://www.ema.europa.eu/en/medicines/human/EPAR/ervebo>
- Emanuel J, Callison J, Dowd KA, Pierson TC, Feldmann H, Marzi A (2018) A VSV-based Zika virus vaccine protects mice from lethal challenge. *Sci Rep* 8(1):11043. <https://doi.org/10.1038/s41598-018-29401-x>
- Evans RK, Nawrocki DK, Isopi LA, Williams DM, Casimiro DR, Chin S, Chen M, Zhu DM, Shiver JW, Volkin DB (2004) Development of stable liquid formulations for adenovirus-based vaccines. *J Pharm Sci* 93(10):2458–2475. <https://doi.org/10.1002/jps.20157>
- FDA (2019) First FDA-approved vaccine for the prevention of Ebola virus disease: marking a critical milestone for public health. FDA. <https://www.fda.gov/news-events/press-announcements/first-fda-approved-vaccine-prevention-ebola-virus-disease-marking-critical-milestone-public-health>
- Geisbert TW, Jones S, Fritz EA, Shurtleff AC, Geisbert JB, Liebscher R, Grolla A, Ströher U, Fernando L, Daddario KM, Guttieri MC, Mothé BR, Larsen T, Hensley LE, Jahrling PB, Feldmann H (2005) Development of a new vaccine for the prevention of Lassa fever. *PLoS Med* 2(6):e183. <https://doi.org/10.1371/journal.pmed.0020183>
- Gélinas J-F, Azizi H, Kiesslich S, Lanthier S, Perderson J, Chahal PS, Ansorge S, Kobinger G, Gilbert R, Kamen AA (2019) Production of rVSV-ZEBOV in serum-free suspension culture of HEK 293SF cells. *Vaccine* 37(44):6624–6632. <https://doi.org/10.1016/j.vaccine.2019.09.044>
- Genzel Y, Dietzsch C, Rapp E, Schwarzer J, Reichl U (2010) MDCK and Vero cells for influenza virus vaccine production: a one-to-one comparison up to lab-scale bioreactor cultivation. *Appl Microbiol Biotechnol* 88(2):461–475. <https://doi.org/10.1007/s00253-010-2742-9>
- Genzel Y, Vogel T, Buck J, Behrendt I, Ramirez DV, Schiedner G, Jordan I, Reichl U (2014) High cell density cultivations by alternating tangential flow (ATF) perfusion for influenza A virus production using suspension cells. *Vaccine* 32(24):2770–2781. <https://doi.org/10.1016/j.vaccine.2014.02.016>
- Göbel S, Jaén KE, Dorn M, Neumeyer V, Jordan I, Sandig V, Reichl U, Altomonte J, Genzel Y (2023a) Process intensification strategies towards cell culture-based high-yield production of a fusogenic oncolytic virus. *Biotechnol Bioeng*. <https://doi.org/10.1002/bit.28353>
- Göbel S, Jaén KE, Fernandes RP, Reiter M, Altomonte J, Reichl U, Genzel Y (2023b) Characterization of a quail suspension cell line for production of a fusogenic oncolytic virus. *Biotechnol Bioeng*. <https://doi.org/10.1002/bit.28530>
- Göbel S, Kortum F, Chavez KJ, Jordan I, Sandig V, Reichl U, Altomonte J, Genzel Y (2022a) Cell-line screening and process development for a fusogenic oncolytic virus in small-scale suspension cultures. *Appl Microbiol Biotechnol* 106(13–16):4945–4961. <https://doi.org/10.1007/s00253-022-12027-5>
- Göbel S, Pelz L, Reichl U, Genzel Y (2022b) Chapter 5 Upstream processing for viral vaccines—Process intensification. In: Amine Kamen LC (ed) *Bioprocessing of viral vaccines*, vol 1. Taylor & Francis Group, <https://www.routledge.com/Bioprocessing-of-Viral-Vaccines/Kamen-Cervera/p/book/9781032132112>, pp 79–137
- Gränicher G, Babakhani M, Göbel S, Jordan I, Marichal-Gallardo P, Genzel Y, Reichl U (2021a) A high cell density perfusion process for modified Vaccinia virus Ankara production: process integration with inline DNA digestion and cost analysis. *Biotechnol Bioeng*. <https://doi.org/10.1002/bit.27937>
- Gränicher G, Coronel J, Trampler F, Jordan I, Genzel Y, Reichl U (2020) Performance of an acoustic settler versus a hollow fiber-based ATF technology for influenza virus production in perfusion. *Appl Microbiol Biotechnol* 104(11):4877–4888. <https://doi.org/10.1007/s00253-020-10596-x>
- Gränicher G, Tapia F, Behrendt I, Jordan I, Genzel Y, Reichl U (2021b) Production of modified Vaccinia Ankara virus by intensified cell cultures: a comparison of platform technologies for viral vector production. *Biotechnol J* 16(1):e2000024. <https://doi.org/10.1002/biot.202000024>
- Hadpe SR, Sharma AK, Mohite VV, Rathore AS (2017) ATF for cell culture harvest clarification: mechanistic modelling and comparison with TFF. *J Chem Technol Biotechnol* 92(4):732–740. <https://doi.org/10.1002/jctb.5165>
- Hein MD, Chawla A, Cattaneo M, Kupke SY, Genzel Y, Reichl U (2021) Cell culture-based production of defective interfering influenza A virus particles in perfusion mode using an alternating tangential flow filtration system. *bioRxiv* 2021.06.07.446880. <https://doi.org/10.1101/2021.06.07.446880>
- Jones SM, Feldmann H, Ströher U, Geisbert JB, Fernando L, Grolla A, Klenk HD, Sullivan NJ, Volchkov VE, Fritz EA, Daddario KM, Hensley LE, Jahrling PB, Geisbert TW (2005) Live attenuated recombinant vaccine protects nonhuman primates against Ebola and Marburg viruses. *Nat Med* 11(7):786–790. <https://doi.org/10.1038/nm1258>
- Kahn JS, Roberts A, Weibel C, Buonocore L, Rose JK (2001) Replication-competent or attenuated, nonpropagating vesicular stomatitis viruses expressing respiratory syncytial virus (RSV) antigens protect mice against RSV challenge. *J Virol*

- 75(22):11079–11087. <https://doi.org/10.1128/jvi.75.22.11079-11087.2001>
- Krabbe T, Marek J, Groll T, Steiger K, Schmid RM, Krackhardt AM, Altomonte J (2021) Adoptive T cell therapy is complemented by oncolytic virotherapy with fusogenic VSV-NDV in combination treatment of murine melanoma. *Cancers* 13(5):1044
- Lauretto F, Chattopadhyay A, de Oliveira França RF, Castro-Jorge L, Rose J, Fonseca BA (2016) Recombinant vesicular stomatitis virus-based dengue-2 vaccine candidate induces humoral response and protects mice against lethal infection. *Human Vaccines Immunother* 12(9):2327–2333. <https://doi.org/10.1080/21645515.2016.1183857>
- Liao JB, Publicover J, Rose JK, DiMaio D (2008) Single-dose, therapeutic vaccination of mice with vesicular stomatitis virus expressing human papillomavirus type 16 E7 protein. *Clin Vaccine Immunol: CVI* 15(5):817–824. <https://doi.org/10.1128/cvi.00343-07>
- Manceur AP, Kim H, Mistic V, Andreev N, Dorion-Thibaudeau J, Lanthier S, Bernier A, Tremblay S, Gélinas A-M, Broussau S, Gilbert R, Ansorge S (2017) Scalable lentiviral vector production using stable HEK293SF producer cell lines. *Hum Gene Ther Methods* 28(6):330–339. <https://doi.org/10.1089/hgtb.2017.086>
- Mendes JP, Fernandes B, Pineda E, Kudugunti S, Bransby M, Gantier R, Peixoto C, Alves PM, Roldão A, Silva RJS (2022) AAV process intensification by perfusion bioreaction and integrated clarification. *Front Bioeng Biotechnol* 10:1020174. <https://doi.org/10.3389/fbioe.2022.1020174>
- Mendonça SA, Lorincz R, Boucher P, Curiel DT (2021) Adenoviral vector vaccine platforms in the SARS-CoV-2 pandemic. *NPJ Vaccines* 6(1):97. <https://doi.org/10.1038/s41541-021-00356-x>
- Moleirinho MG, Silva RJS, Alves PM, Carrondo MJT, Peixoto C (2020) Current challenges in biotherapeutic particles manufacturing. *Expert Opin Biol Ther* 20(5):451–465. <https://doi.org/10.1080/14712598.2020.1693541>
- Nadeau I, Kamen A (2003) Production of adenovirus vector for gene therapy. *Biotechnol Adv* 20(7-8):475–489
- Nikolay A, de Grooth J, Genzel Y, Wood JA, Reichl U (2020) Virus harvesting in perfusion culture: choosing the right type of hollow fiber membrane. *Biotechnol Bioeng* 117(10):3040–3052. <https://doi.org/10.1002/bit.27470>
- Nikolay A, Léon A, Schwamborn K, Genzel Y, Reichl U (2018) Process intensification of EB66® cell cultivations leads to high-yield yellow fever and Zika virus production. *Appl Microbiol Biotechnol* 102(20):8725–8737. <https://doi.org/10.1007/s00253-018-9275-z>
- Palin A, Chattopadhyay A, Park S, Delmas G, Suresh R, Senina S, Perlin DS, Rose JK (2007) An optimized vaccine vector based on recombinant vesicular stomatitis virus gives high-level, long-term protection against *Yersinia pestis* challenge. *Vaccine* 25(4):741–750. <https://doi.org/10.1016/j.vaccine.2006.08.010>
- Pelz L, Göbel S, Chavez K, Reichl U, Genzel Y (2022) Chapter 5 Upstream processing for viral vaccines—general aspects. In: Amine Kamen LC (ed) *Bioprocessing of viral vaccines*, vol 1. Taylor & Francis Group, <https://www.routledge.com/Bioprocessing-of-Viral-Vaccines/Kamen-Cervera/p/book/9781032132112>, pp 79–137
- Roberts A, Kretschmar E, Perkins AS, Forman J, Price R, Buonocore L, Kawaoka Y, Rose JK (1998) Vaccination with a recombinant vesicular stomatitis virus expressing an influenza virus hemagglutinin provides complete protection from influenza virus challenge. *J Virol* 72(6):4704–4711. <https://doi.org/10.1128/jvi.72.6.4704-4711.1998>
- Schneider M, Marison IW, von Stockar U (1996) The importance of ammonia in mammalian cell culture. *J Biotechnol* 46(3):161–185. [https://doi.org/10.1016/0168-1656\(95\)00196-4](https://doi.org/10.1016/0168-1656(95)00196-4)
- Su Y, Wei Z, Miao Y, Sun L, Shen Y, Tang Z, Li L, Quan Y, Yu H, Wang W-C, Zhou W, Tian J (2021) Optimized process operations reduce product retention and column clogging in ATF-based perfusion cell cultures. *Appl Microbiol Biotechnol* 105(24):9125–9136. <https://doi.org/10.1007/s00253-021-11662-8>
- Suder E, Furuyama W, Feldmann H, Marzi A, de Wit E (2018) The vesicular stomatitis virus-based Ebola virus vaccine: from concept to clinical trials. *Human Vaccines Immunother* 14(9):2107–2113. <https://doi.org/10.1080/21645515.2018.1473698>
- Tona RM, Shah R, Middaugh K, Steve J, Marques J, Roszell BR, Jung C (2023) Process intensification for lentiviral vector manufacturing using tangential flow depth filtration. *Mol Ther- Methods Clin Dev* 29:93–107. <https://doi.org/10.1016/j.omtm.2023.02.017>
- Tran MY, Kamen AA (2022) Production of lentiviral vectors using a HEK-293 producer cell line and advanced perfusion processing. *Front Bioeng Biotechnol* 10:887716. <https://doi.org/10.3389/fbioe.2022.887716>
- Ura T, Okuda K, Shimada M (2014) Developments in viral vector-based vaccines. *Vaccines (Basel)* 2(3):624–641. <https://doi.org/10.3390/vaccines2030624>
- Ura T, Yamashita A, Mizuki N, Okuda K, Shimada M (2021) New vaccine production platforms used in developing SARS-CoV-2 vaccine candidates. *Vaccine* 39(2):197–201. <https://doi.org/10.1016/j.vaccine.2020.11.054>
- van den Pol AN, Mao G, Chattopadhyay A, Rose JK, Davis JN (2017) Chikungunya, influenza, Nipah, and Semliki forest chimeric viruses with vesicular stomatitis virus: actions in the brain. *J Virol* 91(6). <https://doi.org/10.1128/jvi.02154-16>
- Vázquez-Ramírez D, Jordan I, Sandig V, Genzel Y, Reichl U (2019) High titer MVA and influenza A virus production using a hybrid fed-batch/perfusion strategy with an ATF system. *Appl Microbiol Biotechnol* 103(7):3025–3035
- Williams T., Goodyear O., Davies L., Knevelman C., Bransby M., Mitrophanous K., J. M (2020) Lentiviral vector manufacturing process enhancement utilizing TFDFTM technology. *Cell Gene Ther Insights*:6:455–467 doi:<https://doi.org/10.18609/cgti.2020.053>
- Wu Y, Bissinger T, Genzel Y, Liu X, Reichl U, Tan W-S (2021) High cell density perfusion process for high yield of influenza A virus production using MDCK suspension cells. *Appl Microbiol Biotechnol* 105(4):1421–1434. <https://doi.org/10.1007/s00253-020-11050-8>
- Yang Z, Paes B, Fulber JPC, Tran MY, Farnós O, Kamen AA (2023) Development of an integrated continuous manufacturing process for the rVSV-Vectorized SARS-CoV-2 candidate vaccine. *Vaccines (Basel)* 11(4). <https://doi.org/10.3390/vaccines11040841>
- Yue J, Liu Y, Zhao M, Bi X, Li G, Liang W (2023) The R&D landscape for infectious disease vaccines. *Nat Rev Drug Discov*. <https://doi.org/10.1038/d41573-023-00119-4>
- Zhan C, Bidkhorji G, Schwarz H, Malm M, Mebrahtu A, Field R, Sellick C, Hatton D, Varley P, Mardinoglu A, Rockberg J, Chotteau V (2020) Low shear stress increases recombinant protein production and high shear stress increases apoptosis in human cells. *iScience* 23(11):101653. <https://doi.org/10.1016/j.isci.2020.101653>
- Zhang Y, Nagalo BM (2022) Immunovirotherapy based on recombinant vesicular stomatitis virus: where are we? *Front Immunol* 13. <https://doi.org/10.3389/fimmu.2022.898631>

Publisher's note Springer Nature remains neutral with regard to jurisdictional claims in published maps and institutional affiliations.

4. Conclusion and Outlook

In this work, virus evolution studies and NGS were used for the identification of IAV DIP candidates with superior antiviral activity and for the elucidation of their molecular characteristics in order to facilitate the development of a safe and efficacious IAV DIP-based treatment of the influenza disease (first manuscript). Studying a wide range of infection conditions of DIPs and STVs helped to analyze the effects of different DIP and STV concentrations on STV replication and virus-induced apoptosis (second manuscript). Moreover, the work revealed that IAV DIPs not only inhibit the propagation of IAV, but also exert broad-spectrum antiviral activity against IFN-sensitive viruses such as RSV, YFV and ZIKV (third manuscript). In addition, a scalable cell culture-based batch process in STR for production of highly effective and almost pure OP7 chimera DIPs in the absence of STVs was developed and optimized (fourth and fifth manuscript). Process intensification for the production of OP7 chimera DIPs was realized by establishment of a perfusion culture using an ATF module for cell retention (fifth manuscript). Finally, the TFDF perfusion system was evaluated for intensified virus production and continuous virus harvesting and clarification to develop more cost-effective and productive production platforms (sixth manuscript).

Selection, production, and characteristics of highly interfering IAV DIP candidates

In this study, IAV DIPs that are highly competitive in replication and packaging were selected. To achieve this, semi-continuous propagation of IAV and its DIPs enabled DIP challenge at different selection pressures. The application of NGS for samples of the supernatant provided the sensitive identification of DI vRNAs at high throughput. In collaboration with Fadi Alnaji (Department of Microbiology at University of Illinois at Urbana-Champaign, processed NGS results via a bioinformatics pipeline), Daniel Rüdiger (MPI, performed computational data analysis) and Tanya Dogra (MPI, conducted rescue of IAV DIPs), it was demonstrated that DIPs harboring DI vRNAs with a high growth rate exhibit a superior antiviral activity, even compared to DI244, and are, thus, highly promising candidates for antiviral therapy. In a previous study,

purely clonal DI244 already showed a high antiviral efficacy and tolerability in mice (Hein et al., 2021a). In follow-up studies, the identified novel cDIPs with improved antiviral activity might be tested in mice, ferrets and cynomolgus macaques towards the initiation of clinical trials in humans. Moreover, as a strong accumulation of deletion junctions on PB1 and PA encoding segments was also found, production and testing of DIPs harboring a deletion in Seg 2 or 3 might be very interesting by employing cell lines stably expressing PB1 and/or PA.

Important steps were made in identifying characteristics of highly competitive DI vRNAs. A predominant location of deletion junctions on the polymerase-encoding segments, and a short, but optimal DI vRNA length for replication was found. Yet, it can be assumed that not only the DI vRNA length but also the deletion junction site might be a determinant for competitive DI vRNAs. As no clear differences in breaking point positions between highly and lowly accumulating DI vRNAs could be found, further research is needed to study the impact of the deletion junction site (e.g. involvement of tertiary structure) on formation and competitiveness of DI vRNAs. For instance, an additional interference mechanism of expressed truncated proteins encoded in the DI vRNAs was identified recently. Those cryptic proteins might, thus, play a further role (Ranum et al., 2024). Moreover, not the entire packaging signal was required for efficient IAV DIP replication indicating that the packaging network of IAV is not yet fully decoded (Jakob et al., 2022).

STV infection using different concentrations of purely clonal DI244 and STVs

In this study, the aim was to obtain a more detailed understanding of DIP and STV replication dynamics on the intracellular and population level of suspension cells. First, infection experiments in MDCK(sus) cells at 12 different infection conditions with purely clonal DI244 (Bdeir et al., 2019, Hein et al., 2021a) and STVs were conducted. This provided an in-depth and time-resolved analysis of the effects of different DI244 and STV concentrations on STV replication and virus-induced apoptosis. It was demonstrated that a high DIP input prevents stimulation of apoptosis and results in very strong suppression of STV replication.

The generated data set was used by Daniel Rüdiger (MPI) to calibrate a multiscale model that describes the replication of IAV DIPs and STVs for a broad range of DIP (MODIP) and STV (MOI) input. In addition, these data provided the foundation to identify the optimal DIP/STV ratio to suppress STV propagation. More specifically, the multiscale model predicted a required ratio of at least 10,000:1 DIPs to STVs to confer a high inhibition of STV propagation of more than four orders of magnitude in cell culture, which is in line with results of *in vivo* studies (Dimmock and Easton, 2015, Hein et al., 2021c).

Future research efforts should comprise the investigation of the spatial IAV DIP and STV spread in cells/tissues of the human pharynx/lung or even in 3D airway models. By mimicking *in vivo* conditions, this could deliver new insights regarding the selection of an optimal DIP dose for use as an antiviral in humans and contribution of an innate defense mechanism (e.g. IFN response, cilia movement) to design clinical trials in humans.

Broad-spectrum antiviral activity of IAV DIPs

In the next part, the broad-spectrum antiviral activity of IAV DIPs against unrelated virus infections was evaluated by performing co-infection experiments in human lung cells. It was demonstrated that DI244 and OP7 suppress the propagation of RSV by stimulating an innate immune response. Our study, thus, provided an important contribution to the potential use of IAV DIPs against IFN-sensitive respiratory viruses such as IAV (Dimmock and Easton, 2015, Dimmock et al., 2008), IBV (Scott et al., 2011), SARS-CoV-2 (Rand et al., 2021), and RSV by intranasal application.

The *in vitro* co-infection experiments have shown that IAV DIPs also suppress the replication of IFN-sensitive viruses (YFV and ZIKV) in human lung cells. Thus, IAV DIPs might also be interesting for use as antivirals against systemic, IFN-sensitive virus infections. Yet, a possible route of administration and antiviral efficacy still needs to be determined in animal trials. In addition, prospective investigations may include high-throughput screening of the antiviral activity of IAV DIPs against a broad range of IFN-sensitive viruses.

In the future, it would be desirable to test the prophylactic effect of IAV DIPs against unrelated virus infections as only co-infection experiments were performed. Moreover, in the *in vitro* co-infection experiments, a higher antiviral activity than for IAV DIPs was found for the small molecule antiviral agents ribavirin (in RSV and ZIKV infection) and fidaxomicin (ZIKV infection). Yet, their use poses significant drawbacks. In order to develop an IAV DIP treatment for human use, testing of IAV DIPs and other relevant antiviral agents in animal trials and clinical trials regarding safety and efficacy should be pursued.

The identification of IFN as crucial factor for IAV DIP-induced antiviral activity against unrelated virus infections was achieved in line with previous studies (Easton et al., 2011, Rand et al., 2021, Scott et al., 2011). In the study, the antiviral activity was determined by an early and enhanced upregulation of the type-I and –III IFN response. Moreover, an absence of antiviral activity in IFN-deficient Vero cells was confirmed. The antiviral effect was caused by signaling through the JAK/STAT pathway and an early upregulation of RIG-I. Future experiments with RIG-I knock-out A549 cells would demonstrate whether the antiviral activity is dependent on vRNA recognition. In the study, the antiviral ISGs Mx1 (YFV and RSV infection), RSAD2 (YFV infection), and IFITM1 (RSV infection) were strongly expressed. In comparison to quantification of selected targets by real-time reverse transcription-quantitative PCR (RT-qPCR), RNA sequencing would provide the detection of a wider spectrum of involved ISGs for in-depth analysis of gene expression.

Cell culture-based production of OP7 chimera DIPs free of STVs in shake flasks

Previous work addressed the development of MDCK(sus) cells grown in chemically defined XenoTM medium (Bissinger et al., 2019). Moreover, MDCK-PB2(adh), HEK-293T-PB2(adh) (Bdeir et al., 2019), and MDCK-PB2(sus) cells (Hein et al., 2021a) were developed for generation and production of purely clonal Seg 1 cDIPs in the absence of STVs. To generate OP7 chimera DIPs that are free of STVs, Tanya Dogra (MPI) developed a plasmid-based production system using reverse genetics that yielded a mixture of OP7 chimera DIPs and Seg 1 DIPs. Moreover, an initial OP7 chimera DIP seed virus was generated.

In the scope of this thesis, this DIP seed was employed for evaluating the impact of the MOI on DIP production in shake flasks in MDCK-PB2(sus) cells and to produce material for testing in mice. For the first time, the production of OP7 (chimera DIPs) in the absence of infectious STVs was demonstrated. The MOI had a strong effect on virus titers, OP7 chimera DIP fractions, and interfering efficacy. The optimal MOI of 10^{-3} and 10^{-4} led to maximum interfering efficacies, however, relatively low virus titers were obtained. Moreover, only a part of the DIP harvest was OP7 chimera DIPs (78.7% and 38.3%) in the mixture with Seg 1 cDIPs. The development of a production process for OP7 chimera DIPs free of STVs eliminated the need for UV inactivation of OP7 harvests. UV irradiation would otherwise reduce antiviral efficacy and pose safety and regulatory concerns regarding potential residual STVs.

The produced OP7 chimera DIP material was evaluated for tolerability and antiviral efficacy in mice by Julia Boehme and Maike Baelkner (Otto von Guericke University Magdeburg and Helmholtz Centre for Infection Research). This material was produced in multiple shake flasks and was subsequently purified and concentrated by SXC by Pavel Marichal-Gallardo (MPI). A high tolerability was demonstrated for the intranasal administration of OP7 chimera DIP material. Moreover, mice were protected against an otherwise lethal challenge and without any signs of clinical disease. Future studies should be performed in cynomolgus macaques as a relevant non-human primate model (Chan et al., 2022) to drive the clinical development of IAV DIPs as novel class of broad-spectrum antiviral.

As IAV DIPs harbor the glycoproteins HA and NA on its surface, intranasal administration of IAV DIPs might stimulate robust and cross-protective mucosal immunity at the predominant site of virus infection. Therefore, IAV DIPs could potentially be deployed as intranasal mucosal live vaccine against IAV. To generate a DIP vaccine, surface proteins will be exchanged with those of current seasonal virus strains. IAV DIP vaccines would act therapeutically by i) replication interference and ii) stimulation of innate immunity to fight acute IAV infections. At the same time, by iii) triggering an adaptive immune response, they serve as prophylactic measure and confer protection. Future studies should target the development of an IAV DIP vaccine and subsequent testing *in vivo* regarding safety and efficacy.

Development of a scalable production process for almost pure OP7 chimera DIPs at high titers

To allow for scalability to large-scale manufacturing of OP7 chimera DIPs, medium dilution (1:2) instead of complete medium exchange (centrifugation) was evaluated to provide fresh substrates and dilute inhibitors in batch mode in shake flasks. The media dilution impaired total virus yields and OP7 chimera DIP fractions. Thus, a temperature reduction from 37°C to 32°C was tested. This provided an 11-fold increase in total virus yields relative to the initial process with complete medium exchange and the presence of almost pure OP7 chimera DIPs (99.7%). Surprisingly, almost no MOI dependency of OP7 production was found indicating that the production at 32°C improved the robustness of the process.

To increase the amount of produced DIP material for *in vivo* studies and evaluate applicability for large-scale manufacturing, the optimized process was transferred to a laboratory-scale STR. Three productions in STR led to similar cell growth dynamics and interfering efficacies, and comparable virus yields relative to productions in shake flasks. Thus, large-scale manufacturing to supply clinical trials and commercial use should be feasible.

Finally, very high-titers for production of OP7 chimera DIPs in perfusion mode by increasing VCC to 25×10^6 cells/mL was achieved. For this, an ATF system equipped with a hollow fiber membrane (polyethersulfone, 0.2 μm pore size) was utilized. This perfusion process involved a perfusion rate control by using a capacitance probe (Gränicher et al., 2021, Nikolay et al., 2018). Up to a 79-fold increase in total virus titers was achieved by perfusion cultivation relative to the initial process in shake flasks and batch mode. Moreover, an increased CSVY (up to 3-fold) and STY (up to 22-fold) were found compared to the STR process in batch mode indicating the possibility for use of a STR with a smaller footprint. Results suggested also that the high cell density effect played no role. Yet, only a part of the produced viruses (26%) could be harvested through the hollow fiber membrane. The use of a membrane allowing for continuous virus harvesting, such as the novel tubular membrane (about 10 μm pore size) (Hein et al., 2021b), would provide immediate cooling of produced viruses, thus,

increasing virus titers and should be considered for a final manufacturing process under GMP.

Important steps were made towards the establishment of a production platform (scalable and very high-titer production process, purification train) for the development of a GMP-compliant process, which is currently transferred to a collaborating partner (Fraunhofer Institute for Toxicology and Experimental Medicine). This involves e.g. establishment of virus and cell banks and production of DIP material for pre-clinical and clinical testing. In addition, it would be desirable to perform single-cell cloning for the generation of a monoclonal production cell line. Process development for pharmaceutical formulation and stability studies are also required. Finally, the mode of action of OP7 needs to be better characterized with regard to its possible use as an antiviral agent.

A novel perfusion system for continuous virus harvesting and clarification in one step

With the aim to identify a scalable perfusion system, which allows for continuous virus harvesting and clarification, the TFDF system was tested for process intensification of rVSV-based vectors. This proof-of-concept study involved the evaluation of the production of two different rVSV-based vectors: i) a rVSV-based vector expressing a green fluorescent protein (rVSV-GFP) in suspension human embryonic kidney 293 (HEK293-SF) cells growing in serum-free medium (part of this PhD thesis), and ii) a rVSV-NDV in suspension BHK-21 cells (conducted by Sven Göbel, MPI). For the rVSV-GFP production, the use of the TFDF system allowed for a maximum VCC of 11.3×10^6 cells/mL, high cell retention efficiency (>99.6%), and a continuous virus harvesting and clarification. Moreover, an up to 1.9-fold increasing STY was found relative to the optimized batch process. This confirms other studies that have demonstrated the successful use of the TFDF as perfusion system for continuous virus harvesting and clarification for rVSV-NDV (Sven Göbel, MPI), AAV (Mendes et al., 2022), LV (Tona et al., 2023, Tran and Kamen, 2022), MLV vectors (Hein et al., 2023) and IAV (Silva et al., 2023). In future studies, the TFDF system should be used for intensified IAV DIP production with MDCK-PB2(sus) cells. The main benefit of the

TFDF system relative to the ATF equipped with the novel tubular membrane (Hein et al., 2021b), which also allowed continuous harvesting of DI244, includes scalability (up to 2000 L) and reduction of process steps (clarification). Overall, the progress made allows for integrated continuous bioprocessing by connecting upstream and downstream unit operations.

In conclusion, important steps have been made in the cell culture-based production of IAV DIPs as safe, effective, affordable antiviral agent with a broad-spectrum antiviral activity. The established high-titer production process for OP7 chimera DIPs can serve as basis for the development of a GMP-compliant manufacturing process. Pre-clinical and clinical studies are now needed to further advance IAV DIPs towards commercialization as a potential new antiviral drug.

List of Figures

Figure 1.: Overview of the state of the art and aim of this doctoral thesis.	4
Figure 2.: Structure of IAV	7
Figure 3.: Replication cycle of IAV	10
Figure 4.: Structure of RSV	12
Figure 5.: Structure of flaviviruses	14
Figure 6.: Genome structure of different types of DI vRNAs of IAV DIPs	18
Figure 7.: IAV infection stimulates an antiviral innate immune response of cells	24
Figure 8.: Schematic illustration of perfusion systems comprising a TFF (a) ...	43

Bibliography

- ABDULLAHI, S., JÄKEL, M., BEHREND, S. J., STEIGER, K., TOPPING, G., KRABBE, T., COLOMBO, A., SANDIG, V., SCHIERGENS, T. S., THASLER, W. E., WERNER, J., LICHTENTHALER, S. F., SCHMID, R. M., EBERT, O. & ALTOMONTE, J. 2018. A Novel Chimeric Oncolytic Virus Vector for Improved Safety and Efficacy as a Platform for the Treatment of Hepatocellular Carcinoma. *J Virol*, 92(23).
- ADAMS, O., BONZEL, L., KOVACEVIC, A., MAYATEPEK, E., HOEHN, T. & VOGEL, M. 2010. Palivizumab-Resistant Human Respiratory Syncytial Virus Infection in Infancy. *Clinical Infectious Diseases*, 51(2):185-188.
- ALNAJI, F. G. & BROOKE, C. B. 2020. Influenza virus DI particles: Defective interfering or delightfully interesting? *PLoS Pathog*, 16(5):e1008436.
- ALNAJI, F. G., HOLMES, J. R., RENDON, G., VERA, J. C., FIELDS, C. J., MARTIN, B. E. & BROOKE, C. B. 2019. Sequencing Framework for the Sensitive Detection and Precise Mapping of Defective Interfering Particle-Associated Deletions across Influenza A and B Viruses. *J Virol*, 93(11).
- ALNAJI, F. G., REISER, W. K., RIVERA-CARDONA, J., VELTHUIS, A. J. W. T. & BROOKE, C. B. 2021. Influenza A Virus Defective Viral Genomes Are Inefficiently Packaged into Virions Relative to Wild-Type Genomic RNAs. *mBio*, 12(6):e02959-21.
- ARORA, P., BDEIR, N., GAERTNER, S., REITER, S., PELZ, L., FELGENHAUER, U., REICHL, U., LUDWIG, S., WEBER, F., HOFFMANN, M., WINKLER, M. & PÖHLMANN, S. 2021. Interferon induction and not replication interference mainly determines anti-influenza virus activity of defective interfering particles. *bioRxiv*:2021.09.20.461172.
- AUSAR, S. F., ESPINA, M., BROCK, J., THYAGARAYAPURAN, N., REPETTO, R., KHANDKE, L. & MIDDAUGH, C. R. 2007. High-throughput screening of stabilizers for respiratory syncytial virus: identification of stabilizers and their effects on the conformational thermostability of viral particles. *Hum Vaccin*, 3(3):94-103.
- BANGHAM, C. M. & KIRKWOOD, T. B. 1990. Defective interfering particles: effects in modulating virus growth and persistence. *Virology*, 179(2):821-826.
- BARIK, S. 2013. Respiratory syncytial virus mechanisms to interfere with type 1 interferons. *Curr Top Microbiol Immunol*, 372:173-91.
- BAUM, A. & GARCÍA-SASTRE, A. 2011. Differential recognition of viral RNA by RIG-I. *Virulence*, 2(2):166-169.
- BAUM, A., SACHIDANANDAM, R. & GARCÍA-SASTRE, A. 2010. Preference of RIG-I for short viral RNA molecules in infected cells revealed by next-generation sequencing. *Proceedings of the National Academy of Sciences*, 107(37):16303-16308.
- BDEIR, N., ARORA, P., GÄRTNER, S., HOFFMANN, M., REICHL, U., PÖHLMANN, S. & WINKLER, M. 2019. A system for production of defective interfering particles in the absence of infectious influenza A virus. *PLoS One*, 14(3):e0212757.
- BDEIR, N., ARORA, P., GÄRTNER, S., PÖHLMANN, S. & WINKLER, M. 2021. Evidence that two instead of one defective interfering RNA in influenza A virus-derived defective interfering particles (DIPs) does not enhance antiviral activity. *Scientific Reports*, 11(1):20477.
- BELICHA-VILLANUEVA, A., RODRIGUEZ-MADOZ, J. R., MAAMARY, J., BAUM, A., BERNAL-RUBIO, D., MINGUITO DE LA ESCALERA, M., FERNANDEZ-SESMA, A. & GARCIA-SASTRE, A. 2012. Recombinant influenza A viruses with enhanced levels of PB1 and PA viral protein expression. *J Virol*, 86(10):5926-30.
- BELSHE, R. B., GRUBER, W. C., MENDELMAN, P. M., CHO, I., REISINGER, K., BLOCK, S. L., WITTES, J., IACUZIO, D., PIEDRA, P., TREANOR, J., KING, J., KOTLOFF, K., BERNSTEIN, D. I., HAYDEN, F. G., ZANGWILL, K., YAN, L. & WOLFF, M. 2000. Efficacy of vaccination with live attenuated, cold-adapted, trivalent, intranasal influenza virus vaccine against a variant (A/Sydney) not contained in the vaccine. *J Pediatr*, 136(2):168-75.
- BERCOVICH-KINORI, A., TAI, J., GELBART, I. A., SHITRIT, A., BEN-MOSHE, S., DRORI, Y., ITZKOVITZ, S., MANDELBOIM, M. & STERN-GINOSSAR, N. 2016. A systematic view on influenza induced host shutoff. *eLife*, 5:e18311.

Bibliography

- BIELSER, J.-M., WOLF, M., SOUQUET, J., BROLY, H. & MORBIDELLI, M. 2018. Perfusion mammalian cell culture for recombinant protein manufacturing – A critical review. *Biotechnology Advances*, 36(4):1328-1340.
- BIN UMAIR, M., AKUSA, F. N., KASHIF, H., SEERAT, E. F., BUTT, F., AZHAR, M., MUNIR, I., AHMED, M., KHALIL, W., SHARYAR, H., RAFIQUE, S., SHAHID, M. & AFZAL, S. 2022. Viruses as tools in gene therapy, vaccine development, and cancer treatment. *Arch Virol*, 167(6):1387-1404.
- BISHNOI, S., TIWARI, R., GUPTA, S., BYRAREDDY, S. N. & NAYAK, D. 2018. Oncotargeting by Vesicular Stomatitis Virus (VSV): Advances in Cancer Therapy. *Viruses*, 10(2).
- BISSINGER, T. 2020. Evaluation of MDCK suspension cell lines for influenza A virus production: media, metabolism, and process conditions. Doctoral Thesis, Otto-von-Guericke-Universität.
- BISSINGER, T., FRITSCH, J., MIHUT, A., WU, Y., LIU, X., GENZEL, Y., TAN, W. S. & REICHL, U. 2019. Semi-perfusion cultures of suspension MDCK cells enable high cell concentrations and efficient influenza A virus production. *Vaccine*, 37(47):7003-7010.
- BORDEN, E. C. & PARKINSON, D. 1998. A perspective on the clinical effectiveness and tolerance of interferon-alpha. *Semin Oncol*, 25(1 Suppl 1):3-8.
- BOUVIER, N. M. & PALESE, P. 2008. The biology of influenza viruses. *Vaccine*, 26 Suppl 4:D49-53.
- BROGGI, A., GHOSH, S., SPOSITO, B., SPREAFICO, R., BALZARINI, F., LO CASCIO, A., CLEMENTI, N., DE SANTIS, M., MANCINI, N., GRANUCCI, F. & ZANONI, I. 2020. Type III interferons disrupt the lung epithelial barrier upon viral recognition. *Science*, 369(6504):706-712.
- BROWN, K. S., SAFRONETZ, D., MARZI, A., EBHARA, H. & FELDMANN, H. 2011. Vesicular stomatitis virus-based vaccine protects hamsters against lethal challenge with Andes virus. *J Virol*, 85(23):12781-91.
- BYRD-LEOTIS, L., JIA, N., MATSUMOTO, Y., LU, D., KAWAOKA, Y., STEINHAEUER, D. A. & CUMMINGS, R. D. 2022. Sialylated and sulfated N-Glycans in MDCK and engineered MDCK cells for influenza virus studies. *Scientific Reports*, 12(1):12757.
- CAINE, E. A., SCHEAFFER, S. M., ARORA, N., ZAITSEV, K., ARTYOMOV, M. N., COYNE, C. B., MOLEY, K. H. & DIAMOND, M. S. 2019. Interferon lambda protects the female reproductive tract against Zika virus infection. *Nat Commun*, 10(1):280.
- CALAIN, P., CURRAN, J., KOLAKOSKY, D. & ROUX, L. 1992. Molecular cloning of natural paramyxovirus copy-back defective interfering RNAs and their expression from DNA. *Virology*, 191(1):62-71.
- CALAIN, P. & ROUX, L. 1988. Generation of measles virus defective interfering particles and their presence in a preparation of attenuated live-virus vaccine. *J Virol*, 62(8):2859-66.
- CAMPOS, G. S., BANDEIRA, A. C. & SARDI, S. I. 2015. Zika virus outbreak, bahia, brazil. *Emerging infectious diseases*, 21(10):1885.
- CAO-LORMEAU, V. M., ROCHE, C., TEISSIER, A., ROBIN, E., BERRY, A. L., MALLET, H. P., SALL, A. A. & MUSSO, D. 2014. Zika virus, French polynesia, South pacific, 2013. *Emerg Infect Dis*, 20(6):1085-6.
- CASE, J. B., ROTHLAUF, P. W., CHEN, R. E., KAFAI, N. M., FOX, J. M., SMITH, B. K., SHRIHARI, S., MCCUNE, B. T., HARVEY, I. B., KEELER, S. P., BLOYET, L. M., ZHAO, H., MA, M., ADAMS, L. J., WINKLER, E. S., HOLTZMAN, M. J., FREMONT, D. H., WHELAN, S. P. J. & DIAMOND, M. S. 2020. Replication-Competent Vesicular Stomatitis Virus Vaccine Vector Protects against SARS-CoV-2-Mediated Pathogenesis in Mice. *Cell Host Microbe*, 28(3):465-474.e4.
- CHAN, M., TIWARY, M., WU, H. L., TAILOR, N., VENDRAMELLI, R., AUDET, J., WARNER, B. M., TIERNEY, K., ALBIETZ, A., TRUONG, T., DOAN, K., BELLO, A., WILLMAN, M., GRIFFIN, B. D., HANLEY, P. W., LOVAGLIO, J., SAFRONETZ, D., STRONG, J., SACHA, J. B. & KOBASA, D. 2022. Pandemic 1918 Influenza Virus Does Not Cause Lethal Infection in Rhesus or Cynomolgus Macaques. *Journal of Virology*, 96(16):e00728-22.
- CHATURVEDI, S., VASEN, G., PABLO, M., CHEN, X., BEUTLER, N., KUMAR, A., TANNER, E., ILLOUZ, S., RAHGOSHAY, D., BURNETT, J., HOLGUIN, L., CHEN, P. Y., NDJAMEN, B., OTT, M., RODICK, R., ROGERS, T., SMITH, D. M. & WEINBERGER, L. S. 2021. Identification of a therapeutic interfering particle-A single-dose SARS-CoV-2 antiviral intervention with a high barrier to resistance. *Cell*, 184(25):6022-6036.e18.
- CHEN, C., WONG, H. E. & GOUDAR, C. T. 2018a. Upstream process intensification and continuous manufacturing. *Current Opinion in Chemical Engineering*, 22:191-198.
- CHEN, J., WANG, J., ZHANG, J. & LY, H. 2021. Advances in Development and Application of Influenza Vaccines. *Frontiers in Immunology*, 12.

Bibliography

- CHEN, X., LIU, S., GORAYA, M. U., MAAROUF, M., HUANG, S. & CHEN, J. L. 2018b. Host Immune Response to Influenza A Virus Infection. *Front Immunol*, 9:320.
- CLINCKE, M.-F., MÖLLERYD, C., SAMANI, P. K., LINDSKOG, E., FÄLDT, E., WALSH, K. & CHOTTEAU, V. 2013. Very high density of Chinese hamster ovary cells in perfusion by alternating tangential flow or tangential flow filtration in WAVE bioreactor™—part II: Applications for antibody production and cryopreservation. *Biotechnology Progress*, 29(3):768-777.
- COLLINS, P. L., FEARNES, R. & GRAHAM, B. S. 2013. Respiratory syncytial virus: virology, reverse genetics, and pathogenesis of disease. *Curr Top Microbiol Immunol*, 372:3-38.
- CÓRDOVA-DÁVALOS, L. E., HERNÁNDEZ-MERCADO, A., BARRÓN-GARCÍA, C. B., ROJAS-MARTÍNEZ, A., JIMÉNEZ, M., SALINAS, E. & CERVANTES-GARCÍA, D. 2022. Impact of genetic polymorphisms related to innate immune response on respiratory syncytial virus infection in children. *Virus Genes*, 58(6):501-514.
- CORONEL, J., BEHRENDT, I., BURGİN, T., ANDERLEI, T., SANDIG, V., REICHL, U. & GENZEL, Y. 2019. Influenza A virus production in a single-use orbital shaken bioreactor with ATF or TFF perfusion systems. *Vaccine*, 37(47):7011-7018.
- CORONEL, J., GRÄNICHER, G., SANDIG, V., NOLL, T., GENZEL, Y. & REICHL, U. 2020. Application of an Inclined Settler for Cell Culture-Based Influenza A Virus Production in Perfusion Mode. *Front Bioeng Biotechnol*, 8:672.
- COX, M. M. & HOLLISTER, J. R. 2009. FluBlok, a next generation influenza vaccine manufactured in insect cells. *Biologicals*, 37(3):182-9.
- CROS, J. F. & PALESE, P. 2003. Trafficking of viral genomic RNA into and out of the nucleus: influenza, Thogoto and Borna disease viruses. *Virus Res*, 95(1-2):3-12.
- DAI, J.-X., YOU, C.-H., QI, Z.-T., WANG, X.-M., SUN, P.-Q., BI, W.-S., QIAN, Y., DING, R.-L., DU, P. & HE, Y. 1987. Children's respiratory viral diseases treated with interferon aerosol. *Chinese Medical Journal*, 100(02):162-166.
- DAVIS, A. R., HITI, A. L. & NAYAK, D. P. 1980. Influenza defective interfering viral RNA is formed by internal deletion of genomic RNA. *Proc Natl Acad Sci U S A*, 77(1):215-9.
- DAVIS, A. R. & NAYAK, D. P. 1979. Sequence relationships among defective interfering influenza viral RNAs. *Proc Natl Acad Sci U S A*, 76(7):3092-6.
- DE MIRANDA, R. M., FERNANDES, R. S., DA SILVA-FERNANDES, A. T., FERREIRA-DE-BRITO, A., MOREIRA, S. B., PEREIRA, R. C., DA SILVA MENDES, Y., DE LIMA, S. M. B., PISSINATTI, A., FREIRE, M. D. S., ALENCAR, J. A. F. & LOURENCO-DE-OLIVEIRA, R. 2022. Neotropical Sylvatic Mosquitoes and *Aedes aegypti* Are Not Competent to Transmit 17DD Attenuated Yellow Fever Virus from Vaccinated Viremic New World Non-Human Primates. *Viruses*, 14(10):2231.
- DE WEERD, N. A. & NGUYEN, T. 2012. The interferons and their receptors--distribution and regulation. *Immunol Cell Biol*, 90(5):483-91.
- DELGADO, M. F., COVIELLO, S., MONSALVO, A. C., MELENDI, G. A., HERNANDEZ, J. Z., BATALLE, J. P., DIAZ, L., TRENTO, A., CHANG, H.-Y., MITZNER, W., RAVETCH, J., MELERO, J. A., IRUSTA, P. M. & POLACK, F. P. 2009. Lack of antibody affinity maturation due to poor Toll-like receptor stimulation leads to enhanced respiratory syncytial virus disease. *Nature Medicine*, 15(1):34-41.
- DIMMOCK, N. J., BECK, S. & MCLAIN, L. 1986. Protection of Mice from Lethal Influenza: Evidence that Defective Interfering Virus Modulates the Immune Response and Not Virus Multiplication. *Journal of General Virology*, 67(5):839-850.
- DIMMOCK, N. J., DOVE, B. K., MENG, B., SCOTT, P. D., TAYLOR, I., CHEUNG, L., HALLIS, B., MARRIOTT, A. C., CARROLL, M. W. & EASTON, A. J. 2012a. Comparison of the protection of ferrets against pandemic 2009 influenza A virus (H1N1) by 244 DI influenza virus and oseltamivir. *Antiviral Res*, 96(3):376-85.
- DIMMOCK, N. J., DOVE, B. K., SCOTT, P. D., MENG, B., TAYLOR, I., CHEUNG, L., HALLIS, B., MARRIOTT, A. C., CARROLL, M. W. & EASTON, A. J. 2012b. Cloned defective interfering influenza virus protects ferrets from pandemic 2009 influenza A virus and allows protective immunity to be established. *PLoS One*, 7(12):e49394.
- DIMMOCK, N. J. & EASTON, A. J. 2014. Defective interfering influenza virus RNAs: time to reevaluate their clinical potential as broad-spectrum antivirals? *J Virol*, 88(10):5217-27.
- DIMMOCK, N. J. & EASTON, A. J. 2015. Cloned Defective Interfering Influenza RNA and a Possible Pan-Specific Treatment of Respiratory Virus Diseases. *Viruses*, 7(7):3768-88.

Bibliography

- DIMMOCK, N. J., RAINSFORD, E. W., SCOTT, P. D. & MARRIOTT, A. C. 2008. Influenza virus protecting RNA: an effective prophylactic and therapeutic antiviral. *J Virol*, 82(17):8570-8.
- DOGRA, T., PELZ, L., BOEHME, J. D., KUECHLER, J., KERSHAW, O., MARICHAL-GALLARDO, P., BAELKNER, M., HEIN, M. D., GRUBER, A. D., BENNDORF, D., GENZEL, Y., BRUDER, D., KUPKE, S. Y. & REICHL, U. 2023. Generation of "OP7 chimera" defective interfering influenza A particle preparations free of infectious virus that show antiviral efficacy in mice. *Scientific Reports*, 13(1):20936.
- DOMACHOWSKIE, J. B., KHAN, A. A., ESSER, M. T., JENSEN, K., TAKAS, T., VILLAFANA, T., DUBOVSKY, F. & GRIFFIN, M. P. 2018. Safety, Tolerability and Pharmacokinetics of MEDI8897, an Extended Half-life Single-dose Respiratory Syncytial Virus Prefusion F-targeting Monoclonal Antibody Administered as a Single Dose to Healthy Preterm Infants. *Pediatr Infect Dis J*, 37(9):886-892.
- DOROSHENKO, A. & HALPERIN, S. A. 2009. Trivalent MDCK cell culture-derived influenza vaccine Optaflu® (Novartis Vaccines). *Expert Review of Vaccines*, 8(6):679-688.
- DUHAUT, S. D. & DIMMOCK, N. J. 1998. Heterologous protection of mice from a lethal human H1N1 influenza A virus infection by H3N8 equine defective interfering virus: comparison of defective RNA sequences isolated from the DI inoculum and mouse lung. *Virology*, 248(2):241-53.
- DUHAUT, S. D. & DIMMOCK, N. J. 2003. Defective influenza A virus generated entirely from plasmids: its RNA is expressed in infected mouse lung and modulates disease. *Journal of Virological Methods*, 108(1):75-82.
- DUHAUT, S. D. & MCCAULEY, J. W. 1996. Defective RNAs inhibit the assembly of influenza virus genome segments in a segment-specific manner. *Virology*, 216(2):326-37.
- DUTTA, S. K. & LANGENBURG, T. 2023. A Perspective on Current Flavivirus Vaccine Development: A Brief Review. *Viruses*, 15(4).
- EASTON, A. J., SCOTT, P. D., EDWORTHY, N. L., MENG, B., MARRIOTT, A. C. & DIMMOCK, N. J. 2011. A novel broad-spectrum treatment for respiratory virus infections: influenza-based defective interfering virus provides protection against pneumovirus infection in vivo. *Vaccine*, 29(15):2777-84.
- EISFELD, A. J., KAWAKAMI, E., WATANABE, T., NEUMANN, G. & KAWAOKA, Y. 2011. RAB11A is essential for transport of the influenza virus genome to the plasma membrane. *J Virol*, 85(13):6117-26.
- ELAHI, S. M., SHEN, C. F. & GILBERT, R. 2019. Optimization of production of vesicular stomatitis virus (VSV) in suspension serum-free culture medium at high cell density. *J Biotechnol*, 289:144-149.
- EMA. 2019. *First vaccine to protect against Ebola* [Online]. Available: <https://www.ema.europa.eu/en/news/first-vaccine-protect-against-ebola> [Accessed September 16 2023].
- EMA. 2023. *Pegays product information* [Online]. Available: https://www.ema.europa.eu/en/documents/product-information/pegasys-epar-product-information_de.pdf [Accessed August 18 2023].
- EMANUEL, J., CALLISON, J., DOWD, K. A., PIERSON, T. C., FELDMANN, H. & MARZI, A. 2018. A VSV-based Zika virus vaccine protects mice from lethal challenge. *Sci Rep*, 8(1):11043.
- EMENY, J. M. & MORGAN, M. J. 1979. Regulation of the interferon system: evidence that Vero cells have a genetic defect in interferon production. *J Gen Virol*, 43(1):247-52.
- ENGELHARDT, O. G., SMITH, M. & FODOR, E. 2005. Association of the Influenza A Virus RNA-Dependent RNA Polymerase with Cellular RNA Polymerase II. *Journal of Virology*, 79(9):5812-5818.
- EYGERIS, Y., GUPTA, M., KIM, J. & SAHAY, G. 2022. Chemistry of Lipid Nanoparticles for RNA Delivery. *Acc Chem Res*, 55(1):2-12.
- FALSEY, A. R. & WALSH, E. E. 2000. Respiratory syncytial virus infection in adults. *Clin Microbiol Rev*, 13(3):371-84.
- FARIA, N. R., KRAEMER, M. U. G., HILL, S. C., GOES DE JESUS, J., AGUIAR, R. S., IANI, F. C. M., XAVIER, J., QUICK, J., DU PLESSIS, L., DELLICOUR, S., THÉZÉ, J., CARVALHO, R. D. O., BAELE, G., WU, C.-H., SILVEIRA, P. P., ARRUDA, M. B., PEREIRA, M. A., PEREIRA, G. C., LOURENÇO, J., OBOLSKI, U., ABADE, L., VASYLYEVA, T. I., GIOVANETTI, M., YI, D., WEISS, D. J., WINT, G. R. W., SHEARER, F. M., FUNK, S., NIKOLAY, B., FONSECA, V., ADELINO, T. E. R., OLIVEIRA, M. A. A., SILVA, M. V. F., SACCHETTO, L., FIGUEIREDO, P. O., REZENDE, I. M., MELLO, E. M., SAID, R. F. C., SANTOS, D. A., FERRAZ, M. L., BRITO,

Bibliography

- M. G., SANTANA, L. F., MENEZES, M. T., BRINDEIRO, R. M., TANURI, A., DOS SANTOS, F. C. P., CUNHA, M. S., NOGUEIRA, J. S., ROCCO, I. M., DA COSTA, A. C., KOMNINAKIS, S. C. V., AZEVEDO, V., CHIEPPE, A. O., ARAUJO, E. S. M., MENDONÇA, M. C. L., DOS SANTOS, C. C., DOS SANTOS, C. D., MARES-GUIA, A. M., NOGUEIRA, R. M. R., SEQUEIRA, P. C., ABREU, R. G., GARCIA, M. H. O., ABREU, A. L., OKUMOTO, O., KROON, E. G., DE ALBUQUERQUE, C. F. C., LEWANDOWSKI, K., PULLAN, S. T., CARROLL, M., DE OLIVEIRA, T., SABINO, E. C., SOUZA, R. P., SUCHARD, M. A., LEMEY, P., TRINDADE, G. S., DRUMOND, B. P., FILIPPIS, A. M. B., LOMAN, N. J., CAUCHEMEZ, S., ALCANTARA, L. C. J. & PYBUS, O. G. 2018. Genomic and epidemiological monitoring of yellow fever virus transmission potential. *Science*, 361(6405):894-899.
- FDA. 2019. *First FDA-approved vaccine for the prevention of Ebola virus disease, marking a critical milestone in public health preparedness and response* [Online]. Available: <https://www.fda.gov/news-events/press-announcements/first-fda-approved-vaccine-prevention-ebola-virus-disease-marking-critical-milestone-public-health> [Accessed September 16 2023].
- FDA. 2023a. *Clinical trial of mRNA universal influenza vaccine candidate begins* [Online]. Available: <https://www.nih.gov/news-events/news-releases/clinical-trial-mrna-universal-influenza-vaccine-candidate-begins> [Accessed February 11 2024].
- FDA. 2023b. *Package Insert - FluMist Quadrivalent* [Online]. Available: <https://www.fda.gov/media/160349/download> [Accessed December 28 2023].
- FDA. 2023c. *Package Insert - IMLYGIC* [Online]. Available: <https://www.fda.gov/vaccines-blood-biologics/cellular-gene-therapy-products/imlygic> [Accessed December 28 2023].
- FDA. 2023d. *Pegasys (peginterferon alfa-2a) Label* [Online]. Available: https://www.accessdata.fda.gov/drugsatfda_docs/label/2011/103964s5204lbl.pdf [Accessed August 14 2023].
- FENG, C., SHI, J., FAN, Q., WANG, Y., HUANG, H., CHEN, F., TANG, G., LI, Y., LI, P., LI, J., CUI, J., GUO, L., CHEN, S., JIANG, M., FENG, L., CHEN, L., LEI, C., KE, C., DENG, X., HU, F., TANG, X. & LI, F. 2021. Protective humoral and cellular immune responses to SARS-CoV-2 persist up to 1 year after recovery. *Nat Commun*, 12(1):4984.
- FITZGERALD-BOCARSLY, P. & FENG, D. 2007. The role of type I interferon production by dendritic cells in host defense. *Biochimie*, 89(6-7):843-55.
- FODOR, E., DEVENISH, L., ENGELHARDT, O. G., PALESE, P., BROWNLEE, G. G. & GARCÍA-SASTRE, A. 1999. Rescue of influenza A virus from recombinant DNA. *J Virol*, 73(11):9679-82.
- FODOR, E. & TE VELTHUIS, A. J. W. 2020. Structure and Function of the Influenza Virus Transcription and Replication Machinery. *Cold Spring Harb Perspect Med*, 10(9).
- FRENSING, T. 2015. Defective interfering viruses and their impact on vaccines and viral vectors. *Biotechnol J*, 10(5):681-9.
- FRENSING, T., PFLUGMACHER, A., BACHMANN, M., PESCHEL, B. & REICHL, U. 2014. Impact of defective interfering particles on virus replication and antiviral host response in cell culture-based influenza vaccine production. *Appl Microbiol Biotechnol*, 98(21):8999-9008.
- FUJII, Y., GOTO, H., WATANABE, T., YOSHIDA, T. & KAWAOKA, Y. 2003. Selective incorporation of influenza virus RNA segments into virions. *Proc Natl Acad Sci U S A*, 100(4):2002-7.
- FULVINI, A. A., RAMANUNNINAIR, M., LE, J., POKORNY, B. A., ARROYO, J. M., SILVERMAN, J., DEVIS, R. & BUCHER, D. 2011. Gene constellation of influenza A virus reassortants with high growth phenotype prepared as seed candidates for vaccine production. *PLoS One*, 6(6):e20823.
- FURUICHI, Y. & SHATKIN, A. J. 2000. Viral and cellular mRNA capping: past and prospects. *Adv Virus Res*, 55:135-84.
- FURUYAMA, W., REYNOLDS, P., HADDOCK, E., MEADE-WHITE, K., QUYNH LE, M., KAWAOKA, Y., FELDMANN, H. & MARZI, A. 2020. A single dose of a vesicular stomatitis virus-based influenza vaccine confers rapid protection against H5 viruses from different clades. *NPJ Vaccines*, 5(1):4.
- GALLO-RAMIREZ, L. E., NIKOLAY, A., GENZEL, Y. & REICHL, U. 2015. Bioreactor concepts for cell culture-based viral vaccine production. *Expert Rev Vaccines*, 14(9):1181-95.
- GARCIA-SASTRE, A. 2011. Induction and evasion of type I interferon responses by influenza viruses. *Virus Res*, 162(1-2):12-8.

Bibliography

- GARD, S. & VON MAGNUS, P. 1947. *Studies on interference in experimental influenza: Purification and centrifugation experiments / By Svend Gard ; Preben von Magnus*, Almqvist & Wiksell.
- GEISBERT, T. W., JONES, S., FRITZ, E. A., SHURTLEFF, A. C., GEISBERT, J. B., LIEBSCHER, R., GROLLA, A., STRÖHER, U., FERNANDO, L., DADDARIO, K. M., GUTTIERI, M. C., MOTHÉ, B. R., LARSEN, T., HENSLEY, L. E., JAHRLING, P. B. & FELDMANN, H. 2005. Development of a New Vaccine for the Prevention of Lassa Fever. *PLOS Medicine*, 2(6):e183.
- GENOYER, E. & LOPEZ, C. B. 2019. The Impact of Defective Viruses on Infection and Immunity. *Annu Rev Virol*, 6(1):547-566.
- GENZEL, Y., BEHRENDT, I., RÖDIG, J., RAPP, E., KUEPPERS, C., KOCHANNEK, S., SCHIEDNER, G. & REICHL, U. 2013. CAP, a new human suspension cell line for influenza virus production. *Appl Microbiol Biotechnol*, 97(1):111-22.
- GENZEL, Y., FISCHER, M. & REICHL, U. 2006. Serum-free influenza virus production avoiding washing steps and medium exchange in large-scale microcarrier culture. *Vaccine*, 24(16):3261-3272.
- GENZEL, Y., VOGEL, T., BUCK, J., BEHRENDT, I., RAMIREZ, D. V., SCHIEDNER, G., JORDAN, I. & REICHL, U. 2014. High cell density cultivations by alternating tangential flow (ATF) perfusion for influenza A virus production using suspension cells. *Vaccine*, 32(24):2770-81.
- GEORGE, M., FAROOQ, M., DANG, T., CORTES, B., LIU, J. & MARANGA, L. 2010. Production of cell culture (MDCK) derived live attenuated influenza vaccine (LAIV) in a fully disposable platform process. *Biotechnol Bioeng*, 106(6):906-17.
- GHENDON, Y. Z., MARKUSHIN, S. G., AKOPOVA, II, KOPTIAEVA, I. B., NECHAEVA, E. A., MAZURKOVA, L. A., RADAIEVA, I. F. & KOLOKOLTSEVA, T. D. 2005. Development of cell culture (MDCK) live cold-adapted (CA) attenuated influenza vaccine. *Vaccine*, 23(38):4678-84.
- GIAS, E., NIELSEN, S. U., MORGAN, L. A. F. & TOMS, G. L. 2008. Purification of human respiratory syncytial virus by ultracentrifugation in iodixanol density gradient. *Journal of Virological Methods*, 147(2):328-332.
- GIOVANETTI, M., DE MENDONÇA, M. C. L., FONSECA, V., MARES-GUIA, M. A., FABRI, A., XAVIER, J., DE JESUS, J. G., GRÄF, T., DOS SANTOS RODRIGUES, C. D., DOS SANTOS, C. C., SAMPAIO, S. A., CHALHOUB, F. L. L., DE BRUYCKER NOGUEIRA, F., THEZE, J., ROMANO, A. P. M., RAMOS, D. G., DE ABREU, A. L., OLIVEIRA, W. K., DO CARMO SAID, R. F., DE ALBURQUE, C. F. C., DE OLIVEIRA, T., FERNANDES, C. A., AGUIAR, S. F., CHIEPPE, A., SEQUEIRA, P. C., FARIA, N. R., CUNHA, R. V., ALCANTARA, L. C. J. & DE FILIPPIS, A. M. B. 2019. Yellow Fever Virus Reemergence and Spread in Southeast Brazil, 2016-2019. *J Virol*, 94(1).
- GIRGIS, S., XU, Z., OIKONOMOPOULOS, S., FEDOROVA, A. D., TCHESNOKOV, E. P., GORDON, C. J., SCHMEING, T. M., GÖTTE, M., SONENBERG, N., BARANOV, P. V., RAGOUSSIS, J., HOBMAN, T. C. & PELLETIER, J. 2022. Evolution of naturally arising SARS-CoV-2 defective interfering particles. *Communications Biology*, 5(1):1140.
- GÖBEL, S., JAÉN, K. E., DORN, M., NEUMEYER, V., JORDAN, I., SANDIG, V., REICHL, U., ALTOMONTE, J. & GENZEL, Y. 2023. Process intensification strategies toward cell culture-based high-yield production of a fusogenic oncolytic virus. *Biotechnology and Bioengineering*, 120:2639-2657.
- GÖBEL, S., KORTUM, F., CHAVEZ, K. J., JORDAN, I., SANDIG, V., REICHL, U., ALTOMONTE, J. & GENZEL, Y. 2022. Cell-line screening and process development for a fusogenic oncolytic virus in small-scale suspension cultures. *Applied Microbiology and Biotechnology*, 106(13):4945-4961.
- GÖBEL, S., PELZ, L., SILVA, C. A. T., BRÜHLMANN, B., HILL, C., ALTOMONTE, J., KAMEN, A., REICHL, U. & GENZEL, Y. 2024. Production of recombinant vesicular stomatitis virus-based vectors by tangential flow depth filtration. *Applied Microbiology and Biotechnology*, 108(1):240.
- GOTO, H., MURAMOTO, Y., NODA, T. & KAWAOKA, Y. 2013. The genome-packaging signal of the influenza A virus genome comprises a genome incorporation signal and a genome-bundling signal. *J Virol*, 87(21):11316-22.
- GOUJON, C., MONCORGÉ, O., BAUBY, H., DOYLE, T., WARD, C. C., SCHALLER, T., HUÉ, S., BARCLAY, W. S., SCHULZ, R. & MALIM, M. H. 2013. Human MX2 is an interferon-induced post-entry inhibitor of HIV-1 infection. *Nature*, 502(7472):559-562.
- GRÄNICHER, G., BABAKHANI, M., GÖBEL, S., JORDAN, I., MARICHAL-GALLARDO, P., GENZEL, Y. & REICHL, U. 2021. A high cell density perfusion process for Modified Vaccinia virus Ankara

Bibliography

- production: Process integration with inline DNA digestion and cost analysis. *Biotechnology and Bioengineering*, 118(12):4720-4734.
- GRÄNICHER, G., CORONEL, J., PRALOW, A., MARICHAL-GALLARDO, P., WOLFF, M., RAPP, E., KARLAS, A., SANDIG, V., GENZEL, Y. & REICHL, U. 2019. Efficient influenza A virus production in high cell density using the novel porcine suspension cell line PBG.PK2.1. *Vaccine*, 37(47):7019-7028.
- GRÄNICHER, G., CORONEL, J., TRAMPLER, F., JORDAN, I., GENZEL, Y. & REICHL, U. 2020. Performance of an acoustic settler versus a hollow fiber-based ATF technology for influenza virus production in perfusion. *Appl Microbiol Biotechnol*, 104(11):4877-4888.
- GRANT, A., PONIA, S. S., TRIPATHI, S., BALASUBRAMANIAM, V., MIORIN, L., SOURISSEAU, M., SCHWARZ, M. C., SANCHEZ-SECO, M. P., EVANS, M. J., BEST, S. M. & GARCIA-SASTRE, A. 2016. Zika Virus Targets Human STAT2 to Inhibit Type I Interferon Signaling. *Cell Host Microbe*, 19(6):882-90.
- GREEN, D. S., YOUNG, H. A. & VALENCIA, J. C. 2017. Current prospects of type II interferon γ signaling and autoimmunity. *J Biol Chem*, 292(34):13925-13933.
- GRÖNER, A. & VORLOP, J. 1997. *Animal cells and processes for the replication of influenza viruses*. PCT/IB97/00403.
- GROOT, R. J. D., MOST, R. G. V. D. & SPAAN, W. J. 1992. The fitness of defective interfering murine coronavirus DI-a and its derivatives is decreased by nonsense and frameshift mutations. *Journal of Virology*, 66(10):5898-5905.
- HALE, B. G., ALBRECHT, R. A. & GARCÍA-SASTRE, A. 2010. Innate immune evasion strategies of influenza viruses. *Future Microbiology*, 5(1):23-41.
- HALL, W. W., MARTIN, S. J. & GOULD, E. 1974. Defective interfering particles produced during the replication of measles virus. *Medical Microbiology and Immunology*, 160(2):155-164.
- HALLER, O., ARNHEITER, H., GRESSER, I. & LINDENMANN, J. 1979. Genetically determined, interferon-dependent resistance to influenza virus in mice. *J Exp Med*, 149(3):601-12.
- HALLER, O., ARNHEITER, H., LINDENMANN, J. & GRESSER, I. 1980. Host gene influences sensitivity to interferon action selectively for influenza virus. *Nature*, 283(5748):660-2.
- HALLER, O., GAO, S., VON DER MALSBERG, A., DAUMKE, O. & KOCHS, G. 2010. Dynamamin-like MxA GTPase: structural insights into oligomerization and implications for antiviral activity. *J Biol Chem*, 285(37):28419-24.
- HALLER, O., STERTZ, S. & KOCHS, G. 2007. The Mx GTPase family of interferon-induced antiviral proteins. *Microbes and Infection*, 9(14):1636-1643.
- HAMILTON, B. S., WHITTAKER, G. R. & DANIEL, S. 2012. Influenza virus-mediated membrane fusion: determinants of hemagglutinin fusogenic activity and experimental approaches for assessing virus fusion. *Viruses*, 4(7):1144-68.
- HAMMITT, L. L., DAGAN, R., YUAN, Y., BACA COTS, M., BOSHEVA, M., MADHI, S. A., MULLER, W. J., ZAR, H. J., BROOKS, D., GRENHAM, A., WÄHLBY HAMRÉN, U., MANKAD, V. S., REN, P., TAKAS, T., ABRAM, M. E., LEACH, A., GRIFFIN, M. P. & VILLAFANA, T. 2022. Nirsevimab for Prevention of RSV in Healthy Late-Preterm and Term Infants. *New England Journal of Medicine*, 386(9):837-846.
- HAN, T. & MARASCO, W. A. 2011. Structural basis of influenza virus neutralization. *Annals of the New York Academy of Sciences*, 1217(1):178-190.
- HARVEY, R., NICOLSON, C., JOHNSON, R. E., GUILFOYLE, K. A., MAJOR, D. L., ROBERTSON, J. S. & ENGELHARDT, O. G. 2010. Improved haemagglutinin antigen content in H5N1 candidate vaccine viruses with chimeric haemagglutinin molecules. *Vaccine*, 28(50):8008-8014.
- HAUSCHILD, A., GOGAS, H., TARHINI, A., MIDDLETON, M. R., TESTORI, A., DRÉNO, B. & KIRKWOOD, J. M. 2008. Practical guidelines for the management of interferon-alpha-2b side effects in patients receiving adjuvant treatment for melanoma: expert opinion. *Cancer*, 112(5):982-94.
- HE, L., YANG, L., ZHANG, H. & LUO, Q. 2020. Efficacy and safety of interferon on neonates with respiratory syncytial virus pneumonia. *Exp Ther Med*, 20(6):220.
- HEFTI, H. P., FRESE, M., LANDIS, H., DI PAOLO, C., AGUZZI, A., HALLER, O. & PAVLOVIC, J. 1999. Human MxA protein protects mice lacking a functional alpha/beta interferon system against La crosse virus and other lethal viral infections. *J Virol*, 73(8):6984-91.
- HEGDE, N. R. 2015. Cell culture-based influenza vaccines: A necessary and indispensable investment for the future. *Human Vaccines & Immunotherapeutics*, 11(5):1223-1234.

Bibliography

- HEIN, M. D. 2022. Cell culture-based production of influenza A virus-derived defective interfering particles. Doctoral Thesis, Otto-von-Guericke-Universität.
- HEIN, M. D., ARORA, P., MARICHAL-GALLARDO, P., WINKLER, M., GENZEL, Y., PÖHLMANN, S., SCHUGHART, K., KUPKE, S. Y. & REICHL, U. 2021a. Cell culture-based production and in vivo characterization of purely clonal defective interfering influenza virus particles. *BMC Biol*, 19(1):91.
- HEIN, M. D., CHAWLA, A., CATTANEO, M., KUPKE, S. Y., GENZEL, Y. & REICHL, U. 2021b. Cell culture-based production of defective interfering influenza A virus particles in perfusion mode using an alternating tangential flow filtration system. *Appl Microbiol Biotechnol*, 105(19):7251-7264.
- HEIN, M. D., KAZENMAIER, D., VAN HEUVEL, Y., DOGRA, T., CATTANEO, M., KUPKE, S. Y., STITZ, J., GENZEL, Y. & REICHL, U. 2023. Production of retroviral vectors in continuous high cell density culture. *Appl Microbiol Biotechnol*, 107:5947-5961.
- HEIN, M. D., KOLLMUS, H., MARICHAL-GALLARDO, P., PÜTTKER, S., BENNDORF, D., GENZEL, Y., SCHUGHART, K., KUPKE, S. Y. & REICHL, U. 2021c. OP7, a novel influenza A virus defective interfering particle: production, purification, and animal experiments demonstrating antiviral potential. *Appl Microbiol Biotechnol*, 105(1):129-146.
- HENLE, W. & HENLE, G. 1943. Interference of Inactive Virus with the Propagation of Virus of Influenza. *Science*, 98(2534):87-89.
- HINSON, E. R. & CRESSWELL, P. 2009. The antiviral protein, viperin, localizes to lipid droplets via its N-terminal amphipathic α -helix. *Proceedings of the National Academy of Sciences*, 106(48):20452-20457.
- HO, T.-H., KEW, C., LUI, P.-Y., CHAN, C.-P., SATOH, T., AKIRA, S., JIN, D.-Y. & KOK, K.-H. 2016. PACT- and RIG-I-Dependent Activation of Type I Interferon Production by a Defective Interfering RNA Derived from Measles Virus Vaccine. *Journal of Virology*, 90(3):1557-1568.
- HOFFMANN, E., NEUMANN, G., KAWAOKA, Y., HOBOM, G. & WEBSTER, R. G. 2000. A DNA transfection system for generation of influenza A virus from eight plasmids. *Proc Natl Acad Sci U S A*, 97(11):6108-13.
- HONARMAND EBRAHIMI, K. 2018. A unifying view of the broad-spectrum antiviral activity of RSAD2 (viperin) based on its radical-SAM chemistry. *Metallomics*, 10(4):539-552.
- HONDA, K., TAKAOKA, A. & TANIGUCHI, T. 2006. Type I interferon gene induction by the interferon regulatory factor family of transcription factors. *Immunity*, 25(3):349-60.
- HORISBERGER, M. A., MCMASTER, G. K., ZELLER, H., WATHELET, M. G., DELLIS, J. & CONTENT, J. 1990. Cloning and sequence analyses of cDNAs for interferon- and virus-induced human Mx proteins reveal that they contain putative guanine nucleotide-binding sites: functional study of the corresponding gene promoter. *Journal of Virology*, 64(3):1171-1181.
- HU, X., LI, J., FU, M., ZHAO, X. & WANG, W. 2021. The JAK/STAT signaling pathway: from bench to clinic. *Signal Transduct Target Ther*, 6(1):402.
- HUANG, A. S. & BALTIMORE, D. 1970. Defective Viral Particles and Viral Disease Processes. *Nature*, 226(5243):325-327.
- HUANG, I. C., BAILEY, C. C., WEYER, J. L., RADOSHITZKY, S. R., BECKER, M. M., CHIANG, J. J., BRASS, A. L., AHMED, A. A., CHI, X., DONG, L., LONGOBARDI, L. E., BOLTZ, D., KUHN, J. H., ELLEDGE, S. J., BAVARI, S., DENISON, M. R., CHOE, H. & FARZAN, M. 2011. Distinct patterns of IFITM-mediated restriction of filoviruses, SARS coronavirus, and influenza A virus. *PLoS Pathog*, 7(1):e1001258.
- HUANG, S., CHEN, J., CHEN, Q., WANG, H., YAO, Y., CHEN, J. & CHEN, Z. 2013. A Second CRM1-Dependent Nuclear Export Signal in the Influenza A Virus NS2 Protein Contributes to the Nuclear Export of Viral Ribonucleoproteins. *Journal of Virology*, 87(2):767-778.
- HUO, C., CHENG, J., XIAO, J., CHEN, M., ZOU, S., TIAN, H., WANG, M., SUN, L., HAO, Z. & HU, Y. 2020. Defective Viral Particles Produced in Mast Cells Can Effectively Fight Against Lethal Influenza A Virus. *Front Microbiol*, 11:553274.
- HUTCHINSON, E. C., VON KIRCHBACH, J. C., GOG, J. R. & DIGARD, P. 2010. Genome packaging in influenza A virus. *J Gen Virol*, 91(Pt 2):313-28.
- IMPACT-RSV-STUDY-GROUP 1998. Palivizumab, a humanized respiratory syncytial virus monoclonal antibody, reduces hospitalization from respiratory syncytial virus infection in high-risk infants. The Impact-RSV Study Group. *Pediatrics*, 102(3 Pt 1):531-7.
- ISAACS, A. & LINDENMANN, J. 1957. Virus interference. I. The interferon. *Proc R Soc Lond B Biol Sci*, 147(927):258-67.

Bibliography

- JAKOB, C., PAUL-STANSILAU, R., SCHWEMMLE, M., MARQUET, R. & BOLTE, H. 2022. The influenza A virus genome packaging network — complex, flexible and yet unsolved. *Nucleic Acids Research*, 50(16):9023-9038.
- JAVANIAN, M., BARARY, M., GHEBREHEWET, S., KOPPOLU, V., VASIGALA, V. & EBRAHIMPOUR, S. 2021. A brief review of influenza virus infection. *Journal of Medical Virology*, 93(8):4638-4646.
- JENNINGS, P. A., FINCH, J. T., WINTER, G. & ROBERTSON, J. S. 1983. Does the higher order structure of the influenza virus ribonucleoprotein guide sequence rearrangements in influenza viral RNA? *Cell*, 34(2):619-627.
- JHA, A., JARVIS, H., FRASER, C. & OPENSHAW, P. 2016. Respiratory syncytial virus. In: HUI, D., ROSSI, G. & JOHNSTON, S. (eds.) *SARS, MERS and other viral lung infections*. Sheffield: European Respiratory Society.
- JOHANSSON, M. A., VASCONCELOS, P. F. & STAPLES, J. E. 2014. The whole iceberg: estimating the incidence of yellow fever virus infection from the number of severe cases. *Trans R Soc Trop Med Hyg*, 108(8):482-7.
- JONES, S. M., FELDMANN, H., STRÖHER, U., GEISBERT, J. B., FERNANDO, L., GROLLA, A., KLENK, H. D., SULLIVAN, N. J., VOLCHKOV, V. E., FRITZ, E. A., DADDARIO, K. M., HENSLEY, L. E., JAHRLING, P. B. & GEISBERT, T. W. 2005. Live attenuated recombinant vaccine protects nonhuman primates against Ebola and Marburg viruses. *Nat Med*, 11(7):786-90.
- JULANDER, J. G., ENNIS, J., TURNER, J. & MORREY, J. D. 2011. Treatment of yellow fever virus with an adenovirus-vectored interferon, DEF201, in a hamster model. *Antimicrob Agents Chemother*, 55(5):2067-73.
- JULANDER, J. G., MORREY, J. D., BLATT, L. M., SHAFER, K. & SIDWELL, R. W. 2007. Comparison of the inhibitory effects of interferon alfacon-1 and ribavirin on yellow fever virus infection in a hamster model. *Antiviral Res*, 73(2):140-6.
- KAPIKIAN, A. Z., MITCHELL, R. H., CHANOCK, R. M., SHVEDOFF, R. A. & STEWART, C. E. 1969. An epidemiologic study of altered clinical reactivity to respiratory syncytial (RS) virus infection in children previously vaccinated with an inactivated RS virus vaccine. *American Journal of Epidemiology*, 89(4):405-421.
- KARST, D. J., SERRA, E., VILLIGER, T. K., SOOS, M. & MORBIDELLI, M. 2016. Characterization and comparison of ATF and TFF in stirred bioreactors for continuous mammalian cell culture processes. *Biochemical Engineering Journal*, 110:17-26.
- KIESSLICH, S., KIM, G. N., SHEN, C. F., KANG, C. Y. & KAMEN, A. A. 2021. Bioreactor production of rVSV-based vectors in Vero cell suspension cultures. *Biotechnol Bioeng*, 118(7):2649-2659.
- KILBOURNE, E. D., SMITH, C., BRETT, I., POKORNY, B. A., JOHANSSON, B. & COX, N. 2002. The total influenza vaccine failure of 1947 revisited: Major intrasubtypic antigenic change can explain failure of vaccine in a post-World War II epidemic. *Proceedings of the National Academy of Sciences*, 99(16):10748-10752.
- KIM, H. W., CANCHOLA, J. G., BRANDT, C. D., PYLES, G., CHANOCK, R. M., JENSEN, K. & PARROTT, R. H. 1969. Respiratory syncytial virus disease in infants despite prior administration of antigenic inactivated vaccine. *American Journal of Epidemiology*, 89(4):422-434.
- KIRKWOOD, J. M., BENDER, C., AGARWALA, S., TARHINI, A., SHIPE-SPOTLOE, J., SMELKO, B., DONNELLY, S. & STOVER, L. 2002. Mechanisms and management of toxicities associated with high-dose interferon alfa-2b therapy. *J Clin Oncol*, 20(17):3703-18.
- KIRKWOOD, T. & BANGHAM, C. 1994. Cycles, chaos, and evolution in virus cultures: a model of defective interfering particles. *Proceedings of the National Academy of Sciences*, 91(18):8685-8689.
- KISTNER, O., BARRETT, P. N., MUNDT, W., REITER, M., SCHOBER-BENDIXEN, S. & DORNER, F. 1998. Development of a mammalian cell (Vero) derived candidate influenza virus vaccine. *Vaccine*, 16(9):960-968.
- KLENK, H. D., GARTEN, WOLFGANG & MATROSOVICH, M. 2013. Pathogenesis. *Textbook of Influenza*.
- KODIHALLI, S., JUSTEWICZ, D. M., GUBAREVA, L. V. & WEBSTER, R. G. 1995. Selection of a single amino acid substitution in the hemagglutinin molecule by chicken eggs can render influenza A virus (H3) candidate vaccine ineffective. *Journal of Virology*, 69(8):4888-4897.

Bibliography

- KOSIK, I. & YEWDALL, J. W. 2019. Influenza Hemagglutinin and Neuraminidase: Yin–Yang Proteins Coevolving to Thwart Immunity. *Viruses*, 11(4):346.
- KOTENKO, S. V., RIVERA, A., PARKER, D. & DURBIN, J. E. 2019. Type III IFNs: Beyond antiviral protection. *Semin Immunol*, 43:101303.
- KRABBE, T. & ALTOMONTE, J. 2018. Fusogenic Viruses in Oncolytic Immunotherapy. *Cancers*, 10(7):216.
- KRABBE, T., MAREK, J., GROLL, T., STEIGER, K., SCHMID, R. M., KRACKHARDT, A. M. & ALTOMONTE, J. 2021. Adoptive T Cell Therapy Is Complemented by Oncolytic Virotherapy with Fusogenic VSV-NDV in Combination Treatment of Murine Melanoma. *Cancers*, 13(5):1044.
- KRAMMER, F., SMITH, G. J. D., FOUCHIER, R. A. M., PEIRIS, M., KEDZIERSKA, K., DOHERTY, P. C., PALESE, P., SHAW, M. L., TREANOR, J., WEBSTER, R. G. & GARCIA-SASTRE, A. 2018. Influenza. *Nat Rev Dis Primers*, 4(1):3.
- KRUG, R. M. & FODOR, E. 2013. The virus genome and its replication. *Textbook of Influenza*.
- KUGEL, D., KOCHS, G., OBOJES, K., ROTH, J., KOBINGER, G. P., KOBASA, D., HALLER, O., STAEHEL, P. & VON MESSLING, V. 2009. Intranasal administration of alpha interferon reduces seasonal influenza A virus morbidity in ferrets. *J Virol*, 83(8):3843-51.
- KUM, D. B., MISHRA, N., VRANCKEN, B., THIBAUT, H. J., WILDER-SMITH, A., LEMEY, P., NEYTS, J. & DALLMEIER, K. 2019. Limited evolution of the yellow fever virus 17d in a mouse infection model. *Emerg Microbes Infect*, 8(1):1734-1746.
- KUPKE, S. Y., RIEDEL, D., FRENSING, T., ZMORA, P. & REICHL, U. 2019. A Novel Type of Influenza A Virus-Derived Defective Interfering Particle with Nucleotide Substitutions in Its Genome. *J Virol*, 93(4):e01786-18.
- LAHAM, F. R., MANSBACH, J. M., PIEDRA, P. A., HASEGAWA, K., SULLIVAN, A. F., ESPINOLA, J. A. & CAMARGO, C. A., JR. 2017. Clinical Profiles of Respiratory Syncytial Virus Subtypes A AND B Among Children Hospitalized with Bronchiolitis. *Pediatr Infect Dis J*, 36(8):808-810.
- LAMB, Y. N. 2019. Cell-Based Quadrivalent Inactivated InfluenzaVirus Vaccine (Flucelvax® Tetra/FlucelvaxQuadrivalent®): A Review in the Prevention of Influenza. *Drugs*, 79(12):1337-1348.
- LAMPEJO, T. 2020. Influenza and antiviral resistance: an overview. *European Journal of Clinical Microbiology & Infectious Diseases*, 39(7):1201-1208.
- LASKE, T., HELDT, F. S., HOFFMANN, H., FRENSING, T. & REICHL, U. 2016. Modeling the intracellular replication of influenza A virus in the presence of defective interfering RNAs. *Virus Res*, 213:90-99.
- LAURETTI, F., CHATTOPADHYAY, A., DE OLIVEIRA FRANÇA, R. F., CASTRO-JORGE, L., ROSE, J. & FONSECA, B. A. 2016. Recombinant vesicular stomatitis virus-based dengue-2 vaccine candidate induces humoral response and protects mice against lethal infection. *Hum Vaccin Immunother*, 12(9):2327-33.
- LAZEAR, H. M., SCHOGGINS, J. W. & DIAMOND, M. S. 2019. Shared and Distinct Functions of Type I and Type III Interferons. *Immunity*, 50(4):907-923.
- LE BON, A. & TOUGH, D. F. 2002. Links between innate and adaptive immunity via type I interferon. *Current Opinion in Immunology*, 14(4):432-436.
- LEE, S. & RYU, J. H. 2021. Influenza Viruses: Innate Immunity and mRNA Vaccines. *Front Immunol*, 12:710647.
- LEVI, L. I., REZELJ, V. V., HENRION-LACRITICK, A., ERAZO, D., BOUSSIER, J., VALLET, T., BERNHAUEROVA, V., SUZUKI, Y., CARRAU, L., WEGER-LUCARELLI, J., SALEH, M. C. & VIGNUZZI, M. 2021. Defective viral genomes from chikungunya virus are broad-spectrum antivirals and prevent virus dissemination in mosquitoes. *PLoS Pathog*, 17(2):e1009110.
- LEVIYANG, S. & GRIVA, I. 2018. Investigating Functional Roles for Positive Feedback and Cellular Heterogeneity in the Type I Interferon Response to Viral Infection. *Viruses*, 10(10):517.
- LI, D., LIN, M. H., RAWLE, D. J., JIN, H., WU, Z., WANG, L., LOR, M., HUSSAIN, M., AASKOV, J. & HARRICH, D. 2021. Dengue virus-free defective interfering particles have potent and broad anti-dengue virus activity. *Commun Biol*, 4(1):557.
- LI, L., LOK, S.-M., YU, I.-M., ZHANG, Y., KUHN, R. J., CHEN, J. & ROSSMANN, M. G. 2008. The Flavivirus Precursor Membrane-Envelope Protein Complex: Structure and Maturation. *Science*, 319(5871):1830-1834.

Bibliography

- LIANG, W., TAN, T. J. C., WANG, Y., LV, H., SUN, Y., BRUZZONE, R., MOK, C. K. P. & WU, N. C. 2022. Egg-adaptive mutations of human influenza H3N2 virus are contingent on natural evolution. *PLOS Pathogens*, 18(9):e1010875.
- LIN, M. H., LI, D., TANG, B., LI, L., SUHRBIER, A. & HARRICH, D. 2022. Defective Interfering Particles with Broad-Acting Antiviral Activity for Dengue, Zika, Yellow Fever, Respiratory Syncytial and SARS-CoV-2 Virus Infection. *Microbiol Spectr*, 10(6):e0394922.
- LINDENBACH, B. D., RANDALL, G., BARTENSCHLAGER, R. & RICE, C. M. 2020. Flaviviridae: The viruses and Their Replication. In: HOWLEY, P. M. & KNIPE, D. M. (eds.) *Fields Virology: Emerging Viruses*. 7 ed.: Wolters Kluwer.
- LIU, G., LU, Y., THULASI RAMAN, S. N., XU, F., WU, Q., LI, Z., BROWNLIE, R., LIU, Q. & ZHOU, Y. 2018. Nuclear-resident RIG-I senses viral replication inducing antiviral immunity. *Nature Communications*, 9(1):3199.
- LIU, G., PARK, H.-S., PYO, H.-M., LIU, Q. & ZHOU, Y. 2015. Influenza A Virus Panhandle Structure Is Directly Involved in RIG-I Activation and Interferon Induction. *Journal of Virology*, 89(11):6067-6079.
- LIU, J., SHI, X., SCHWARTZ, R. & KEMBLE, G. 2009. Use of MDCK cells for production of live attenuated influenza vaccine. *Vaccine*, 27(46):6460-6463.
- LO, M. S., BRAZAS, R. M. & HOLTZMAN, M. J. 2005. Respiratory syncytial virus nonstructural proteins NS1 and NS2 mediate inhibition of Stat2 expression and alpha/beta interferon responsiveness. *J Virol*, 79(14):9315-9.
- LOHR, V., RATH, A., GENZEL, Y., JORDAN, I., SANDIG, V. & REICHL, U. 2009. New avian suspension cell lines provide production of influenza virus and MVA in serum-free media: studies on growth, metabolism and virus propagation. *Vaccine*, 27(36):4975-82.
- MALIK, G. & ZHOU, Y. 2020. Innate Immune Sensing of Influenza A Virus. *Viruses*, 12(7).
- MANCEUR, A. P., KIM, H., MISIC, V., ANDREEV, N., DORION-THIBAudeau, J., LANTHIER, S., BERNIER, A., TREMBLAY, S., GELINAS, A. M., BROUSSAU, S., GILBERT, R. & ANSORGE, S. 2017. Scalable Lentiviral Vector Production Using Stable HEK293SF Producer Cell Lines. *Hum Gene Ther Methods*, 28(6):330-339.
- MANINI, I., TROMBETTA, C. M., LAZZERI, G., POZZI, T., ROSSI, S. & MONTOMOLI, E. 2017. Egg-Independent Influenza Vaccines and Vaccine Candidates. *Vaccines (Basel)*, 5(3).
- MANZONI, T. B. & LÓPEZ, C. B. 2018. Defective (interfering) viral genomes re-explored: impact on antiviral immunity and virus persistence. *Future Virology*, 13(07):493-503.
- MARBÁN-CASTRO, E., GONCÉ, A., FUMADÓ, V., ROMERO-ACEVEDO, L. & BARDAJÍ, A. 2021. Zika virus infection in pregnant women and their children: A review. *European Journal of Obstetrics & Gynecology and Reproductive Biology*, 265:162-168.
- MARRIOTT, A. C. & DIMMOCK, N. J. 2010. Defective interfering viruses and their potential as antiviral agents. *Rev Med Virol*, 20(1):51-62.
- MARTIN, K. & HELENIUS, A. 1991. Transport of incoming influenza virus nucleocapsids into the nucleus. *Journal of Virology*, 65(1):232-244.
- MARTINI, M., GAZZANIGA, V., BRAGAZZI, N. L. & BARBERIS, I. 2019. The Spanish Influenza Pandemic: a lesson from history 100 years after 1918. *J Prev Med Hyg*, 60(1):E64-E67.
- MATROSOVICH, M., MATROSOVICH, T., CARR, J., ROBERTS, N. A. & KLENK, H.-D. 2003. Overexpression of the α -2,6-Sialyltransferase in MDCK Cells Increases Influenza Virus Sensitivity to Neuraminidase Inhibitors. *Journal of Virology*, 77(15):8418-8425.
- MATSUMOTO, M. & SEYA, T. 2008. TLR3: Interferon induction by double-stranded RNA including poly(I:C). *Advanced Drug Delivery Reviews*, 60(7):805-812.
- MCLELLAN, J. S., CHEN, M., LEUNG, S., GRAEPEL, K. W., DU, X., YANG, Y., ZHOU, T., BAXA, U., YASUDA, E., BEAUMONT, T., KUMAR, A., MODJARRAD, K., ZHENG, Z., ZHAO, M., XIA, N., KWONG, P. D. & GRAHAM, B. S. 2013. Structure of RSV Fusion Glycoprotein Trimer Bound to a Prefusion-Specific Neutralizing Antibody. *Science*, 340(6136):1113-1117.
- MENDELMAN, P. M., RAPPAPORT, R., CHO, I., BLOCK, S., GRUBER, W., AUGUST, M., DAWSON, D., CORDOVA, J., KEMBLE, G., MAHMOOD, K., PALLADINO, G., LEE, M. S., RAZMPOUR, A., STODDARD, J. & FORREST, B. D. 2004. Live attenuated influenza vaccine induces cross-reactive antibody responses in children against an a/Fujian/411/2002-like H3N2 antigenic variant strain. *Pediatr Infect Dis J*, 23(11):1053-5.
- MENDES, J. P., FERNANDES, B., PINEDA, E., KUDUGUNTI, S., BRANSBY, M., GANTIER, R., PEIXOTO, C., ALVES, P. M., ROLDAO, A. & SILVA, R. J. S. 2022. AAV process intensification by perfusion bioreaction and integrated clarification. *Front Bioeng Biotechnol*, 10:1020174.

Bibliography

- MENDES, M. & RUSSELL, A. B. 2021. Library-based analysis reveals segment and length dependent characteristics of defective influenza genomes. *PLoS Pathog*, 17(12):e1010125.
- MERCADO-LÓPEZ, X., COTTER, C. R., KIM, W.-K., SUN, Y., MUÑOZ, L., TAPIA, K. & LÓPEZ, C. B. 2013. Highly immunostimulatory RNA derived from a Sendai virus defective viral genome. *Vaccine*, 31(48):5713-5721.
- MEYERS, G., THIEL, H. J. & RÜMENAPF, T. 1996. Classical swine fever virus: recovery of infectious viruses from cDNA constructs and generation of recombinant cytopathogenic defective interfering particles. *J Virol*, 70(3):1588-95.
- MICHAEL LAVIGNE, G., RUSSELL, H., SHERRY, B. & KE, R. 2021. Autocrine and paracrine interferon signalling as 'ring vaccination' and 'contact tracing' strategies to suppress virus infection in a host. *Proc Biol Sci*, 288(1945):20203002.
- MICHALSKA, A., BLASZCZYK, K., WESOLY, J. & BLUYSSSEN, H. A. R. 2018. A Positive Feedback Amplifier Circuit That Regulates Interferon (IFN)-Stimulated Gene Expression and Controls Type I and Type II IFN Responses. *Frontiers in Immunology*, 9.
- MILIAN, E. & KAMEN, A. A. 2015. Current and emerging cell culture manufacturing technologies for influenza vaccines. *Biomed Res Int*, 2015:504831.
- MONATH, T. P. 2008. Treatment of yellow fever. *Antiviral Res*, 78(1):116-24.
- MOORE, E. C., BARBER, J. & TRIPP, R. A. 2008. Respiratory syncytial virus (RSV) attachment and nonstructural proteins modify the type I interferon response associated with suppressor of cytokine signaling (SOCS) proteins and IFN-stimulated gene-15 (ISG15). *Virology*, 5:116.
- MORENS, D. M., TAUBENBERGER, J. K. & FAUCI, A. S. 2009. The persistent legacy of the 1918 influenza virus. *N Engl J Med*, 361(3):225-9.
- MUDHASANI, R., TRAN, J. P., RETTERER, C., RADOSHITZKY, S. R., KOTA, K. P., ALTAMURA, L. A., SMITH, J. M., PACKARD, B. Z., KUHN, J. H., COSTANTINO, J., GARRISON, A. R., SCHMALJOHN, C. S., HUANG, I.-C., FARZAN, M. & BAVARI, S. 2013. IFITM-2 and IFITM-3 but Not IFITM-1 Restrict Rift Valley Fever Virus. *Journal of Virology*, 87(15):8451-8464.
- MURPHY, B. R., PRINCE, G. A., WALSH, E. E., KIM, H. W., PARROTT, R. H., HEMMING, V. G., RODRIGUEZ, W. J. & CHANOCK, R. M. 1986. Dissociation between serum neutralizing and glycoprotein antibody responses of infants and children who received inactivated respiratory syncytial virus vaccine. *Journal of clinical microbiology*, 24(2):197-202.
- MUSSO, D., BOSSIN, H., MALLET, H. P., BESNARD, M., BROULT, J., BAUDOUIN, L., LEVI, J. E., SABINO, E. C., GHAWCHE, F., LANTERI, M. C. & BAUD, D. 2018. Zika virus in French Polynesia 2013–14: anatomy of a completed outbreak. *The Lancet Infectious Diseases*, 18(5):e172-e182.
- NAIR, H., NOKES, D. J., GESSNER, B. D., DHERANI, M., MADHI, S. A., SINGLETON, R. J., O'BRIEN, K. L., ROCA, A., WRIGHT, P. F., BRUCE, N., CHANDRAN, A., THEODORATOU, E., SUTANTO, A., SEDYANINGSIH, E. R., NGAMA, M., MUNYWOKI, P. K., KARTASASMITA, C., SIMÕES, E. A., RUDAN, I., WEBER, M. W. & CAMPBELL, H. 2010. Global burden of acute lower respiratory infections due to respiratory syncytial virus in young children: a systematic review and meta-analysis. *Lancet*, 375(9725):1545-55.
- NARUSE, T., FUKUDA, T., TANABE, T., ICHIKAWA, M., ODA, Y., TOCHIHARA, S., KIMACHI, K., KINO, Y. & UEDA, K. 2015. A clinical phase I study of an EB66 cell-derived H5N1 pandemic vaccine adjuvanted with AS03. *Vaccine*, 33(45):6078-6084.
- NAYAK, D., SHIVAKOTI, S., BALOGUN, R. A., LEE, G. & ZHOU, Z. H. 2013. Structure, disassembly, assembly, and budding of influenza viruses. *Textbook of Influenza*.
- NAYAK, D. P., BALOGUN, R. A., YAMADA, H., ZHOU, Z. H. & BARMAN, S. 2009. Influenza virus morphogenesis and budding. *Virus Res*, 143(2):147-61.
- NAYAK, D. P., CHAMBERS, T. M. & AKKINA, R. K. 1985. Defective-Interfering (DI) RNAs of Influenza Viruses: Origin, Structure, Expression, and Interference. In: COOPER, M., EISEN, H., GOEBEL, W., HOFSCHEIDER, P. H., KOPROWSKI, H., MELCHERS, F., OLDSTONE, M., ROTT, R., SCHWEIGER, H. G., VOGT, P. K. & WILSON, I. (eds.) *Current Topics in Microbiology and Immunology*. Berlin, Heidelberg: Springer Berlin Heidelberg.
- NAYAK, D. P. & SIVASUBRAMANIAN, N. 1983. The Structure of Influenza Virus Defective Interfering (DI) RNAs and Their Progenitor Genes. In: PALESE, P. & KINGSBURY, D. W. (eds.) *Genetics of Influenza Viruses*. Vienna: Springer Vienna.
- NAYAK, D. P., SIVASUBRAMANIAN, N., DAVIS, A. R., CORTINI, R. & SUNG, J. 1982. Complete sequence analyses show that two defective interfering influenza viral RNAs contain a single internal deletion of a polymerase gene. *Proc Natl Acad Sci U S A*, 79(7):2216-20.

Bibliography

- NEUMANN, G., WATANABE, T. & KAWAOKA, Y. 2000. Plasmid-driven formation of influenza virus-like particles. *J Virol*, 74(1):547-51.
- NGUYEN, H. A., COOKE, G. S., DAY, J. N., FLOWER, B., PHUONG, L. T., HUNG, T. M., DUNG, N. T., KHOA, D. B., HUNG, L. M., KESTELYN, E., THWAITES, G. E., CHAU, N. V. V. & TURNER, H. C. 2019. The direct-medical costs associated with interferon-based treatment for Hepatitis C in Vietnam. *Wellcome Open Res*, 4:129.
- NIKOLAY, A., DE GROOTH, J., GENZEL, Y., WOOD, J. A. & REICHL, U. 2020. Virus harvesting in perfusion culture: Choosing the right type of hollow fiber membrane. *Biotechnology and Bioengineering*, 117(10):3040-3052.
- NIKOLAY, A., LEON, A., SCHWAMBORN, K., GENZEL, Y. & REICHL, U. 2018. Process intensification of EB66(R) cell cultivations leads to high-yield yellow fever and Zika virus production. *Appl Microbiol Biotechnol*, 102(20):8725-8737.
- NODA, T. 2021. Selective Genome Packaging Mechanisms of Influenza A Viruses. *Cold Spring Harb Perspect Med*, 11(7).
- NODA, T. & KAWAOKA, Y. 2010. Structure of influenza virus ribonucleoprotein complexes and their packaging into virions. *Rev Med Virol*, 20(6):380-91.
- NODA, T., SUGITA, Y., AOYAMA, K., HIRASE, A., KAWAKAMI, E., MIYAZAWA, A., SAGARA, H. & KAWAOKA, Y. 2012. Three-dimensional analysis of ribonucleoprotein complexes in influenza A virus. *Nature Communications*, 3(1):639.
- O'HANLON, R. & SHAW, M. L. 2019. Baloxavir marboxil: the new influenza drug on the market. *Curr Opin Virol*, 35:14-18.
- ODAGIRI, T. & TASHIRO, M. 1997. Segment-specific noncoding sequences of the influenza virus genome RNA are involved in the specific competition between defective interfering RNA and its progenitor RNA segment at the virion assembly step. *J Virol*, 71(3):2138-45.
- OH, D. Y., BARR, I. G., MOSSE, J. A. & LAURIE, K. L. 2008. MDCK-SIAT1 cells show improved isolation rates for recent human influenza viruses compared to conventional MDCK cells. *J Clin Microbiol*, 46(7):2189-94.
- OPENSHAW, P. J., CULLEY, F. J. & OLSZEWSKA, W. 2001. Immunopathogenesis of vaccine-enhanced RSV disease. *Vaccine*, 20 Suppl 1:S27-31.
- OSADA, N., KOHARA, A., YAMAJI, T., HIRAYAMA, N., KASAI, F., SEKIZUKA, T., KURODA, M. & HANADA, K. 2014. The genome landscape of the african green monkey kidney-derived vero cell line. *DNA Res*, 21(6):673-83.
- OWEN, K. L., BROCKWELL, N. K. & PARKER, B. S. 2019. JAK-STAT Signaling: A Double-Edged Sword of Immune Regulation and Cancer Progression. *Cancers*, 11(12):2002.
- PATERSON, D. & FODOR, E. 2012. Emerging Roles for the Influenza A Virus Nuclear Export Protein (NEP). *PLOS Pathogens*, 8(12):e1003019.
- PAU, M. G., OPHORST, C., KOLDIJK, M. H., SCHOUTEN, G., MEHTALI, M. & UYTDEHAAG, F. 2001. The human cell line PER.C6 provides a new manufacturing system for the production of influenza vaccines. *Vaccine*, 19(17-19):2716-21.
- PAULES, C. & SUBBARAO, K. 2017. Influenza. *The Lancet*, 390(10095):697-708.
- PAVLOVIC, J., HALLER, O. & STAEHEL, P. 1992. Human and mouse Mx proteins inhibit different steps of the influenza virus multiplication cycle. *Journal of virology*, 66(4):2564-2569.
- PELZ, L., DOGRA, T., MARICHAL-GALLARDO, P., HEIN, M. D., HEMISSI, G., KUPKE, S. Y., GENZEL, Y. & REICHL, U. 2024. Production of antiviral "OP7 chimera" defective interfering particles free of infectious virus. *Appl Microbiol Biotechnol*, 108(1):97.
- PELZ, L., GÖBEL, S., JAEN, K., REICHL, U. & GENZEL, Y. 2022. Upstream processing for viral vaccines-General aspects. In: KAMEN, A. & CERVERA, L. (eds.) *Bioprocessing of Viral Vaccines*. Boca Raton: CRC Press.
- PELZ, L., PIAGNANI, E., MARSALL, P., WYNSERSKI, N., HEIN, M. D., MARICHAL-GALLARDO, P., KUPKE, S. Y. & REICHL, U. 2023. Broad-Spectrum Antiviral Activity of Influenza A Defective Interfering Particles against Respiratory Syncytial, Yellow Fever, and Zika Virus Replication In Vitro. *Viruses*, 15(9):1872.
- PELZ, L., RÜDIGER, D., DOGRA, T., ALNAJI, F. G., GENZEL, Y., BROOKE, C. B., KUPKE, S. Y. & REICHL, U. 2021. Semi-continuous Propagation of Influenza A Virus and Its Defective Interfering Particles: Analyzing the Dynamic Competition To Select Candidates for Antiviral Therapy. *Journal of Virology*, 95(24):e01174-21.

Bibliography

- PENN, R., TREGONING, J. S., FLIGHT, K. E., BAILLON, L., FRISE, R., GOLDHILL, D. H., JOHANSSON, C. & BARCLAY, W. 2022. Levels of Influenza A Virus Defective Viral Genomes Determine Pathogenesis in the BALB/c Mouse Model. *Journal of Virology*, 96(21):e01178-22.
- PÉREZ RUBIO, A. & EIROS, J. M. 2018. Cell culture-derived flu vaccine: Present and future. *Human Vaccines & Immunotherapeutics*, 14(8):1874-1882.
- PETIOT, E., JACOB, D., LANTHIER, S., LOHR, V., ANSORGE, S. & KAMEN, A. A. 2011. Metabolic and Kinetic analyses of influenza production in perfusion HEK293 cell culture. *BMC Biotechnology*, 11(1):84.
- PIERSON, T. C. & DIAMOND, M. S. 2020. The continued threat of emerging flaviviruses. *Nature Microbiology*, 5(6):796-812.
- PIERSON, T. C., LAZEAR, H. M. & DIAMOND, M. S. 2020. Flaviviruses: Dengue, Zika, West Nile, Yellow Fever and Other Flaviviruses. In: HOWLEY, P. M. & KNIPE, D. M. (eds.) *Fields Virology: Emerging Viruses*. 7 ed.: Wolters Kluwer.
- PINTO, R. M., LYCETT, S., GAUNT, E. & DIGARD, P. 2021. Accessory Gene Products of Influenza A Virus. *Cold Spring Harb Perspect Med*, 11(12).
- PIRES DE MELLO, C. P., DRUSANO, G. L., RODRIQUEZ, J. L., KAUSHIK, A. & BROWN, A. N. 2018. Antiviral Effects of Clinically-Relevant Interferon-alpha and Ribavirin Regimens against Dengue Virus in the Hollow Fiber Infection Model (HFIM). *Viruses*, 10(6).
- PLATANIAS, L. C. 2005. Mechanisms of type-I- and type-II-interferon-mediated signalling. *Nature Reviews Immunology*, 5(5):375-386.
- PLEVKA, P., BATTISTI, A. J., JUNJHON, J., WINKLER, D. C., HOLDAWAY, H. A., KEELAPANG, P., SITTISOMBUT, N., KUHN, R. J., STEVEN, A. C. & ROSSMANN, M. G. 2011. Maturation of flaviviruses starts from one or more icosahedrally independent nucleation centres. *EMBO Rep*, 12(6):602-6.
- PLOTCH, S. J., BOULOY, M., ULMANEN, I. & KRUG, R. M. 1981. A unique cap(m7GpppXm)-dependent influenza virion endonuclease cleaves capped RNAs to generate the primers that initiate viral RNA transcription. *Cell*, 23(3):847-858.
- POLACK, F. P., TENG, M. N., COLLINS, P. L., PRINCE, G. A., EXNER, M., REGELE, H., LIRMAN, D. D., RABOLD, R., HOFFMAN, S. J., KARP, C. L., KLEEBERGER, S. R., WILLS-KARP, M. & KARRON, R. A. 2002. A role for immune complexes in enhanced respiratory syncytial virus disease. *J Exp Med*, 196(6):859-65.
- POON, L. L. M., PRITLOVE, D. C., FODOR, E. & BROWNLIE, G. G. 1999. Direct Evidence that the Poly(A) Tail of Influenza A Virus mRNA Is Synthesized by Reiterative Copying of a U Track in the Virion RNA Template. *Journal of Virology*, 73(4):3473-3476.
- PRIMORAC, D., VRDOLJAK, K., BRLEK, P., PAVELIĆ, E., MOLNAR, V., MATIŠIĆ, V., ERCEG IVKOŠIĆ, I. & PARČINA, M. 2022. Adaptive Immune Responses and Immunity to SARS-CoV-2. *Frontiers in Immunology*, 13.
- QUINLIVAN, M., ZAMARIN, D., GARCÍA-SASTRE, A., CULLINANE, A., CHAMBERS, T. & PALESE, P. 2005. Attenuation of Equine Influenza Viruses through Truncations of the NS1 Protein. *Journal of Virology*, 79(13):8431-8439.
- RABINOWITZ, S. G. & HUPRIKAR, J. 1979. The influence of defective-interfering particles of the PR-8 strain of influenza A virus on the pathogenesis of pulmonary infection in mice. *J Infect Dis*, 140(3):305-15.
- RAJARAM, S., BOIKOS, C., GELONE, D. K. & GANDHI, A. 2020. Influenza vaccines: the potential benefits of cell-culture isolation and manufacturing. *Ther Adv Vaccines Immunother*, 8:2515135520908121.
- RAND, U., KUPKE, S. Y., SHKARLET, H., HEIN, M. D., HIRSCH, T., MARICHAL-GALLARDO, P., CICIN-SAIN, L., REICHL, U. & BRUDER, D. 2021. Antiviral Activity of Influenza A Virus Defective Interfering Particles against SARS-CoV-2 Replication In Vitro through Stimulation of Innate Immunity. *Cells*, 10(7).
- RANUM, J. N., LEDWITH, M. P., ALNAJI, F. G., DIEFENBACHER, M., ORTON, R., SLOAN, E., GÜERECA, M., FELTMAN, E. M., SMOLLETT, K., DA SILVA FILIPE, A., CONLEY, M., RUSSELL, A. B., BROOKE, C. B., HUTCHINSON, E. & MEHLE, A. 2024. Cryptic proteins translated from deletion-containing viral genomes dramatically expand the influenza virus proteome. *Nucleic Acids Res*, Feb 26:gkae133.
- REHWINKEL, J., TAN, C. P., GOUBAU, D., SCHULZ, O., PICHLMAIR, A., BIER, K., ROBB, N., VREEDE, F., BARCLAY, W., FODOR, E. & REIS E SOUSA, C. 2010. RIG-I Detects Viral Genomic RNA during Negative-Strand RNA Virus Infection. *Cell*, 140(3):397-408.

Bibliography

- REICH, S., GUILLIGAY, D., PFLUG, A., MALET, H., BERGER, I., CRÉPIN, T., HART, D., LUNARDI, T., NANAŌ, M., RUIGROK, R. W. H. & CUSACK, S. 2014. Structural insight into cap-snatching and RNA synthesis by influenza polymerase. *Nature*, 516(7531):361-366.
- REZELJ, V. V., CARRAU, L., MERWAISS, F., LEVI, L. I., ERAZO, D., TRAN, Q. D., HENRION-LACRITICK, A., GAUSSON, V., SUZUKI, Y., SHENGJULER, D., MEYER, B., VALLET, T., WEGER-LUCARELLI, J., BERNHAUEROVA, V., TITIEVSKY, A., SHAROV, V., PIETROPAOLI, S., DIAZ-SALINAS, M. A., LEGROS, V., PARDIGON, N., BARBA-SPAETH, G., BRODSKY, L., SALEH, M. C. & VIGNUZZI, M. 2021. Defective viral genomes as therapeutic interfering particles against flavivirus infection in mammalian and mosquito hosts. *Nat Commun*, 12(1):2290.
- ROBERTSON, J. S., NICOLSON, C., NEWMAN, R., MAJOR, D., DUNLEAVY, U. & WOOD, J. M. 1992. High growth reassortant influenza vaccine viruses: New approaches to their control. *Biologicals*, 20(3):213-220.
- ROBERTSON, J. S., SCHUBERT, M. & LAZZARINI, R. A. 1981. Polyadenylation sites for influenza virus mRNA. *Journal of Virology*, 38(1):157-163.
- ROGOVIK, A. L., CARLETON, B., SOLIMANO, A. & GOLDMAN, R. D. 2010. Palivizumab for the prevention of respiratory syncytial virus infection. *Can Fam Physician*, 56(8):769-72.
- ROSSMAN, J. S. & LAMB, R. A. 2011. Influenza virus assembly and budding. *Virology*, 411(2):229-36.
- ROUX, L. & WALDVOGEL, F. A. 1981. Establishment of Sendai virus persistent infection: Biochemical analysis of the early phase of a standard plus defective interfering virus infection of BHK cells. *Virology*, 112(2):400-410.
- RÜDIGER, D., PELZ, L., HEIN, M. D., KUPKE, S. Y. & REICHL, U. 2021. Multiscale model of defective interfering particle replication for influenza A virus infection in animal cell culture. *PLoS Comput Biol*, 17(9):e1009357.
- SAIRA, K., LIN, X., DEPASSE, J. V., HALPIN, R., TWADDLE, A., STOCKWELL, T., ANGUS, B., COZZI-LEPRI, A., DELFINO, M., DUGAN, V., DWYER, D. E., FREIBERG, M., HORBAN, A., LOSSO, M., LYNFIELD, R., WENTWORTH, D. N., HOLMES, E. C., DAVEY, R., WENTWORTH, D. E., GHEDIN, E., GROUP, I. F. S. & GROUP, I. F. S. 2013. Sequence analysis of in vivo defective interfering-like RNA of influenza A H1N1 pandemic virus. *J Virol*, 87(14):8064-74.
- SAMJI, T. 2009. Influenza A: understanding the viral life cycle. *Yale J Biol Med*, 82(4):153-9.
- ŠANTAK, M., MARKUŠIĆ, M., BALIJA, M. L., KOPAČ, S. K., JUG, R., ÖRVELL, C., TOMAC, J. & FORČIĆ, D. 2015. Accumulation of defective interfering viral particles in only a few passages in Vero cells attenuates mumps virus neurovirulence. *Microbes Infect*, 17(3):228-36.
- SARKER, A., GU, Z., MAO, L., GE, Y., HOU, D., FANG, J., WEI, Z. & WANG, Z. 2022. Influenza-existing drugs and treatment prospects. *European Journal of Medicinal Chemistry*, 232:114189.
- SCHMALJOHN, C. & BLAIR, C. D. 1977. Persistent infection of cultured mammalian cells by Japanese encephalitis virus. *Journal of Virology*, 24(2):580-589.
- SCHMID, S., MORDSTEIN, M., KOCHS, G., GARCÍA-SASTRE, A. & TENOEVER, B. R. 2010. Transcription Factor Redundancy Ensures Induction of the Antiviral State. *Journal of Biological Chemistry*, 285(53):42013-42022.
- SCHNEIDER, M., MARISON, I. W. & VON STOCKAR, U. 1996. The importance of ammonia in mammalian cell culture. *J Biotechnol*, 46(3):161-85.
- SCHNEIDER, W. M., CHEVILLOTTE, M. D. & RICE, C. M. 2014. Interferon-stimulated genes: a complex web of host defenses. *Annu Rev Immunol*, 32:513-45.
- SCHOENBORN, J. R. & WILSON, C. B. 2007. Regulation of Interferon- γ During Innate and Adaptive Immune Responses. *Advances in Immunology*. Academic Press.
- SCHOGGINS, J. W. 2019. Interferon-Stimulated Genes: What Do They All Do? *Annual Review of Virology*, 6(1):567-584.
- SCHWARZ, H., ZHANG, Y., ZHAN, C., MALM, M., FIELD, R., TURNER, R., SELICK, C., VARLEY, P., ROCKBERG, J. & CHOTTEAU, V. 2020. Small-scale bioreactor supports high density HEK293 cell perfusion culture for the production of recombinant Erythropoietin. *J Biotechnol*, 309:44-52.
- SCOTT, P. D., MENG, B., MARRIOTT, A. C., EASTON, A. J. & DIMMOCK, N. J. 2011. Defective interfering influenza A virus protects in vivo against disease caused by a heterologous influenza B virus. *J Gen Virol*, 92(Pt 9):2122-2132.

Bibliography

- SEITZ, C., FRENSING, T., HOPER, D., KOCHS, G. & REICHL, U. 2010. High yields of influenza A virus in Madin-Darby canine kidney cells are promoted by an insufficient interferon-induced antiviral state. *J Gen Virol*, 91(Pt 7):1754-63.
- SEITZ, C., ISKEN, B., HEYNISCH, B., RETTKOWSKI, M., FRENSING, T. & REICHL, U. 2012. Trypsin promotes efficient influenza vaccine production in MDCK cells by interfering with the antiviral host response. *Appl Microbiol Biotechnol*, 93(2):601-11.
- SEO, J. Y., YANEVA, R. & CRESSWELL, P. 2011. Viperin: a multifunctional, interferon-inducible protein that regulates virus replication. *Cell Host Microbe*, 10(6):534-9.
- SEQIRUS. 2023. *Australian product information - Flucelvax® Quad (Influenza virus haemagglutinin)* [Online]. Available: <https://labeling.seqirus.com/PI/AU/Flucelvax/EN/Flucelvax-Product-Information.pdf> [Accessed December 28 2023].
- SILVA, C. A. T., KAMEN, A. A. & HENRY, O. 2023. Intensified Influenza Virus Production in Suspension HEK293SF Cell Cultures Operated in Fed-Batch or Perfusion with Continuous Harvest. *Vaccines*, 11(12):1819.
- SKEHEL, J. J. & WILEY, D. C. 2000. Receptor Binding and Membrane Fusion in Virus Entry: The Influenza Hemagglutinin. *Annual Review of Biochemistry*, 69(1):531-569.
- SMITH, S. E., BUSSE, D. C., BINTER, S., WESTON, S., SORIA, C. D., LAKSONO, B. M., CLARE, S., NIEUWKOOP, S. V., HOOGEN, B. G. V. D., CLEMENT, M., MARSDEN, M., HUMPHREYS, I. R., MARSH, M., SWART, R. L. D., WASH, R. S., TREGONING, J. S. & KELLAM, P. 2019. Interferon-Induced Transmembrane Protein 1 Restricts Replication of Viruses That Enter Cells via the Plasma Membrane. *Journal of Virology*, 93(6):10.1128/jvi.02003-18.
- SMITHER, S. J., GARCIA-DORIVAL, I., EASTAUGH, L., FINDLAY, J. S., O'BRIEN, L. M., CARRUTHERS, J., WILLIAMSON, E. D., MOLINA-PARÍS, C., HISCOX, J. A. & LAWS, T. R. 2020. An Investigation of the Effect of Transfected Defective, Ebola Virus Genomes on Ebola Replication. *Frontiers in Cellular and Infection Microbiology*, 10.
- SOLÓRZANO, A., WEBBY, R. J., LAGER, K. M., JANKE, B. H., GARCÍA-SASTRE, A. & RICHT, J. A. 2005. Mutations in the NS1 Protein of Swine Influenza Virus Impair Anti-Interferon Activity and Confer Attenuation in Pigs. *Journal of Virology*, 79(12):7535-7543.
- SPANN, K. M., TRAN, K. C., CHI, B., RABIN, R. L. & COLLINS, P. L. 2004. Suppression of the induction of alpha, beta, and lambda interferons by the NS1 and NS2 proteins of human respiratory syncytial virus in human epithelial cells and macrophages [corrected]. *J Virol*, 78(8):4363-9.
- SPARROW, E., WOOD, J. G., CHADWICK, C., NEWALL, A. T., TORVALDSEN, S., MOEN, A. & TORELLI, G. 2021. Global production capacity of seasonal and pandemic influenza vaccines in 2019. *Vaccine*, 39(3):512-520.
- STAEHELI, P., HALLER, O., BOLL, W., LINDENMANN, J. & WEISSMANN, C. 1986. Mx protein: constitutive expression in 3T3 cells transformed with cloned Mx cDNA confers selective resistance to influenza virus. *Cell*, 44(1):147-58.
- STANIFER, M. L., PERVOLARAKI, K. & BOULANT, S. 2019. Differential Regulation of Type I and Type III Interferon Signaling. *Int J Mol Sci*, 20(6).
- STAUFFER THOMPSON, K. A., REMPALA, G. A. & YIN, J. 2009. Multiple-hit inhibition of infection by defective interfering particles. *J Gen Virol*, 90(Pt 4):888-899.
- STEWART, A. J. & DEVLIN, P. M. 2006. The history of the smallpox vaccine. *Journal of Infection*, 52(5):329-334.
- STRAHLE, L., GARCIN, D. & KOLAKOFSKY, D. 2006. Sendai virus defective-interfering genomes and the activation of interferon-beta. *Virology*, 351(1):101-111.
- SUBBARAO, K. 2021. Live Attenuated Cold-Adapted Influenza Vaccines. *Cold Spring Harb Perspect Med*, 11(9).
- SUBBARAO, K., CHEN, H., SWAYNE, D., MINGAY, L., FODOR, E., BROWNLIE, G., XU, X., LU, X., KATZ, J., COX, N. & MATSUOKA, Y. 2003. Evaluation of a genetically modified reassortant H5N1 influenza A virus vaccine candidate generated by plasmid-based reverse genetics. *Virology*, 305(1):192-200.
- SUDER, E., FURUYAMA, W., FELDMANN, H., MARZI, A. & DE WIT, E. 2018. The vesicular stomatitis virus-based Ebola virus vaccine: From concept to clinical trials. *Hum Vaccin Immunother*, 14(9):2107-2113.
- SUN, Y., JAIN, D., KOZIOL-WHITE, C. J., GENOYER, E., GILBERT, M., TAPIA, K., PANETTIERI, R. A., JR., HODINKA, R. L. & LOPEZ, C. B. 2015. Immunostimulatory Defective Viral Genomes from Respiratory Syncytial Virus Promote a Strong Innate Antiviral Response during Infection in Mice and Humans. *PLoS Pathog*, 11(9):e1005122.

Bibliography

- SUN, Y. & LOPEZ, C. B. 2016. Preparation of Respiratory Syncytial Virus with High or Low Content of Defective Viral Particles and Their Purification from Viral Stocks. *Bio Protoc*, 6(10).
- SUNG, R. Y., YIN, J., OPPENHEIMER, S. J., TAM, J. S. & LAU, J. 1993. Treatment of respiratory syncytial virus infection with recombinant interferon alfa-2a. *Archives of Disease in Childhood*, 69(4):440-442.
- SZRETTER, K. J., GANGAPPA, S., BELSER, J. A., ZENG, H., CHEN, H., MATSUOKA, Y., SAMBHARA, S., SWAYNE, D. E., TUMPEY, T. M. & KATZ, J. M. 2009. Early Control of H5N1 Influenza Virus Replication by the Type I Interferon Response in Mice. *Journal of Virology*, 83(11):5825-5834.
- TAKADA, K., KAWAKAMI, C., FAN, S., CHIBA, S., ZHONG, G., GU, C., SHIMIZU, K., TAKASAKI, S., SAKAI-TAGAWA, Y., LOPES, T. J. S., DUTTA, J., KHAN, Z., KRITI, D., VAN BAKEL, H., YAMADA, S., WATANABE, T., IMAI, M. & KAWAOKA, Y. 2019. A humanized MDCK cell line for the efficient isolation and propagation of human influenza viruses. *Nature Microbiology*, 4(8):1268-1273.
- TANI, H., MORIKAWA, S. & MATSUURA, Y. 2011. Development and Applications of VSV Vectors Based on Cell Tropism. *Front Microbiol*, 2:272.
- TANNER, E. J., JUNG, S.-Y., GLAZIER, J., THOMPSON, C., ZHOU, Y., MARTIN, B., SON, H.-I., RILEY, J. L. & WEINBERGER, L. S. 2019. Discovery and Engineering of a Therapeutic Interfering Particle (TIP): a combination self-renewing antiviral. *bioRxiv*:820456.
- TAO, Y., SHIH, J., SINACORE, M., RYLL, T. & YUSUF-MAKAGIANSAR, H. 2011. Development and implementation of a perfusion-based high cell density cell banking process. *Biotechnology Progress*, 27(3):824-829.
- TAPIA, F., LASKE, T., WASIK, M. A., RAMMHOLD, M., GENZEL, Y. & REICHL, U. 2019. Production of Defective Interfering Particles of Influenza A Virus in Parallel Continuous Cultures at Two Residence Times-Insights From qPCR Measurements and Viral Dynamics Modeling. *Front Bioeng Biotechnol*, 7:275.
- TAPIA, K., KIM, W.-K., SUN, Y., MERCADO-LÓPEZ, X., DUNAY, E., WISE, M., ADU, M. & LÓPEZ, C. B. 2013. Defective Viral Genomes Arising In Vivo Provide Critical Danger Signals for the Triggering of Lung Antiviral Immunity. *PLOS Pathogens*, 9(10):e1003703.
- TE VELTHUIS, A. J. W. & FODOR, E. 2016. Influenza virus RNA polymerase: insights into the mechanisms of viral RNA synthesis. *Nature Reviews Microbiology*, 14(8):479-493.
- THEILER, M. & SMITH, H. H. 1937. The effect of prolonged cultivation in vitro upon the pathogenicity of yellow fever virus. *Journal of Experimental Medicine*, 65(6):767-786.
- THIMME, R., FRESE, M., KOCHS, G. & HALLER, O. 1995. Mx1 but Not MxA Confers Resistance against Tick-Borne Dohi Virus in Mice. *Virology*, 211(1):296-301.
- THOMSON, M., WHITE, C. L. & DIMMOCK, N. J. 1998. The Genomic Sequence of Defective Interfering Semliki Forest Virus (SFV) Determines Its Ability to Be Replicated in Mouse Brain and to Protect against a Lethal SFV Infection in Vivo. *Virology*, 241(2):215-223.
- TILSTON-LUNEL, N. L., WELCH, S. R., NAMBULLI, S., VRIES, R. D. D., HO, G. W., WENTWORTH, D. E., SHABMAN, R., NICHOL, S. T., SPIROPOULOU, C. F., SWART, R. L. D., RENNICK, L. J. & DUPREX, W. P. 2021. Sustained Replication of Synthetic Canine Distemper Virus Defective Genomes In Vitro and In Vivo. *mSphere*, 6(5):e00537-21.
- TONA, R. M., SHAH, R., MIDDAUGH, K., STEVE, J., MARQUES, J., ROSZELL, B. R. & JUNG, C. 2023. Process intensification for lentiviral vector manufacturing using tangential flow depth filtration. *Mol Ther Methods Clin Dev*, 29:93-107.
- TRAN, M. Y. & KAMEN, A. A. 2022. Production of Lentiviral Vectors Using a HEK-293 Producer Cell Line and Advanced Perfusion Processing. *Front Bioeng Biotechnol*, 10:887716.
- TRÉPANIÉ, P., PAYMENT, P. & TRUDEL, M. 1981. Concentration of human respiratory syncytial virus using ammonium sulfate, polyethylene glycol or hollow fiber ultrafiltration. *Journal of Virological Methods*, 3(4):201-211.
- UEDA, M., NAKAJIMA, K. & SUGIURA, A. 1980. Extra RNAs of von Magnus particles of influenza virus cause reduction of particular polymerase genes. *J Virol*, 34(1):1-8.
- URA, T., YAMASHITA, A., MIZUKI, N., OKUDA, K. & SHIMADA, M. 2021. New vaccine production platforms used in developing SARS-CoV-2 vaccine candidates. *Vaccine*, 39(2):197-201.
- VÁZQUEZ-RAMÍREZ, D., JORDAN, I., SANDIG, V., GENZEL, Y. & REICHL, U. 2019. High titer MVA and influenza A virus production using a hybrid fed-batch/perfusion strategy with an ATF system. *Applied Microbiology and Biotechnology*, 103(7):3025-3035.

Bibliography

- VERHELST, J., HULPIAU, P. & SAELENS, X. 2013. Mx proteins: antiviral gatekeepers that restrain the uninvited. *Microbiol Mol Biol Rev*, 77(4):551-66.
- VERHELST, J., PARTHOENS, E., SCHEPENS, B., FIERS, W. & SAELENS, X. 2012. Interferon-inducible protein Mx1 inhibits influenza virus by interfering with functional viral ribonucleoprotein complex assembly. *J Virol*, 86(24):13445-55.
- VESTER, D., RAPP, E., KLUGE, S., GENZEL, Y. & REICHL, U. 2010. Virus–host cell interactions in vaccine production cell lines infected with different human influenza A virus variants: A proteomic approach. *Journal of Proteomics*, 73(9):1656-1669.
- VIGNUZZI, M. & LOPEZ, C. B. 2019. Defective viral genomes are key drivers of the virus-host interaction. *Nat Microbiol*, 4(7):1075-1087.
- VOGEL, O. A. & MANICASSAMY, B. 2020. Broadly Protective Strategies Against Influenza Viruses: Universal Vaccines and Therapeutics. *Front Microbiol*, 11:135.
- VOISARD, D., MEUWLY, F., RUFFIEUX, P. A., BAER, G. & KADOURI, A. 2003. Potential of cell retention techniques for large-scale high-density perfusion culture of suspended mammalian cells. *Biotechnol Bioeng*, 82(7):751-65.
- VON MAGNUS, P. 1951. Propagation of the PR8 strain of influenza A virus in chick embryos. II. The formation of incomplete virus following inoculation of large doses of seed virus. *Acta Pathol Microbiol Scand*, 28(3):278-93.
- VREEDE, F. T., GIFFORD, H. & BROWNLEE, G. G. 2008. Role of initiating nucleoside triphosphate concentrations in the regulation of influenza virus replication and transcription. *J Virol*, 82(14):6902-10.
- WANG, C., FORST, C. V., CHOU, T. W., GEBER, A., WANG, M., HAMOU, W., SMITH, M., SEBRA, R., ZHANG, B., ZHOU, B. & GHEDIN, E. 2020. Cell-to-Cell Variation in Defective Virus Expression and Effects on Host Responses during Influenza Virus Infection. *mBio*, 11(1).
- WANG, C., HONCE, R., SALVATORE, M., CHOW, D., RANDAZZO, D., YANG, J., TWELLS, N. M., MAHAL, L. K., SCHULTZ-CHERRY, S. & GHEDIN, E. 2023. Influenza Defective Interfering Virus Promotes Multiciliated Cell Differentiation and Reduces the Inflammatory Response in Mice. *Journal of Virology*, 97(6):e00493-23.
- WANG, N., DONG, Q., LI, J., JANGRA, R. K., FAN, M., BRASIER, A. R., LEMON, S. M., PFEFFER, L. M. & LI, K. 2010. Viral Induction of the Zinc Finger Antiviral Protein Is IRF3-dependent but NF- κ B-independent. *Journal of Biological Chemistry*, 285(9):6080-6090.
- WANG, S., GODFREY, S., RAVIKRISHNAN, J., LIN, H., VOGEL, J. & COFFMAN, J. 2017. Shear contributions to cell culture performance and product recovery in ATF and TFF perfusion systems. *Journal of Biotechnology*, 246:52-60.
- WANG, W.-C., SAYEDAHMED, E. E., SAMBHARA, S. & MITTAL, S. K. 2022. Progress towards the Development of a Universal Influenza Vaccine. *Viruses*, 14(8):1684.
- WANG, X., HINSON, E. R. & CRESSWELL, P. 2007. The interferon-inducible protein viperin inhibits influenza virus release by perturbing lipid rafts. *Cell Host Microbe*, 2(2):96-105.
- WASIK, M. A., EICHWALD, L., GENZEL, Y. & REICHL, U. 2018. Cell culture-based production of defective interfering particles for influenza antiviral therapy. *Applied Microbiology and Biotechnology*, 102(3):1167-1177.
- WEBER, M., GAWANBACHT, A., HABJAN, M., RANG, A., BORNER, C., SCHMIDT, ANNA M., VEITINGER, S., JACOB, R., DEVIGNOT, S., KOCHS, G., GARCÍA-SASTRE, A. & WEBER, F. 2013. Incoming RNA Virus Nucleocapsids Containing a 5'-Triphosphorylated Genome Activate RIG-I and Antiviral Signaling. *Cell Host & Microbe*, 13(3):336-346.
- WEIR, J. P. & GRUBER, M. F. 2016. An overview of the regulation of influenza vaccines in the United States. *Influenza Other Respir Viruses*, 10(5):354-60.
- WELCH, S. R., SPENGLER, J. R., HARMON, J. R., COLEMAN-MCCRAY, J. D., SCHOLTE, F. E. M., GENZER, S. C., LO, M. K., MONTGOMERY, J. M., NICHOL, S. T. & SPIROPOULOU, C. F. 2022. Defective Interfering Viral Particle Treatment Reduces Clinical Signs and Protects Hamsters from Lethal Nipah Virus Disease. *mBio*, 13(2):e03294-21.
- WELCH, S. R., TILSTON, N. L., LO, M. K., WHITMER, S. L. M., HARMON, J. R., SCHOLTE, F. E. M., SPENGLER, J. R., DUPREX, W. P., NICHOL, S. T. & SPIROPOULOU, C. F. 2020. Inhibition of Nipah Virus by Defective Interfering Particles. *J Infect Dis*, 221(Suppl 4):S460-S470.
- WESTON, S., CZIESO, S., WHITE, I. J., SMITH, S. E., KELLAM, P. & MARSH, M. 2014. A Membrane Topology Model for Human Interferon Inducible Transmembrane Protein 1. *PLOS ONE*, 9(8):e104341.

Bibliography

- WHITTAKER, G., BUI, M. & HELENIUS, A. 1996. The role of nuclear import and export in influenza virus infection. *Trends in Cell Biology*, 6(2):67-71.
- WOODGATE, J. M. 2018. Chapter 37 - Perfusion N-1 Culture—Opportunities for Process Intensification. In: JAGSCHIES, G., LINDSKOG, E., ŁACKI, K. & GALLIHER, P. (eds.) *Biopharmaceutical Processing*. Elsevier.
- WU, M., ZHOU, E., SHENG, R., FU, X., LI, J., JIANG, C. & SU, W. 2022. Defective Interfering Particles of Influenza Virus and Their Characteristics, Impacts, and Use in Vaccines and Antiviral Strategies: A Systematic Review. *Viruses*, 14(12):2773.
- WU, W., ZHANG, W., DUGGAN, E. S., BOOTH, J. L., ZOU, M. H. & METCALF, J. P. 2015. RIG-I and TLR3 are both required for maximum interferon induction by influenza virus in human lung alveolar epithelial cells. *Virology*, 482:181-8.
- WU, Y., BISSINGER, T., GENZEL, Y., LIU, X., REICHL, U. & TAN, W. S. 2021. High cell density perfusion process for high yield of influenza A virus production using MDCK suspension cells. *Appl Microbiol Biotechnol*, 105(4):1421-1434.
- XIAO, H., KILLIP, M. J., STAEHELI, P., RANDALL, R. E. & JACKSON, D. 2013. The Human Interferon-Induced MxA Protein Inhibits Early Stages of Influenza A Virus Infection by Retaining the Incoming Viral Genome in the Cytoplasm. *Journal of Virology*, 87(23):13053-13058.
- XIAO, Y., LIDSKY, P. V., SHIROGANE, Y., AVINER, R., WU, C. T., LI, W., ZHENG, W., TALBOT, D., CATCHING, A., DOITSH, G., SU, W., GEKKO, C. E., NAYAK, A., ERNST, J. D., BRODSKY, L., BRODSKY, E., ROUSSEAU, E., CAPPONI, S., BIANCO, S., NAKAMURA, R., JACKSON, P. K., FRYDMAN, J. & ANDINO, R. 2021. A defective viral genome strategy elicits broad protective immunity against respiratory viruses. *Cell*, 184(25):6037-6051 e14.
- XU, J., MERCADO-LOPEZ, X., GRIER, J. T., KIM, W. K., CHUN, L. F., IRVINE, E. B., DEL TORO DUANY, Y., KELL, A., HUR, S., GALE, M., JR., RAJ, A. & LOPEZ, C. B. 2015. Identification of a Natural Viral RNA Motif That Optimizes Sensing of Viral RNA by RIG-I. *mBio*, 6(5):e01265-15.
- XU, J., SUN, Y., LI, Y., RUTHEL, G., WEISS, S. R., RAJ, A., BEITING, D. & LÓPEZ, C. B. 2017. Replication defective viral genomes exploit a cellular pro-survival mechanism to establish paramyxovirus persistence. *Nature Communications*, 8(1):799.
- YAMAGATA, Y., MURAMOTO, Y., MIYAMOTO, S., SHINDO, K., NAKANO, M. & NODA, T. 2019. Generation of a purely clonal defective interfering influenza virus. *Microbiol Immunol*, 63(5):164-171.
- YANG, Y., LYU, T., ZHOU, R., HE, X., YE, K., XIE, Q., ZHU, L., CHEN, T., SHEN, C., WU, Q., ZHANG, B. & ZHAO, W. 2019. The Antiviral and Antitumor Effects of Defective Interfering Particles/Genomes and Their Mechanisms. *Front Microbiol*, 10:1852.
- YAO, S., NARAYANAN, A., MAJOWICZ, S. A., JOSE, J. & ARCHETTI, M. 2021. A synthetic defective interfering SARS-CoV-2. *PeerJ*, 9:e11686.
- YONEYAMA, M., KIKUCHI, M., MATSUMOTO, K., IMAIZUMI, T., MIYAGISHI, M., TAIRA, K., FOY, E., LOO, Y. M., GALE, M., JR., AKIRA, S., YONEHARA, S., KATO, A. & FUJITA, T. 2005. Shared and unique functions of the DExD/H-box helicases RIG-I, MDA5, and LGP2 in antiviral innate immunity. *J Immunol*, 175(5):2851-8.
- YONEYAMA, M., KIKUCHI, M., NATSUKAWA, T., SHINOBU, N., IMAIZUMI, T., MIYAGISHI, M., TAIRA, K., AKIRA, S. & FUJITA, T. 2004. The RNA helicase RIG-I has an essential function in double-stranded RNA-induced innate antiviral responses. *Nat Immunol*, 5(7):730-7.
- YUE, J., LIU, Y., ZHAO, M., BI, X., LI, G. & LIANG, W. 2023. The R&D landscape for infectious disease vaccines. *Nature reviews. Drug discovery*, 22(11):867-868.
- ZANLUCA, C., MELO, V. C. A. D., MOSIMANN, A. L. P., SANTOS, G. I. V. D., SANTOS, C. N. D. D. & LUZ, K. 2015. First report of autochthonous transmission of Zika virus in Brazil. *Memórias do Instituto Oswaldo Cruz*, 110:569-572.
- ZHANG, W., ZHANG, L., ZAN, Y., DU, N., YANG, Y. & TIEN, P. 2015. Human respiratory syncytial virus infection is inhibited by IFN-induced transmembrane proteins. *Journal of General Virology*, 96(1):170-182.
- ZHANG, Y. & NAGALO, B. M. 2022. Immunovirotherapy Based on Recombinant Vesicular Stomatitis Virus: Where Are We? *Front Immunol*, 13:898631.
- ZHAO, H., TO, K. K. W., CHU, H., DING, Q., ZHAO, X., LI, C., SHUAI, H., YUAN, S., ZHOU, J., KOK, K. H., JIANG, S. & YUEN, K. Y. 2018. Dual-functional peptide with defective interfering genes effectively protects mice against avian and seasonal influenza. *Nat Commun*, 9(1):2358.

Bibliography

- ZHAO, Z., ANSELMO, A. C. & MITRAGOTRI, S. 2022. Viral vector-based gene therapies in the clinic. *Bioengineering & Translational Medicine*, 7(1):e10258.
- ZHOU, B., MELIOPOULOS, V. A., WANG, W., LIN, X., STUCKER, K. M., HALPIN, R. A., STOCKWELL, T. B., SCHULTZ-CHERRY, S. & WENTWORTH, D. E. 2016. Reversion of Cold-Adapted Live Attenuated Influenza Vaccine into a Pathogenic Virus. *J Virol*, 90(19):8454-63.
- ZHU, Q., LU, B., MCTAMNEY, P., PALASZYNSKI, S., DIALLO, S., REN, K., ULBRANDT, N. D., KALLEWAARD, N., WANG, W., FERNANDES, F., WONG, S., SVABEK, C., MOLDT, B., ESSER, M. T., JING, H. & SUZICH, J. A. 2018. Prevalence and Significance of Substitutions in the Fusion Protein of Respiratory Syncytial Virus Resulting in Neutralization Escape From Antibody MEDI8897. *The Journal of Infectious Diseases*, 218(4):572-580.
- ZINNECKER, T., BADRI, N., ARAUJO, D., THIELE, K., REICHL, U. & GENZEL, Y. 2024. From single-cell cloning to high-yield influenza virus production – implementing advanced technologies in vaccine process development. *Engineering in Life Sciences*:2300245.
- ZOST, S. J., PARKHOUSE, K., GUMINA, M. E., KIM, K., DIAZ PEREZ, S., WILSON, P. C., TREANOR, J. J., SANT, A. J., COBEY, S. & HENSLEY, S. E. 2017. Contemporary H3N2 influenza viruses have a glycosylation site that alters binding of antibodies elicited by egg-adapted vaccine strains. *Proceedings of the National Academy of Sciences*, 114(47):12578-12583.
- ZÜRCHER, T., PAVLOVIC, J. & STAEHEL, P. 1992. Mouse Mx2 protein inhibits vesicular stomatitis virus but not influenza virus. *Virology*, 187(2):796-800.

Appendix

Appendix A - SOP: Preparation of Xeno™ medium

- (1) Add the final volume of Milli-Q® water at 30–37°C
- (2) Start stirring, but avoid bubbles
- (3) Gently add Xeno™ powder at 20.02 g/L to water and mix for 20 min
- (4) Adjust pH to 6.3–6.7 with sodium hydroxide powder and mix for 20 min
- (5) Precisely add 2.00 g/L sodium bicarbonate powder and mix for 20 min
- (6) When everything is completely dissolved, adjust pH to 6.8–7.2 (if needed)
- (7) Filter sterilize by 0.22 µm pore size membrane filtration
- (8) After filtration, store at 2–8°C for up to one month. Protect from light.
- (9) Add glutamine before usage

Appendix B - List of chemicals and reagents

Chemicals and reagents used for studies at MPI and McGill University, Montreal, Canada are listed in Table A1 and the corresponding paper, respectively.

Table A1: List of chemicals and reagents

Name	Manufacturer	Article Number
Acetic acid 99%	Roth	7332.1
Aceton 100%	Roth	9372.6
Agar	Roth	AE93.1
Agarose	Roth	3810.5
Alexa Fluor 488-donkey anti-sheep igG cross-adsorbed antibody	Thermo Fisher Scientific	A-11015
Alexa Fluor 647-conjugated polyclonal goat anti-mouse	Thermo Fisher Scientific	A21235
BSA	Merck	A3912
Buffer solution	Mettler Toledo	Technical Buffer Solution 7.00 and 9.21
Carboxymethyl cellulose	Merck	21902
Crystal violet	Merck	42555
DAPI	Invitrogen	D1306
Dimethyl sulphoxide	Roth	A994.1
DMEM	Thermo Fisher Scientific	41966029
dNTPs	Thermo Fisher Scientific	R0182
EDTA	Merck	ED2SS
Ethanol 70% (v/v)	Roth	T868.2
Ethanol 96%	Roth	P075.4
FastDigest Green Buffer	Thermo Fisher Scientific	B72
FBS	Merck Thermo Fisher Scientific	F7524 10270
Fidaxomicin	MedChemExpress	HY-17580
GeneRuler DNA Ladder Mix	Thermo Fisher Scientific	SM0333
Gentamicin	Thermo Fisher Scientific	15710-049
Glycin	Roth	3908.2
Glyoxal 40%	Roth	HN492
GMEM	Thermo Fisher Scientific	221000093
IFN- β -1a	PBL assay Science	11410
Isopropanol	Roth	6752.5
L-glutamine	Merck	G8540
Maxima H minus reverse transcriptase	Thermo Fisher Scientific	EP0751
Methanol	Roth	4627.6
Naphthalin blue black	Merck	N3393
NucleoSpin RNA kit	Macherey-Nagel	740955
NucleoSpin RNA virus kit	Macherey-Nagel	740956
Penicillin Streptomycin	Thermo Fisher Scientific	15140122
PFA 4%	Morphisto	11762
Phusion High-Fidelity DNA Polymerase 5x Phusion HF Buffer 5x Phusion GC Buffer MgCl ₂	Thermo Fisher Scientific	F530L
Puromycin	Thermo Fisher Scientific	A1113803
QuantiNova SYBR green PCR master mix	Qiagen	208056
Ribavirin	Cayman	16757-5

Appendix

RiboLock RNase inhibitor	Thermo Fisher Scientific	EO0384
Roti-GelStain	Roth	3865.1
Rotor-Gene SYBR Green PCR kit	Qiagen	204074
RPMI1640	Thermo Fisher Scientific	12633012
Ruxolitinib	Cayman	11609
Sodium acetate powder	Merck	S2889
Sodium bicarbonate powder	Roth	HN01.3
Sodium hydroxide pellets	Merck	1310-73-2
Sodium hypochlorite solution	Roth	9062.3
Sorbitol	Merck	S1876
Sucrose	Merck	84097
Trypan blue	Merck	93595
Trypsin	Thermo Fisher Scientific	27250
Tryptose/Peptone	Lab M	MC033
VP-SFM	Thermo Fisher Scientific	11681020
β -mercaptoethanol	Merck	M6250

Appendix C - List of equipment and consumables

Equipment and consumables used for studies at MPI and McGill University, Montreal, Canada are listed in Table A2 and the corresponding paper, respectively.

Table A2: List of equipment and consumables

Name	Manufacturer	Article Number
125 mL shake flasks	Corning Thermo Fisher Scientific	1356244 4116-0125
24-well plate	Greiner	662160
250 mL shake flasks	Corning Thermo Fisher Scientific	1356246 4116-0250
6-well plate	Greiner	657160
96-well plate F-bottom	Greiner	655180
96-well plate U-bottom	Greiner	650101
Agarose gel electrophoresis equipment	Neolab VWR Biometra	Elektrophoresekammer Power Source 300V BioDocAnalyzer
ATF system with controller	Repligen	ATF2 with C24U-v2 controller
Autoclave	HP Medizintechnik	Varioklav 65T Varioklav 135S
Balance	Sartorius	Cubis Precision
Bioreactor System	Eppendorf	DASGIP Parallel Bioreactor System
Bottle-top sterile filter unit	Nalgene	Z358215
Capacitance sensor equipment	Hamilton	Incyte Unit DN12-220 Arc View 265 Analog 4–20 mA Output Box
Cell counter	Beckman Coulter	Vi-Cell XR
Centrifuge	Sigma Thermo Scientific Thermo Scientific Nippon Genetics	4-16KS Heraeus Biofuge Primo R Heraeus Pico 17 FastGene Plate Centrifuge
CO ₂ incubator	Heracell	150i
DO probe	Hamilton	OxyFerm FDA 225
Heating water bath	IKA	HB 4 basic
Imaging Flow Cytometer	Cytek	ImageStreamX MkII
Incubation shaker	Infors HT	Multitron Pro
Metabolite analyzer	Roche	Cedex Bio Analyzer
Microplate reader	Tecan	Infinite 200 Pro NanoQuant
Microscope	Zeiss	Axiovert A1
Polyethersulfone membrane (0.2 µm, 470 cm ²)	Spectrum Labs	
pH meter	inoLab	pH7110
pH probe	Hamilton	EasyFerm Plus PHI K8 225
Platform shaker	Heidolph	Duomax 1030
Pump	Watson-Marlow	120U
Qiagility	Qiagen	9001908
Real-time PCR cyclcr	Qiagen	Rotor-Gene Q
Rotor-Disc Heat Sealer	Qiagen	9019725
T175 flasks	Greiner	660175
T75 flasks	Greiner	658175
Temperature probe	Eppendorf	78103304

Appendix

TFDF system	Repligen	Krosflo
Thermocycler	Biometra	T Professional Thermocycler
Ultrasonic homogenizer	Hielscher	UP200St
Vortexer	Heidolph	Reax control

Curriculum Vitae

The Curriculum Vitae section is empty in the electronic PDF version of this dissertation according to paragraph 4.1.1. of the Regulations for the submission of depositary copies to the library of the Otto von Guericke University Magdeburg within the framework of doctoral and habilitation procedures as of 5th November 2019.

List of Publications

Publications of this cumulative dissertation

First Manuscript:

Pelz, L.*; Rüdiger, D.*; Dogra, T.*; Alnaji, F.G.; Genzel, Y.; Brooke, C.B.; Kupke, S.Y.; Reichl, U. (2021) Semi-continuous propagation of influenza A virus and its defective interfering particles: Analyzing the dynamic competition to select candidates for antiviral therapy. *J Virol* 95:e01174-21

Individual contribution: In the study of the first manuscript, I carried out the semi-continuous propagation of IAV and DIPs (Figure 1), multiplication of new candidate Seg 1 DIPs in MDCK-PB2(sus) cells and interference assay (Figure 7). In addition, I investigated the processed NGS data for Figure 2, 3, 4, 5, 6 with Daniel Rüdiger, who performed the computational data analysis. Moreover, I wrote major parts of the manuscript.

Second Manuscript:

Rüdiger, D.*; **Pelz, L.*;** Hein, M.D.; Kupke, S.Y.; Reichl, U. (2021) Multiscale model of defective interfering particle replication for influenza A virus infection in animal cell culture. *PLoS Comput Biol* 17(9): e1009357

Individual contribution: In the study of the second manuscript, I generated data for mathematical modeling that includes performing infection experiments and quantification of “active DIP titer” by plaque assay (both together with Marc Hein), analyzing real-time RT-qPCR data and conducting of imaging flow cytometry. Moreover, I wrote corresponding parts of the materials & methods section.

Third manuscript:

Pelz, L.; Piagnani, E.; Marsall, P.; Wynserski, N.; Hein, M.D.; Marichal-Gallardo, P.; Kupke, S.Y.; Reichl, U. (2023) Broad-spectrum antiviral activity of influenza A virus defective interfering particles against respiratory syncytial, yellow fever and Zika virus replication in vitro. *Viruses* 2023, 15, 1872

Individual contribution: The study of the third manuscript comprises parts of the supervised Master’s theses of Elena Piagnani (RSV) and Patrick Marsall (YFV) and experiments carried out by Nancy Wynserski (ZIKV). I designed experiments, analyzed and visualized data, and wrote the manuscript.

Fourth manuscript:

Dogra, T.; **Pelz, L.;** Böhme, J.D.; Küchler, J.; Kershaw, O.; Marichal-Gallardo, P.; Bälkner, M.; Hein, M.D.; Gruber, A.; Benndorf, D.; Genzel, Y.; Bruder, D.; Kupke, S.Y.; Reichl, U. (2023) Generation of “OP7 chimera” defective interfering influenza A particle preparations free of infectious virus that show antiviral efficacy in mice. *Scientific Reports* (2023) 13:20936

List of Publications

Individual contribution: In the study of the fourth manuscript, I carried out the cell culture-based production for Figure 2, 3, and 4, and performed the in vitro interference assay shown in Figure 4. Moreover, I produced OP7 chimera DIP material in shake flasks for testing in animals shown in Figure 5 and 6. In addition, I analyzed and visualized data, wrote results section, and minor parts of materials & methods and discussion sections.

Fifth manuscript:

Pelz, L.; Dogra, T.; Marichal-Gallardo, P.; Hein, M.D.; Hemissi, G.; Kupke, S.Y.; Genzel, Y.; Reichl, U. (2024) Production of antiviral “OP7 chimera” defective interfering particles free of infectious virus. *Appl Microbiol Biotechnol* 108, 97

Individual contribution: In the study of the fifth manuscript, I carried out the experiments shown in Figure 2, 3, and 5. In addition, I visualized data, wrote the abstract and results section (except for Figure 4) and major parts of materials & methods and discussion section.

Sixth manuscript

Göbel, S.*; **Pelz, L.*;** Silva, C.A.T.; Brühlmann, B.; Hill, C.; Altomonte, J.; Kamen, A.; Reichl, U.; Genzel, Y. (2023) Production of recombinant vesicular stomatitis virus-based vectors by tangential flow depth filtration. *Appl Microbiol Biotechnol* 108, 240

Individual contribution: In the study of the sixth manuscript, for Figure 6 and 7, I carried out the experiments, visualized data, wrote the results, discussion, and materials & methods section.

*These authors contributed equally to this work.

Book chapters

Pelz, L.; Göbel, S.; Jaen, K.; Reichl, U.; Genzel, Y. (2022) Upstream processing for viral vaccines - General aspects. In: Kamen A, Cervera L (eds) *Bioprocessing of Viral Vaccines*. CRC Press, Boca Raton

Göbel, S.; **Pelz, L.;** Reichl, U.; Genzel, Y. (2022) Upstream processing for viral vaccines - Process Intensification. In: Kamen A, Cervera L (eds) *Bioprocessing of Viral Vaccines*. CRC Press, Boca Raton

Supervised theses

Baumeister, M. (2021) Evolution of influenza A virus defective interfering particles in a continuous culture. Master's thesis. Department of Biotechnology, University of Applied Sciences Mannheim, Germany

Marsall, P. (2021) Yellow fever virus replication: Inhibition by influenza A virus defective interfering particles. Master's thesis. Faculty of Life Sciences, Albstadt-Sigmaringen University, Germany

Piagnani, E. (2022) Respiratory syncytial virus replication: Inhibition by influenza A virus defective interfering particles. Master's thesis. Department of Biotechnology, University of Rijeka, Croatia

Talks

Pelz, L.; Rüdiger, D.; Alnaji, F.G.; Genzel, Y.; Brooke, C.B.; Kupke, S.Y.; Reichl, U. (2020) Evolution and selection of influenza A virus defective interfering particles in a semi-continuous production system for the use as antiviral. 7th ESWI Influenza Conference, virtual

Pelz, L.; Rüdiger, D.; Dogra, T.; Alnaji, F.G.; Genzel, Y.; Brooke, C.B.; Kupke, S.Y.; Reichl, U. (2022) Long-term propagation of influenza A virus and its defective interfering particles: Analyzing dynamic competition to select antiviral candidates. Vaccine Technology VIII, Sitges, Spain (poster short talk)

Pelz, L.; Rüdiger, D.; Dogra, T.; Alnaji, F.G.; Genzel, Y.; Brooke, C.B.; Kupke, S.Y.; Reichl, U. (2022) Semi-continuous propagation of influenza A virus and its defective interfering particles: Analyzing the dynamic competition to select antiviral candidates. 27th ESACT Meeting, Lisbon, Portugal (poster students highlights presentation)

Pelz, L.; Dogra, T.; Böhme, J.D.; Hein, M.D.; Marichal-Gallardo, P.; Genzel, Y.; Bruder, D.; Kupke, S.Y.; Reichl, U. (2023) Influenza A virus OP7 defective interfering particles: Cell culture-based production and antiviral efficacy in vivo. Cell Culture Engineering XVIII, Cancun, Mexico (flask talk)

Posters

Pelz, L.; Rüdiger, D.; Alnaji, F.G.; Genzel, Y.; Brooke, C.B.; Kupke, S.Y.; Reichl, U. (2021) Semi-continuous propagation of influenza A virus and its defective interfering particles: Analyzing the dynamic competition to select antiviral candidates. 30th Annual Meeting of the Society for Virology 2021, virtual

Pelz, L.; Rüdiger, D.; Dogra, T.; Alnaji, F.G.; Genzel, Y.; Brooke, C.B.; Kupke, S.Y.; Reichl, U. (2022) Long-term propagation of influenza A virus and its defective interfering particles: Analyzing dynamic competition to select antiviral candidates. Vaccine Technology VIII, Sitges, Spain

Pelz, L.; Rüdiger, D.; Dogra, T.; Alnaji, F.G.; Genzel, Y.; Brooke, C.B.; Kupke, S.Y.; Reichl, U. (2022) Semi-continuous propagation of influenza A virus and its defective interfering particles: Analyzing the dynamic competition to select antiviral candidates. 27th ESACT Meeting, Lisbon, Portugal

List of Publications

Pelz, L.; Dogra, T.; Böhme, J.D.; Marichal-Gallardo, P.; Hein, M.D.; Genzel, Y.; Bruder, D.; Kupke, S.Y.; Reichl, U. (2023) Influenza A virus chimeric OP7 defective interfering particles: Cell culture-based production and in vivo antiviral efficacy. 32th Annual Meeting of the Society for Virology 2023, Ulm, Germany

Pelz, L.; Dogra, T.; Böhme, J.D.; Hein, M.D.; Marichal-Gallardo, P.; Genzel, Y.; Bruder, D.; Kupke, S.Y.; Reichl, U. (2023) Influenza A virus OP7 defective interfering particles: Cell culture-based production and antiviral efficacy in vivo. Cell Culture Engineering XVIII, Cancun, Mexico

Pelz, L.; Dogra, T.; Böhme, J.D.; Marichal-Gallardo, P.; Hein, M.D.; Genzel, Y.; Bruder, D.; Kupke, S.Y.; Reichl, U. (2023) A scalable high-yield process for production of influenza A virus defective interfering particles and in vivo studies. Himmelfahrtstagung on Bioprocess Engineering 2023, Weimar, Germany

Declaration of Honor

I hereby declare that I produced this thesis without prohibited external assistance and that none other than the listed references and tools have been used.

In the case of co-authorship, especially in the context of a cumulative dissertation, the own contribution is correctly and completely stated. I did not make use of any commercial consultant concerning graduation. A third party did not receive any nonmonetary perquisites neither directly nor indirectly for activities which are connected with the contents of the presented thesis. All sources of information are clearly marked, including my own publications.

In particular I have not consciously:

- Fabricated data or rejected undesired results,
- Misused statistical methods with the aim of drawing other conclusions than those warranted by the available data,
- Plagiarized data or publications,
- Presented the results of other researchers in a distorted way.

I do know that violations of copyright may lead to injunction and damage claims of the author and also to prosecution by the law enforcement authorities.

I hereby agree that the thesis may need to be reviewed with an electronic data processing for plagiarism.

This work has not yet been submitted as a doctoral thesis in the same or a similar form in Germany or in any other country. It has not yet been published as a whole.

Penzberg, 15.03.2024

Lars Pelz